TECHNISCHE UNIVERSITÄT DRESDEN

Faculty of Physics Institute of Solid State and Materials Physics, Chair of Surface Physics

Two-dimensional ferromagnetism, strong Rashba effect and valence changes in lanthanide intermetallics

A photoemission study

Susanne Schulz

Dissertation

TECHNISCHE UNIVERSITÄT DRESDEN

Faculty of Physics Institute of Solid State and Materials Physics, Chair of Surface Physics

Two-dimensional ferromagnetism, strong Rashba effect and valence changes in lanthanide intermetallics

A photoemission study

Susanne Schulz

Dissertation

to achieve the academic degree

Doktor der Naturwissenschaften (Dr. rer. nat.)

Supervisors
Professor Denis V. Vyalikh (DIPC)
Professor Clemens Laubschat (TU Dresden)

Submitted on: 24 October 2022
Defended on: 1 March 2023

First referee
Professor Clemens Laubschat

Second referee
Professor Evgueni V. Chulkov

Kurzzusammenfassung

Die Suche nach neuartigen Technologien wie spinbasierte Elektronik sowie nach geeigneten Materialien für entsprechende Bauteile erfordert ein tiefgreifendes Verständnis der Wechselwirkungen des Elektronenspins und damit verbundener Materialeigenschaften. Mit der zunehmenden Miniaturisierung von Bauteilen gewinnen in diesem Zusammenhang auch Oberflächenphänomene zunehmend an Bedeutung. In dieser Arbeit untersuchen wir die elektronischen und magnetischen Eigenschaften quasizweidimensionaler elektronischer Zustände an metallischen Oberflächen unter dem Einfluss des Rashba-Effekts und der Austauschwechselwirkung mit lokalisierten $4f$ Momenten, die bei tiefen Temperaturen magnetisch ordnen. Dabei liegt die Besonderheit der untersuchten Systeme darin, dass beide Wechselwirkungen von vergleichbarer Stärke sind. Dieser Fall ist in der Fachliteratur bislang unterrepräsentiert. Unser Modellsystem ist die (001)-Oberfläche intermetallischer $Ln\mathrm{Ir_2Si_2}$ Verbindungen mit $\mathrm{ThCr_2Si_2}$ Struktur, wobei Ln ein Lanthanoidenelement darstellt. Dabei führen wir die langjährige und systematische Untersuchung von $LnT_2\mathrm{Si_2}$ Verbindungen mit $T = \mathrm{Rh}$ fort, in denen die Rashba-artige Spin-Bahn-Kopplung ungefähr 100-mal schwächer als die Austauschwechselwirkung ist.

Mit Hilfe von winkelaufgelöster Photoelektronenspektroskopie (ARPES) und Dichtefunktionaltheorie (DFT) erkunden wir mit $\mathrm{GdIr_2Si_2}$ und $\mathrm{EuIr_2Si_2}$ zwei Vertreter der $LnT_2\mathrm{Si_2}$ Familie, die beide durch die Insensibilität der $4f$ Schale gegenüber dem Kristallfeld ausgezeichnet sind. Zugleich haben sie grundsätzlich verschiedene Volumeneigenschaften. $\mathrm{GdIr_2Si_2}$ ist ein robuster Volumenantiferromagnet mit einer hohen Ordnungstemperatur von 87 K, wohingegen $\mathrm{EuIr_2Si_2}$ eine gemischtvalente Verbindung mit einem nicht-magnetischen Volumengrundzustand ist. Die mittlere Eu Valenz ist stark temperaturabhängig, sie ändert sich kontinuierlich von einer nahezu zweiwertigen Konfiguration bei Raumtemperatur zu einem beinahe dreiwertigen, nicht-magnetischen Eu Zustand unterhalb von ~ 50 K.

Die Untersuchung der Oberflächenzustände in beiden Verbindungen zeigt, dass die Stärke der Rashba-artigen Spin-Bahn-Kopplung gegenüber den isoelektronischen Rh Verbindungen erheblich zunimmt. Dies spiegelt sich in einer riesigen Aufspaltung der Oberflächenbänder wider und unterstreicht die Bedeutung der atomaren Spin-Bahn-Kopplung in Elementen mit großer Kernzahl Z für die Stärke des Rashba-Effekts. Unsere DFT Rechnungen reproduzieren die gemessene Bandstruktur mit hoher Genauigkeit und offenbaren dieselbe Dreifachwindung des Spins entlang der Konturen konstanter Energie, die schon als kubischer Rashba-Effekt in den Rh Verbindungen beobachtet wurde. Hierin zeigt sich das allgemeingültige Wesen der Oberflächenzustände und deren universelle Eigenschaften in den betrachteten $LnT_2\mathrm{Si_2}$ Verbindungen. Das Ordnen der $4f$ Momente bei niedrigen Temperaturen führt zu starken Veränderungen in der Spinstruktur und der Dispersion der Oberflächenbänder durch die einsetzende Austauschwechselwirkung. In der Bandstruktur bilden sich starke Asymmetrien, aus denen die Magnetisierungsachse bestimmt werden kann. Wir zeigen, dass dies sogar dann noch möglich ist, wenn sich spektrale Strukturen überlagern, die von unterschiedlichen magnetischen Domänen stammen. Besonders bemerkenswert ist, dass entsprechende Asymmetrien auch in $\mathrm{EuIr_2Si_2}$ auftreten, trotz des nahezu

dreiwertigen und damit nicht-magnetischen Eu bei tiefen Temperaturen. Mit komplementären experimentellen Methoden wie Röntgenabsorption, linearem und zirkularem Röntgendichroismus als auch durch die Berücksichtigung von Beugungseffekten in der Photoelektronenspektroskopie zeigen wir, dass Eu im Si–Ir–Si–Eu Oberflächenblock beinahe zweiwertig und magnetisch aktiv ist. Die zugehörigen Eu Momente ordnen unterhalb von 49 K ferromagnetisch. Im Fall der Eu-Terminierung stellen wir fest, dass auch die $4f$ Momente der zweiwertigen Eu-Ionen an der Oberfläche unterhalb von 10 K ferromagnetisch geordnet sind, und enthüllen damit ein weiteres Vorkommen zweidimensionalen, oberflächenbezogenen Magnetismus in derselben, nichtmagnetischen Volumenverbindung. Gleichzeitig spiegeln sich die gemischtvalenten Eigenschaften von $EuIr_2Si_2$ deutlich in der elektronischen Volumenbandstruktur in einer kontinuierlichen Ausdehnung der Doughnut-Fermifläche mit steigender Temperatur wider. Dies interpretieren wir als Bandfüllungseffekt.

Unsere Ergebnisse zeigen die hohe Einstellbarkeit des Elektronenspins durch die Kombination von Spin-Bahn-Kopplung und struktureller Inversionsasymmetrie mit der Austauschwechselwirkung, was die Grundlage für Anwendungen in der spinbasierten Elektronik bildet. Die Enthüllung von kontrollierbarem, zweidimensionalem Magnetismus an der Oberfläche einer Verbindung mit instabiler $4f$ Schale, die im Volumen nicht-magnetisch ist, nominiert gemischtvalente $4f$ Verbindungen, insbesondere mit Eu und Sm, als vielversprechende Kandidaten für Grundlagenforschung und Anwendungen. Unsere Studie zeigt zudem den Reichtum und die Vielseitigkeit von $4f$ Systemen, deren Eigenschaften sich an der Oberfläche deutlich vom Volumen unterscheiden können.

Abstract

The search for novel technologies like spin-based electronics and suitable materials for respective devices requires a profound understanding of fundamental interactions regarding electron spin and related properties. In the same context, with ongoing device miniaturisation, surface-related phenomena become increasingly important. Here, we study the electronic and magnetic properties of quasi-2D electron states at a metallic surface under the influence of the Rashba effect and exchange coupling to localised $4f$ moments that order magnetically at low temperatures. Particularly, in the considered systems, both interactions are of similar strengths, a case which is rather unexplored in the literature. Our model system is the (001) surface of intermetallic $Ln Ir_2Si_2$ compounds with $ThCr_2Si_2$ structure, where Ln = lanthanide. With this work, we continue our long-term systematic study of the LnT_2Si_2 compounds with T = Rh, where the Rashba-like spin-orbit coupling is about a hundred times weaker than the exchange interaction.

Using ARPES and DFT we explore with $GdIr_2Si_2$ and $EuIr_2Si_2$ two representatives of the $Ln Ir_2Si_2$ family, which are both characterised by the insensitivity of the $4f$ shell to the crystal electric field. On the other hand, they have fundamentally different bulk properties. $GdIr_2Si_2$ is a robust bulk antiferromagnet with a high ordering temperature of 87 K, whereas $EuIr_2Si_2$ is a mixed-valent material with a non-magnetic ground state in the bulk. The mean Eu valency is strongly temperature dependent, changing

continuously from a nearly divalent magnetic configuration at room temperature to a nearly trivalent non-magnetic Eu state below $\sim 50\,\mathrm{K}$.

Studying the surface states in both compounds we find that the magnitude of the Rashba-like spin-orbit interaction increases tremendously in comparison to the isoelectronic Rh compounds. This is reflected in a huge splitting of the surface state bands and emphasizes the importance of atomic spin-orbit coupling in high Z elements for the strength of the Rashba effect. Employing DFT, which reproduces the measured band structure very accurately, we find the same exotic triple winding of the electron spin along the isoenergy contours of the surface state bands as reported in terms of a cubic Rashba effect for the Rh compounds. This proves the generic nature of the surface states and their universal properties in the considered LnT_2Si_2 compounds. With the ordering of the $4f$ moments at low temperatures, spin structure and surface band dispersion undergo significant changes induced by the exchange interaction. Pronounced asymmetries emerge in the band dispersion, which allow for the determination of the magnetisation axis. We demonstrate that this is even possible if spectral structures originating from different magnetic domains overlap in the spectra. Remarkably, we find respective asymmetries in $EuIr_2Si_2$, too, despite the almost trivalent, and thus non-magnetic Eu state at low temperatures. With complementary experimental techniques like x-ray absorption, x-ray linear and circular dichroism as well as by taking photoelectron diffraction into account, we demonstrate that in the surface Si–Ir–Si–Eu four-layer block Eu is nearly divalent and magnetically active. The associated Eu moments order ferromagnetically below 49 K. In the case of Eu termination, we find that the $4f$ moments of the divalent Eu ions at the surface order ferromagnetically below 10 K, too, and unveil thus another occurrence of 2D surface-related magnetism in the same non-magnetic bulk compound. Simultaneously, the mixed-valent properties of $EuIr_2Si_2$ and the strong temperature dependence of the mean Eu valency are clearly reflected in the electronic structure of the bulk in a smooth expansion of the Doughnut Fermi surface sheet with increasing temperature, which is interpreted as a band-filling effect.

Our results show the high tunability of the electron spin by combining spin-orbit coupling and structural inversion asymmetry with the exchange interaction, which is at the heart of spintronics applications. The disclosure of controllable 2D magnetism at the surface of a non-magnetic bulk compound, which is enabled by an instability in the $4f$ shell, nominates valence fluctuating $4f$ compounds, especially with Eu and Sm, to be promising candidates for fundamental studies and applications. Our study moreover demonstrates the richness and versatility of $4f$ physics that may differ significantly at the surface and in the bulk.

Contents

1. Introduction **17**

2. Preliminary Studies **23**
2.1. Short introduction to lanthanides and $4f$ physics 23
2.2. LnT_2Si_2 compounds 29

3. Foundations **37**
3.1. Band structure 37
3.2. Bulk states, surface states and surface resonances 39
3.3. The principles of photoelectron spectroscopy 41
3.4. Angle-resolved photoelectron spectroscopy 44
3.5. Photoabsorption and resonant photoelectron spectroscopy 49
3.6. X-ray absorption spectroscopy 50
3.6.1. X-ray magnetic circular dichroism 51
3.6.2. X-ray magnetic linear dichroism 52
3.7. Photoelectron diffraction 52
3.8. Synchrotron and synchrotron radiation 54
3.9. Density functional theory 58

4. Methods **63**
4.1. Experimental details 63
4.2. DFT calculations 65

5. $GdIr_2Si_2$ **69**
5.1. Introduction 69
5.2. Results and discussion 70
5.2.1. Paramagnetic phase 70
5.2.2. Magnetically ordered phase 81
5.3. Summary 93

6. $EuIr_2Si_2$ **95**
6.1. Introduction 95

6.2. Results and discussion 101
6.2.1. Photoemission from the Eu $4f$ shell 101
6.2.2. ARPES on the Si-terminated surface 103
6.2.3. X-ray magnetic linear and circular dichroism 108
6.2.4. Eu termination 113
6.2.5. Determination of the mean Eu valency in the subsurface layers 114
6.2.6. Bulk properties 118
6.3. Summary 119

7. Conclusion **121**

Bibliography **125**

A. Surface relaxation effects **139**

List of publications **141**

Acknowledgements **145**

Statement of authorship **147**

List of Figures

2.1. Eu valency and phase diagram in intermetallic compounds 27
2.2. Eu $4f$ multiplet in photoemission 28
2.3. Crystal structure and Brillouin zone of the $ThCr_2Si_2$ structure 30
2.4. Termination-specific features in the electronic structure of LnT_2Si_2 crystals 30
2.5. Time-reversal and structure inversion symmetries 32
2.6. Classical Rashba effect - dispersion and spin-momentum locking 33
2.7. Generic surface states of the Si-terminated surface in LnT_2Si_2 compounds 34
2.8. Surface state calculated within a tight-binding model for different interactions 35

3.1. Crystal potential in the bulk and at the surface with corresponding solutions of the electronic Schrödinger equation 40
3.2. Relation between PE spectrum and band structure 44
3.3. ARPES setup 45
3.4. Universal curve for the inelastic mean free path 46
3.5. Geometry of an ARPES experiment 47
3.6. Illustration of the deflection mode in ARPES 49
3.7. Photoelectron diffraction - principles 53
3.8. Photoelectron diffraction - data acquisition and stereographic projection 54
3.9. Layout of a synchrotron 55
3.10. Beamline design 57

5.1. Distinguishing surface terminations of $GdIr_2Si_2$ in ARPES 70
5.2. Calculated band weights of $GdIr_2Si_2$ surface states 72
5.3. Single and triple-winding spin structure of the surface states α and γ . 73
5.4. Illustration of different winding numbers 75
5.5. Effective Rashba field for different winding numbers 77
5.6. Comparison of effective Rashba field and spin structure of the surface states 78
5.7. Surface state spin structure calculated with perturbation theory 80

5.8. Magnetic domains reflected in the surface band structure measured with ARPES . . . 82
5.9. Schematic illustration of joint action of Rashba and exchange fields on the spin . . . 83
5.10. $\boldsymbol{k}_{\parallel}$-dependent magnitude of surface-band splitting for Rashba effect and exchange interaction . . . 85
5.11. Details of the surface states' spin and band structure in the PM and magnetically ordered phases . . . 88
5.12. Evolution of the triple spin winding under the influence of the exchange field . . . 91
5.13. Disclosure of the magnetisation direction with ARPES and DFT in presence of magnetic domains . . . 92
5.14. Possible origin of magnetic domains . . . 93

6.1. Temperature of mean Eu valency and lattice parameters of $EuIr_2Si_2$. 96
6.2. Structural, thermal, magnetic and electric properties of $EuIr_2Si_2$ and di- and trivalent reference compounds . . . 98
6.3. Phase diagram of $Eu(Rh_{1-x}Ir_x)Si_2$ . . . 99
6.4. Eu $4f$ resonant photoemission spectra compared for different terminations and temperatures . . . 101
6.5. ARPES- and DFT-derived Fermi maps for the Si-terminated surface of $EuIr_2Si_2$ for different temperatures . . . 104
6.6. Electronic and spin structure of the Si-terminated surface of $EuIr_2Si_2$. 105
6.7. Determination of the onset of the magnetic ordering in the subsurface of $EuIr_2Si_2$ . . . 107
6.8. XMCD for $EuIr_2Si_2$ and a trivalent reference compound . . . 109
6.9. XMLD measured for $EuIr_2Si_2$ . . . 110
6.10. Magnetic circular dichroism in PE from Si-terminated surface of $EuIr_2Si_2$ 112
6.11. Determination of the ordering temperature of Eu at the surface of $EuIr_2Si_2$ 113
6.12. Experimental and calculated PED patterns for Si- and Eu-terminated surfaces of $EuIr_2Si_2$ . . . 115
6.13. PED patterns of single Eu $4f$ multiplet lines for a Si-terminated $EuIr_2Si_2$ surface . . . 117
6.14. Temperature behaviour of the bulk-like band structure of $EuIr_2Si_2$ . . 119

A.1. Dependence of the surface-state bands' energy positions on the interlayer spacings . . . 139

List of Tables

2.1. Electronic configuration of the lanthanide atoms 23
2.2. Quantum numbers of the free lanthanide ions 24

5.1. Magnitude of the extrema in the surface-state band splittings 86

6.1. Comparison of structural parameters for di-, tri- and mixed valent Eu compounds at different temperatures 96

1. Introduction

In traditional electronic devices founded on Si-based semiconductor technology, the processing and storage of information rely on the charge of the electron, which is easily controllable via electric fields. With progressive digitalisation and the continuously growing amount of data, the requirements for the size and performance of electronic devices increase steadily [1]. In 1965 Intel co-founder Moore announced that in regular intervals of about two years the size of computer chips will halve without loss of performance [2]. Nowadays, integrated circuits are already produced at the nanoscale with the size of single components like transistors approaching atomic dimensions. At some point, however, fundamental physical laws will impose a threshold to the ongoing device miniaturisation [3, 4], which stimulates the search for new concepts in information technology and brought another intrinsic property of the electron into focus – the spin. Having all characteristics of a quantised angular momentum the electron spin is associated with an intrinsic spin magnetic moment which can be manipulated by a magnetic field.

Exploiting the spin in addition to (or rather than) the charge of the electron is the idea behind spintronics which promise novel devices with reduced power consumption and increasing memory and processing capabilities in comparison to traditional electronics [5]. With the proposal of the SFET – a spin field effect transistor by Datta and Das in 1990 [6, 7], spintronics started to be seriously considered to become a key element in next-generation information technology and further spin-based concepts have been proposed. Nowadays, intense research is conducted to explore new materials and fundamental mechanisms that allow for full spin control [5, 8] including the generation of spin-polarised currents, spin transport and spin transfer torque [9].

A popular model system for respective studies is the two-dimensional electron gas (2DEG). In real systems, quasi 2DEGs exist in 2D materials or can form at surfaces and interfaces of three-dimensional systems in terms of surface, interface or quantum-well states [10]. In particular, the naturally broken inversion symmetry at surfaces/interfaces in combination with the spin-orbit interaction lead to the spin polarisation and splitting of the quasi-2D states without inducing a net magnetisation; this is known as the Rashba effect [11, 12]. Phenomenologically, the spin splitting of the 2D states in momentum space can be described by an effective magnetic field, the Rashba field, which is theoretically controllable by tuning the electric field emerging

from the surface/interface potential gradient. It is indeed the electric-field control of the spin that makes the Rashba effect so attractive for device application [13]. Particularly, the ability to tune the Rashba field gives control over the spin precession in the SFET, while spin-orbit torque can be used to change the magnetisation direction in storage media [13, 14, 15, 16, 17, 18].

In his original work which dates back to 1959 Rashba conducted a theoretical study on the symmetry of bulk bands in the non-centrosymmetric wurtzite structure type in which many semiconductors crystallise. He predicted a spin splitting of s states near the Γ point ($\boldsymbol{k} = 0$), which increases from zero at Γ linearly and isotropically with crystal momentum $\boldsymbol{k}$ [11, 19]. In the early days, experimental studies of the Rashba effect were thus conducted on bulk materials [19]. In 1984 Rashba and Bychkov showed that the Rashba model is applicable to spin splitting in quasi-2D systems, too, considering the particular case of semiconductor hetero junctions [12, 20]. In 1997 it was shown that the strength of the Rashba spin-orbit interaction is indeed tunable by the application of an external gate voltage [21]. The study of the Rashba effect spilt over to metal surfaces, where in 1996 it was reported for the first time in the context of an ARPES study of the Au(111) surface [22, 23]. In the following, the Rashba effect has been observed for the surface state of Ag(111) [24] and many other metals with a large atomic number Z. Huge splittings were found for Bi(111) [25, 26] and Ir(111) [27] being two orders of magnitude larger than at semiconductor interfaces. The study of metal surfaces revealed the important role of both the atomic spin-orbit coupling as well as the surface potential gradient for the strength of the Rashba effect [19, 22]. For the Ag(111) surface it was shown that the Rashba splitting can be notably increased by alloying the surface with Bi [28]. Meanwhile, 2D states at semiconductor quantum wells and surfaces/interfaces of transition-metal oxides came into the focus of research, too. More exotic realisations of the Rashba effect have been discovered, for instance in heavy-hole states a cubic Rashba effect has been reported that is characterised by a rotation of the pseudospin of the heavy hole that is three times faster than in a classical Rashba system [29, 30].

While the Rashba effect results from broken translational symmetry, the simultaneous breaking of time-reversal symmetry opens another channel for the manipulation of the Rashba-induced spin structure and splitting. This can be realised, for example, via an exchange coupling of the 2DEG spins to collectively ordered magnetic moments. This was first shown in 2005 in the work of Krupin et al. who studied 2DEGs at the Gd(0001) surface and in the Gd(0001)/GdO interface and found that asymmetries evolve in the surface band dispersion if the electrons are subject to both the Rashba effect and exchange interaction with the ferromagnetically ordered Gd $4f$ moments, simultaneously [31]. In these and related lanthanide-based systems studied by Krupin et al., the Rashba spin-orbit interaction is much weaker than the exchange interaction and therefore the observed asymmetry is small [32]. Carbone et al. conducted similar studies on Ag_2Bi/Ag(111) thin films, where the Rashba and exchange interactions are of comparable strength. Their joint action creates asymmetric band gaps which form due to a $\boldsymbol{k}$ and spin-dependent hybridisation between the electron-like surface and hole-like interlayer states and generates spin-polarised currents [33].

In this work, we consider the surface of $4f$ intermetallics investigating the Rashba spin-orbit interaction and its combination with strong and tunable 2D ferromagnetism.

The basis for this study was laid with the discovery of surface states in the Si–Rh–Si–Ln four-layer block at the surface of $Ln\mathrm{Rh_2Si_2}$ compounds [34, 35, 36, 37], where Ln = lanthanide. In particular, one of the surface states shows the cubic Rashba effect with a triple winding of the electron spin along its isoenergy contours. With the magnetic ordering of the $4f$ moments the spin and band structure experience significant changes [37]. A high tunability in addition to the generic nature of the 2DEGs in the family of $LnT_2\mathrm{Si_2}$ compounds, with T being one of the isoelectronic elements Co, Rh or Ir, make the silicide surface an ideal model system for systematic studies of the Rashba effect and its combination with exchange interaction. The strength of the Rashba effect can be tuned via the spin-orbit coupling through the atomic number Z of the transition metal element. The exchange interaction can be controlled by temperature and the magnetisation axis of the ordered $4f$ moments. Here, we investigate the respective surface states for T = Ir which has with $Z = 77$ a much larger atomic number than isoelectronic Rh ($Z = 45$). Since the surface states are to a large extent built from transition metal d states, the spin-orbit coupling and the Rashba effect in $Ln\mathrm{Ir_2Si_2}$ compounds are much stronger than in $Ln\mathrm{Rh_2Si_2}$, reaching the same order of magnitude as the exchange interaction [38, 39]. For our study, we consider first the simplest system, the robust antiferromagnet $\mathrm{GdIr_2Si_2}$ with its half-filled $4f$ shell. This configuration is of interest for two reasons. Firstly, the spherical $4f$ shell can be regarded to be insensitive to the crystal electric field (CEF). Secondly, this insensitivity can be accompanied by the tunability of the magnetisation axis under the preservation of the antiferromagnetic (AFM) order with short laser pulses, as it was shown for $\mathrm{GdRh_2Si_2}$ [40]. This makes respective systems attractive for AFM spintronics applications [41, 42, 43, 44].

The $LnT_2\mathrm{Si_2}$ compounds belong to the large group of $4f$ intermetallics which crystallise in the famous $\mathrm{ThCr_2Si_2}$ structure [45] and attract great interest due to their rich variety in exotic properties including Kondo physics [46], quantum criticality [47], unconventional superconductivity [48], exotic magnetic phases and mixed-valent phenomena [49], which are related to the interaction of localised $4f$ with itinerant valence or conduction electrons. On the one hand, the $4f$ electrons are localised close to the atomic core and efficiently screened from the surroundings by the completely filled $5s$ and $5p$ shells. On the other hand, the binding energy of the $4f$ states is small and hybridisation with valence and conduction band states is possible. Of particular interest for fundamental studies are compounds in which the $4f$ shell becomes unstable [50]. This is the case when the energy needed to promote an electron from the localised $4f$ shell into a bonding valence state is similar to the energy that can be gained if this electron participates in chemical bonding. This situation is typically met for the lanthanide elements where the electronic configuration is close to an empty, half-filled or completely filled $4f$ shell [51]. Due to the proximity of the $4f^n(5d6s)^m$ and $4f^{n-1}(5d6s)^{m+1}$ configurations with n, m being non-negative integers, respective systems can be tuned from one toward the other configuration, for example, through temperature, external or chemical pressure as well as exposure to a magnetic field, which often leads to a mixed valence state characterised by a non-integer mean valency. In particular Eu systems are known for mixed-valent states where the mean valency deviates strongly from the purely di- or trivalent state [52, 53]. For divalent $\mathrm{EuRh_2Si_2}$ a first-order phase transition is accompanied by a valence transition from the divalent

into a mixed-valent state at pressures of about 1 GPa, while the divalent state can be recovered by the application of an external magnetic field [54, 55]. Moreover, valence crossovers have been found in different Eu compounds including $EuPd_2Si_2$ [56] and $EuIr_2Si_2$ [57]. In these systems, the mean valency changes smoothly with temperature from an almost divalent to an almost trivalent Eu state in a broad temperature range. In comparison to intermediate valent Ce or Yb systems, mixed-valent behaviour in Eu-based compounds is much less explored [53, 58]. Therefore, the second part of this thesis is dedicated to mixed-valent $EuIr_2Si_2$ where the value of the mean Eu valency changes smoothly from an almost divalent to a nearly trivalent state between room temperature and $\sim$ 50 K [59]. Our study aims at the electronic properties in the near-surface region concerning the mixed-valent state and the modifications of the electronic structure with temperature.

For our study of the electronic structure of the (001) surface in $GdIr_2Si_2$ and $EuIr_2Si_2$ we employed surface-sensitive ARPES with photon energies in the ultraviolet and modelled the experimental results utilizing band structure calculations within the framework of DFT. To investigate the mixed-valent properties of Eu we tuned the photon energy towards the $4d \rightarrow 4f$ absorption threshold, which leads to the resonant enhancement of the photoemission intensity from the $4f$ shell. We moreover conducted x-ray magnetic linear and circular dichroism experiments that are valuable techniques to detect magnetic order with the possibility to distinguish between bulk and surface. Consideration of photoelectron diffraction in our resonant photoemission experiments allowed us to access single Eu layers separately for studying their individual properties.

The most important findings of this work can be summarised as follows. First of all, we find that the replacement of Rh by Ir in the LnT_2Si_2 compounds significantly increases the Rashba effect, which is reflected in a huge splitting of the surfaces state bands in the paramagnetic phase that we probed with ARPES for both $GdIr_2Si_2$ and $EuIr_2Si_2$. The exotic triple-winding spin structure persists in the Ir compound emphasising the generic character of the surface states and the close relation to the crystal structure. Studying the magnetic phase of $GdIr_2Si_2$ we could identify the yet unknown magnetisation axis to coincide with the [110] direction. Since the Rashba-like spin-orbit coupling and the exchange interaction between the itinerant surface state electrons and the ordered $4f$ moments are of similar magnitude, we find strong asymmetries in the surface band dispersion of the magnetic phase which are most pronounced when the strongly $\boldsymbol{k}_{\parallel}$ dependent Rashba and the exchange field which is unidirectional in $\boldsymbol{k}_{\parallel}$ space, are collinear. For mixed-valent $EuIr_2Si_2$ we found a ferromagnetically ordered Eu monolayer under the Si-terminated surface and thus quasi-2D magnetism at the surface of a material that is non-magnetic in the bulk, which, up to our knowledge is the first observation of this kind for a valence-fluctuating Eu system. The magnetic order is enabled by a deviation of the valency from its mean value in the bulk towards a divalent configuration. The magnetic ordering was detected by exploiting the sensitivity of the surface state to the magnetic ordering of the $4f$ moments in the subsurface layer which is reflected in the evolution of the pronounced asymmetry in the band dispersion in comparison to the paramagnetic phase. For the Eu-terminated surface where due to the surface-core-level shift Eu is stable divalent, we observe the magnetic ordering of the respective $4f$ moments at low temperatures. With this, we find a second source of 2D ferromagnetism at the surface of this actually

non-magnetic Eu system. In contrast, bulk-like features in the electronic structure change their size with temperature, thus reflecting the change of the intermediate valency.

This thesis is structured as follows. At first, an introduction into the properties of the lanthanides in their elemental form as well as in metals or compounds is given with a special focus on the role of the incompletely filled $4f$ shell. This is followed by a short review of the previous studies on the surface electronic structure of $Ln\mathrm{Rh_2Si_2}$ compounds which form the starting point for this work. Then, we continue withthe fundamentals that are relevant for understanding the results presented here. This also comprises the experimental methods that were applied, ARPES, x-ray linear and circular dichroism in x-ray absorption spectroscopy and photoelectron diffraction. For the theoretical modelling, we used DFT and its implementation in the FPLO code which both are introduced. An overview is given of the underlying physics, focussing on band theory with the fundamental Bloch theorem in periodic solids and the implications for the electronic structure of crystals in the bulk and at the surface. Before we start with the results, the methods are shortly presented. In the two following chapters that form the heart of this thesis, the results for the antiferromagnet $\mathrm{GdIr_2Si_2}$ and the mixed-valent $\mathrm{EuIr_2Si_2}$ are presented and discussed.

2. Preliminary Studies

2.1. Short introduction to lanthanides and 4*f* physics

The elements with the atomic number Z ranging from 57 (lanthanum) to 71 (lutetium) are known as the lanthanides[1] and are distinguished by the increasing filling of the $4f$ shell along the series. The electronic configuration of the lanthanide atoms is $[\mathrm{Xe}]4f^n5d^m6s^2$ with $n \in \{0, 1, \ldots, 14\}$ and $m \in \{0, 1\}$. Depending on the number m of $5d$ electrons the free ions have thus an either divalent ($m = 0$) or trivalent ($m = 1$) oxidation state. In Tab. 2.1 the number of $4f$ and $5d$ electrons is given for each element of the lanthanide series. Most of the free ions are divalent except La, Ce, Gd and Lu,

Tab. 2.1.: Number of electrons in the $4f$ and $5d$ shells for the lanthanide elements in the ground state of the free atom.

	La	Ce	Pr	Nd	Pm	Sm	Eu	Gd	Tb	Dy	Ho	Er	Tm	Yb	Lu
$4f^n$	0	1	3	4	5	6	7	7	9	10	11	12	13	14	14
$5d^m$	1	1	0	0	0	0	0	1	0	0	0	0	0	0	1

which form trivalent ions due to their $5d$ electron. In solids, however, the lanthanides are typically in a trivalent oxidation state. By promoting an electron from the $4f$ shell into a valence state cohesive energy can be gained when this electron participates in chemical bonding. The cohesive energy is defined as

$$E^{\mathrm{coh}} = E^{\mathrm{crystal}} - \sum_{i}^{N} E_i^{\mathrm{atom}}, \tag{2.1}$$

where E^{crystal} is the total energy of the crystal and the sum is over the number N of isolated atoms from which the crystal is built. Exceptions are Eu and Yb which retain their atomic divalent character also in the pure metals as well as in many compounds.

In many cases, the great importance of lanthanides and their compounds derives from their magnetic properties. Due to the incomplete filling of the $4f$ shell, most

[1] In spoken language and the literature the term *rare earth* is often used rather than *lanthanide*. The rare earths include also the non-$4f$ elements scandium and yttrium.

Tab. 2.2.: Theoretical values of angular momentum L, spin momentum S and total angular momentum J for the $4f$ shell of the trivalent lanthanides according to Hund's rules in units of $\hbar$. The resulting Landé factor g_J (dimensionless) and magnetic moment μ_J in multiples of the Bohr magneton μ_B are given following Eqns. 2.2 and 2.3.

	Ce^{3+}	Pr^{3+}	Nd^{3+}	Pm^{3+}	Sm^{3+}	Eu^{3+}	Gd^{3+}	Tb^{3+}	Dy^{3+}	Ho^{3+}	Er^{3+}	Tm^{3+}	Yb^{3+}
$4f^n$	1	2	3	4	5	6	7	8	9	10	11	12	13
L	3	5	6	6	5	3	0	3	5	6	6	5	3
S	1/2	1	3/2	2	5/2	3	7/2	3	5/2	2	3/2	1	1/2
J	5/2	4	9/2	4	5/2	0	7/2	6	15/2	8	15/2	6	7/2
g_J	6/7	4/5	8/11	3/5	2/7	-	2	3/2	4/3	5/4	6/5	7/6	8/7
μ_J	2.54	3.58	3.62	2.68	0.85	0	7.94	9.72	10.65	10.6	9.58	7.56	4.54

of the lanthanide elements possess a large magnetic moment which is important for technical applications. The probably most popular examples are neodymium- (NdFeB) and samarium-based magnets (SmCo), which are the strongest available permanent magnets produced on a large industrial scale [60, 61, 62]. The electronic configuration of the $4f$ shell is determined by the exchange interaction between the electron spins, the Coulomb interactions of the electron charge and the spin-orbit coupling (SOC) for which the Russell-Saunders scheme has proven to give an appropriate description. Altogether, these interactions lead to **Hund's rules** for the ground state:

1. Spin $S = \sum m_s$ largest possible with $m_s = \pm\frac{1}{2}$
2. Angular momentum $L = \sum m_l$ largest possible with $m_l \in \{0, \pm1, \pm2, \pm3\}$
3. Total angular momentum J is given by
   (a) $J = |L - S|$ for elements with up to a half-filled $4f$ shell
   (b) $J = |L + S|$ for elements with more than seven $4f$ electrons

The total angular momentum J is associated with the magnetic moment μ_J given by

$$\mu_J = g_J \cdot \sqrt{J(J+1)} \tag{2.2}$$

with

$$g_J = 1 + \frac{J(J+1) - L(L+1) + S(S+1)}{2J(J+1)} \tag{2.3}$$

being the Landé g factor. In Tab. 2.2 the values of L, S, J, g_J and μ_J for the free trivalent lanthanide ions are listed. Due to localisation and effective screening, the magnetic properties of the $4f$ shell are widely preserved in the solid state. On the other hand, the localised character leads to a negligibly small overlap of the $4f$ wave functions localised on neighbouring atoms, which prevents a direct exchange coupling of the magnetic moments. Nonetheless, the $4f$ metals and compounds typically have a magnetically ordered ground state. The long-range magnetic order of the localised $4f$ moments, which typically persists up to finite temperatures, is established via a conduction-electron mediated indirect exchange coupling that has been explained

on the basis of a theory developed by the physicists Ruderman, Kittel, Kasuya and Yosida and is hence known as the **RKKY interaction**. In combination with the spin-orbit interaction (SOI) which leads to a coupling of the electron spin to the CEF different kinds of long-range magnetic order accompanied by strong magneto-crystalline anisotropy are observed in magnetically active lanthanide systems, including ferromagnetic, antiferromagnetic, ferrimagnetic spiral and helical structures. In that sense, the ${}^8S_{7/2}$ configuration of the $4f$ shell with $L = 0$ and the pure spin total angular moment $J = S = 7/2$ characteristic of Gd, is of great importance in systematic studies of exchange interactions, which for the corresponding spherical symmetry of the half-filled $4f$ shell, are not influenced by the CEF. This moreover allows, for example, for systematic studies of how magnetism is influenced by band-filling effects [63].

The magnetic ${}^8S_{7/2}$ configuration of the $4f$ shell is found in Eu metal and many Eu compounds, too, but due to the different number of $5d$ electrons, divalent Eu and trivalent Gd compounds have in general slightly different properties. For example, the magnetic ordering temperature is typically lower for Eu than for Gd compounds which is related to the nature of the RKKY interaction. Since for Eu the di- and trivalent configurations are close in energy, in some compounds Eu is in the trivalent $4f^6(5d6s)^3$ state. For the half-filled $4f$ shell with a maximal number of parallel spins, the polarisation energy (also referred to as Hund's rule correlation energy) is very large. It is therefore energetically quite expensive to promote an electron from the $4f$ shell into a $5d$ state. For a particular system it depends on the energy that can be gained if an additional electron participates in chemical bonding which Eu valency is realised. Characteristic of the divalent configuration is a large radius of the Eu^{2+} ion which leads to larger lattice parameters for divalent Eu compounds in comparison to materials with a trivalent Eu state. Moreover, in the case of Eu^{3+} $L = S = 3$ and thus the total angular momentum vanishes ($J = 0$). This implies that the Eu^{3+} ion does not carry a magnetic moment in its ground state and limits the magnetic properties of Eu^{3+} to the possible occurrence of Van-Vleck paramagnetism.

Mixed Valency Due to the energetic proximity of the di- and trivalent configurations of Eu, already small changes in parameters like external or chemical pressure, temperature, doping level or external magnetic field are sufficient to switch a system from a divalent to a trivalent configuration or vice versa, in many cases even a non-integer (mixed) valency is realised. In general, there are two fundamentally different types of mixed valency: In inhomogeneous mixed-valence systems the non-integer valency results from inequivalent crystallographic sites in the lattice at which the lanthanide ions have a different *integer* valence due to a different local environment. In homogeneous mixed-valent systems, in contrast, the lanthanide ions sit at equivalent lattice sites. Here, a further distinction is sometimes made between intermediate-valent and valence-fluctuating systems which have rather different phase diagrams [58]. The former term is typically used for Ce or Yb-based systems, where the $c - f$ hybridisation between itinerant conduction-band (c) and localised $4f$ states leads to the non-integer valency. For Eu systems, the non-integral valence is often described in a picture of thermal valence fluctuations between the two integral-valence states with a back-and-forth transfer of a charge between the $4f$ shell and the conduction

band. In this view, the $4f^n(5d6s)^m$ and the $4f^{n-1}(5d6s)^{m+1}$ configurations of the lanthanide element must be nearly degenerate in energy and located at or in the immediate vicinity to the Fermi level E_F to ensure that the transition between the two configurations occurs without energy cost. However, in such a two-level model Eu should have an integer valence of $\nu = 3$ in the ground state, which is not observed for mixed-valent Eu systems, indicating that hybridisation plays an important role as in intermediate valence systems. In this sense, it seems more appropriate to think of mixed valency in terms of a quantum-mechanical mixing of the $4f^n(5d6s)^m$ and $4f^{n-1}(5d6s)^{m+1}$ configurations. A review of particular models and valence fluctuating lanthanide compounds can be found, for example, in Ref. [51].

Mixed-valent behaviour is predominantly observed in compounds with Ce, Sm, Eu, Tm and Yb, i.e. at the beginning, in the end and in the middle of the lanthanide series. Except for Ce[2], a valence transition occurs usually at the surface of the respective pure metals, i.e. the lanthanide ions at the metal-vacuum boundary are in a purely divalent valence state even for a trivalent configuration in the bulk. At the surface the coordination is reduced which destabilises the trivalent configuration because the gain in cohesive energy becomes smaller than the energy that is needed to excite an electron from a $4f$ into a $5d$ state. **Surface-valence transitions** occur not only in the pure metals but are equally observed for lanthanide-terminated surfaces of many compounds. Another phenomenon that is related to the reduced coordination at the surface, too, is the **surface-core-level shift**. It consists in a shift of all localised states including the $4f$s to higher binding energies. In monocrystalline Eu films, for example, the surface $4f$ level is separated by 480 meV from the respective core level [64].

Phase diagram of intermetallic Eu compounds The chemical composition of compounds plays an important role for the valence state of Eu. Fig. 2.1(a) schematically shows the valency of Eu in ternary EuT_2Si_2 intermetallics for different transition-metal elements T. Light blue, yellow and light green background colours mark the transition metals for which Eu is in a trivalent, divalent or mixed-valent state, respectively. The general trend shows a mixed-valent state for the diagonal formed by Cu, Pd and Ir; for the transition metals to the left Eu is in a trivalent state, and for those on the right the divalent configuration is stabilised. This is consistent with an increase in the Fermi level for the transition metal elements from left to right in a row, or from top to bottom in a column of the periodic table. An exception forms divalent $EuRh_2Si_2$, which has been explained by strong hybridisation of Eu $4f$ with Rh $4d$ states [59]. Later studies of the alloy series $Eu(Pd_{1-x}Au_x)_2Si_2$ [65], $Eu(Pt_{1-x}Ni_x)_2Si_2$ [66] and $Eu(Rh_{1-x}Ir_x)_2Si_2$ [67] demonstrated how the Eu valency changes under incremental substitution of one transition metal with another. Based on these studies and related pressure experiments, the generic phase diagram, Fig. 2.1(b), has been obtained that shows how the bulk Eu valency can be tuned from a divalent to a trivalent or mixed-valent state through the application of external pressure p or increasing the concentration x of the substituting transition-metal element. Note, that increasing pressure and alloying enhance the $f - d$ hybridisation in Eu. For small hybridisation,

[2] In the case of Ce systems, the reduced coordination at the surface leads to a decrease of the $4f$ hybridisation known as the α-to-γ transition.

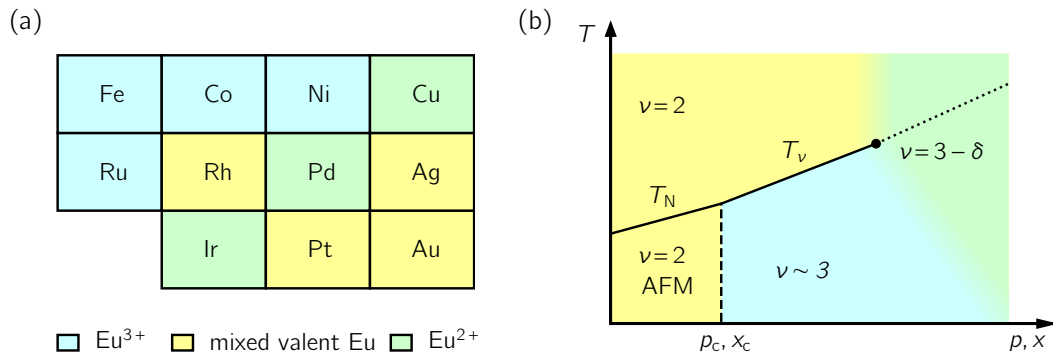

Fig. 2.1.: Valency in Eu intermetallics. (a) Trivalent (light blue), divalent (yellow) and mixed-valent (light green) Eu in EuT_2Si$_2$ compounds. (b) Phase diagram of Eu compounds. T, p and x are temperature, external pressure and substituent concentration in alloys, respectively. Reproduced from Refs. [59] and [58].

the valency is stably divalent with a temperature-induced phase transition from the AFM ground state to a paramagnetic (PM) state. With increasing hybridisation, the Néel temperature increases very slightly until the critical value is reached at which the magnetic transition is superseded by a first-order phase transition between an almost trivalent ground state and a divalent Eu state that is restored when the transition temperature T_ν is exceeded. The phase diagram shows, that T_ν increases with increasing hybridisation up to a critical endpoint at which the first-order phase transition transforms into a valence crossover indicated by the light green colour.

Photoemission from the Eu-4*f* shell and final-state multiplets Photoemission (PE) probes the $4f$ shell after the removal of an electron from the $4f^n$ ground state, which leaves the $4f$ shell in one of the possible excited $4f^{n-1}$ final states. The multiplet is the entirety of the reachable $4f^{n-1}$ final states, describing the energy separation and the intensity ratios of the single lines. In PE, the 2+ and 3+ configurations of Eu can thus be easily identified by their respective $4f^6$ and $4f^5$ final-state multiplets which reflect the highly localised, atomic-like character of the $4f$ electrons. In Fig. 2.2(a) exemplary $4f$ PE spectra are shown to illustrate the Eu^{2+} and Eu^{3+} final-state multiplets for different EuT_2Si$_2$ compounds where Eu is in a purely divalent, purely trivalent or valence-fluctuating state. The angle-integrated ARPES spectra belong to $EuCo_2Si_2$ representing a compound with trivalent Eu, $EuRh_2Si_2$ where Eu is purely divalent as well as $EuPd_2Si_2$ and $EuIr_2Si_2$ which are systems with a fluctuating Eu valence. The spectra were acquired at different synchrotron radiation facilities using $h\nu = 145\,\mathrm{eV}$ (144 eV for $EuPd_2Si_2$) at which the emission from Eu^{3+} is resonantly enhanced. Areas under the curves that are highlighted in purple and green colours mark the PE intensity associated with the $4f^5$ and $4f^6$ final-state multiplets, respectively. For purely trivalent $EuCo_2Si_2$, we find the peaked structure of the PE signal due to the Eu^{3+} multiplet between 6.5 eV and 10.5 eV binding energy. In purely divalent $EuRh_2Si_2$ the Eu^{2+} signal is located close to the Fermi level. The peak at about 2 eV is a signature of Eu atoms at the surface for which the $4f$ level experiences a surface-core-level shift. Due to the short mean free path of the photoelectrons of about 5 Å at these photon energies,

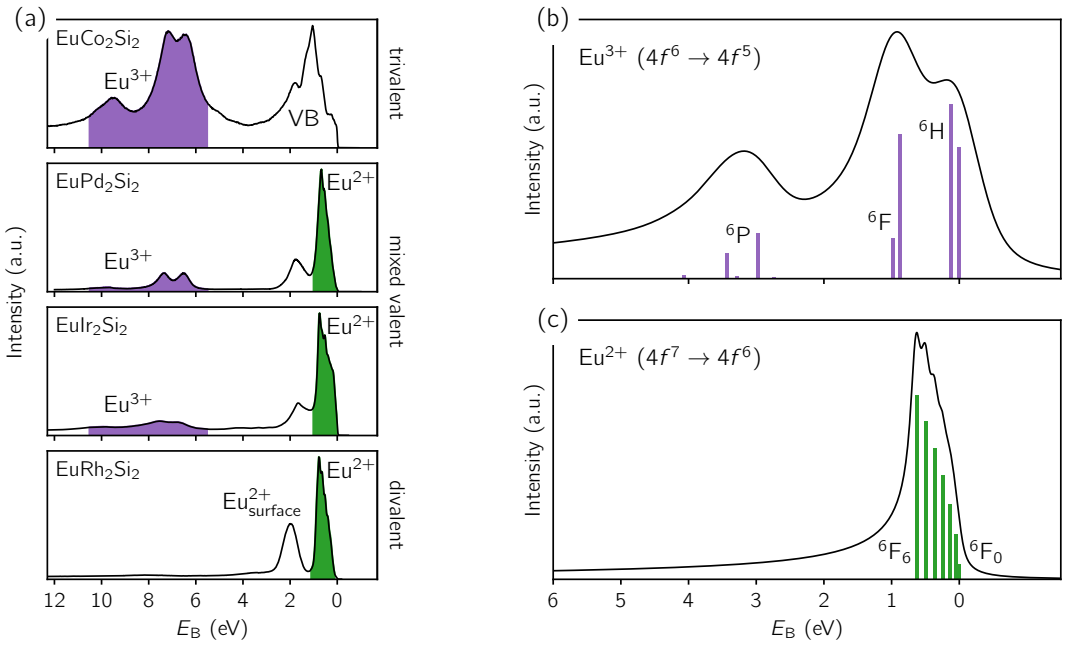

Fig. 2.2.: Eu $4f$ multiplets in photoemission. (a) Angle-integrated ARPES spectra from the Si-terminated surfaces of EuT_2Si$_2$ compounds with $T = \mathrm{Co, Pd, Ir, Rh}$ in which different Eu valencies are realised, acquired in the Beutler-Fano resonance of Eu^{3+} with $h\nu = 145\,\mathrm{eV}$, except for the Pd compound, which was measured with 144 eV. PE signals of the $4f^5$ and $4f^6$ final-state multiplets of Eu^{3+} and Eu^{2+} are highlighted in purple and green, respectively. The appearance of a small peak at a binding energy of $\sim 2\,\mathrm{eV}$ in some of the spectra is a signature of Eu atoms at the surface, particularly for $EuRh_2Si_2$. The high intensity in the $EuCo_2Si_2$ spectrum at low binding energies originates from the valence band (VB) and possibly from divalent Eu at the surface. Calculated final-state multiplets in direct photoemission for (b) Eu^{3+} and (c) Eu^{2+} using an intermediate coupling scheme, adapted from Gerken [68].

for a pure Eu termination the PE intensity exceeds the bulk signal by an order of magnitude, see for example Fig. 6.11. Note, that due to the modified coordination in comparison to the bulk, at the surface Eu is usually in a divalent state. This is even the case for trivalent compounds like $EuCo_2Si_2$ [69, 70, 71, 72, 73]. In the spectra of the valence-fluctuating compounds $EuPd_2Si_2$ and $EuIr_2Si_2$, we observe both the Eu^{3+} and Eu^{2+} multiplets. Their energy separation is a measure of the Coulomb repulsion energy between the two configurations. Since a fluctuation of the valency is energetically only possible, if both the Eu^{2+} and Eu^{3+} initial states have an energy at or very close to the Fermi level, the $4f^6$ final state of Eu^{2+}, which coincides with the initial state of Eu^{3+}, i.e. with the ground state, is found close to the Fermi level. In the spectra of the divalent and mixed-valent Eu compounds the valence band (VB) states near E_F are almost completely outshone by the resonantly enhanced signal of Eu^{2+}. This effect is amplified by the fact that the transition metal $3d$ and $4d$ states which contribute significantly to the valence band, have a Cooper minimum near the employed photon energies, i.e. their excitation is strongly suppressed.

For all lanthanides, the final-state multiplets have been calculated in an intermediate-

coupling scheme[3] by Gerken [68]. In Fig. 2.2 the results of Gerken for trivalent and divalent Eu are reproduced in (b) and (c), respectively. In the calculated Eu^{2+} spectrum shown in (c), we find the multiplet to consist of seven lines, each of which corresponds to one possible $4f^6$ final state of the $4f$ shell. The single lines are labelled in LS coupling nomenclature according to the main contributor in the intermediate coupling scheme using term symbols with F_J for $L = 3$ and $J \in \{0, 1, 2, 3, 4, 5, 6\}$ with the total spin $S = 3$. In the Eu^{3+} multiplet the six dominating lines can be regarded to form three pairs of H_J ($L = 5$), F_J ($L = 3$) and P_J ($L = 1$) states. Due to the larger number of possible final states with different angular momenta L, a splitting of the Eu^{3+} multiplet over a wide energy range of about 4 eV is observed in the spectra. Note that a similar splitting of the Eu^{2+} multiplet is missing in the calculated spectra because in the direct PE process spin-flip transitions are forbidden by the dipole selection rules. In resonant photoemission spin flips are in principle possible [74], however, in the spectra given above there is no evidence for a notable contribution of the latter.

2.2. LnT_2Si_2 compounds

The LnT_2Si_2 ternary silicides, where Ln = lanthanide and T = Co, Rh, Ir belong to the large family of the 122 intermetallics. Some of the LnT_2Si_2 compounds are polymorphs, i.e. they can crystallise in both the primitive $CaBe_2Ge_2$ structure with space group P4/nmm and the body-centred $ThCr_2Si_2$ structure with space group I4/mmm, depending on the crystal growth parameters. Here, we consider only the $ThCr_2Si_2$ type, which is characterised by the stacking of mono-atomic layers in the sequence Ln–Si–T–Si along the c axis of the tetragonal crystal.[4] The corresponding unit cell is shown in Fig. 2.3(a) with Ln, T and Si atoms coloured in purple, orange and green, respectively. The occupied Wyckoff positions are $2a$ for Ln which sits at (0, 0, 0), $4d$ for T at (0, 0.5, 0.25) and $4e$ for Si at (0, 0, z_{Si}) with z_{Si} being the only free parameter. Thanks to the layered crystal structure and the tighter bonding within the Si–T–Si block in comparison to the bonds between Si and Ln atoms, the crystals can be easily cleaved perpendicular to the c axis. The resulting (001) surface is terminated either by Si or Ln, which form atomically flat areas that are large enough to be studied with ARPES. The different terminations of the (001) surface are sketched in Fig. 2.3(b), while in Fig. 2.3(c) the Brillouin zones (BZs) of the bulk and the (001) surfaces are shown in black and red colours, respectively. The three-dimensional bulk BZ of the $ThCr_2Si_2$-structure type with space group I4/mmm has the shape of a truncated octahedron, while the 2D surface Brillouin zone (SBZ) forms a square. $\overline{\Gamma}$, $\overline{\mathrm{M}}$ and $\overline{\mathrm{X}}$ are the high-symmetry points of the SBZ that are located at the centre, the corners and the middle of the sides, respectively.

[3] Intermediate coupling is an improvement over LS coupling in the case of strong SOI because the mixing of states with the same total angular momentum J but different quantum numbers LS is considered, too.

[4] In the $CaBe_2Ge_2$ structure the stacking sequence is Ln–Si–T–Si–Ln–T–Si-T, i.e. the Ln layers are separated in alternating order by Si–T–Si and T–Si–T trilayer blocks, or in comparison to the $ThCr_2Si_2$ structure, T and Si are interchanged in every second trilayer block.

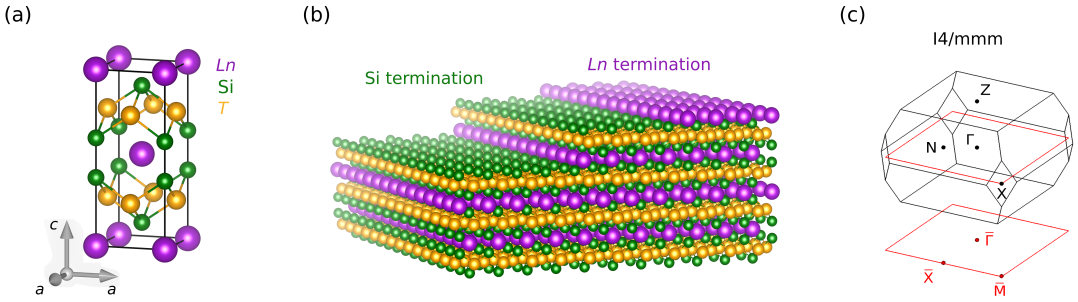

Fig. 2.3.: Crystal structure of LnT_2Si_2 compounds. (a) Tetragonal (primitive and conventional) unit cell of the bulk. The tight bonding within the Si–T–Si trilayer block is indicated by lines connecting the atoms. (b) Schematic view on the two possible terminations of the (001) surface by Si or Ln. Surface states are localised in the surface Si–T–Si–Ln block of the Si-terminated surface. (c) Bulk and surface Brillouin zones with selected high-symmetry points shown in black and red colours, respectively.

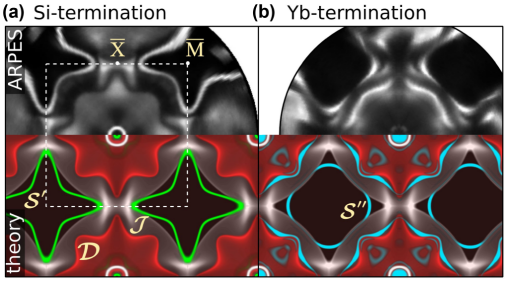

Label	Type	Allocation
$\mathcal{D}$	bulk state	bulk
$\mathcal{S}''$	surface resonance	Ln surface
$\mathcal{S}'$	surface state	Si surface

Fig. 2.4.: Electronic structure of the (001) surface of LnT_2Si_2 compounds. ARPES-derived Fermi maps and corresponding DFT modelling are shown in the upper and lower row, respectively for (a) Si, and (b) Ln terminations. The white-dashed square marks the SBZ. Around the $\overline{\text{M}}$ point the star-shaped Fermi contours formed by the surface state $\mathcal{S}'$ are seen for Si termination only. Characteristic of the Ln termination are a gap around $\overline{\text{M}}$ and the surface-resonant state $\mathcal{S}''$. The most prominent bulk features are the Doughnut $\mathcal{D}$ which is projected onto the SBZ. In the calculated maps, $\mathcal{S}'$, $\mathcal{S}''$ and $\mathcal{D}$ are highlighted in green, cyan and red, respectively. From [75].

Band structure Surface-sensitive ARPES studies on the (001) surface in the Rh series of the LnT_2Si_2 compounds unveiled several features in the electronic structure that are characteristic of the bulk, and Si or Ln terminations and closely related to the crystal structure. In Fig. 2.4 an overview of the most prominent features is given. Around $\overline{\Gamma}$ the projection of the so-called "Doughnut" Fermi-surface sheet onto the SBZ is seen for both terminations. In the calculated spectra this bulk feature is highlighted in red and labelled $\mathcal{D}$. The size of the Doughnut varies with the valency of the Ln element. For divalent lanthanides, the Doughnut is large. In this case, its necks pointing in the direction of the $\overline{\text{X}}$ point of the SBZ are open and interconnected. In the case of the small Doughnut in trivalent systems, the necks are closed and there is no overlap between the Doughnuts of neighbouring BZs. This difference in size is caused by $\mathcal{D}$'s hole-like character. With the additional valence electron in the trivalent lanthanides the band filling increases which makes the Doughnut shrink in

comparison to the divalent configuration. Another possibility for a large Doughnut is an admixture of $4f$ degrees of freedom in Kondo system like $YbRh_2Si_2$. Although Yb is nearly trivalent in this system, hybridisation of $4f$ states with itinerant valence band states leads to the formation of a large Doughnut [75, 76]. Note, that in a recent Compton-scattering experiment it was demonstrated that the Doughnut collapses to its small version after the Kondo breakdown when the $4f$ degrees of freedom are removed from the Fermi surface [77].

Surface states Of different nature is the Fermi contour that has the shape of a four-cornered star, disperses symmetrically around the $\overline{\mathrm{M}}$ point of the SBZ and is seen for Si termination only. In the calculated spectrum it is labelled $\mathcal{S}'$ and coloured in green. Comparison between (a) and (b) shows that this Fermi contour is located within a large gap of projected bulk bands. This spectral feature represents a Shockley surface state that is confined to the surface Si–Rh–Si–Ln four-layer block and highly spin polarised due to the Rashba effect. In the example of $YbRh_2Si_2$ given here, the Rashba splitting of the Fermi contour is too small to be resolved with ARPES.

Rashba effect The Rashba effect emerges as a combination of structure-inversion asymmetry and SOC. The coupling of the spin to the orbital motion of the electron is a relativistic effect. In an atom, electrons with spin $\boldsymbol{S}$ move in the rest frame of the nucleus in the electric field of the latter. In the rest frame of the electron, however, the nucleus orbits around the electron inducing a magnetic field to which the electron spin $\boldsymbol{S}$ couples. In its property as angular momentum, each spin is linked up with a magnetic moment $\boldsymbol{\mu}$. Since the energy of a magnetic moment in a magnetic field $\boldsymbol{B}$ is given by $-\boldsymbol{\mu}\boldsymbol{B}$, spin-up and spin-down electrons have different energies in the magnetic field of the nucleus. In solids, this can lead to a Zeeman-like splitting of electron bands, provided that there are no symmetry constraints imposed by the crystal structure. To demonstrate the symmetry constraints for the spin-orbit splitting of Bloch states we consider a spin-orbit Hamiltonian of the form

$$H_{\mathrm{SOC}}^{\mathrm{crys}} \propto (\nabla V \times \boldsymbol{k}) \cdot \boldsymbol{\sigma} \tag{2.4}$$

with V being the crystal potential, $\boldsymbol{k}$ the crystal momentum and $\boldsymbol{\sigma}$ the vector of Pauli matrices which account for the spin ($\boldsymbol{S} = \frac{\hbar}{2}\boldsymbol{\sigma}$). The Hamiltonian in Eqn. 2.4 is invariant under time reversal, i.e. the replacements $\boldsymbol{k} \rightarrow -\boldsymbol{k}$ and $\boldsymbol{\sigma} \rightarrow -\boldsymbol{\sigma}$ leave the spin-orbit Hamiltonian unaltered. If the potential V is moreover invariant under structure inversion, i.e. $V(\boldsymbol{r}) = V(-\boldsymbol{r})$, a spin-orbit splitting of crystal states $|\boldsymbol{k}, \sigma\rangle$ is prohibited and the solutions to Eqn. 2.4 will be degenerate in energy, see Fig. 2.5. In non-centrosymmetric systems, however, a spin-orbit splitting of bands can occur due to the absence of inversion symmetry. Surfaces and interfaces always lack inversion symmetry, which leads to the spin-orbit splitting of the quasi-2D surface and interface states by the effective electric potential gradient along the normal of the surface/interface. This is known as the Rashba effect and reflected by a $\boldsymbol{k}_{\parallel}$ dependent lifting of spin degenerate states. The strength of the Rashba splitting depends on the electric field gradient and scales with the strength of the atomic SOC which is related to the atomic number Z. Therefore, the Rashba effect can be increased either by choosing high Z elements or

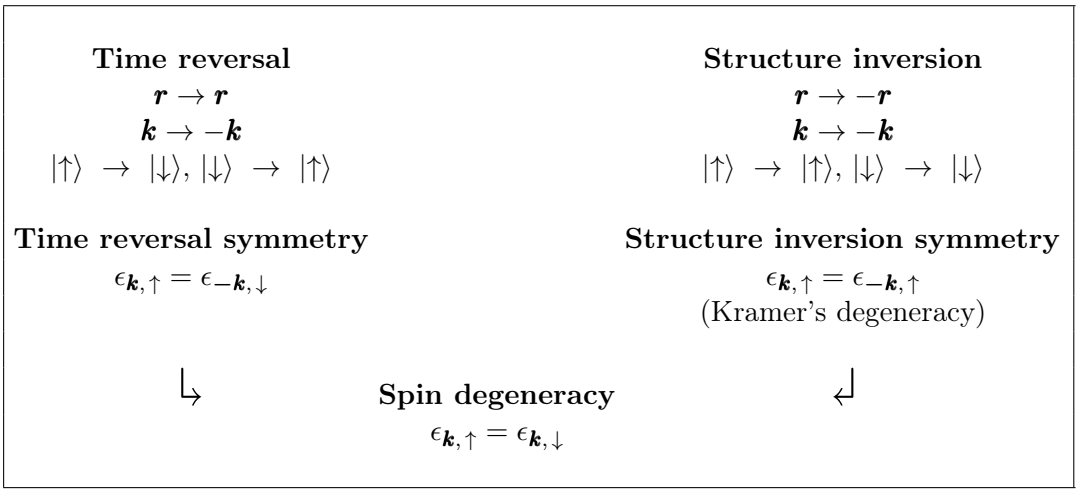

Fig. 2.5.: Transformation behaviour of position $\boldsymbol{r}$, crystal momentum $\boldsymbol{k}$ and spin $\sigma_z \in (\uparrow, \downarrow)$ under time reversal and structure inversion and the implications for the eigenvalues ϵ of the Hamiltonian if it has time reversal or structure inversion symmetry. If both symmetries apply, the states are Kramer's degenerate.

by creating a large potential gradient, which can in certain systems be tuned via an external voltage. In its classical form, the Rashba effect induces an orthogonal spin-momentum locking which consists in a helical spin structure along the constant-energy contours (CECs) as schematically illustrated in Fig. 2.6 for the nearly-free-electron paraboloid. Note, that spin rotates in opposite direction along the inner and outer CECs, according to $\epsilon_{\boldsymbol{k},\uparrow} = \epsilon_{-\boldsymbol{k},\downarrow}$, see Fig. 2.5.

For the surface state $\mathcal{S}'$ in the $Ln\mathrm{Rh_2Si_2}$ compounds, however, the bands deviate from the parabolic dispersion of the free electron gas, in particular due to the four-fold warping that creates the star-like shape of the CECs. Interestingly, also the spin structure has been found to deviate significantly from that of a classical Rashba system. Namely, the electron spin rotates three times faster on a closed loop along the CECs of surface state's CECs introduced in Fig. 2.4(a) or in other words, the spin completes three full rotations by 2π. This exotic spin structure which was first predicted on the basis of DFT calculations for $\mathrm{GdRh_2Si_2}$ by Monika Güttler, has been confirmed experimentally through spin-resolved ARPES experiments on $\mathrm{TbRh_2Si_2}$ [37].

Exchange interaction Another intriguing property of the surface state $\mathcal{S}'$ is the exchange coupling of the itinerant spins to magnetically ordered $4f$ moments in the first (subsurface) Ln layer below the Si-terminated surface. Most of the $LnT_2\mathrm{Si_2}$ compounds order antiferromagnetically at low temperatures due to the AFM stacking of ferromagnetically ordered Ln layers along the tetragonal c axis. The ordering of the $4f$ moments leads to a huge splitting of the surface state bands. The exchange interaction, which is the fundamental interaction that leads to collective magnetic order is actually a consequence of the indistinguishability of electrons and their non-integer spin. The many-body wave function describing a system of N electrons must be anti-symmetric under exchange, i.e. if two electrons in the system are interchanged the

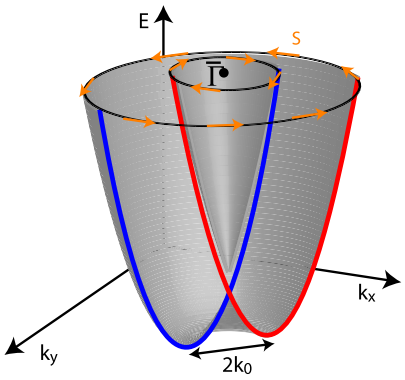

Fig. 2.6.: Classical Rashba effect in a 2DEG with the typical splitting of the nearly-free-electron paraboloid into two bands. Blue and red parabolas indicate the opposite spin polarisation of the Rashba-split bands. Small orange arrows illustrate the characteristic orthogonal spin-momentum locking with a single helical winding of the spin along the CECs with opposite chirality on the inner and outer CECs. Image from Ref. [78].

spin-statistic theorem imposes that the wave function must change sign. The exchange symmetry leads to an additional term in the expectation value of the Hamiltonian called the exchange energy, which gains in importance when the temperature lowers and the system approaches its ground state. In models, the exchange symmetry is taken into account in terms of an effective exchange interaction of spins interacting with each other or a mean field.

With its large exchange splitting the surface state $\mathcal{S}'$ in the $Ln\mathrm{Rh_2Si_2}$ compounds can be regarded as a detector for the magnetic ordering in the subsurface layer, whereby the splitting contains information about the orientation of the magnetisation, too. In $\mathrm{EuRh_2Si_2}$ and $\mathrm{GdRh_2Si_2}$ the $4f$ moments align ferromagnetically within the ab plane. For the heavy lanthanides with a non-spherical symmetry of the $4f$ shell, however, the CEF tilts the $4f$ moments out of the ab plane. In the $E(\boldsymbol{k}_\parallel)$ curves, this is reflected in different behaviour of the surface-state bands near the $\overline{\mathrm{M}}$ point. This is illustrated in Fig. 2.7 where ARPES-derived band maps along $\overline{\mathrm{X}}$–$\overline{\mathrm{M}}$–$\overline{\mathrm{X}}$ are shown for $\mathrm{HoRh_2Si_2}$ (a, b) and $\mathrm{EuRh_2Si_2}$ (c, d) in the PM and AFM phases. In the PM phase the bands of the surface state $\mathcal{S}'$, which is labelled $\mathsf{S_e}$ in Fig. 2.7, are degenerate in the $\overline{\mathrm{M}}$ point. This is best seen in the second-derivatives of the ARPES data which are shown as insets in (a) and (c) for $\mathrm{HoRh_2Si_2}$ and $\mathrm{EuRh_2Si_2}$, respectively. In the AFM phases, a large splitting of the surface-state bands in the $\overline{\mathrm{M}}$ point is seen in (c) for $\mathrm{HoRh_2Si_2}$ due to the out-of-plane orientation of the $4f$ moments. In contrast, when the moments order perpendicular to the c axis as it is the case in $\mathrm{EuRh_2Si_2}$, the bands remain two-fold degenerate in the $\overline{\mathrm{M}}$ point, Fig. 2.7. Note, that the $\overline{\mathrm{M}}$ point is a time-reversal invariant momentum (TRIM) of the SBZ, i.e. forming the corner of the SBZ it is symmetric under time reversal. This symmetry, however, is broken when the $4f$ moments point out of the ab plane.

Since the wave function is confined to the topmost four atomic layers, the surface state is sensitive to magnetic order in the subsurface Ln layer only. Therefore, we use the Curie temperature T_C in the discussion of the magnetic properties of the surface rather than the AFM Néel temperature T_N. For $\mathrm{EuRh_2Si_2}$ and $\mathrm{GdRh_2Si_2}$ different

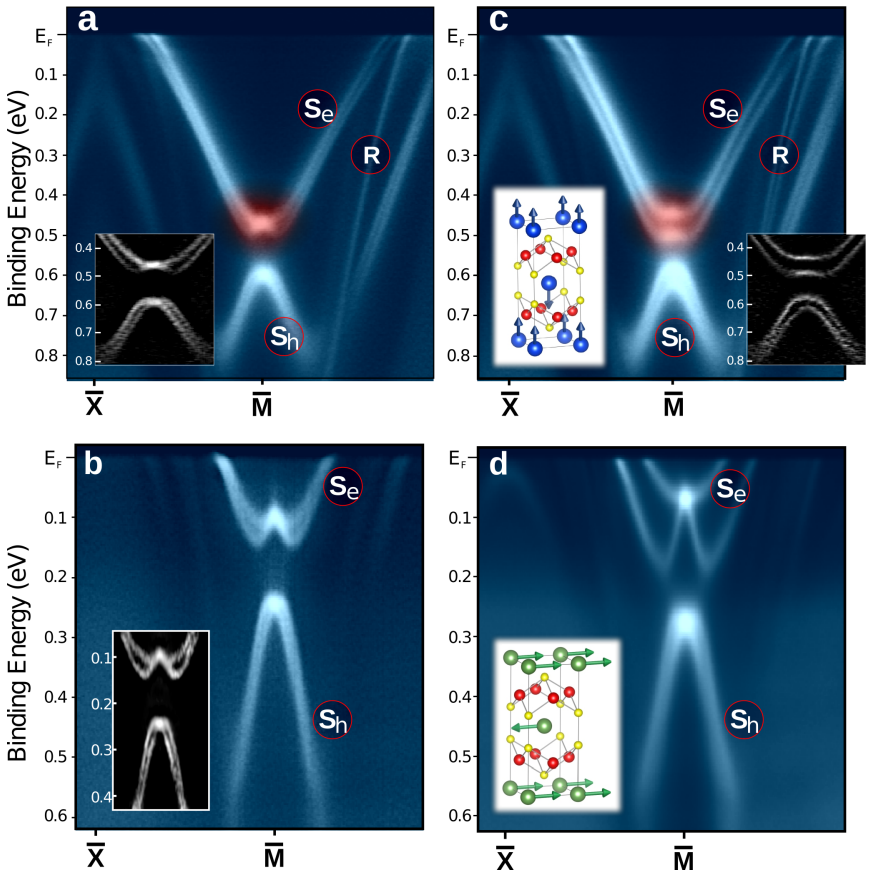

Fig. 2.7.: Shockley state at the Si-terminated surface of (a, c) $HoRh_2Si_2$ and (b,d) $EuRh_2Si_2$ in the PM (a, b) and AFM (c, d) phases forming the bands S_e and S_h with electron- and hole-like dispersion, respectively. Insets show the details of the surface state bands after curvature/first/second derivative treatment. In the insets showing the bulk unit cell the orientation of the magnetic moments is indicated by arrows. From [79].

temperature scales were found for the magnetic ordering in the bulk and at the surface. In $EuRh_2Si_2$ $T_N = 24.5\,K$, while for the subsurface $T_C = 41\,K$ is about 40 % higher [79]. In $GdRh_2Si_2$ the opposite case has been observed with $T_C = 90\,K$ being lower than in the bulk where $T_N = 106\,K$ [35]. This large difference has been discussed as follows. Firstly, the additional exchange interaction with the Shockley state increases the ordering temperature at the surface. Secondly, the reduced coordination at the surface lowers T_C. For $EuRh_2Si_2$, which is a quasi-2D magnet with a small AFM interlayer coupling, the first mechanism prevails, while the impact of the missing neighbouring Eu layer at the surface is comparably small. In $GdRh_2Si_2$, in turn, the AFM interlayer coupling is very strong and thus essential in stabilising the magnetic order. Therefore the existence of the surface constitutes a strong perturbation which leads to a significant reduction of the ordering temperature that cannot be compensated by the energy gained due to the exchange coupling with the surface state [35].

In the ARPES spectra in Fig. 2.7, the hole-like bands of a second surface state labelled S_h are seen below the bands of S_e that have been in the focus of our discussion

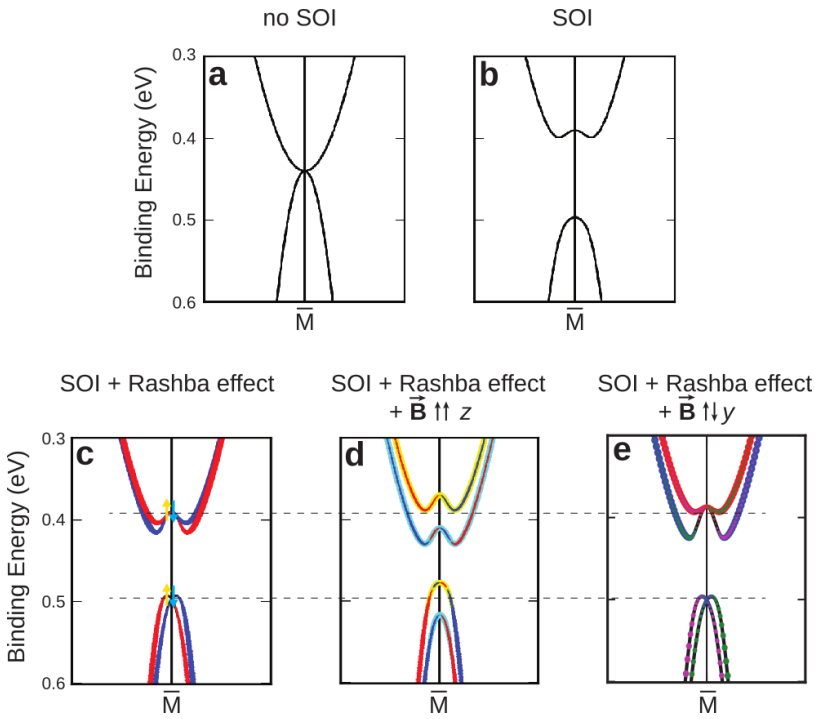

Fig. 2.8.: Tight-binding model describing the Shockley surface states $\mathsf{S_e}$ and $\mathsf{S_h}$ at the Si-terminated surface of LnT_2Si_2 compounds considering different interactions. (a) Without SOI, (b) with SOI and structure inversion symmetry, (c) with SOI and Rashba effect (structure inversion asymmetry), (d) with SOI, Rashba effect and exchange interaction along z, and (e) with SOI, Rashba effect and effective exchange field in y direction. From Ref. [80].

so far. Note the different binding energies of the surface states in $HoRh_2Si_2$ and $EuRh_2Si_2$ in Fig. 2.7. For the former, the binding energy of the upper bands is about 0.5 eV in the $\overline{\mathrm{M}}$ point, whereas it is only about 0.1 eV for $EuRh_2Si_2$. The difference is related to the additional $5d$ electron in trivalent lanthanides like Ho and Gd which shifts the Fermi level upward.

Modelling DFT proved to reproduce the measured surface-state bands very accurately but it cannot be used to disentangle the Rashba-like SOC, which is a consequence of the inversion-symmetry breaking at the surface, from the intrinsic SOC. Separation of both effects requires effective models. In the following, we have a short look at the instructive results obtained from a tight-binding model developed by Marc Höppner in which the intrinsic SOC, the surface gradient and the exchange interaction acting on the $Ln Rh_2Si_2$ surface states can be switched on and off individually. In Fig. 2.8(a), we start with two parabolic bands that represent the surface states $\mathsf{S_e}$ and $\mathsf{S_h}$ in absence of any interactions. In this case, the bands are doubly-degenerate in spin and of electron-like ($\mathsf{S_e}$) and hole-like ($\mathsf{S_h}$) characters, respectively. At the $\overline{\mathrm{M}}$ point $\mathsf{S_e}$ and $\mathsf{S_h}$ are degenerate. In (b), we switch on the intrinsic SOI which results in the opening of a large gap in the vicinity of the $\overline{\mathrm{M}}$ point that separates the two bands by about 100 meV and lifts the fourfold degeneracy in the $\overline{\mathrm{M}}$ point. Simultaneously, the

two-fold degeneracy of the bands is retained due to the structure inversion symmetry. Note the hole-like deformation of $\mathsf{S_e}$ band near the $\overline{\mathrm{M}}$ point which reflects the mixing of the $\mathsf{S_e}$ and $\mathsf{S_h}$ states by the intrinsic SOI. In the next step, Fig. 2.8(c), we simulate the surface and break the inversion symmetry by adding a potential gradient to our model. This lifts the two-fold degeneracy of the $\mathsf{S_e}$ and $\mathsf{S_h}$ bands and induces the familiar Rashba-like spin-structure, represented in red and blue colours for $S_y > 0$ and $S_y < 0$, respectively. S_y is the expectation value of the y component of the electron spin. At the $\overline{\mathrm{M}}$ point, which is a TRIM, $\mathsf{S_e}$ and $\mathsf{S_h}$ remain two-fold degenerate. Note, that the tight-binding model does not correctly reproduce the DFT-derived spin structure in the region close to the $\overline{\mathrm{M}}$ point for which DFT predicts identical sign of the spin expectation value on the split bands of both $\mathsf{S_e}$ and $\mathsf{S_h}$. This effect is due to a hidden spin polarisation [81] that cannot be described within this simple tight-binding model.[5] In the next step, Fig. 2.8(d), we consider in addition to the intrinsic SOI and the Rashba effect, an effective exchange field along the z direction. It can be seen that this induces a spin component along the z axis. $S_z > 0$ and $S_z < 0$ are plotted in yellow and light-blue colours, respectively. Although the spins are rotated out of the ab plane $S_y \neq 0$ and its sign remains the same as in (c). We moreover observe that the splitting of the bands increases and the degeneracy in the $\overline{\mathrm{M}}$ point is lifted. If the field is applied within the plane, Fig. 2.8(e), the degeneracy in the $\overline{\mathrm{M}}$ point is not lifted, while the overall $k_{\|}$-dependent magnitude of the spin polarisation and splitting increase significantly. The details of the tight-binding model can be found in the supplementary file to Ref. [36].

Within a rather simple tight-binding model dispersion, splitting and the spin structure (for $k_{\|}$ that are not in the immediate vicinity of the $\overline{\mathrm{M}}$ point) of the surface state can be correctly reproduced by tuning respective model parameters. However, some limitations are found in the incorrect description of the spin structure close to $\overline{\mathrm{M}}$. Note that meanwhile a six-band $\boldsymbol{k \cdot p}$ model has been developed, which is capable of precisely reproducing dispersion and spin structure of the surface states in the Si–T–Si–Ln surface block [39]. Since the $\boldsymbol{k \cdot p}$ Hamiltonian is built from the DFT-derived wave functions of the surface state, it intrinsically contains all the symmetries in the system. In particular, it correctly describes the spin structure in the vicinity of $\overline{\mathrm{M}}$ and shows that the single surface states interact with each other. Note further, that a detailed DFT study on the formation and composition of the surface states in the considered $LnT_2\mathrm{Si}_2$ compounds has been conducted by Alexandra Vyazovskaya et al. using the example of $\mathrm{GdRh}_2\mathrm{Si}_2$ [82].

[5] The hidden spin polarisation is a consequence of intrinsic SOC and the existence of two crystallographic inequivalent T sites in the ab plane of the crystal. Considered separately, each site is almost completely spin-polarised with opposite signs. Considered as an entity, they cancel each other almost completely.

3. Foundations

3.1. Band structure

Macroscopic properties of materials like their conductivity, electrical resistivity, specific heat, optical absorption or magnetism can be understood on an atomic and subatomic scale studying the properties of the electrons. Band theory is a microscopic model that has proven very successful in describing the electronic structure of periodic solids.

In quantum mechanics a physical system is completely determined by its wave function $|\Psi\rangle$, which, in a non-relativistic framework[1], can be obtained by solving the stationary Schrödinger equation $H|\Psi\rangle = E|\Psi\rangle$. The eigenvalue E of the Hamiltonian H is then the total energy of the system under study. Here, the physical systems of interest are single crystals, which are built of positively charged nuclei (subscript n) periodically arranged in a crystal lattice, and negatively charged electrons (subscript e). All particles comprising the many-body systems are mutually interacting with each other through the Coulomb interaction. The corresponding Hamiltonian

$$H = \underbrace{T_n + T_e}_{\text{kinetic energy}} + \underbrace{V_{nn} + V_{ee} + V_{en}}_{\text{Coulomb interaction}} \tag{3.1}$$

comprises the electron-electron (V_{ee}), nucleus-nucleus (V_{nn}) and electron-nucleus (V_{en}) interactions as well as the kinetic energies T_n and T_e of nuclei and electrons, respectively. The explicit expressions for the kinetic and potential energies of an $\tilde{N}$-particle system are

$$T = \sum_{i=1}^{\tilde{N}} \Big(-\frac{\hbar^2 \nabla_i^2}{2m_0} \Big)$$

and

$$V = \frac{1}{2} \sum_{i=1}^{\tilde{N}} \sum_{j \neq i}^{\tilde{N}} \frac{Z_i Z_j}{4\pi\epsilon_0 |r_i - r_j|}$$

with m_0, Z_i and r_i being rest mass, charge and position of the i-th particle, ∇_i is the nabla operator acting on particle i and ϵ_0 the dielectric constant in vacuum. Plugging

[1] In fully relativistic quantum mechanics the Dirac equation takes the Schrödinger equation's place.

these expressions into Eqn. 3.1 gives

$$\begin{aligned} H = &- \frac{\hbar^2}{2}\left[\sum_{I=1}^{M}\frac{\nabla_I^2}{m_{I,\mathrm{n}}} + \frac{1}{m_\mathrm{e}}\sum_{i=1}^{N}\nabla_i^2\right] \\ &+ \frac{1}{4\pi\epsilon_0}\left[\sum_{I=1}^{M}\sum_{J\neq I}^{M}\frac{1}{2}\frac{Z_I Z_J}{|r_I - r_J|} + \sum_{i=1}^{N}\sum_{j\neq i}^{N}\frac{1}{2}\frac{e^2}{|r_i - r_j|} - \sum_{I=1}^{M}\sum_{i=1}^{N}\frac{Z_I e}{|r_I - r_i|}\right], \end{aligned} \tag{3.2}$$

where upper and lower case indices are used for nuclei and electrons, respectively, with m_n and m_e being the corresponding rest masses. The sums are over the numbers M and N of nuclei and electrons, respectively, and $\tilde{N} = N+M$. The huge number of particles in the order of 10^{23} in a crystal requires reasonable and powerful approximations, otherwise the problem given in Eqn. 3.2 is infeasible. A first step is to neglect the motion of the nuclei and to treat their positions as bare parameters. This is known as the *Born-Oppenheimer* or *adiabatic* approximation and justified by the fact, that the rest mass of a proton exceeds that of an electron by a factor of 1836. Since the inverse mass enters the expression for the kinetic energy in Eqn. 3.2, this term is negligibly small in comparison to T_e. The Born-Oppenheimer approximation thus allows us to decouple the motion of electrons and nuclei and to reformulate Eqn. 3.2 in terms of a pure electronic problem expressed by the Hamiltonian (in atomic units: $e = h = m_e = 4\pi\epsilon_0 = 1$)

$$H_e = \sum_{i=1}^{N}\left\{ -\frac{\nabla_i^2}{2} - \sum_{I=1}^{M}\frac{Z_I}{|r_I - r_j|}\right\} + \frac{1}{2}\sum_{i=1}^{N}\sum_{j\neq i}^{N}\frac{1}{|r_i - r_j|} + E_{II} \tag{3.3}$$

where the exclusively nuclear contributions are absorbed into the additive constant E_{II}. Eqn. 3.3 thus describes the motion of the electrons in a fixed arrangement of nuclei. The wave function $\langle \boldsymbol{r} = \{\boldsymbol{r}_1, \boldsymbol{r}_2, ..., \boldsymbol{r}_N\}| \, |\Psi\rangle = \Psi(\boldsymbol{r}_1, \boldsymbol{r}_2, ..., \boldsymbol{r}_N)$ solving Eqn. 3.3 is, in accordance with the Pauli exclusion principle, the anti-symmetrised product of single-particle orbitals.

Independent-particle approximations A further simplification of Eqn. 3.3 is achieved within independent-particle approximations which can be divided into two subclasses considering non-interacting (Hartree-like) or interacting (Hartree-Fock) electrons. In either case, electron correlations are included only in terms of the Pauli exclusion principle[2] and the resulting demand for the asymmetry of the wave function under the exchange of two electrons. In non-interacting particle approximations, a single-particle Schrödinger equation is solved for an effective potential V_eff,

$$H\phi_\nu = \left(\frac{\boldsymbol{p}^2}{2m} + V_\mathrm{eff}\right)\phi_\nu = \epsilon_\nu\phi_\nu, \tag{3.4}$$

where ϕ_ν is a single-particle wave function (orbital) and ν represents all quantum numbers to describe a pure state. From the solutions ϕ_ν the anti-symmetrised N-electron product function can be built using a Slater determinant. Depending on the choice of V_eff electron-electron interactions may be included implicitly.

[2] All electrons must have a different set of quantum numbers.

Periodic lattice and Bloch waves For a periodic crystal the effective potential is given by the crystal potential V_{crys} with $V_{\text{crys}}(\boldsymbol{r}+\boldsymbol{T}) = V_{\text{crys}}(\boldsymbol{r})$. The Hamiltonian

$$H = \frac{\boldsymbol{p}^2}{2m} + V_{\text{crys}} \tag{3.5}$$

is invariant under translations by a lattice vector $\boldsymbol{T} = n_1\boldsymbol{a}_1 + n_2\boldsymbol{a}_2 + n_3\boldsymbol{a}_3$ with the n_i being integers and the $\boldsymbol{a}_i$ basis vectors of the crystal lattice. Bloch's theorem states that the eigenstates of an electron that moves in a periodic potential have the form

$$\varphi_{\boldsymbol{k}}(\boldsymbol{r}) = u_{\boldsymbol{k}}(\boldsymbol{r})e^{i\boldsymbol{k}\boldsymbol{r}}, \tag{3.6}$$

where $e^{i\boldsymbol{k}\boldsymbol{r}}$ is a plane wave and $u_{\boldsymbol{k}}$ is a function with the periodicity of the lattice, i.e. $u_{\boldsymbol{k}}(\boldsymbol{r}) = u_{\boldsymbol{k}}(\boldsymbol{r}+\boldsymbol{T})$. The crystal momentum $\boldsymbol{k}$ is a quantum number that characterises an electron state in the crystal with energy $E(\boldsymbol{k})$. Note, that for a periodic potential $\hbar\boldsymbol{k}$ is not identical to the electron momentum $\boldsymbol{p} = -ih\nabla$ as in the case of a free electron. Due to the periodicity of the reciprocal lattice $\boldsymbol{k}$ is not unique and $\varphi_{\boldsymbol{k}+\boldsymbol{G}} = \varphi_{\boldsymbol{k}}$, where $\boldsymbol{G}$ is a vector of the reciprocal lattice. This implies that all energy solutions to the Schrödinger equation can be considered in the first BZ of the reciprocal lattice by replacing $\boldsymbol{k}$ with $\boldsymbol{k}' = \boldsymbol{k} + \boldsymbol{G}$, such that $\boldsymbol{k}'$ lies within the first BZ. In this case, one speaks of the reduced zone scheme. After the back-folding of $E(\boldsymbol{k})$ branches from higher BZs into the first BZ, many energy eigenvalues are assigned to each $\boldsymbol{k}$. A positive integer n, the band index, is therefore introduced to distinguish states with the same crystal momentum but different energies. The dispersion relation $E_n(\boldsymbol{k})$, i.e. the relation between the single-particle energy E_n of an electron in the crystal and its wave vector $\boldsymbol{k}$, is what we call an electron band and the entirety of all bands the band structure.

3.2. Bulk states, surface states and surface resonances

For a crystal that is periodic in three dimensions of space $\boldsymbol{k}$ must be real, because otherwise the wave function cannot be normalised. For complex $\boldsymbol{k}$ with $\boldsymbol{k} = \boldsymbol{k}_1 + i\,\boldsymbol{k}_2$ where $(\boldsymbol{k}_1,\ \boldsymbol{k}_2) \in \mathbb{R}$

$$\exp\big(i\,[\boldsymbol{k}_1 + i\,\boldsymbol{k}_2]\,\boldsymbol{r}\big) = \exp(i\,\boldsymbol{k}_1\boldsymbol{r})\exp(-\boldsymbol{k}_2\boldsymbol{r}), \tag{3.7}$$

where for $\boldsymbol{k}_2 > 0$ the wave function is exponentially damped for $\boldsymbol{r} \to -\infty$ but diverges for $\boldsymbol{r} \to \infty$. A corresponding argumentation holds for $\boldsymbol{k}_2 < 0$. It follows that solutions of Eqn. 3.3 with complex $\boldsymbol{k}$ are forbidden. This leads to energy gaps in the band structure of the crystal. Note, that the periodic potential is, of course, an idealisation. First of all, because real crystals are always finite in size. Nonetheless, Bloch's theorem remains valid since inside the bulk of a crystal, far away from the edges the assumption of a periodic potential is justified. This does not hold anymore close to a surface (or interface), which breaks the translational symmetry along the direction of the surface normal. In the simplest approach for the description of a crystal with a surface the potential can be assumed to be periodic parallel to the surface, say in the $(x,\, y)$ plane, and semi-infinite for the z direction as sketched in Fig. 3.1. Then, Bloch's theorem is

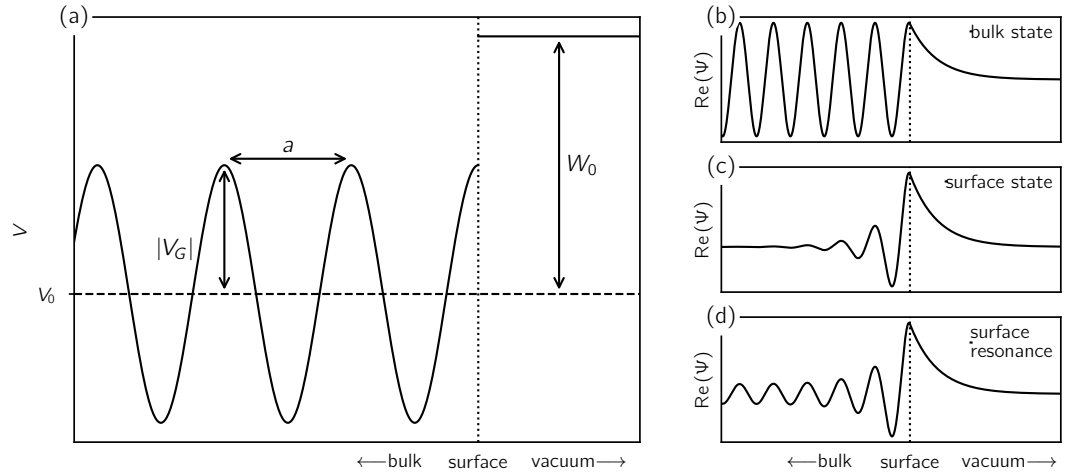

Fig. 3.1.: Periodic crystal with a surface. (a) Simple model considering the potential V along the direction of the surface normal to change at the surface from cosine-like to constant with $V = W_0$ in vacuum. (b–d) Real part of wave functions that are possible solutions to the Schrödinger equation for the potential in (a) in the case of (b) a bulk state, (c) a surface state and (d) a surface-resonant state.

still valid in the plane parallel to the surface and the wave function

$$\Psi = \psi_0(z) u_{\boldsymbol{k}_\parallel} e^{-i\boldsymbol{k}_\parallel \boldsymbol{r}_\parallel} \tag{3.8}$$

separates into the solution $\Psi_0(z)$ of Eqn. 3.5 for the one-dimensional problem accounting for the surface and the solution for an infinite crystal in two dimensions, $u_{\boldsymbol{k}_\parallel} e^{-i\boldsymbol{k}_\parallel \boldsymbol{r}_\parallel}$ underlying Bloch's theorem. $k_\parallel = (k_x, k_y)$. To calculate $\Psi_0(z)$ Eqn. 3.5 must be solved for a potential of the type schematically sketched in Fig. 3.1 which is periodic in the bulk and constant in vacuum chosen here as

$$V(z) = V_0 + W_0 \Theta(-z) + V_G \cos(Gz)\Theta(z) \tag{3.9}$$

with the step function $\Theta(z)$ defined as

$$\Theta(z) = \begin{cases} 0 & z < 0 \\ 1 & z \geq 0 \end{cases}$$

with the surface being at $z = 0$. In real crystals, of course, the potential changes smoothly at the surface but for a qualitative treatment, the assumption of a jump at the crystal-vacuum boundary suffices. The solutions take the form

$$\Psi(z) = \begin{cases} B u_{-k_z} e^{-ik_z z} + C u_{k_z} e^{ik_z z} & z < 0 \\ A\, e^{k_z z} & z \geq 0 \end{cases} \tag{3.10}$$

i.e. inside the crystal ($z < 0$) the ansatz for the wave function is of the Bloch type, while it must decay exponentially into the vacuum ($z > 0$). The coefficients A, B and C are determined by application of the matching conditions for the two solutions and

their first derivatives at $z = 0$ giving the three types of solutions sketched in Fig. 3.1. Those are (a) bulk Bloch waves, (b) surface states which are localised at the surface and damp exponentially in the bulk, and (c) surface resonances that penetrate deep into the bulk but have an enhanced amplitude at the surface. The energy is given by

$$E = E_0 + \frac{\hbar^2 \boldsymbol{k}_\parallel^2}{2m^*}, \tag{3.11}$$

where E_0 is the energy eigenvalue of the surface state Ψ_0 and $E_\parallel$ that of $\Psi_\parallel$ with the effective mass m^*. In difference to the bulk where only real $\boldsymbol{k}$ are allowed, the surface states must have a complex wave number k_z to guarantee the exponential damping in the bulk. This can be seen from Eqn. 3.10. For $z < 0$ and $k_z = k_{z1} + ik_{z2}$ the wave functions reads

$$\left(Bu_{-k_z} e^{-ik_{z1}|z|} + Cu_{k_z} e^{ik_{z1}|z|}\right) e^{k2|x|}.$$

If for the imaginary part $k_{z2} = 0$ one gets a bulk Bloch wave as shown in Fig. 3.1(a). A surface state on the contrary requires a complex k_z with $k_{z2} < 0$ to obtain the exponential damping. The complex wave number of a surface state implies that the energy of the latter lies in a forbidden gap of the bulk band structure. The electronic band structure of the bulk and the surface can be measured with angle-resolved photoelectron spectroscopy.

3.3. The principles of photoelectron spectroscopy

Photoelectron or photoemission spectroscopy (PES) is based on the photoelectric effect, which was discovered in 1887 by Hertz and Hallwachs and interpreted by Einstein in 1905. It is nowadays widely used to study the electronic and magnetic structure of matter. In photoemission an electron gets released from a bound state in an atom, molecule or solid into the vacuum after the absorption of a photon with energy $h\nu$. Measured is the intensity distribution, i.e. the number of photoexcited electrons with kinetic energy E_{kin} upon irradiating a sample with monochromatic light. Additional information can be gained by considering other experimental parameters like the light polarisation, the angle of incidence and the direction of the released photoelectrons, too. We start with the formal description of the PE process considering a system of N electrons in some initial state (index i) that is described by the many-body wave function $|\Psi_i^N\rangle$. With the absorption of an incident photon with energy $h\nu$ which leads to the liberation of one of the electrons, the system undergoes a transition into an excited final state $|\Psi_f^N\rangle$ (index f). In the excitation process the conservation laws for energy E and momentum $\boldsymbol{k}$,

$$E_f^N - E_i^N = h\nu \tag{3.12}$$

$$\boldsymbol{k}_f^N - \boldsymbol{k}_i^N = \boldsymbol{k}_{h\nu}, \tag{3.13}$$

must be fulfilled. Here, $\boldsymbol{k}_{h\nu}$ is the photon momentum, while $\boldsymbol{k}^N$ is the momentum of the N-electron state. The transition probability $\omega_{i\to f}$ between the initial and final state this given by Fermi's Golden rule

$$\omega_{i\to f} = \frac{2\pi}{\hbar} |\langle \Psi_f^N | H_{\text{int}} | \Psi_i^N \rangle|^2 \, \delta(E_f^N - E_i^N - h\nu), \tag{3.14}$$

where the δ-function ensures the energy conservation within the N particle system. The interaction Hamiltonian

$$H_{\mathrm{int}} = \boldsymbol{A} \cdot \boldsymbol{p} \tag{3.15}$$

accounts for the coupling of the electromagnetic field of the photon described by the vector potential $\boldsymbol{A}$, to the charge of an electron with momentum $\boldsymbol{p}$. In the derivation of Eqn. 3.15 certain assumptions are made: (1) $\boldsymbol{A}^2$ is negligible with respect to the linear terms in $\boldsymbol{A}$; (2) $\boldsymbol{A}$ is constant over atomic dimensions and thus $\nabla \boldsymbol{A} = 0$ (dipole approximation), which holds in the ultraviolet; (3) For a scalar potential Φ the gauge is chosen $\Phi = 0$. The expression for the interaction Hamiltonian in Eqn. 3.15 is known as dipole approximation. Note, that H_{int} does not explicitly depend on the spin, since the electromagnetic field interacts only with the charge of the electron. Now we will see how the transition probabilities $\omega_{i\to f}$ can be related to the intensity distribution of photoelectrons with kinetic energy E_{kin}. In the calculation of the $\omega_{i\to f}$, it is convenient to assume that the removal of the electron happens instantaneously, i.e. without any interactions between the ejected photoelectron and the remaining $(N-1)$-electron system. This is called the *sudden approximation* and allows for factorisation of the final-state wave function into a product function of a single-electron wave function $|\varphi_f^{\boldsymbol{k}}\rangle$ that describes a photoelectron with momentum $\boldsymbol{k}$, and the wave function $|\Psi_m^{N-1}\rangle$ that can be chosen to be an eigenstate of the excited $(N-1)$ electron system. Because of the fermionic nature of electrons, the product function must be anti-symmetric which is ensured by the anti-symmetric operator $\mathcal{A}$. This leads us to the final approximation for the final-state wave function

$$|\Psi_f^N\rangle = \mathcal{A}\,|\varphi_f^{\boldsymbol{k}}\rangle\,|\Psi_m^{N-1}\rangle\,, \tag{3.16}$$

where m indicates that we are dealing with an eigenstate of the excited $(N-1)$ electron system with energy E_m. The same formal expression can be used for the initial state, where, however, $|\Psi_i^{N-1}\rangle$ is not an eigenstate of the $(N-1)$-electron system. The expectation value in Eqn. 3.14 then reads

$$\langle\Psi_f^N|H_{\mathrm{int}}|\Psi_i^N\rangle = \underbrace{\langle\varphi_f^{\boldsymbol{k}}|H_{\mathrm{int}}|\varphi_i^{\boldsymbol{k'}}\rangle}_{=:\mathcal{M}_{f,\,i}^{\boldsymbol{k}}}\underbrace{\langle\Psi_m^{N-1}|\Psi_i^{N-1}\rangle}_{=:c_{m,i}}, \tag{3.17}$$

where the $\mathcal{M}_{f,\,i}^{\boldsymbol{k}}$ are the one-electron dipole matrix elements and the $c_{m,i}$ the overlap integrals, which describe the probability that the removal of an electron from the initial state leaves the $(N-1)$-electron system in the excited state m. What we determine in photoemission is thus the state of an $(N-1)$-electron system, which may deviate significantly from the initial N-electron state. This is particularly important in spectroscopic studies on atoms and molecules, where ionised final states can be created that couple differently to each other and have energy eigenvalues which are completely different from the neutral element. In solid-state spectroscopy the situation is different. Since N is very large, the difference between the N and $(N-1)$-electron system consists essentially in a macroscopic charging of the sample. If the latter is grounded, a respective charging is neutralised due to the electrostatic screening by the conduction electrons. The screening charge occupies a state near the Fermi energy which turns the $(N-1)$-electron system efficiently back into a system of N electrons.

While this argumentation is widely valid for itinerant electrons, it is problematic for more localised states, i.e. core states, and in particular the $4f$ electrons which play a central role in this work. The corresponding wave function of the $(N-1)$-electron system is strongly localised at the respective ionic core. In contrast, the state of the screening charge is built from the outer valence orbitals of the atoms. As Bloch waves, they have wavelengths larger than the lattice constant and thus they cannot completely neutralise the charge distribution of the photo-hole inside the atom. The result is a shift to higher binding energies and multiplet splittings which are caused by different couplings of states of the local $(N-1)$ system. Except for a scaling factor of only a few per cent, which takes the particular screening of the final state into account, it is identical with respective multiplet structures of free atoms.

Returning to quantitative description of photoemission, the total intensity is given by

$$I(\boldsymbol{k}, E_{\mathrm{kin}}) = \sum_{i,\,f} \omega_{i\to f} \propto \sum_{i,\,f} |\mathcal{M}^{\boldsymbol{k}}_{f,\,i}|^2 \sum_{m} |c_{m,i}|^2 \delta(E_{\mathrm{kin}} + E^{N-1}_{m} - E^{N}_{i} - h\nu). \quad (3.18)$$

In a system of non-interacting electrons, $\Psi^{N-1}_{i} = \Psi^{N-1}_{m}$ for $m = m_0$, i.e. only $c_{m=m_0,i} \neq 0$. If also for the corresponding matrix element $\mathcal{M}^{\boldsymbol{k}}_{f,i} \neq 0$, the PE intensity $I(\boldsymbol{k}, E_{\mathrm{kin}})$ is given by a single Delta function. In this case, the final state of the photoelectron can be directly related to its initial state by exploiting the energy conservation law

$$E_{kin} = h\nu - E_{\mathrm{B}} - \Phi_0, \quad (3.19)$$

where E_{B} is the binding energy of the photoelectron prior to its excitation and Φ_0 is the material-specific work function. In contrast, for a correlated system, several of the $c_{m,i}$ contribute to the sum in Eqn. 3.18 and the PE spectrum will consist of a main peak with several satellites. To describe correlations properly typically a more convenient approach is used which is given within the theoretical framework of the Green's function formalism, see for example Ref. [83]. Note, that the contribution of an extrinsic continuous background due to inelastically scattered electrons are not taken into account in Eqn. 3.18. Moreover, experimental broadening due to finite resolution or lifetime has to be considered, too, when it comes to the modelling of PE spectra.

We continue the discussion for non- or only weakly correlated electrons in crystalline solids. Fig. 3.2 illustrates the different reference frames for the energy of an electron bound in a solid and of a free electron in the vacuum as well as their relation according to Eqn. 3.19. In the sample the electrons has a binding energy E_{B} which is referenced to the Fermi level E_{F}, i.e. $E_{\mathrm{B}} = 0$ at E_{F}. The kinetic energy of the photoelectron is referenced to the vacuum level E_{vac}, which is defined by $E_{\mathrm{kin}} = 0$. The distance between Fermi and vacuum levels is given by the material-specific work function Φ_0, which is a measure of the minimal photon energy that is required to release an electron from the sample. Moreover, Fig. 3.2 illustrates how the PE spectrum $N(E_{\mathrm{kin}})$ relates to the density of states $N(E)$ in the sample. Straight lines in the sample's diagram on the left indicate the non-dispersive core states. Due to their discrete binding energy and their non-dispersive character, they appear in the PE spectrum as sharp peaks, whereas valence-band emissions form a broad feature that falls off to zero at the Fermi

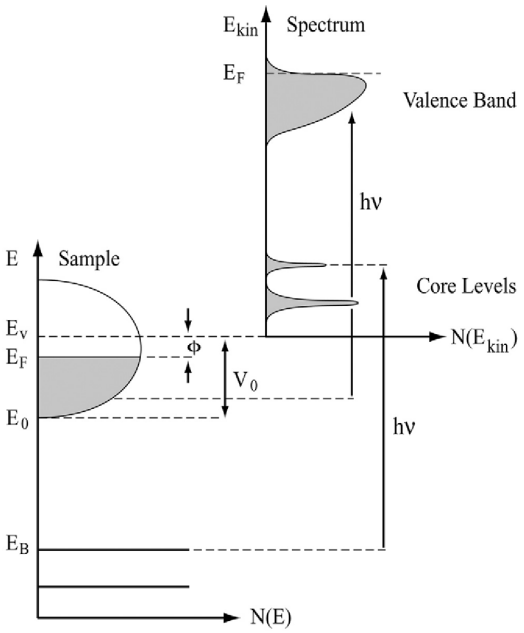

Fig. 3.2: Relation between the band structure of a crystalline, metallic sample and the PE spectrum for a system of non- or weakly interacting particles. E_B is the binding energy of the photoelectron prior to its excitation and referenced to the Fermi energy E_F at which, by definition, $E_\mathrm{B} = 0$. Φ_0 is the work function, E_0 is the energy of the bottom of the valence band and V_0 is the inner potential. In the PE spectrum E_kin is the kinetic energy of the photoelectrons which is referenced to the vacuum energy E_vac which corresponds to $E_\mathrm{kin} = 0$. $N(E)$ and $N(E_\mathrm{kin})$ are the density of states in the solid and the intensity distribution of the photoelectrons, respectively. From Ref. [83].

edge. Since the valence band is occupied only up to E_F as it is indicated by the grey shaded area in the parabolic density of states on the left, in photoemission there is a rather sudden intensity drop at the high-kinetic-energy side of the spectrum. Thermal occupation of states near but above E_F and finite resolution lead to a broadening of the Fermi edge such that the measured intensity drops smoothly to zero. Note, that in general, the valence-band emission is not identical to the number of occupied states in the sample because depending on photon polarisation or energy the excitation probability can vanish. Resulting intensity variations in the PE spectra are referred to as matrix-element effects (cf. $\mathcal{M}_{ij}$ in Eqn. 3.18).

3.4. Angle-resolved photoelectron spectroscopy

Angle-resolved photoelectron spectroscopy or shortly ARPES, sometimes ARUPS if the use of photons with energies in the ultraviolet (UV) is to be emphasized, is the principal experimental technique to study the electronic structure of materials and the main tool used in this work. In contrast to ordinary photoemission, in ARPES also the angular distribution of the photoelectrons is measured giving an intensity distribution $I = I(E_\mathrm{kin}, \theta, \varphi) = I(E_\mathrm{kin}, \boldsymbol{K})$, where $\boldsymbol{K}$ is the momentum of the photoelectron. The emission angles θ and φ are defined in Fig. 3.3, where the geometry of an ARPES experiment is sketched. θ is the angle between the propagation direction of the photoelectron and the surface normal which is parallel to the z axis in Fig. 3.3, while φ is the azimuthal angle within the surface plane. Measuring E_kin, θ and φ the momentum $\boldsymbol{K} = (K_x, K_y, K_z)^T$ of the photoelectron in the vacuum can be easily

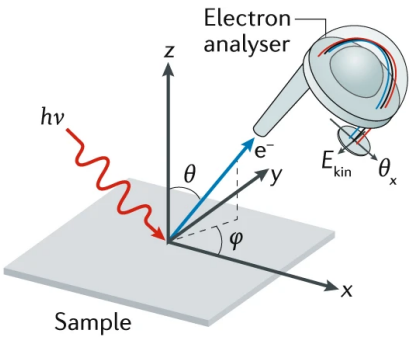

Fig. 3.3.: Monochromatic light with energy $h\nu$ liberates electrons from the sample. For certain emission directions the emitted photoelectrons enter and pass the hemispherical electron analyser and get detected. From Ref. [84].

calculated using

$$K = |\boldsymbol{K}| = \sqrt{2mE_{\text{kin}}/\hbar^2} \tag{3.20}$$
$$K_x = |K| \sin\theta \cos\varphi \tag{3.21}$$
$$K_y = |K| \sin\theta \sin\varphi \tag{3.22}$$
$$K_z = |K| \cos\theta \tag{3.23}$$

To relate the momentum of the free photoelectron to the crystal momentum in its initial state in the crystal, it must be taken into account that in the PE process only $\boldsymbol{k}_{\parallel}$, the component of the crystal momentum that is parallel to the surface is conserved, while the component $\boldsymbol{k}_{\perp}$ that is perpendicular to the surface is not because the surface breaks the symmetry of the periodic lattice. This leads to a potential barrier at the surface in the direction z of the surface normal that the electron has to overcome and results in the following relations for the momentum of the photoelectron prior to its excitation

$$k_x = K_x \tag{3.24}$$
$$k_y = K_y \tag{3.25}$$
$$k_z = \sqrt{2m(E_{\text{kin}} \cos^2\theta + V_0)/\hbar^2} \quad (\neq K_z), \tag{3.26}$$

in the extended zone scheme with V_0 being the inner potential, see Fig. 3.2. Note, that the momentum of the photon is negligible in the UV range in which ARPES experiments are typically conducted. Considering the momentum conservation, Eqn. 3.13, this implies that we are dealing with vertical transitions in the reduced zone scheme, i.e.transitions of the type $\boldsymbol{k}_f = \boldsymbol{k}_i + \boldsymbol{G}$, where $\boldsymbol{G}$ is a reciprocal lattice vector.

Surface sensitivity To achieve good energy and momentum resolution, ARPES experiments are most often conducted using photon energies in the UV (3.3 eV to 100 eV or low-energy soft x-ray radiation, which makes ARPES an extremely surface-sensitive technique. The attenuation of the PE signal with increasing distance from the surface is given by an exponential law of the form $e^{-x/\lambda}$, where x is the distance from the

surface and λ the inelastic mean free path, i.e. the distance that an electron can on average travel through the solid without being inelastically scattered. Fig. 3.4 shows the inelastic mean free path for different elements in dependence on kinetic energy. The solid line is a fit of the data points known as the universal curve. For the energies

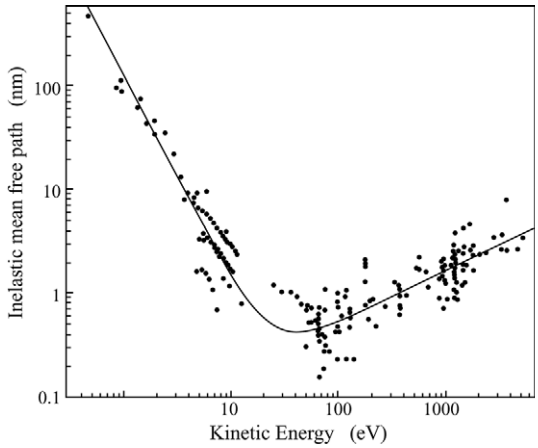

Fig. 3.4.: Universal curve for the inelastic mean free path in dependence on the kinetic energy of electrons moving in a crystal. From Ref. [83].

that we deal with in ARPES experiments, λ is below 10 Å. To increase the probing depth, soft x-rays of higher energies are used which may increase the inelastic mean free path from about 5 Å in the UV to about 20 Å in the soft x-ray, however, at the cost of resolution. Besides the high surface sensitivity, a small inelastic mean free path λ has also another consequence. Although the Bloch waves extend over the entire crystal, vertical to the surface they are probed only in an interval in the size of λ. If λ is notably smaller than the lattice constant in this direction, which is, in particular, the case in the layered compounds discussed in this work, the uncertainty relation leads to the smearing out of the $\boldsymbol{k}_\perp$ component in the order of magnitude of the respective reciprocal lattice vector. Instead of discrete inter-band transitions, we observe transitions into final states in which $\boldsymbol{k}_\parallel$ is well defined, whereas $\boldsymbol{k}_\perp$ can take all values between $\pm\boldsymbol{G}_\perp$. We thus observe the projected band structure along the $\boldsymbol{k}_\perp$ axis.

The surface sensitivity requires an atomically clean and well-ordered surface. ARPES is hence conducted under ultra-high vacuum (UHV) conditions to minimise contamination of the sample surface and scattering of the emitted photoelectrons at air molecules on their way to the detector. A convenient way to prepare an atomically clean and flat surface that does not immediately become contaminated, is to cleave a single-crystalline sample in the UHV. For this purpose, a so-called top post is glued onto the sample which is a small pin of cylindrical shape. In the UHV system, the sample can be cleaved from the outside by exploiting the lever principle applying a force onto the top post with a wobble stick. Alternative surface-preparation techniques can be the removal of a few layers on the top by argon sputtering, heating the sample to remove adsorbates or in-site growth of thin films in the UHV.

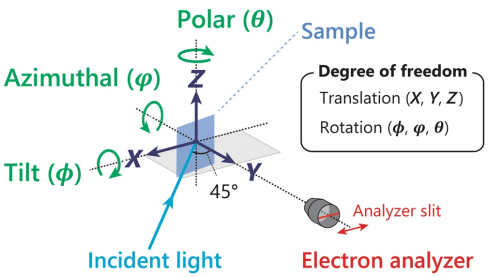

Fig. 3.5.: Translational (X, Y, Z) and rotational (φ, θ, ϕ) degrees of freedom of a six-axes manipulator used in ARPES experiments. Image from Ref. [85].

Experimental setup To move and align the sample within the UHV the sample holder with the sample is mounted on a manipulator that ideally provides six degrees of freedom, three translational and three rotational about the $\boldsymbol{X}$, $\boldsymbol{Y}$, $\boldsymbol{Z}$ axes as it is illustrated in Fig. 3.5. The translational degrees of freedom allow for moving the sample upward/downward (Z), right/left (X) and toward/away (Y, focus) from the analyser. The corresponding angles are termed azimuth φ for rotations about the axis defined by the surface normal, polar θ for rotations about the axis that is perpendicular to the entrance slit of the analyser and tilt ϕ for rotations about the axis parallel to the slit. Note, that since the Y axis forms an angle of 45° with the beam, changing the focus inevitably changes the illuminated position on the sample. Equivalently, if the polar or tilt angles are changed, also the focus changes slightly.

Spectrometer The spectrometer consists of an electrostatic input lens system, a spherical deflection analyser (SDA) and an electron detector. An SDA is built of two concentric hemispheres with radii R_1 and R_2, which lie on different potentials. The potential difference ΔV between the inner and outer hemispheres generates a spherical electrostatic field in which the photoelectrons that are reaching the analyser are deflected by the electrostatic force acting on their charge. Only electrons with kinetic energies in a small range centred around the so-called pass energy E_{pass}, which is given by $E_{\text{pass}} = e\Delta V(R_1/R_2 - R_2/R_1)$, can pass the electrostatic field between the two hemispheres and reach the detector. The emitted electrons enter the analyser through an entrance slit which selects the emission angles. Before the photoelectrons reach the entrance slit they pass an electrostatic lens system, where a retarding potential decelerates them to E_{pass}. Moreover, the lens system is responsible for the focussing of the electron beam onto the entrance slit. Electrons with the same kinetic energy are focussed onto the same spot in the entrance slit before they get deflected when they pass the SDA. They leave the SDA through an exit slit and propagate further to the detector. The two projected directions of the entrance slit can be understood as follows. The parallel direction along the slit is proportional to the emission angle and thus represents the $\boldsymbol{k}$ dependence, while the orthogonal direction to the slit corresponds to the electron dispersion depending on their kinetic energy. The two-dimensional detector is located behind the focal plane and is built of two micro-channel plates followed by a phosphorus plate and a CCD camera. The micro-channel plates serve as

electron multipliers for the impinging photoelectrons with one axis accounting for the kinetic energy and the other for the angular distribution α, originally defined by the entrance slit. Hitting the phosphorus plate, the secondary electrons produce photoluminescence which is detected by a CCD camera that converts the light intensity into a current.

Experimental Resolution The energy resolution ΔE_{spec} of the spectrometer is given by

$$\Delta E_{\mathrm{spec}} = E_{\mathrm{pass}}(w/R_0 + \alpha^2/4) \tag{3.27}$$

where $R_0 = (R_1 + R_2)/2$, α is the acceptance angle of the analyser and w is the width of the entrance slit. Note that reducing the pass energy and decreasing the width of the entrance slit lowers the intensity, hence the resolution of the spectrometer cannot be tuned towards arbitrarily small values by simply reducing these parameters. The total energy resolution ΔE_{tot} depends also on the bandwidth $\Delta\nu$ of the synchrotron radiation, being

$$(\Delta E_{\mathrm{tot}})^2 = (h\Delta\nu)^2 + (\Delta E_{\mathrm{spec}})^2 \tag{3.28}$$

For momentum resolution, the finite bandwidth of the radiation plays a minor role. It is given by

$$\Delta k_{\parallel} \simeq \sqrt{2mE_{\mathrm{kin}}/\hbar^2}\cos\vartheta\Delta\vartheta, \tag{3.29}$$

with $\Delta\vartheta$ being the angular resolution of the spectrometer, which is nowadays about 0.1°. The finite resolution leads to the broadening of the experimental data that is described by a Gaussian with an FWHM given by the experimental energy and momentum resolution. Experimental broadening is also influenced by the quality of the sample and the surface and the associated probability for elastic scattering events.

Deflector In most cases already a small rotation of the sample causes a change in the position at which the beam hits the surface. This is a large drawback and particularly disadvantageous when it comes to isoenergy mapping covering a large region of the BZ. Fortunately, this difficulty is partly overcome thanks to new state-of-the-art spectrometers that come with a deflector mode, i.e. with deflecting electrodes in the lens system that allow for rasterisation of the beam of photoelectrons emitted from the sample. This is sketched schematically in Fig. 3.6, where a top view on the emission cones is given with each circle corresponding to a certain kinetic energy. The axes α_x and α_y correspond to the detector and deflector angles, respectively, and the green rectangle represents the probed region for a given deflector angle. With deflection mode, the emission cone can be mapped without rotating the sample and changing the deflector angle α_y, i.e. changing the deflector voltage, is much faster than a mechanical rotation of the sample. Lately, most of the ARPES end stations at synchrotron radiation sources upgraded their spectrometer with a deflection mode.

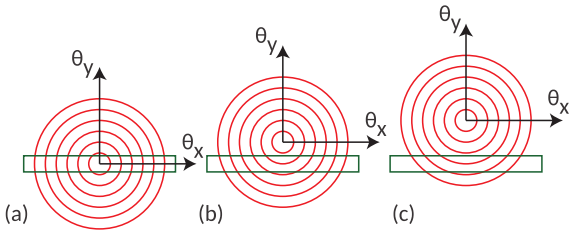

Fig. 3.6.: ARPES mapping using the deflection mode. The red circles represent the emission cone with each circle corresponding to a particular kinetic energy for a given pair (θ_x, θ_y) of detector and deflector angles. The outermost circle corresponds to the acceptance cone of the analyser, the green rectangle marks the probed area (a) without deflection and (b, c) with deflection for different deflector angles θ_y. Image from Ref. [86].

3.5. Photoabsorption and resonant photoelectron spectroscopy

When the photon energy is close to the binding energy of a core level a core electron can be excited into an unoccupied state above the Fermi level, a process which is known as photo- or x-ray absorption (XA). The de-excitation of the excited state may be realised radiatively or non-radiatively. In both cases, the core hole is filled by an outer-shell or valence electron. In a radiative decay process also known as fluorescence, the energy gained by filling the core hole is emitted in form of a photon. In the case of the non-radiative or Auger decay, the energy is transferred to another electron which is excited into the vacuum. The Auger decay can be understood as an auto-ionisation process in which a sudden change of the potential is induced by the virtual excitation of the primary electron into a localised intermediate state with the energy being transferred to a third electron. In the general case the electronic levels that are involved in the absorption and the Auger decay, i.e. the core level A where the hole is produced, the level B from which the core hole is filled, and the level C from which the Auger electron is liberated into the vacuum, have different principal quantum numbers n. In the special case where the two levels in ABC have the same principal quantum number, the Auger process is called a *Koster-Kronig decay.* If all three levels have the same n one speaks of a *super-Koster-Kronig decay* (SKK). As an example of the latter, we consider the $4d \rightarrow 4f$ absorption threshold in the lanthanides,

$$4d^{10}4f^n + h\nu \xrightarrow{XA} 4d^9 4f^{n+1} \xrightarrow{SKK} 4d^{10}4f^{n-1} + e^-, \tag{3.30}$$

where e^- is the emitted Auger electron. After absorption of the photon, an electron from the $4d$ core level is excited into an empty $4f$ state. Within the super-Coster-Kronig decay, one $4f$ electron fills the core hole, while another one is liberated into the vacuum.

The final state in 3.30 can be reached via direct photoemission, too. In **resonant photoelectron spectroscopy (RPES)** the photon energy is chosen such, that the

direct PE process, i.e.

$$4d^{10}4f^n + h\nu \longrightarrow 4d^{10}4f^{n-1} + e^- \tag{3.31}$$

in the case of the example given above, and the (super-) Koster-Kronig decay quantum-mechanically interfere with each other because they both lead to the same final state. Thus, the PE signal from a valence-band state can be resonantly enhanced by tuning the photon energy close to the absorption threshold of a core level. The resonance measured in dependence on the photon energy has an asymmetric line shape which is known as *Fano profile*. When approaching the resonance energy the PE intensity passes a minimum which corresponds to destructive interference of the two excitation channels. In this minimum, the emission from the final state under consideration is almost completely suppressed. Therefore, if $h\nu$ is chosen for the Fano minimum one speaks of an *off-resonance* PE experiment for the final state under consideration, whereas the term *on-resonance* is used if the energy is chosen at the maximum of the Fano resonance, also known as Beutler-Fano resonance [87, 88]. Note, that in RPES the photoabsorption and the Auger decay must be viewed as a coherent one-step process. Moreover, the interaction Hamiltonian H_{int} in Eqn. 3.15 must be extended, i.e. the second order perturbation term has to be included, too. Mathematically, the interference of the two excitation channels results from summing up the respective transition matrix elements. The benefit of the RPES is the element and orbital selectivity which allows to switch the PE signal from a particular initial state on ("on resonance") or off ("off resonance") by the proper choice of the photon energy.

3.6. X-ray absorption spectroscopy

In solid-state physics, x-ray absorption spectroscopy (XAS) is widely used as a probe of the local atomic structure and the local environment in compounds which are constituted of different types of atoms. Measured is the absorption of monochromatic radiation incident on a sample in dependence on the photon energy. The dominating absorption process is photoexcitation, where the energy and momentum of the photon are completely transferred to an electron leading typically to its liberation into a free vacuum state. However, if the energy of the incident light corresponds to an absorption threshold a second excitation channel opens in which core electrons are excited into unoccupied states above E_{F} localised by the potential of the photohole, which leads to a resonant enhancement of the absorption. The characteristic energy of transitions at the absorption edges makes XAS an element- and orbital-selective technique. Prominent examples are the $L_{2,3}$ edge for $3d$ transition metals, i.e. excitation from the spin-orbit split $2p_{1/2,3/2}$ core into $3d$ valence bands states, and the $M_{4,5}$ edge for lanthanides with $3d_{3/2,5/2} \rightarrow 4f$. The two principal detection modes in XAS experiments are the total electron yield (TEY) and the total fluorescence yield (TFY), respectively. The term *total* indicates that all electrons/photons are counted independent of their kinetic/photon energy and emission angle. Due to the small escape depth of photoelectrons, especially in the soft x-ray regime, TEY probes mostly the surface region, whereas TFY is rather bulk sensitive. Therefore the combination of both detection modes allows for a distinction between surface and bulk properties.

3.6.1. X-ray magnetic circular dichroism

Dichroism in XAS describes the polarisation dependence of the light absorption due to asymmetries in the distribution of the electronic charge or the magnetisation around an atom [89]. Magnetic dichroism is widely used to study magnetic materials with collinear order but can be also applied to the investigation of non-collinear systems. The difference in the absorption of *circularly* left and right polarised light is known as x-ray magnetic circular dichroism (XMCD) and proportional to $\langle \boldsymbol{M} \rangle$, the expectation value of the magnetisation. More precisely, the XMCD sum rules allow for relating the XAS and XMCD spectra to the expectation values $\langle \boldsymbol{L}_z \rangle$ and $\langle \boldsymbol{S}_z \rangle$, the z components of angular momentum and spin operators, respectively, and thus, for separate determination of the angular and spin magnetic moments in the ground state [90]. The XMCD will be strongest if the propagation vector $\boldsymbol{u_k}$ of the incident light and the magnetisation $\boldsymbol{M}$ are collinear because the matrix elements are proportional to the scalar product $\langle \boldsymbol{M} \cdot \boldsymbol{u_k} \rangle$. Therefore the sample is typically magnetised by an external magnetic field in the direction of the propagation vector of the incident light.

For systems with itinerant magnetism like the $3d$ transition metals XMCD is usually explained in a single-particle picture using a two-step model and the general optical selection rules for electronic dipole transitions $\Delta l = \pm 1$, $\Delta m_l = 0, \pm 1$ and $\Delta m_s = 0$. In the first step, the circularly polarised light produces a spin-polarised current of photoelectrons. Changing the polarisation changes the sign and the absolute value of the photocurrent's spin polarisation. In the second step, the excited electrons reach for unoccupied states in the valence band. Since spin flips are forbidden by the selection rules, the electrons can only occupy states with the same spin. Thus, if there is a spin imbalance in the available valence band states the absorption will be larger for the spin sort that has a larger number of unoccupied valence states at its disposal. For example, in the magnetic $3d$ transition metals like Co, Fe or Ni, electrons that carry the minority spin have a higher probability to reach the valence band than those with majority spins, because most majority-spin states are occupied. It follows that the absorption cross-sections differ for opposite light polarisation and XMCD will be observed. A prerequisite for producing a spin-polarised current in the first step is spin-orbit coupling which is the only way to partly transfer the angular momentum of the photon to the spin of the electron (recall that H_{int} in Eqn. 3.15 is independent on spin). Since the absorption depends strongly on the available spin states in the valence band, the latter is said to act as a spin detector.

In the case of local-moment magnetism like in the $4f$ materials, the atomic configuration must be considered rather than a single-electron picture because the atomic properties of the $4f$ shell are preserved in compounds. Here, the transitions are of the type $J \rightarrow J'$ with selection rules $\Delta J = \pm 1$ and $\Delta M_J = 0, \pm 1$. If the $4f$s are magnetically ordered, the single M_J levels are Zeeman split and at $T = 0\,\mathrm{K}$ only the lowest level with $M_J = -J$ is occupied. Taking the example of absorption at the $M_{4,5}$ edge of trivalent Yb the transition is from $3d^{10}4f^{13}$ ($J = 7/2$) to $3d^{9}4f^{14}$ ($J = 5/2$). In the ground state, where only the $M_J = -7/2$ level is occupied only transitions into $M'_{J\prime} = -5/2$ of the $J' = 5/2$ final state are allowed. In this particular case and under the assumption that there is no configurational mixing, absorption can take place only for one type of circular polarisation. Note that with increasing temperatures

the probability for the occupation of higher M_J levels grows and hence, the XMCD spectrum will in general show a temperature dependence.

3.6.2. X-ray magnetic linear dichroism

X-ray linear dichroism (XLD) describes the differential absorption of x-rays with linear polarisation parallel and perpendicular to a given quantisation axis defined, for example, by a molecular orbital, a directional bond or the symmetry axis of a crystal. The difference in the absorption of mutually perpendicularly polarised light originates from anisotropies in the charge distribution. The oscillation of the $\boldsymbol{E}$ vector of the linearly polarised light defines the axis along which the sample is scanned by the incident light. Therefore, $\boldsymbol{E}$ is said to act as a searchlight for occupied or unoccupied states along its oscillation axis. Consequently, XLD, i.e. the difference between spectra acquired with either light polarisation, is largest if the oscillation axis of $\boldsymbol{E}$ coincides for one polarisation with a given symmetry axis of the sample. In x-ray magnetic linear dichroism (XMLD), which is used to gain information about the magnetic properties of a sample with ferro-, ferri- or antiferromagnetic order, the symmetry axis is given by the magnetisation axis. In difference to XMCD, the XMLD signal is proportional to $\langle \boldsymbol{M}^2 \rangle$ and therefore sensitive to antiferromagnetic order. It is observed because the coupling of the spin to the angular momentum of the electron leads to the deformation of the charge cloud when the spins order magnetically. Using sum rules the sizes, directions and anisotropies (sizes in different directions) of the atomic magnetic moments can be determined from respective XMLD spectra [91]. Due to the nature of linear polarisation, possible transitions have $\Delta m_l = 0$. Note, that XMLD is also used in investigations of non-collinear magnetic order with a canted or spiral magnetic structure for which the relative orientation of the sublattice magnetisation directions can be determined.

3.7. Photoelectron diffraction

Elastic scattering of a photo-excited core electron at neighbouring atoms leads to angle-dependent intensity variations in the angular distribution of the photoemission spectrum. To understand this one must consider the wave picture in which the primary wave describing the photoelectron interferes with itself after being elastically scattered by surrounding atoms as it is schematically illustrated in Fig. 3.7(a). Depending on the path difference at the position $\boldsymbol{r}$ between the primary wave $\phi_0(\boldsymbol{r}, \boldsymbol{k})$ and the scattered wave $\phi_j(\boldsymbol{r}, \boldsymbol{r}_j \rightarrow \boldsymbol{k})$, where $\boldsymbol{r}_j$ is the vector between the emitter atom and the scatterer atom j, and $\boldsymbol{k}$ the wave vector in vacuum, the two waves may interfere constructively or destructively which results in modulations in the photoemission intensity for different emission angles. From these modulations, structural information can be gained, for example about interlayer spacings, bonding lengths or position and orientation of adsorbed molecules at the surface. This requires a detailed model of the system under study, a so-called cluster, Fig. 3.7(b), on the basis of which the photoelectron diffraction (PED) spectra can be simulated with the help of dedicated computer codes and compared to the experimental results. Within the framework of a reliability- or R-factor analysis, which quantifies the agreement of the model with

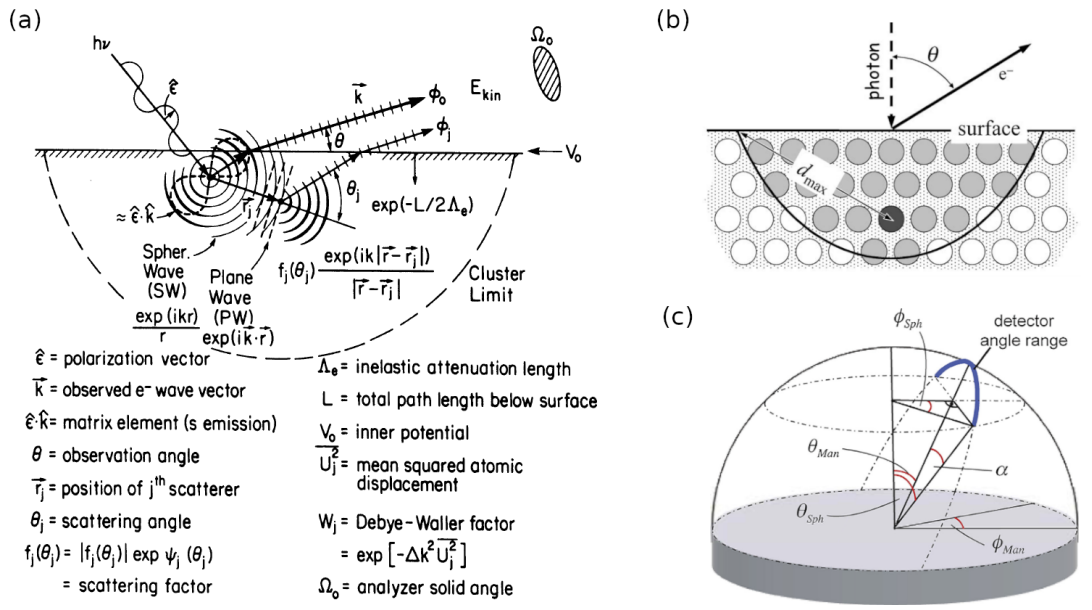

Fig. 3.7.: (a) In the wave picture a photoexcited core electron leaves the emitter atom as spherical wave, which scatters at neighbouring scatterer atoms. Depending on the path difference between the primarily emitted wave and the scattered wave for a given scattering angle θ_j it comes to constructive or destructive interference, which is seen as intensity modulation in a core-level PE spectrum. Image from Ref. [92]. (b) Cluster as it is used in the modelling of PED data. Circles represent atoms with the one shaded in dark grey being the emitter. For scattering only the grey-coloured atoms are considered which fulfil the criterion that the sum of their distances from the emitter and the surface is smaller $d_{\max}$. Image from [93]. (c) Experimental geometry from Ref. [94].

the experiment, model parameters (e.g. the interlayer distance between the first and second layer of some compound) are tuned until the best agreement of the simulation with the experiment is obtained.

A PED experiment is conducted as a series of ARPES experiments in which a specific core level is probed for a given excitation energy $h\nu$ and all accessible emission directions. Fig. 3.8(a) illustrates the data collection process. The grey-shaded circle represents the sample surface, and the dashed-dotted line in the centre indicates the normal emission direction. The hemisphere is the constant-kinetic-energy isosurface of the liberated photoelectrons in the upper-half space, that are emitted from the point where the normal-emission line cuts the surface plane. For a fixed manipulator angle ϕ_{Man} (see Fig. 3.7(c)), a set of ARPES spectra is acquired for different polar angles θ_{Man} with a well-defined step size $\Delta\theta_{\mathrm{Man}}$ as indicated by the black circular arcs on the hemispherical isoenergy surface, where each line corresponds to a different θ_{Man}. The length of the lines corresponds to the acceptance range for emission angles α of the spectrometer. After a full set is measured for a given ϕ_{Man}, azimuth is changed and another set of spectra is measured. This repeats until the whole hemisphere, i.e. all

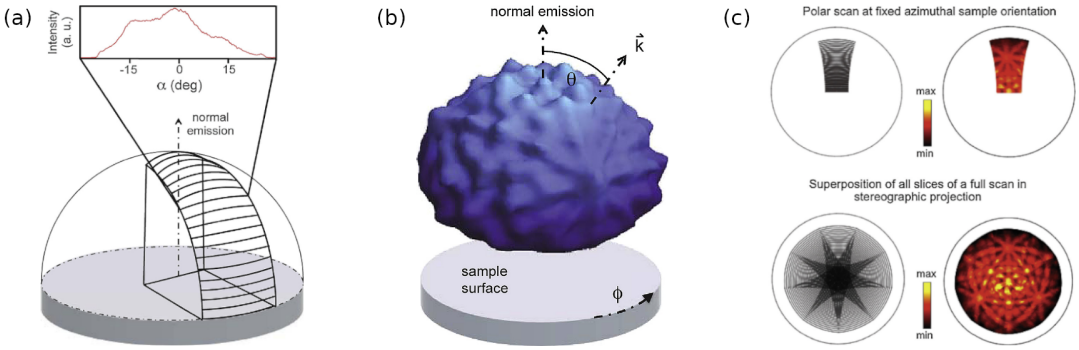

Fig. 3.8.: PED experiment. (a) Isoenergy hemisphere centred at the normal emission line which simultaneously marks the spot on the sample surface from which the photoelectrons are emitted. The circular arcs drawn in black show which cut on the isoenergy hemisphere, where a single arc corresponds to an ARPES spectrum for a fixed pair of azimuthal and polar manipulator angles (ϕ_{Man}, θ_{Man}). Each scan contributes the intensity distribution over the detector angle α for a given energy as shown in the upper window. (b) 3D representation of the data acquired in a PED experiment for fixed kinetic energy that determines the radius of the hemisphere. The intensity modulations are plotted onto the hemisphere, appearing as hills and valleys. (c) The resulting diffraction pattern after using the method of stereographic projection is shown for a complete polar scan at a fixed azimuthal angle (upper panel) and a complete set of azimuthal angles (lower panel). Pictures from Ref. [94].

emission directions, has been rasterised. In Fig. 3.8(b) a 3D view of the acquired data for a complete set of measurements is given, showing the PE intensity plotted onto the isoenergy surface of the selected E_{kin} introduced in (a). In a quite elaborate process, the single ARPES spectra are then combined to construct a diffraction pattern of the selected core level under study, projecting the angular dependent intensities onto the (k_x, k_y) plane using for example the method of stereographic projection [94]. The result is a diffraction pattern similar to that shown in Fig. 3.8(c). There, the grey plots on the left illustrate the projection of the probed angles, while on the right the projected data are shown for a single azimuthal angle and a complete polar scan in the upper, and a complete data set in the lower row. Since information should be gained about a designated emitter atom and its environment the photon energy is chosen for the excitation of electrons from an element-specific core level of the emitter. To cover all accessible directions the sample must be rotated without changing the irradiated spot on the sample surface throughout the entire measurement. Therefore, a manipulator that allows for translations and rotations about the x, y and z axes is indispensable for a PED experiment.

3.8. Synchrotron and synchrotron radiation

The experimental techniques described above benefit strongly from the availability of synchrotron radiation that is generated at dedicated synchrotron radiation facilities (synchrotrons). In general, the term synchrotron radiation refers to the light emitted by a relativistic charged particle tangentially to the direction of movement due to its radial acceleration. Photon science strongly benefits from the technical availability of

① Electron gun; LINAC
② Booster synchrotron
③ Storage ring
④ Beamlines
⑤ Front end
⑥ Optics hutch
⑦ Experimental hutch
⑧ Control hutch

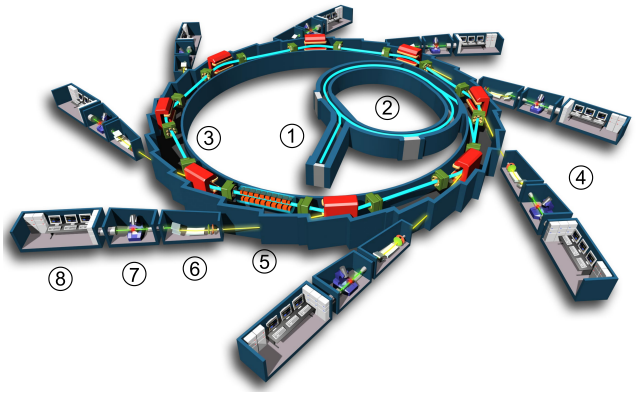

Fig. 3.9.: Layout of a synchrotron radiation source. Image from Ref. [95].

synchrotron radiation, which has many advantages over lab sources like gas-discharge lamps or x-ray tubes: the photon energy can be chosen from a continuous spectrum ranging from the far-infrared to hard x-rays and is tunable within a wide range; the light is of high intensity; the photon beam has a small spot size; synchrotron radiation is highly polarised. Two important parameters used to describe the quality of the radiation, and thus for comparison of different radiation sources, are the spectral flux, that is the number of photons hitting the sample per second and unit bandwidth[3], and the brightness or brilliance, that is the spectral flux per unit solid angle per unit area, which is a measure for the spatial dependence of a source's intensity for a given energy. Dedicated synchrotron radiation sources are typically electron storage rings, where the light is produced by electrons that are circulating in an evacuated ring with a velocity close to the speed of light. The radiation which is emitted in the forward direction, when the electron gets radially accelerated in a magnetic field, forms a strongly collimated cone. This is a relativistic effect that results from the high velocity of the electrons. A typical layout of a synchrotron is given in Fig. 3.9. The electrons are produced by an electron gun and pre-accelerated in a linear accelerator. With relativistic energies of several hundred MeV, they enter the booster synchrotron where they are accelerated further reaching a velocity close to the speed of light at which they are injected in time intervals of a few seconds into the storage ring. This operation mode is called *Top-Up*. Note, that the bunch length and the time between injections can be tuned to realise, for example, time-resolved experiments down to the pico-second scale. In the storage ring, the electron bunches move on a closed loop with an energy that is in the order of a few GeV[4]. The larger the energy of the electrons in the storage ring, the higher the photon energies that can be reached and the more collimated the radiated light cone. Exploiting the Lorentz force, the trajectory of the electron beam is controlled by magnetic fields. Travelling through the storage ring the electrons pass homogeneous magnetic fields induced by dipole (bending) magnets installed along the storage ring. The field lines run vertical to the horizontal plane

[3] For synchrotrons the unit band with is defined as 0.1 %.
[4] Storage ring energies at different synchrotron light sources: DLS: 3 GeV, BESSY II: 1.7 GeV, SLS: 2.4 GeV, MAX IV: 3 GeV, SOLARIS: 1.5 GeV, SOLEIL: 2.75 GeV

of the storage ring and thus, to the velocity vector of the electrons guiding them on a circular trajectory. Passing the bending magnet, the electrons emit synchrotron radiation in a wide spectral range. In the straight segments between two bending magnets radiation is produced by so-called insertion devices, which are described below in more detail. Within each loop through the storage ring, the electrons pass radio-frequency cavities to compensate for the energy loss due to the emission of radiation. To keep the beam focused and to correct the path of the electrons, other types of magnets are used including quadrupole, sextupole, octopole and higher-order magnets. At the front ends the radiation is directed through a beamline, i.e. an evacuated straight tube, to the experiment, passing monochromatising and focussing optics.

Insertion devices are wigglers or undulators, i.e. arrays of dipole magnets with alternating polarisation. In the resulting sinusoidal magnetic field, the electrons are forced on a wiggling or undulating path on which they emit radiation. The radiation produced by a wiggler is incoherent and basically that of a series of bending magnets. Therefore, the continuous spectrum is characterised by a large bandwidth and high intensity. For experiments that require a sharp energy the large bandwidth of a wiggler is disadvantageous because the required monochromatisation leads to undesired heat production in the optical devices. In the smaller magnetic field of an undulator, the amplitude of the oscillations of the electrons is much smaller than in a wiggler, which enables the interference of the emitted radiation cones. Since, depending on the wavelength, the radiation interferes constructively as well as destructively, undulators generate a spectrum of highly intense radiation peaks with a sharp energy instead of a broad continuous spectrum. By tuning the period length between the undulator's dipole magnets the photon energy can be tuned to the required value. Another advantage of undulators over wigglers or bending magnets is the larger collimation of the beam and the resulting higher brilliance.

Light Polarisation Many experimental techniques, like XMCD and XMLD require polarised light. Since electromagnetic radiation is a transverse wave, the mutually perpendicular vectors of the electric field $\boldsymbol{E}$ and magnetic field $\boldsymbol{B}$ span a plane that is orthogonal to the direction of propagation. If they oscillate along a fixed axis the light wave is linearly polarised, while elliptical or circular light polarisation is given if the field vectors rotate in the plane perpendicular to the propagation direction. Since the electric field vector may rotate clockwise or counter-clockwise there are two possible realisations of circular polarisation, namely circular left (CL) and circular right (CR). In the literature different conventions for the definition of CL and CR polarisations exist because the rotational direction of the $\boldsymbol{E}$ field depends on the position of the observer. Ambiguity and confusion can be avoided using the helicity instead, i.e. the projection of the photon spin onto its momentum, rather than the polarisation giving $+\hbar$ and $-\hbar$ for the photon spin parallel or antiparallel to momentum, respectively.

Synchrotron facilities usually offer light of linear, elliptical and circular polarisation. Planar undulators and wigglers, just like bending magnets, produce radiation that is linearly polarised in the storage-ring plane. If the $\boldsymbol{E}$ vector oscillates in the plane of

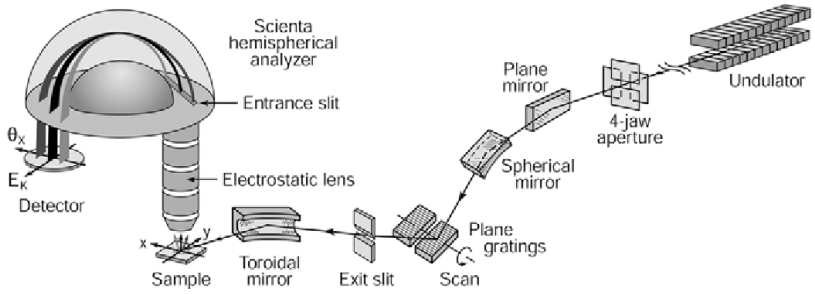

Fig. 3.10.: Design of an ARPES beamline. The light produced by the undulator is directed towards the sample passing different optics that serve for monochromatisation (mirrors and plane gratings) and focussing (mirrors) of the radiation as well as the adjustment of the intensity (exit slit). From Ref. [83].

the latter we speak of linear horizontal (LH) polarisation, while linear vertical (LV) polarisation is used if the oscillation is along the axis perpendicular to the plane of the storage ring. Out of the storage-ring plane, the light has elliptical polarisation. Producing brilliant light of non-linear polarisation requires special undulators or wigglers, for example using helical fields that force the electrons on a spiral trajectory. Modern undulators exploit that circularly polarised light results from the superposition of LH and LV polarised waves of the same amplitude and phase. Finally note, that in the literature also the terms s and p polarised light are met, which refer to a perpendicular or parallel oscillation axis of $\boldsymbol{E}$ with respect to a symmetry axis or plane defined by the geometry of the experiment but not actually to the storage-ring plane.

Beamline The beamline is the connecting element between the insertion device or bending magnet where the light is produced, and the experimental end station where the measurements are conducted. An exemplary beamline setup is shown in Fig. 3.10. Along the beamline, optical devices like mirrors and plane gratings are installed to monochromatise the radiation produced by the undulator, wiggler or bending magnet. Insertion device, beamline and end station form a unity in the sense, that they are well-matched to meet the requirements of a particular experimental technique. ARPES, e.g. requires UV and soft x-ray photons which are ideally available in linear and circular polarisations. Moreover, highly monochromatic light, high flux and a small spot size of the photon beam are desirable. Which photon-energy range is available at an end station is determined by the insertion device. A slit that partly blocks the beam can be further opened or closed to increase or decrease the intensity of the radiation. The energy resolution of the beamline is determined by the resolution ΔE_m of the monochromator, which depends on the slits. The ultimate resolution is given by the monochromator's resolving power $E/\Delta E_m$, where E is the photon energy. Slits account for a vertical and/or horizontal definition of the beam size, mirrors for focussing and the plane grating monochromator (PGM) monochromatises the radiation exploiting the principle of diffraction.

3.9. Density functional theory

Theorems of Hohenberg and Kohn

In density functional theory (DFT) the problem of solving the stationary Schrödinger equation for the electronic many-body Hamiltonian in Eqn. 3.3 is circumvented by mapping the infeasible interacting problem onto a solvable non-interacting problem. DFT is built upon the theorems of Hohenberg and Kohn [96], which state that the external potential V_{ext} is a unique functional of the ground state density n_0. This implies that n_0 determines the Hamiltonian and thus, the ground state wave function $|\Psi_0\rangle$. It follows that n_0 contains all information about the system under consideration and instead of calculating an N-particle wave function, one needs to find only a scalar function $n_0(\boldsymbol{r})$. For that, the energy functional is written as

$$\begin{aligned} E[n] &= \langle\Psi[n]|\hat{H}|\Psi[n]\rangle && (3.32)\\ &= \langle\Psi[n]|\hat{T}+\hat{V}+\hat{U}|\Psi[n]\rangle && (3.33)\\ &= T[n]+V[n]+U[n] && (3.34)\end{aligned}$$

with T and U being universal density functionals describing the kinetic energy and the electron-electron interactions, respectively. The term "universal" means that T and U are the same for any system of interacting electrons, while V depends on the system under study. In their second theorem Hohenberg and Kohn state that for an arbitrary density $n(\boldsymbol{r})$ with $n(\boldsymbol{r}) \geq 0$ and $\int d\boldsymbol{r}\; n(\boldsymbol{r}) = N$

$$E_0 = E[n_0(\boldsymbol{r})] \leq E[n(\boldsymbol{r})], \tag{3.35}$$

i.e. the ground state energy E_0 forms a lower bound for the energy functional $E[n(\boldsymbol{r})]$ where equality is only given if $n(\boldsymbol{r})$ equals the ground state density $n_0(\boldsymbol{r})$. Eqn. 3.35 allows us to apply the variational principle

$$\left.\frac{\delta E[n(\boldsymbol{r})]}{\delta n(\boldsymbol{r})}\right|_{n=n_0} = 0 \tag{3.36}$$

providing a practical guideline for the calculation of n_0 and thus, of any observable. However, straightforward application of the theorems of Hohnenberg and Kohn requires explicit knowledge of the energy functional in Eqn. 3.34, yet only $V[n]$ is known to be

$$V[n] = \int d\boldsymbol{r}\, V_{\text{ext}}(\boldsymbol{r})\, n(\boldsymbol{r}), \tag{3.37}$$

where V_{ext} is the external potential describing, for example, the electric field of the nuclei in a crystal. Similar expressions for $T[n]$ and $U[n]$ are not known.

Kohn-Sham theory

Kohn and Sham developed a formalism [97] to solve the variational problem given in Eqn. 3.36. In the Kohn-Sham formalism, the interacting N-electron system is replaced

by a non-interacting N-electron system that has the same density $n(\boldsymbol{r})$. The energy functional 3.34 takes the form

$$E[n] = T_{\mathrm{KS}}[n] + V_{\mathrm{KS}}[n]$$

with

$$T_{\mathrm{KS}}[n] = -\frac{1}{2}\sum_{i}^{N}\langle\phi_i|\nabla_i^2|\phi_i\rangle$$

accounting for the kinetic energy of the fictive, non-interacting system expressed by the single-particle orbitals $|\phi_i\rangle$. Further,

$$V_{\mathrm{KS}}[n] = V_{\mathrm{ext}}[n] + V_{\mathrm{H}}[n] + E_{\mathrm{xc}}[n]$$

comprises the functionals associated with the external potential V_{ext} and the electron-electron Coulomb interaction in terms of the Hartree term V_{H}

$$V_{\mathrm{H}}[n] = \int d\boldsymbol{r}\,\frac{n(\boldsymbol{r})\,n(\boldsymbol{r}_i)}{|r - r_i|}.$$

The remaining contribution E_{xc} is the so-called exchange-correlation functional, which is defined as

$$E_{\mathrm{xc}} = (T - T_{\mathrm{KS}}) + (V_{\mathrm{ee}} - V_{\mathrm{H}})$$

comprising the difference in energy between the interacting and non-interacting systems. Application of the variational principle given in Eqn. 3.36 gives

$$\left[-\frac{\nabla^2}{2} + v_{\mathrm{ext}}(r) + \int d\boldsymbol{r}'\frac{n(\boldsymbol{r}')}{|\boldsymbol{r} - \boldsymbol{r}'|} + v_{\mathrm{xc}}(\boldsymbol{r})\right]\phi_i(\boldsymbol{r}) = \epsilon_i\phi_i(\boldsymbol{r}) \tag{3.38}$$

with the Kohn-Sham energies ϵ_i and the Kohn-Sham orbitals ϕ_i being the solutions to the non-linear, single-particle Kohn-Sham equations, where the newly introduced local potential v_{xc} is the functional derivative of the exchange-correlation functional,

$$v_{\mathrm{xc}} = \frac{\delta E_{\mathrm{xc}}[n]}{\delta n(\boldsymbol{r})}.$$

If v_{xc} was known, the original problem of the N-electron interacting system could be solved exactly. However, since this is not the case good approximations are indispensable.

Exchange-correlation functionals

There are many approaches for the description of the exchange-correlation functional $E_{\mathrm{xc}}[n]$. Two of them which will be used in this thesis are the linear density approximation (LDA) and the generalised gradient approximation (GGA). In LDA it is assumed that the inhomogeneous density can be approximated by decomposing the system into sufficiently small volume elements with a homogeneous density. The LDA exchange-correlation functional takes the form

$$E_{\mathrm{xc}}[n] \approx E_{\mathrm{xc}}^{\mathrm{LDA}}[n] = \int d\boldsymbol{r}\,e_{\mathrm{xc}}^{\mathrm{hom}}(n)\Big|_{n\to n(\boldsymbol{r})} = \int d\boldsymbol{r}\,e_{\mathrm{xc}}^{\mathrm{hom}}(n(\boldsymbol{r})) \tag{3.39}$$

with $e_{\mathrm{xc}}^{\mathrm{LDA}}$ being the exchange energy of the homogeneous electron liquid.

Aiming at a more realistic description of the spatial dependence of the density, in GGA functions f that depend in addition to the density n also on the gradient $|\nabla n(\boldsymbol{r})|$ are constructed. $E_{\mathrm{xc}}^{\mathrm{GGA}}$ takes the form

$$E_{\mathrm{xc}}^{\mathrm{GGA}}[n] = \int d\boldsymbol{r}\ f(n(\boldsymbol{r}), \nabla n(\boldsymbol{r})). \tag{3.40}$$

DFT+U

Strong on-site Coulomb repulsion between localised electrons in partially filled shells, like the $4f$ electrons in the lanthanides, are not well described by the LDA and GGA exchange-correlation functionals which tend to over-delocalise these electrons. Improvement can be achieved by the DFT+U method which is basically the incorporation of the Hubbard model into the DFT energy functional $E[n]$ [98]. In its simplest form, the Hubbard model comprises nearest-neighbour hopping of electrons between sites i and j, i.e. an effective de-localisation of the electrons, and a second term which accounts for Coulomb interactions between electrons centred at the same atomic site i. The corresponding Hamiltonian reads

$$H_{\mathrm{Hub}} = t \sum_{\langle i,j\rangle),\,\sigma} \left(c_{i,\sigma}^{\dagger} c_{j,\,\sigma} + \mathrm{h.c.}\right) + U \sum_{i} n_{i,\uparrow} n_{i,\downarrow} \tag{3.41}$$

where t is the hopping amplitude, $c^{\dagger}$ and c are creation and annihilation operators, σ describes the spin coordinate with $\uparrow$ and $\downarrow$ for spin up and down, respectively, and U is the so-called Hubbard U describing the on-site Coulomb interaction. Incorporating Eqn. 3.41 into the DFT functional the LDA+U[5] energy functional takes the form

$$E_{\mathrm{LDA}+U}[n(\boldsymbol{r})] = E_{\mathrm{LDA}}[n(\boldsymbol{r})] + E_{\mathrm{Hub}}[\{n_{mm'}^{l\sigma}\}] - E_{\mathrm{dc}}[\{n^{l\sigma}\}]. \tag{3.42}$$

With this, the Hubbard term E_{Hub}, which derives from the Hubbard Hamiltonian and acts only on the correlated states, is added to the LDA energy functional. Since the correlated electrons are now included in both the LDA and the Hubbard functional, a term E_{dc} must be subtracted to avoid double counting. The indices l and m are the orbital and magnetic quantum numbers, respectively, and emphasize that only the correlated states are affected by the Hubbard term. The two implementations of the double-counting functional are known as *fully-localised* or *atomic limit* (AL) and *around mean field* (AMF). In practice, DFT+U calculations consist in a proper choice of the effective Coulomb interaction U and exchange interaction J included in E_{Hub} and E_{dc}, such that a good agreement with experimental data is achieved. An instructive review of the fundamentals of the DFT+U method can be found in Ref. [99].

Self-consistency cycle

The Kohn-Sham equations are solved numerically in a self-consistency cycle for the appropriate exchange-correlation functional. The procedure involves

[5] Accordingly for GGA. Note, that DFT+U is only meaningful with spin polarisation.

1. Choosing a start density n^{init}.
2. Calculating $V_{\text{KS}}^{\text{init}}$ for n^{init}.
3. Calculating the ϕ_i solving Eqn. 3.38 for $V_{\text{KS}}^{\text{init}}$.
4. Calculating a new density n_1 using $n = \sum_{i=1}^{N} \int d\boldsymbol{r}\ \phi_i^* \phi_i$
5. Repeating steps 2 to 4 until the convergence criterion is met.

FPLO

The full-potential non-orthogonal local-orbital minimum-basis band structure scheme (FPLO) [100], belongs to the class of LCAO (linear combination of atomic orbitals) methods which have the advantage of being computationally much less expensive than methods based on plane waves. This has the advantage that a calculation can be run on a single core of a laptop without the need to apply for computational time on a supercomputer. The extended wave functions of the crystal, the crystal density and the potential are constructed using only local atomic-like functions. *Full potential* means that the real crystal potential is used rather than an approximate representation. Each atom in the unit cell located at site $\boldsymbol{s}$ contributes a set of basis functions. FPLO optimises the basis functions in each iteration cycle by solving a single-particle Schrödinger equation for the potential

$$v^{\text{at}}(\boldsymbol{r}) = \frac{1}{4\pi} \int d\Omega\ v(\boldsymbol{r} - \boldsymbol{R} - \boldsymbol{s}) + v^{\text{conf}}, \tag{3.43}$$

where the first term is the spherically averaged crystal potential and v^{conf} a confining potential. $\boldsymbol{R}$ is a Bravais vector. The confining potential compresses the valence orbitals thus increasing their energy which makes them more suitable for the construction of extended crystal states. The FPLO basis functions are local, non-orthogonal, atomic-like orbitals of the form

$$\langle \boldsymbol{r} | \boldsymbol{R}\boldsymbol{s}L \rangle = \phi_{\boldsymbol{s}}^{l}(|\boldsymbol{r} - \boldsymbol{R} - \boldsymbol{s}|) Y_L(\boldsymbol{r} - \boldsymbol{R} - \boldsymbol{s}), \tag{3.44}$$

where $\phi_{\boldsymbol{s}}^{l}$ is the radial part of the basis function with angular momentum l and the Y_L are real spherical harmonics with $L = ml$ being angular momentum quantum numbers. The solutions to Eqn. 3.43 are classified as core, semi-core and valence orbitals. Core orbitals are defined by

$$\langle \boldsymbol{R}'\boldsymbol{s}'L' | \boldsymbol{R}\boldsymbol{s}L \rangle = \delta_{L'L} \delta_{\boldsymbol{R}'+\boldsymbol{s}', \boldsymbol{R}+\boldsymbol{s}}, \tag{3.45}$$

that is, there is no overlap between core orbitals centred at different sites, whereas overlapping orbitals are assigned to the valence basis. However, there are border cases where a clear assignment to core or valence orbital is difficult. For example, this is the case for the $4f$ orbitals in rare earths. On the one hand, due to their strong localisation, they should be assigned to the core basis. On the other hand, their low binding energies are in the region of the valence electrons. Within the so-called *open-core approach* basis functions can be manually defined as core states. In this

case, the occupancy of the core-shifted valence orbitals is chosen by the user and fixed throughout the calculation.

The extended wave functions $|\boldsymbol{k}n\rangle$, where $\boldsymbol{k}$ is the crystal momentum and n the band index, are expanded in terms of the basis orbitals as linear combinations of Bloch sums:

$$|\boldsymbol{k}n\rangle = \sum_{\boldsymbol{R}\boldsymbol{s}L} |\boldsymbol{R}\boldsymbol{s}L\rangle c_{L\boldsymbol{s}}^{\boldsymbol{k}n} e^{i\boldsymbol{k}(\boldsymbol{R}+\boldsymbol{s})}. \tag{3.46}$$

with the coefficients $c_{L\boldsymbol{s}}^{\boldsymbol{k}n}$. Plugged into the Kohn-Sham equation $H|\boldsymbol{k}n\rangle = |\boldsymbol{k}n\rangle\epsilon_{\boldsymbol{k}n}$ the equation

$$\sum_{\boldsymbol{R}\boldsymbol{s}L} [\langle 0\boldsymbol{s}'L'|H|\boldsymbol{R}\boldsymbol{s}L\rangle - \langle 0\boldsymbol{s}'L'|H|\boldsymbol{R}\boldsymbol{s}L\rangle \epsilon^{\boldsymbol{k}n}] c_{L\boldsymbol{s}}^{\boldsymbol{k}n} e^{i\boldsymbol{k}(\boldsymbol{R}+\boldsymbol{s}-\boldsymbol{s}')} = 0 \tag{3.47}$$

is solved, giving the $|\boldsymbol{k}n\rangle$ from which the density is calculated using

$$n = \sum_{\boldsymbol{k}n}^{occ} = |\boldsymbol{k}n\rangle\langle\boldsymbol{k}n|, \tag{3.48}$$

where the sum is over all occupied states. In each step of the Kohn-Sham self-consistency cycle, the total energy is calculated from Eqn. 3.34. The computational effort is reduced by the exploitation of symmetries, minimisation of the basis set and differentiation of the latter into core and valence orbitals.

Note, that the introduction to FPLO given here is valid for non-relativistic systems. However, DFT solvers like FPLO would be of little use if they would not allow for a relativistic treatment. In the case of scalar-relativistic calculations, the kinetic energy is treated relativistically but the spin-orbit coupling is neglected. The basis functions are two-component-spinor wave functions that are solutions of the Pauli equation. In the fully relativistic setup, which is the method of choice if SOC is of importance, the basis functions are Dirac spinors which are used to solve the relativistic Kohn-Sham-Dirac equations. Moreover, with FPLO collinear magnetic order can be modelled.

4. Methods

4.1. Experimental details

Single crystals

All ARPES experiments presented in this thesis have been conducted on single crystalline samples that were provided by our collaborators. In the group of Cornelius Krellner at the Goethe University Frankfurt am Main $GdIr_2Si_2$ single crystals [101] were grown by Kristin Kliemt. $EuIr_2Si_2$ single crystals [67] were grown in the group of Christoph Geibel at the Max Planck institute Dresden for chemical physics of solids by Silvia Seiro and Nubia Caroca-Canales.

For the growth of both $GdIr_2Si_2$ and $EuIr_2Si_2$ single crystals, an indium-flux technique has been applied. The high-temperature metal-flux method is used to combine lanthanides which have a high vapour pressure and react with oxygen and humidity, with high-melting-point elements like the transition metals and Si. The constituting high-purity elements Gd or Eu, Ir and Si get first solved in the metal flux, which is then cooled following a precise protocol known as the Bridgman method. For each compound, the particular crystal-growth parameters must be optimised individually. The resulting single crystals have a black colour and form flat platelets with their smallest extension along the c axis, while the longest edges form typically along the [100] or [110] crystallographic directions.

Measurements

All experiments were conducted with synchrotron radiation at dedicated facilities, including the Diamond Light Source (DLS) in Oxfordshire, UK, the MAX IV laboratory in Lund, Sweden, the European Synchrotron Radiation Facility (ESRF) in Grenoble, France and the Swiss Light Source (SLS) in Villigen, Switzerland. To prepare a clean surface we transferred the samples with a small screw glued on top into the ultra-high vacuum chamber in which the sample is installed on the cryogenic manipulator and cooled down. When the desired temperature is reached the top post is removed with the help of a wobble stick. This cleaves the sample leaving a part of the sample with a clean surface on the holder for the experiment. To delay surface contaminations

and prevent quick ageing of the sample for measurements at different temperatures we preferably begin at the higher temperature and cool down.

In the case of $GdIr_2Si_2$ ARPES measurements were conducted at the Bloch beamline [102] at the MAX IV laboratory, which is optimised for photon energies between 10 and 200 eV and provides both linearly and circularly polarised light that is produced with an undulator. The end station is equipped with a six-axis cryomanipulator and a DA30 hemispherical deflection analyser from ScientaOmicron. The deflector is a large benefit since Fermi maps can be acquired without rotating the sample. An angular and energy resolution of 0.1° and 2 meV, respectively, and temperatures down to 20 K can be reached. Another large advantage of the Bloch end station is the small spot size of the beam which can be tuned to $10\,\mu m \times 10\,\mu m$. A photon energy of 55 eV and linear light polarisation proved to be ideal for the investigation of the Shockley surface states at the Si-terminated surface.

The ARPES data shown for $EuIr_2Si_2$ have been acquired at the HRPES end station of the I05 undulator beamline [103] at the Diamond Light Source. This end station provides a six-axis cryomanipulator, where temperatures down to 7 K can be reached. The beamline is optimised for energies between 18 and 240 eV, the spot size of the photon beam is $50\,\mu m$ by $50\,\mu m$ and linear as well as circular light polarisations are available. In normal emission the incidence angle of the light is 50°. A polar rotation towards negative angles is more grazing, while positive polar is towards normal incidence, i.e. towards the beam and a positive emission angle in the measured spectra corresponds to an emission above the plane of incidence. The analyser is a Scienta R4000, the analyser slit is oriented vertically. For energy and angle a resolution of 2 meV and 0.1° can be reached, respectively.

Also here, we used a photon energy of 55 eV for our study of the Shockley surface state. To gain deeper insight into the mixed-valent properties we also investigated the $4f$ emission from the Eu $4f$ shell for Si termination using photon energies of 141 eV and 145 eV that correspond to the maxima of the Beutler-Fano resonance for emission from divalent and trivalent Eu, respectively. To gain information about the magnetic properties of the Eu-terminated surface we measured the temperature dependence of the $4f$ emission. The measurements were performed at the ULTRA end station [104] at the Surface and Interface beamline SIS at the SLS, which has a 6-axis cryomanipulator on which the sample can be cooled down to 4 K. The spectrometer is a Scienta Omicron DA30-L with an energy resolution down to 1.6 meV, and an angular resolution of 0.1° reachable. The available photon energies are ranging from 10 to 800 eV with linear and circular light polarisations.

At the PEARL beamline [105], which is located at the SLS, too, the light is produced by a bending magnet. We used it to conduct PED measurements to determine the Eu valency for individual single layers at and near the surface. The spectrometer is a Scienta EW4000 with an acceptance angle of 60°. Radiation with an energy between 60 to 2000 eV is available with linear and partly circular polarisation. The sample is mounted on a six-axis cryomanipulater with the lowest temperature that can be reached being 30 K. In our experiments, we considered the Eu $4f$ multiplets which we measured in the Beutler-Fano resonance using a photon energy of 141 eV for the divalent final-state multiplets of surface and bulk europium and 145 eV for the trivalent $4f$ multiplet. The analysis of the data and the theoretical modelling have

been realised by Dmitry Usachov and his team using the EDAC code [106] for the PED modelling.

XMCD and XMLD measurements in TEY and TFY were performed at the ID32 undulator beamline [107] at the ESRF to uncover the magnetic properties of Eu. Details on the experiments, which have been conducted and evaluated by Kurt Kummer are given in the main chapter on $EuIr_2Si_2$.

4.2. DFT calculations

All DFT calculations presented in this thesis have been performed using the version *fplo18.00-53-x86_64* of the FPLO code.

$GdIr_2Si_2$ To model the electronic structure of $GdIr_2Si_2$ we started with the determination of the lattice parameters that minimise the total energy using the GGA functional [108] for the exchange-correlation energy. In our initial setup, we considered a bulk unit cell with the experimental lattice parameters a and c given in Ref. [101]. For the calculation we used the DFT+U approach in the atomic-limit configuration for the Gd $4f$ states with the Slater parameters $F^0 = 6.7\,\text{eV}$, $F^2 = 8.2817\,\text{eV}$, $F^4 = 5.697\,81\,\text{eV}$ and $F^6 = 4.099\,441\,5\,\text{eV}$, which correspond to $U = 6.7\,\text{eV}$ and $J = 0.7\,\text{eV}$[1]. In the given case using the Hubbard U has the effect of shifting the $4f$ states away from the Fermi level to a binding energy of approximately 8 eV, where the final-state multiplet of the Gd $4f$ shell appears in photoemission spectra. The k mesh was chosen $16 \times 16 \times 16$ and the convergence criteria for density and energy set to $1e^{-6}\,\text{Å}^{-3}$ and $1e^{-8}\,\text{Ha}$, respectively. The optimisation was performed in the scalar-relativistic approach, where relativistic effects are only considered for the kinetic energy, while the spin-orbit coupling is neglected. To take the AFM order into account, we modelled the bulk in space group P4/mmm (123) with 5 atoms in the unit cell. For the $4f$ magnetic moments carried by the Gd atoms that occupy two distinct Wyckoff positions, we put the opposite orientation in the initial setup. The AFM order retained throughout the iteration process until the calculation converged with a magnetic moment of $\mu_{\text{Gd}} \approx \pm 7.24\,\mu_B$ per Gd atom. The relative z coordinate of Si as the only free parameter has been optimised for each set of lattice parameters $\{a, c\}$ using the force-driven optimisation routine implemented in FPLO for scalar relativistic calculations. The convergence criterion for the forces has been set to $1e^{-3}\,\text{eV/Å}$. We obtained the lattice parameters $a = 4.096\,\text{Å}$ and $c = 10.049\,\text{Å}$ which are in good agreement with the experimental lattice parameters from which they deviate by about 1 %. For Si, we obtained $z_{\text{Si}} = 0.379$ which deviates by $-2.3\,\%$ from the literature value. With the optimised parameters a, c and z_{Si} we repeated the calculation in a fully relativistic setup where the spin-orbit coupling is automatically taken into account since the Kohn-Sham-Dirac equation is solved. From this, we calculated the bulk band structure. For the respective modelling of the paramagnetic phase, we used the same optimised parameters but calculated in the open-core approximation, where the Gd $4f$ states are removed from the valence basis and treated as core orbitals. Paramagnetism with randomly oriented magnetic moments cannot be treated in FPLO. Therefore,

[1] For f electrons J is given by $J = (286F^2 + 195F^4 + 250F^6)/6435$ [109].

we used an unpolarised $4f$ shell in which the seven $4f$ electrons of Gd are evenly distributed over the $2(2l+1)$ states with each state $|m_l, \sigma\rangle$ being occupied by half an electron.

To compute the electronic structure of the (001) surface we built an asymmetric slab of 16 atomic layers terminated by Si on the one, and Gd on the other side, separated by a vacuum of approximately 21 Å, thereby using the lattice parameters obtained from the optimisation of the bulk structure. The slab was modelled in space group P4mm (99). Before calculating the band structure, the slab has been relaxed using the force method implemented in FPLO for scalar-relativistic calculations. Following symmetry constraints, in the relaxation procedure only the z coordinates, i.e. the relative position of each atomic layer along the tetragonal c axis can change. This leads to changes in the interlayer spacings, especially in the atomic layers near the surfaces. We calculated the band structure for the relaxed slab coordinates where in the modelling of the magnetically ordered phase the Gd $4f$s were treated within DFT+U, while for the paramagnetic phase the open-core approximation with the unpolarised $4f$ shell was used. Note, that in the scalar-relativistic approach spin is independent of the angular momentum and thus a good quantum number. Therefore, there is no magnetic anisotropy, i.e. for a magnetically ordered system the total energy does not depend on the magnetisation axis. This is not the case for a full-relativistic treatment, where the spin can couple to the orbital motion and is thus in general no good quantum number anymore. For systems like $GdIr_2Si_2$ with a collinear magnetic order, a quantisation axis must be defined that simultaneously fixes the magnetisation axis. Since the latter was unknown for $GdIr_2Si_2$, we calculated the band structure for the quantisation axes [100] and [110]. The results for the calculated band and spin structure of $GdIr_2Si_2$ have been double-checked by Alexandra Vyazovskaya from the Tomsk State University, who performed respective calculations with the Vienna ab-initio simulation package (VASP) [110]. This DFT solver is, in difference to the FPLO code, a plane-wave method.

$EuIr_2Si_2$ For the DFT modelling of $EuIr_2Si_2$ we used exclusively the open-core approximation in the linear spin density approximation (LSDA) [111], which has the advantage of fixing the occupancy of the Eu $4f$ shell to any arbitrary value and facilitates the computational treatment of the non-integer Eu valency in this mixed-valent compound. For the bulk different values of the valency ranging from 2.0 to 3.0 have been considered in steps of 0.1, which corresponds to the occupancy of the Eu $4f$ shell ranging from 7 to 6. For each configuration, the lattice parameters a and c as well as z_{Si} have been optimised for the minimal total energy as described above. The bulk unit cell has been modelled in space group I4/mmm (139) with 3 Wyckoff positions, one for Si, one for Ir and one for Eu with the only free parameter being the z component of Si. With the optimised values for lattice parameters and Si position, the calculations were repeated in a fully relativistic setup in which also the band structure was computed.

To model the surface we built a slab of 19 atomic layers using the space group P4/nmm (129) with Si termination on both sides of the slab. Surface relaxation has been taken into account for the first four layers on each side of the slab, while the remaining bulk-like layers were fixed. For Eu in the first layer below the Si-terminated

surfaces, we assumed a valency of 2.0, i.e. seven electrons in the $4f$ shell. In the modelling of the paramagnetic phase, an unpolarised $4f$ shell was used, while for the ferromagnetically ordered Eu layer the same spin was assigned to each of the seven $4f$ electrons. The quantisation axis which is antiparallel to the orientation of the magnetic moments was set to [100]. Here, the computational results were double-checked by Ilya Nechaev, who was at that time affiliated with the Centro de Física de Materiales in Donostia, Spain.

5. $GdIr_2Si_2$

This chapter is dedicated to the electronic structure of the Si-terminated surface of the layered 122 material $GdIr_2Si_2$ in the PM and AFM phases which we investigated using ARPES and DFT. Herein, the main focus lies on the two surface states α and γ, which reside in a large gap of projected bulk bands around the $\overline{\mathrm{M}}$ point of the SBZ and are subject to linear and cubic Rashba effects, respectively. While the spin structure of the γ state describes the well-known Rashba pattern, the cubic Rashba effect creates an exotic triple spin winding along the CECs of α. In combination with the exchange interaction, the strong Rashba-like SOC leads to intriguing asymmetries in the band dispersion and the CECs. Moreover, the observation of domains is discussed. Please note, that parts of this chapter are taken from Ref. [112] and the corresponding supplementary information.

5.1. Introduction

$GdIr_2Si_2$ has been subject to studies for more than five decades [63, 101, 113, 114, 115, 116, 117, 118, 119]. It is known for polymorphism, existing in the I-type ($ThCr_2Si_2$ structure) and P-type ($CaBe_2Ge_2$ structure) with both structural phases showing AFM order with Néel temperatures of $T_\mathrm{N} = 87\,\mathrm{K}$ for the I-type and $T_\mathrm{N} = 12\,\mathrm{K}$ in the case of the primitive structure [119]. In the following, we consider only the $ThCr_2Si_2$-type. Since Ir does not carry a magnetic moment the magnetic properties of $GdIr_2Si_2$ are exclusively determined by the Gd ions, primarily by the $4f$ electrons. From Mössbauer studies a magnetic moment of $8.05\,\mu_\mathrm{B}$ has been obtained, which is larger than the theoretical value for a free Gd^{3+} ion, cf. Tab. 2.2. The excess moment has been ascribed to Gd $5d$ electrons being induced by the $4f - 5d$ exchange interaction [117]. In a recent study on single-crystalline samples, an even larger value of the effective moment has been reported being $8.2\,\mu_\mathrm{B}$ or $8.3\,\mu_\mathrm{B}$ depending on the direction of the applied magnetic field [119]. In the same work, a small magnetic anisotropy has been observed in the susceptibility curves for $T > T_\mathrm{N}$. This is rather surprising because with $L = 0$ the Gd $4f$ shell is supposed to be insensitive to the CEF and for vanishing angular momentum the observed anisotropy cannot be explained by the coupling of the spin to the crystal lattice either. Below $T_\mathrm{N} = 87\,\mathrm{K}$ the Gd moments order antiferromagnetically. In the basal plane, the Gd moments are perpendicular to

the c axis. As for many other members of the LnT_2Si_2 family, the AFM order consists in an AFM stacking of ferromagnetically ordered Gd layers along the tetragonal c axis with an alternating sign of the magnetisation in subsequent layers mediated via the RKKY interaction. The rather high Néel temperature indicates a strong intralayer exchange coupling between the Gd moments.

5.2. Results and discussion

5.2.1. Paramagnetic phase

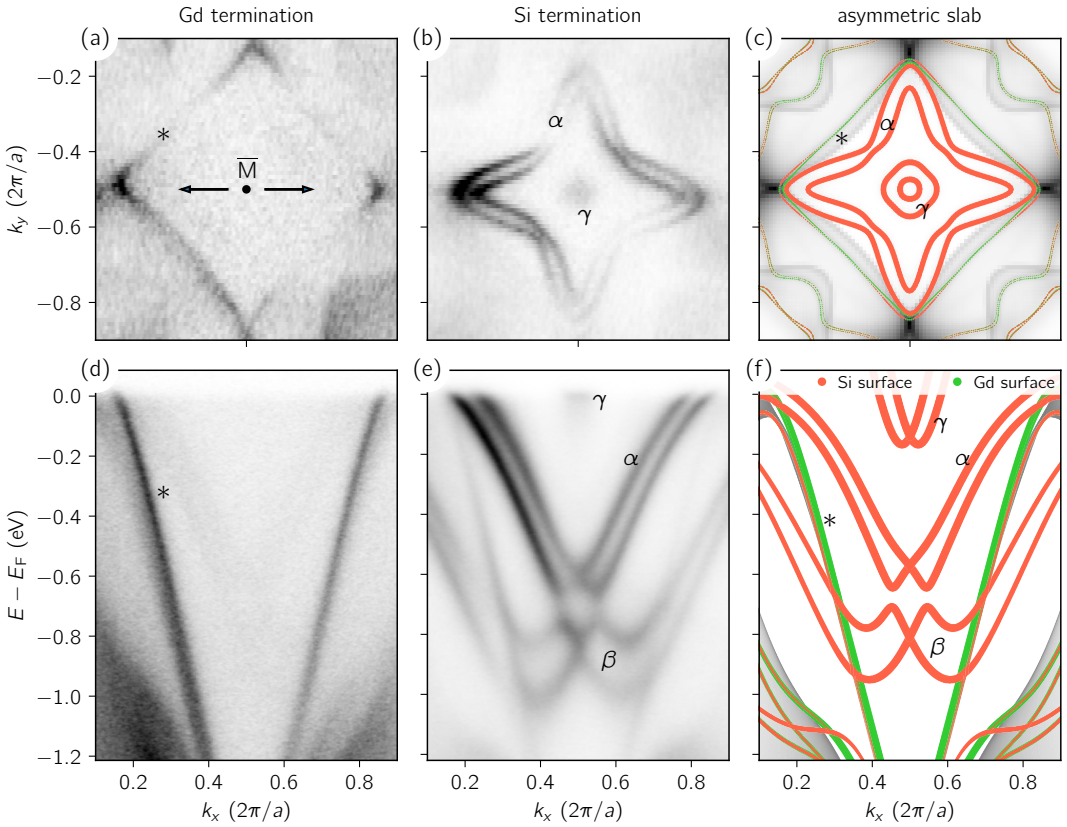

Fig. 5.1.: Electronic structure of the Si- and Gd-terminated (001) surfaces of $GdIr_2Si_2$ in the PM phase. Shown are ARPES spectra acquired with $h\nu = 55\,\mathrm{eV}$ and respective DFT modelling for an asymmetric slab that allows us to model both terminations within a single calculation. The asterisk marks a surface-resonant state, while the surface states are labelled α, β and γ. In the upper and lower rows, Fermi and $E(k_\parallel)$ maps along $\overline{\mathrm{X}}$–$\overline{\mathrm{M}}$–$\overline{\mathrm{X}}$ are given, respectively. ARPES results shown in (a, d) are obtained for Gd, in (b, e) for Si termination. In the modelled data given in (c, f) contributions of the topmost Si-Ir-Si block of the Si-terminated surface are plotted in orange, while green represents the topmost Gd-Si-Ir-Si block for Gd termination. Bulk bands projected onto the SBZ are shown in grey.

We start our discussion of the surface electronic structure of $GdIr_2Si_2$ with the comparison of ARPES spectra acquired with $h\nu = 55\,\mathrm{eV}$ from Gd- and Si-terminated

surfaces. The experimental results are given in Fig. 5.1 and compared to respective DFT band-structure calculations. In the upper row, Fermi maps are shown for (a) Gd and (b) Si termination, below we present respective cuts along the $\overline{\mathrm{X}}$–$\overline{\mathrm{M}}$–$\overline{\mathrm{X}}$ high-symmetry direction. It can be seen that the two possible surface terminations are clearly distinguishable in ARPES. The spectra in (a, d) acquired from the Gd-terminated surface show the characteristic gap around the $\overline{\mathrm{M}}$ point enclosed by the surface resonance (∗), which is seen as a distorted square in the Fermi map. Along the high-symmetry direction $\overline{\mathrm{X}}$–$\overline{\mathrm{M}}$–$\overline{\mathrm{X}}$ it has a parabolic character. In the ARPES maps taken for Si termination, the bulk gap is populated by the spectral features of the surface states α, β and γ.[1] The α state forms a pair of electron-like bands with parabolic-like dispersion, which are strongly split due to the Rashba effect. In the Fermi map they are seen as two well-separated concentric CECs with the shape of a four-cornered star centred at the $\overline{\mathrm{M}}$ point. Note, that the fourfold symmetry of the CECs impressively represents the C_{4v} symmetry of the surface. The hole-like dispersing bands of the surface state β are strongly Rashba-split, too. Close to $k_x = (0.5 \pm 0.1)2\pi/a$ they cross the bunch of bulk bands that form the gap border and disperse further towards the $\overline{\mathrm{X}}$ point with slightly decreasing intensity. The γ state of which only the band bottom is occupied, hardly crosses the Fermi level and appears in the Fermi map as a circular intensity spot at the $\overline{\mathrm{M}}$ point. Note the very weak signature of the α and β bands within the band gap in (d), which indicates a tiny admixture of Si termination to the mainly Gd-terminated probed area. Near the corners of the Fermi maps, along the $\overline{\mathrm{M}}-\overline{\Gamma}$ direction, parts of the projected Doughnut are visible for both terminations. In the calculated spectra the features of the Si- and Gd-terminated surfaces are plotted in orange and green colours, respectively, while the surface-projected bulk bands are shown as grey shading. It can be seen, that DFT reproduces all experimental features with great precision. The only notable deviation from the experimental findings consists in the relatively large shift of the calculated γ bands below E_{F}, which is attributable to limitations of DFT in correctly describing the relaxation of the surface and discussed in detail in the Appendix [A].

Dispersion Fig. 5.1 proves that DFT is capable of accurately describing the experimental results obtained with ARPES. We will thus utilise it to gain deeper insight into the properties of the surface states at the Si-terminated surface. DFT also allows us to switch on and off particular interactions like SOC and thus, to get an idea which effect SOI has on the surface states from first-principles calculations. Fig. 5.2 illustrates how the bands get modified under the action of SOI with the computational results for α, β and γ shown in orange, blue and green colours, respectively. In (a) and (c) the band structure is shown for calculations where SOI is switched off and on. Without SOI we find each surface state α, β and γ to form two bands, which are doubly degenerate in spin. At the $\overline{\mathrm{M}}$ point the bands formed by α and β are degenerate, too, there the total degeneracy is thus fourfold. Switching on SOI we reproduce the huge Rashba-type splitting that we observed experimentally for all states. Only in near the $\overline{\mathrm{M}}$ point the α and β bands deviate from the parabolic dispersion that is seen without SOI. As

[1] Note, that α is the same surface state like $\mathcal{S}'$ or $\mathsf{S_e}$ introduced in section 2.2, while β corresponds to $\mathsf{S_h}$. γ is above E_{F} in most of the $LnT_2\mathrm{Si}_2$ compounds and was not introduced before.

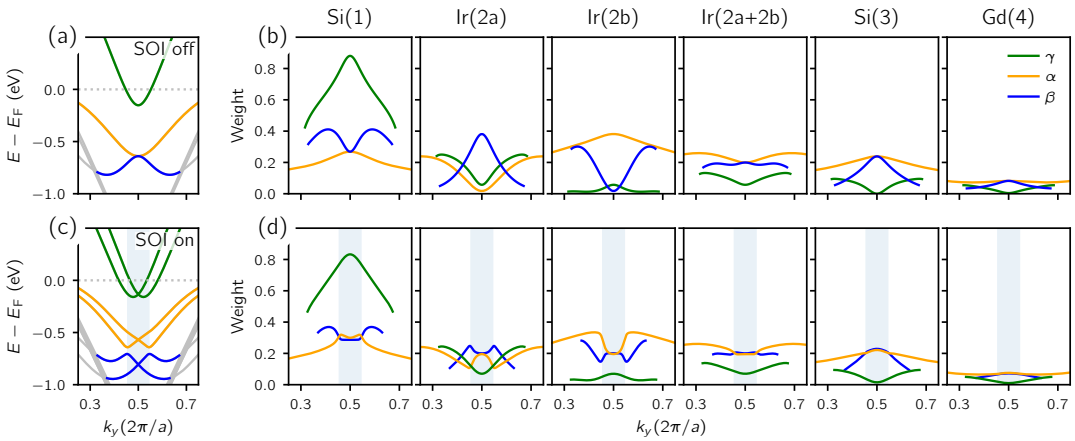

Fig. 5.2.: Surface state dispersion and k_y-resolved per-layer weight along $\overline{\mathrm{X}}$–$\overline{\mathrm{M}}$–$\overline{\mathrm{X}}$ calculated (a, b) without and (c,d) with SOI. In brackets the layer count is given with (1) corresponding to the surface layer, (2) to the first layer below the surface and so on. Orange, blue and green graphs represent the results for the surface states α, β and γ, respectively. Grey stripes in the lower row mark the region of intrinsic SOI.

demonstrated in Ref. [79] by means of a tight-binding model and shown in Fig. 2.8 the deviation is due to the intrinsic SOC that causes a mixing of the two bands and leads to the opening of the large spin-orbit gap.

Weights In Fig. 5.2 the band weights of the surface states are shown for the individual layers of the surface Si–Ir–Si–Gd four-layer block, comparing the cases (b) without SOI and (d) if SOI is taken into account. The plots for each layer are labelled by the elemental symbol and the layer position in the slab, where the counting starts from the surface Si layer Si(1). Note that the Ir layer is represented by three plots because the Ir Wyckoff position comprises two symmetrically non-equivalent crystallographic sites which give different contributions to the surface states' wave functions. The first and second Ir plots show the weights from either site, while the third one represents the average weight from both sites.

The weights are a measure of how much a particular atom contributes to the wave function of a band state. At first, we consider the case without SOI (upper row). For γ the dominating contribution comes from the surface Si layer reaching a value of 90 % at $\overline{\mathrm{M}}$ which, however, reduces to 40 % at a distance of about $\pm 0.2\,\frac{2\pi}{a}$ from the $\overline{\mathrm{M}}$ point. With decreasing contribution from Si(1), the admixture of the adjacent Ir layer increases from 10 % to 17 % and also contributions from the subsurface Si and Gd layers, which are almost zero at $\overline{\mathrm{M}}$, increase up to 10 % and 5 % within the given distance, respectively. γ states with a wave vector close to the $\overline{\mathrm{M}}$ point are thus strongly localised within the two topmost Si and Ir layers, whereas with increasing distance from the $\overline{\mathrm{M}}$ point the wave functions reach increasingly deeper into the surface four-layer block with a small but finite probability in the Gd layer. In difference, α and β are built to almost the same amount by basis orbitals from the three outermost Si and Ir layers, whose contribution reaches in dependence on $k_\parallel$ between 15 % and 25 %. The Gd layer contributes between 5 % and 7 %. We may thus conclude, that α and β

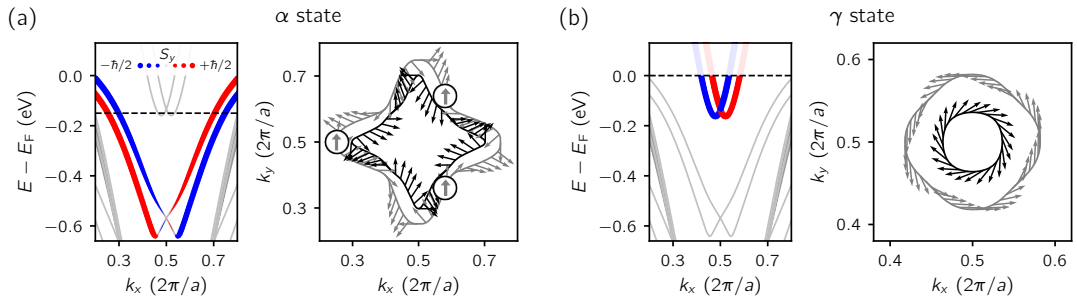

Fig. 5.3.: Spin structure of the surface states (a) α and (b) γ. For the high-symmetry direction $\overline{\mathrm{X}}$–$\overline{\mathrm{M}}$–$\overline{\mathrm{X}} \parallel k_x$ the expectation value of the y component of the spin is shown in red ($S_y > 0$) and blue ($S_y < 0$), the line width reflects the absolute value of S_y. The CECs of the states α and γ are given at $-0.13\,\mathrm{eV}$ and $0\,\mathrm{eV}$, respectively. Gray and black arrows represent the spin $\boldsymbol{S}$ for states on the outer and inner CECs, respectively.

stretch out over the whole surface four-layer block in accordance with the findings for related $EuRh_2Si_2$[34] and $GdRh_2Si_2$[35] compounds. Comparing this to the results of the calculation with SOI, shown in Fig. 5.2(d), we generally find a very similar k_y dependence of the band weights. For α and β, however, a difference is seen in the vicinity of the $\overline{\mathrm{M}}$ point, where the intrinsic SOI becomes important. This region is highlighted in light blue. There, the strongest changes are seen in the weight functions of the individual Ir sites, Ir(2a) and Ir(2b), where the α bands seem to become more β like and vice versa which we interpreted as a mixing of the two states. When the edge of the exotic region is reached the weight functions are qualitatively the same as in the case without SOI. Note, that for $k_\parallel \neq \overline{\mathrm{M}}$ the contributions of the split bands have been summed up for each surface state.

Spin structure Fig. 5.3(a) and (b) show the calculated spin structure for the surface states α and γ, respectively, along the high-symmetry direction $\overline{\mathrm{X}}$–$\overline{\mathrm{M}}$–$\overline{\mathrm{X}}$ parallel k_x and CECs. Since we are going to discuss the spin structure in the light of the Rashba effect, we omit the β state, whose bands lie mostly within the exotic region around the $\overline{\mathrm{M}}$ point.[2] In systems with strong SOC, m_s is not a good quantum number. Therefore, we analyse the spin structure in terms of the spin expectation values $S_x = \langle S_x \rangle$ and $S_y = \langle S_y \rangle$ for the x and y components of the electron spin. Note, that due to the fourfold rotational symmetry in combination with time-reversal symmetry $S_z = 0$ for all $\boldsymbol{k}_\parallel$, which is explicitly shown below. Along the $\overline{\mathrm{X}}$–$\overline{\mathrm{M}}$–$\overline{\mathrm{X}}$ cuts shown in Fig. 5.3 $S_x = 0$. Red and blue colours correspond to $S_y > 0$ and $S_y < 0$, respectively, while the line width is proportional to the absolute value of S_y. On the CECs the expectation values of the single spin components are combined to the spin expectation value

[2] As we discussed above, the intrinsic SOI mixes α and β states which leads to a vanishing spin polarisation, as can be seen in Fig. 5.3(a) for α. The spin polarisation of states in this region is hidden due to the crystallographic inequivalent Ir sites. If the spin expectation values are calculated separately one finds strongly spin-polarised states with opposite polarisation on the two sites. In the total wave function, however, the two contributions almost cancel each other, which results in the weak polarisation. A detailed discussion of the hidden spin polarisation is given in Ref. [81]. For the specific case of the surface states of the Si-terminated surface of LnT_2Si_2 compounds, the site-resolved spin structure is shown and discussed in Ref. [39].

$\langle \boldsymbol{S} \rangle = (S_x, S_y, 0)^T$, which is visualised by small arrows.

The spin structure of the γ state, Fig. 5.3(b), is reminiscent of a classical Rashba system, where the spin is locked perpendicularly to the momentum and rotates into opposite directions along the inner and outer CECs completing one full rotation by 2π on a closed loop. In the case of the Fig. 5.3(b) shows, that along γ's CECs spin rotates smoothly in the clockwise direction on the inner, and in the counter-clockwise direction on the outer CECs, whereby it completes one full rotation by 2π on a closed loop. In difference to a classical Rashba system, however, there are deviations from the perpendicular spin-momentum locking. Along $\overline{\mathrm{X}}$–$\overline{\mathrm{M}}$–$\overline{\mathrm{X}}$, we find a similar spin structure for α, Fig. 5.3(a), except for the region near the $\overline{\mathrm{M}}$ point, which we exclude from our discussion of the Rashba effect. In difference to the $E(k_x)$ cut which might suggest that the α state is subject to the classical Rashba effect, too, a look at the CECs reveals a very different spin structure which is characterised by a triple winding of the electron spin. Namely, on a closed loop around the CECs, the spin completes *three* full rotations by 2π, instead of one in the case of the classical Rashba effect. To emphasize the triple winding three encircled arrows mark three states on α's outer CEC with the same spin. Along a segment of the CEC that connects two of those points, the spin performs a single winding, i.e. one complete rotation by 2π.

Spin winding For a consistent description of the rotation of the spin along a CEC, we introduce the following definitions. The winding number $n \in \mathbb{Z}$ is defined in such a way that $2\pi n$ describes the angle of rotation of the spin when performing a closed loop along the contour. Since for a closed contour the spin at the start and end has to coincide, the winding number n has to be an integer and therefore expresses the number of full rotations of the spin. On the other hand, the sign of n represents the sense of rotation of the spin. When moving along the CEC in a counterclockwise direction, the spin can turn counterclockwise or clockwise. Hence, if the spin rotates in the same direction as the movement direction along the CEC, we define n to be positive, while an opposite rotation of the spin to the movement along the CEC has a negative sign. In Fig. 5.4 we illustrate the spin winding through a hypothetical spin structure on a circular CEC for different winding numbers n ranging from ± 1 to ± 5. For a better visualisation we use a colour scheme that ranges from orange for $\boldsymbol{S} = \hbar/2\boldsymbol{e}_x$ over red for $\boldsymbol{S} = \hbar/2\boldsymbol{e}_y$ to light blue for $\boldsymbol{S} = -\hbar/2\boldsymbol{e}_x$ to blue for $\boldsymbol{S} = -\hbar/2\boldsymbol{e}_y$ which are equally expressed by the angle $\varphi_{\boldsymbol{S}}$ in the coordinate system of the spin illustrated in the upper right. In a system without symmetry restrictions, any winding number is allowed. For the surface of $GdIr_2Si_2$, however, some winding numbers n are forbidden by the underlying C_{4v} symmetry. The winding of the spin $\boldsymbol{S}(\varphi_{\boldsymbol{k}})$ along the CEC, where $\varphi_{\boldsymbol{k}}$ is the polar angle that defines a point on the CEC, has to follow this four-fold symmetry of the crystal, meaning that the spin $\boldsymbol{S}(\varphi_{\boldsymbol{k}} + \frac{\pi}{2}) = R_z(\frac{\pi}{2})\boldsymbol{S}(\varphi_{\boldsymbol{k}})$ with R_z being the rotation matrix about the rotation axis z. In other words, the spin needs to rotate by $2\pi\eta + \frac{\pi}{2}$ with $\eta \in \mathbb{Z}$ when moving along the CEC by an angle of $\frac{\pi}{2}$. This way, the full rotation around the closed contour $2\pi n = 4(2\pi\eta + \frac{\pi}{2})$ leads to the allowed winding numbers $n = 4\eta + 1$. The simplest allowed winding of the spin is thus $n = 1$ with $\eta = 0$, meaning that the spin performs one full rotation when moving along the closed CEC. Here, the spin rotates in the same direction as the movement along the

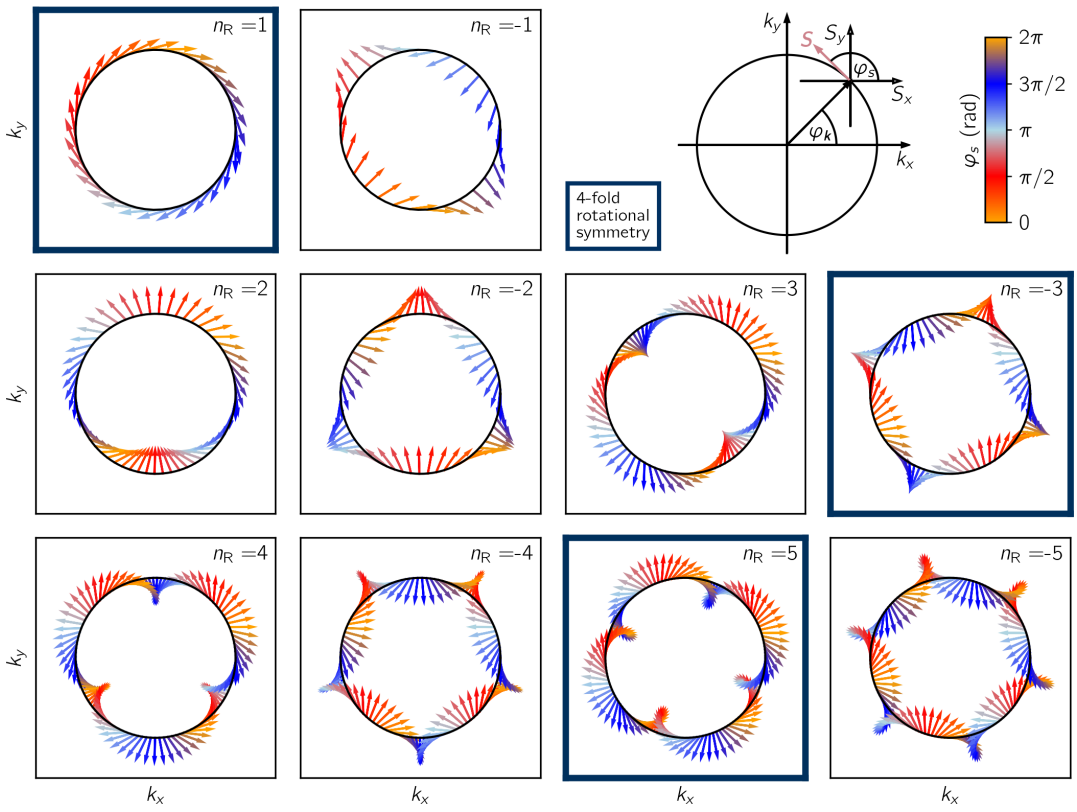

Fig. 5.4.: Illustration of different winding numbers n_R on the circular CEC of a hypothetical spin-1/2 system. The arrows represent the electron spin. The geometry is shown in the upper right, with the (k_x, k_y) axes being the coordinate system of the CEC and the (S_x, S_y) axes that of the spin at a given point on the CEC determined by the angle $\varphi_{\boldsymbol{k}}$. The expectation value of the spin is determined by the angle $\varphi_{\boldsymbol{S}}$ with $\varphi_{\boldsymbol{S}} = (0, \pi/2, \pi, 3\pi/2)$ corresponding to $\boldsymbol{S} = (\hbar/2\boldsymbol{e}_x, \hbar/2\boldsymbol{e}_y, -\hbar/2\boldsymbol{e}_x, -\hbar/2\boldsymbol{e}_y)$, respectively. Accordingly, the colour map ranges from orange to red and light blue to blue. The cases that are allowed in a system with fourfold rotational symmetry are highlighted.

CEC. We will call this rotation henceforth *single winding*. The next lowest number of rotations is $n = -3$ for $\eta = -1$. In this case, the spin rotates oppositely to the direction taken along the closed CEC performing three full rotations. This rotation of the spin is therefore called *triple winding*. In principle, higher orders of rotation are possible with alternating sense of rotation ($n = 5, -7, 9\ldots$). Another consequence of the C_{4v} symmetry is that S_z vanishes for all $\boldsymbol{k}_\parallel$. Since S_z must be invariant under rotations by integer multiples of $\pi/2$ about the z axis it must hold that

$$S_z(\boldsymbol{k}_\parallel) = S_z(-\boldsymbol{k}_\parallel). \tag{5.1}$$

At the same time, time-reversal symmetry implies that

$$S_z(\boldsymbol{k}_\parallel) = -S_z(-\boldsymbol{k}_\parallel). \tag{5.2}$$

Eqns. 5.1 and 5.2 can be fulfilled simultaneously only if $S_z = 0$ proofing that all spins lie within the ab plane. That this is indeed a feature of the fourfold rotational

symmetry can be seen by comparison to the spin structure of the surface state of the Au(111) surface, which has a threefold symmetry and for which a tiny but finite S_z component has been observed with spin-resolved ARPES [120].

Based on the definitions given above, we can now evaluate the CECs in Fig. 5.3(a) and (b) for α and γ, respectively. Starting with the inner contour of γ shown in black, we can see that the spin rotates clockwise when moving along the contour in the clockwise direction and performs one full rotation of 2π along the closed contour. The same applies to the outer contour of γ shown in grey, hence we find the winding number to be $n_\gamma = 1$ for the inner and outer contours. For the more complex-looking CECs of α, we perform the analysis in the same way. Let us start at the uppermost point of the outer contour ($k_x = 0.5\frac{2\pi}{a}$, $k_y \approx 0.73\frac{2\pi}{a}$) with the spin pointing to the right along the k_x direction. Moving now a small section along the contour in the clockwise direction, the spin starts to rotate counterclockwise pointing more and more to the top of the figure along the k_y direction. Thus, the winding number has to be negative. Following the spin along the closed contour, it performs three full rotations, highlighted by the three encircled arrow marks of the spin pointing along the k_y direction, which are related by a full rotation of the spin by 2π. The inner contour behaves in the same way, resulting in a winding number of $n = -3$ for α.

Effective Rashba field To describe the spin-orbit induced spin structures we introduce a Rashba-like Hamiltonian $H_\mathrm{R} \propto \boldsymbol{B}_\mathrm{R}\boldsymbol{\sigma}$ with $\boldsymbol{B}_\mathrm{R}$ being an effective magnetic field and $\boldsymbol{\sigma}$ the vector of Pauli matrices accounting for the spin. For a general description, we can expand $\boldsymbol{B}_\mathrm{R}$ in terms of rotations n_R with

$$\boldsymbol{B}_\mathrm{R}^{(n_\mathrm{R})} \propto \mathrm{sgn}(n_\mathrm{R})k^{|n_\mathrm{R}|}(\sin n_\mathrm{R}\varphi_{\boldsymbol{k}}, -\cos n_\mathrm{R}\varphi_{\boldsymbol{k}}, 0), \tag{5.3}$$

where $\varphi_{\boldsymbol{k}}$ is the polar angle of the wave vector $\boldsymbol{k}$ in the (k_x, k_y)-plane. From Eqn. 5.3, we clearly see that the different signs of n_R are connected by $\boldsymbol{B}_\mathrm{R}^{(n_\mathrm{R})} = (1, -1, 0)\boldsymbol{B}_\mathrm{R}^{(-n_\mathrm{R})}$ expressing the different senses of rotation. In Fig. 5.5 the effective Rashba field introduced in Eqn. 5.3 is shown for different winding numbers n_R. Since we are interested in the orientation of $\boldsymbol{B}_\mathrm{R}^{(n_\mathrm{R})}$ rather than in its absolute value, we neglect the k dependence, setting $|\boldsymbol{B}_\mathrm{R}^{(n_\mathrm{R})}| = 1$ for all k. To visualise the n_R-fold symmetry of $\boldsymbol{B}_\mathrm{R}^{(n_\mathrm{R})}$ a colour scheme is used for the polar angle $\varphi_{\boldsymbol{B}}$ of $\boldsymbol{B}_\mathrm{R}^{(n_\mathrm{R})}$ at a given point in $\boldsymbol{k}_\parallel$ space. For example $\varphi_{\boldsymbol{B}} = 0$ corresponds to $\boldsymbol{B}_\mathrm{R}^{(n_\mathrm{R})} = B_\mathrm{R}^{(n_\mathrm{R})}\boldsymbol{e}_x$ as illustrated in the legend in the upper right of Fig. 5.5. The orientation of $\boldsymbol{B}_\mathrm{R}^{(n_\mathrm{R})}$ is additionally represented by small black arrows. The configurations with $n = (1, -3, 5)$ that are allowed by the four-fold C_{4v} symmetry of the surface of $GdIr_2Si_2$ are highlighted in yellow. Since $\boldsymbol{B}_\mathrm{R}^{(n_\mathrm{R})}$ has to follow the crystal symmetry too, $n_\mathrm{R} = 4\eta + 1$ ($\eta \in \mathbb{Z}$). Hence, the lowest order term with $n_\mathrm{R} = 1$ results in $\boldsymbol{B}_\mathrm{R}^{(1)} = k(\sin\varphi_{\boldsymbol{k}}, -\cos\varphi_{\boldsymbol{k}}, 0)$, which corresponds to the classical linear Rashba term. The resulting spin structure of the linear Rashba term is a single winding of the spin making this the dominating term for the γ state. The next higher order is $n_\mathrm{R} = -3$ with $\boldsymbol{B}_\mathrm{R}^{(-3)} = -k^3(\sin -3\varphi_{\boldsymbol{k}}, -\cos -3\varphi_{\boldsymbol{k}}, 0) = k^3(\sin 3\varphi_{\boldsymbol{k}}, \cos 3\varphi_{\boldsymbol{k}}, 0)$ resulting in a triple winding of the spin. Hence, this is the dominant term to describe

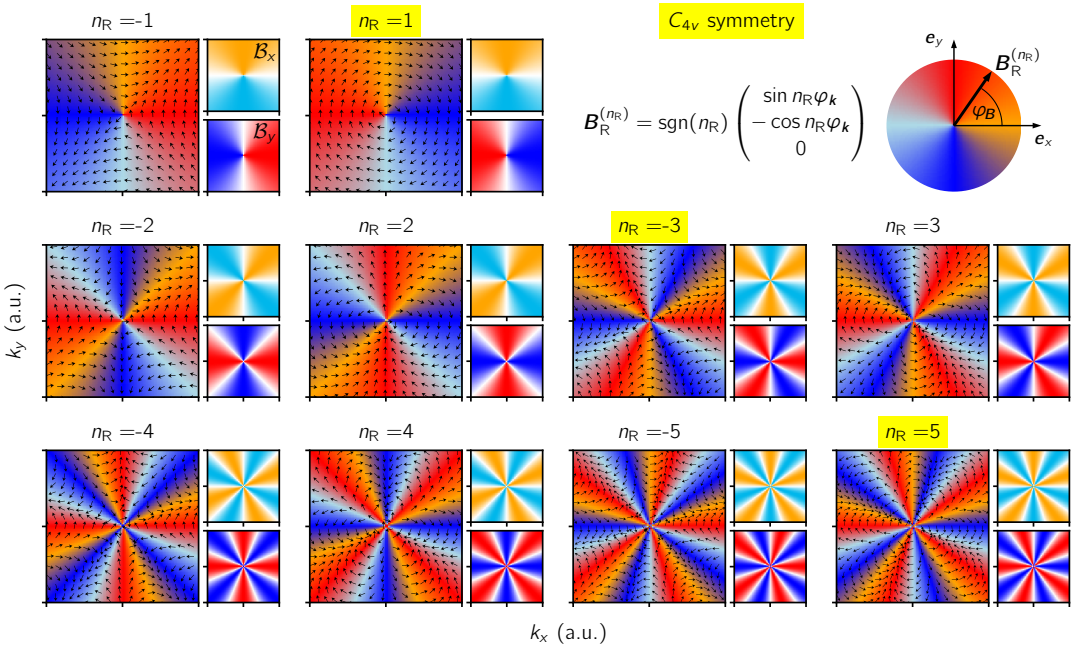

Fig. 5.5.: Effective Rashba field $\boldsymbol{B}_{\mathrm{R}}^{(n_{\mathrm{R}})}$ calculated with Eqn. 5.3 for different winding numbers n_{R} and $k = 1$ (neglecting the $k_{\parallel}$ dependence of the field strength). The orientation of $\boldsymbol{B}_{\mathrm{R}}^{(n_{\mathrm{R}})}$ is illustrated by small black arrows and the colour scheme which indicates the polar angle $\varphi_{\boldsymbol{B}}$ of $\boldsymbol{B}_{\mathrm{R}}^{(n_{\mathrm{R}})}$ as shown in the upper right. Winding numbers that are compatible with the C_{4v} symmetry are highlighted in yellow.

the spin structure of the surface state α.[3] Higher orders can be used to describe more complex spin rotations [121].

In Fig. 5.6 we compare the effective fields $\boldsymbol{B}_{\mathrm{R}}^{(n_{\mathrm{R}})}$ for (a) $n_{\mathrm{R}} = 1$ and (d) and $n_{\mathrm{R}} = -3$ with the energy-projected spin structure of the states γ and α considering the inner and outer bands formed by each surface state separately. Obviously, the symmetry of the $\boldsymbol{B}_{\mathrm{R}}^{(1)}$ field in (a) coincides with the symmetry of the spin structure of (b) the outer and (c) the inner γ bands. For the outer band, the spin and effective Rashba fields have opposite signs, which corresponds to an antiparallel configuration of the spin and the effective field, while for the inner band spin and field are parallel. This is not surprising, since an antiparallel alignment of spin and the magnetic field is energetically favourable. For the bands formed by α we find the spin structure to correspond equally well to the effective $\boldsymbol{B}_{\mathrm{R}}^{(-3)}$ field. Note, however, that for an exact description of the spin structure by the effective Rashba field, for both α and γ states a small admixture of the $\boldsymbol{B}_{\mathrm{R}}^{(1)}$ and the $\boldsymbol{B}_{\mathrm{R}}^{(-3)}$ fields must be taken into account, respectively.

[3] Note that it is quite common to drop the sign of n_{R} in 5.3 and to use $\boldsymbol{B}_{\mathrm{R}}^{(n_{\mathrm{R}})}$ interchangeably for $\boldsymbol{B}_{\mathrm{R}}^{(n_{\mathrm{R}})}$ and $\boldsymbol{B}_{\mathrm{R}}^{(-n_{\mathrm{R}})}$ [37, 121]. The same problem has to be kept in mind when using the names *linear* and *cubic* Rashba term as they can be ascribed to $\boldsymbol{B}_{\mathrm{R}}^{(1)}$ or $\boldsymbol{B}_{\mathrm{R}}^{(-1)}$ and $\boldsymbol{B}_{\mathrm{R}}^{(3)}$ or $\boldsymbol{B}_{\mathrm{R}}^{(-3)}$, respectively.

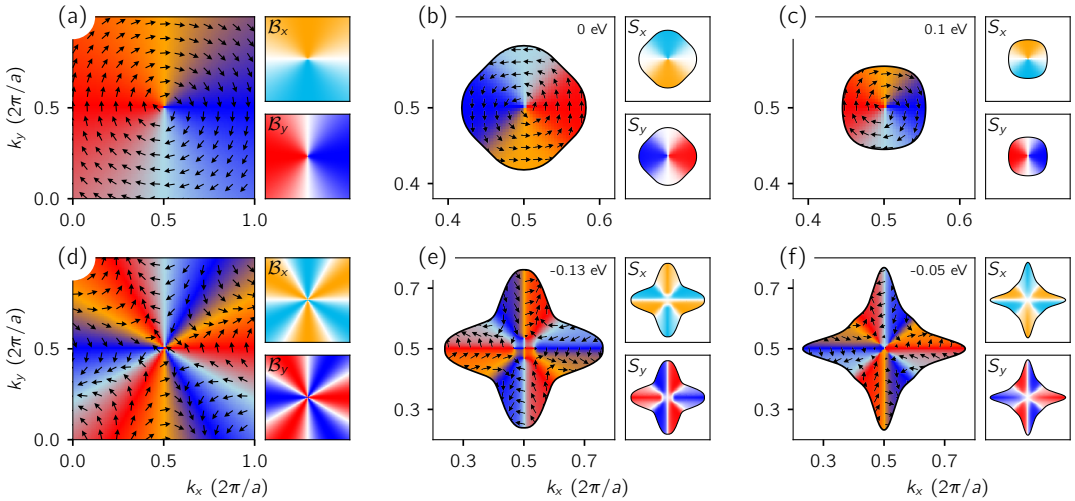

Fig. 5.6.: Comparison of $\boldsymbol{B}_{\mathrm{R}}^{(n)}$ from Eqn. 5.3 for (a) $n = 1$ with the DFT-calculated spin structure of (b) the outer and (c) the inner bands of the state γ and for (d) $n = -3$ with the spin structure of (e) the outer and (f) the inner band of the state α. The colour scheme represents the polar angle φ of $\boldsymbol{B}_{\mathrm{R}}^{(n)}$ and spin $\boldsymbol{S}$ as introduced in Fig.5.5.

Origin of single and triple winding That the leading contribution to $\boldsymbol{B}_{\mathrm{R}}$ differs strongly between the α and γ states can be understood as a direct consequence of their different orbital composition. In the following, we will see that consideration of SOI as a small perturbation to the local-orbital eigenfunctions ϕ of the scalar-relativistic DFT calculation, reproduces the above spin structure. We start with the Schrödinger equation of the unperturbed Hamiltonian H_0 with eigenenergies E_0

$$H_0\phi = E_0\phi$$

The perturbed Hamiltonian due to the spin-orbit interaction H_{SO} reads

$$H = H_0 + H_{\mathrm{SO}}\,,$$

with

$$H_{SO} = \frac{\hbar}{2m^2c^2}\frac{1}{r}\frac{dV}{dr}\boldsymbol{l}\cdot\boldsymbol{s} \equiv \xi\,\boldsymbol{l}\cdot\boldsymbol{\sigma} = \xi\begin{pmatrix} l_z & l_- \\ l_+ & -l_z \end{pmatrix},$$

where $\boldsymbol{l}$ and $\boldsymbol{s}$ describe the angular and spin momenta, respectively, $\xi = \xi(\boldsymbol{r})$ includes the potential gradient, $\boldsymbol{\sigma}$ is a vector of Pauli matrices, and $l_\pm = l_x \pm i l_y$. The effective SO field is defined as

$$\boldsymbol{B} \equiv \langle\phi \mid \xi\boldsymbol{l} \mid \phi\rangle\,.$$

Defining

$$B_\pm = B_x \pm iB_y,$$

the Hamiltonian matrix takes the form

$$H = \begin{pmatrix} E_0 + B_z & B_- \\ B_+ & E_0 - B_z \end{pmatrix}.$$

From the diagonalisation of this matrix, we obtain the dispersion to be

$$E_{\pm}(\boldsymbol{k}) = E_0(\boldsymbol{k}) \pm |\boldsymbol{B}(\boldsymbol{k})| \,.$$

and the wave functions

$$\psi_{\pm} = \frac{\phi}{2}\left(1 \pm \frac{B_z}{|\boldsymbol{B}|}\right)\begin{pmatrix} 1 \\ 0 \end{pmatrix} + \frac{\phi}{2}\left(1 \pm \frac{-B_z}{|\boldsymbol{B}|}\right)\begin{pmatrix} 0 \\ 1 \end{pmatrix} .$$

Spin expectation values (in atomic units) are obtained as

$$\boldsymbol{S}_{\pm} = \frac{1}{2}\langle \psi_{\pm} \mid \boldsymbol{\sigma} \mid \psi_{\pm} \rangle = \pm \frac{\boldsymbol{B}}{2|\boldsymbol{B}|} \,.$$

Now we expand ϕ in spherical harmonics Y_l^m

$$\phi = \sum_{\boldsymbol{R}_a} \mathrm{e}^{i\boldsymbol{k}\cdot\boldsymbol{R}_a} \sum_{lm} C_{alm}(\boldsymbol{k}) Y_l^m R_{al}(|\boldsymbol{r} - \boldsymbol{R}_a|),$$

where the $\boldsymbol{R}_a$ are the positions of nuclei in the unit cell, R_{al} is the radial wave function and C_{alm} are the expansion coefficients. Taking into account that SOI is non-vanishing only close to the nucleus (strong potential gradient, large ξ), we consider only one-centre contributions to SOC. Then, we obtain

$$\begin{aligned} B_+ = \langle \phi \mid \xi l_+ \mid \phi \rangle = \sum_{\boldsymbol{R}_a, \boldsymbol{R}_{a'}} \delta_{\boldsymbol{R}_a, \boldsymbol{R}_{a'}} \sum_{lml'm'} \zeta_{al} \langle C_{lm} Y_l^m \mid l_+ \mid C_{l'm'} Y_{l'}^{m'} \rangle = \\ = \sum_{\boldsymbol{R}_a, l, m} \zeta_{al} C_{l,m+1}^* C_{lm} \sqrt{l(l+1) - m(m+1)} \,, \end{aligned} \quad (5.4)$$

where ζ is a radial integral accounting for the strength of SOI.

Si 3*p* In the particular case of one atom in the unit cell with only one shell $l = 1$ (p-orbitals), we obtain

$$B_+ = \zeta\sqrt{2}(C_{10}^* C_{1-1} + C_{11}^* C_{10}) \,.$$

Transformation of the basis from complex spherical functions to real orbitals leads to

$$S_x = \pm \frac{\mathrm{Re}\, B_+}{2|\boldsymbol{B}|} = \frac{\pm\zeta}{|\boldsymbol{B}|} \mathrm{Im}\,(-C_{p_z}^* C_{p_y}) \quad (5.5)$$

and

$$S_y = \pm \frac{\mathrm{Im}\, B_+}{2|\boldsymbol{B}|} = \frac{\pm\zeta}{|\boldsymbol{B}|} \mathrm{Im}\,(C_{p_z}^* C_{p_x}) \,. \quad (5.6)$$

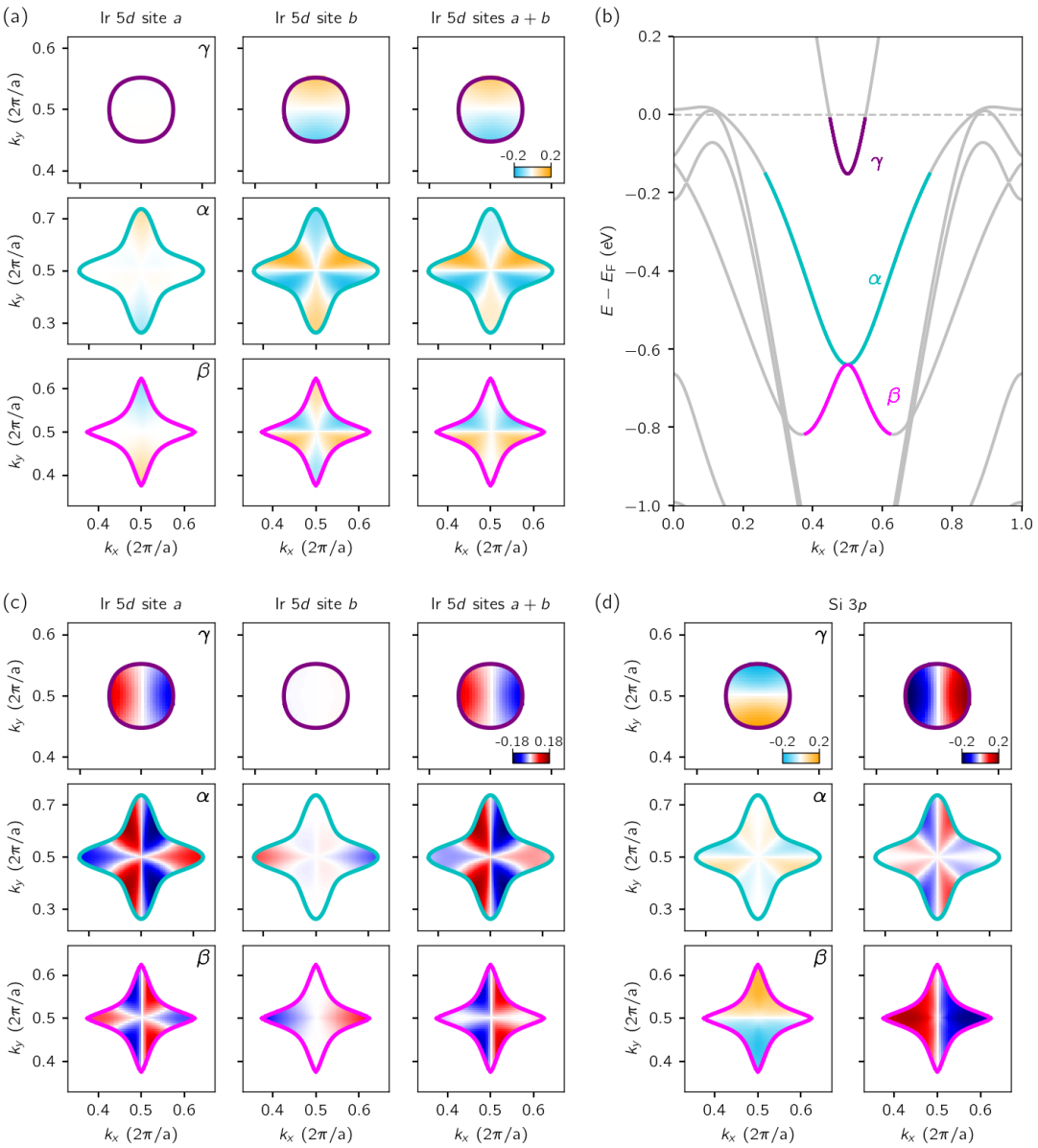

Fig. 5.7.: Spin structure of the surface states α, β and γ determined from the orbital composition of scalar-relativistic wave functions calculated in DFT by treating SOI as a small perturbation. The resulting spin expectation values calculated for $5d$ states of Ir in the subsurface layer of the Si-terminated surface are given for (a) S_x and (c) S_y according to Eqns. 5.8 and 5.9, respectively, in orange (red) for $S_x > 0$ ($S_y > 0$) and light blue (dark blue) for $S_x < 0$ ($S_y < 0$). Shown are the results for each of the two Ir sites separately as well as the sum over both sites. In (b) the band dispersion is shown with the states on the α, β and γ bands for which the spin expectation values have been calculated highlighted in cyan, pink and purple colours, respectively. In (d) the spin structure obtained for the $3p$ coefficients of the surface Si layer according to Eqns. 5.5 and 5.6 are given.

Ir 5*d* For the case of $l = 2$ (d-orbitals) we get

$$B_+ = \zeta \left[2(C^*_{2-1}C_{2-2} + C^*_{22}C_{21}) + \sqrt{6}(C^*_{20}C_{2-1} + C^*_{21}C_{20}) \right] .$$

Transformation to a real orbital basis leads to

$$B_+ = 2\zeta[i\mathrm{Im}\, C^*_{xz}C_{x^2-y^2} - \mathrm{Im}\, C^*_{xz}C_{xy} + \mathrm{Im}\, C^*_{yz}C_{x^2-y^2} + i\mathrm{Im}\, C^*_{yz}C_{xy} + \sqrt{3}(i\mathrm{Im}\, C^*_{z^2}C_{xz} - \mathrm{Im}\, C^*_{z^2}C_{yz})] \quad (5.7)$$

Finally, we obtain

$$S_{x\pm} = \pm\frac{\mathrm{Re}\, B_+}{2|\boldsymbol{B}|} = \frac{\pm\zeta}{|\boldsymbol{B}|}\mathrm{Im}\left(C^*_{yz}C_{x^2-y^2} - C^*_{xz}C_{xy} - \sqrt{3}C^*_{z^2}C_{yz}\right) \quad (5.8)$$

and

$$S_{y\pm} = \pm\frac{\mathrm{Im}\, B_+}{2|\boldsymbol{B}|} = \frac{\pm\zeta}{|\boldsymbol{B}|}\mathrm{Im}\left(C^*_{xz}C_{x^2-y^2} + C^*_{yz}C_{xy} + \sqrt{3}C^*_{z^2}C_{xz}\right) . \quad (5.9)$$

These equations relate the spin structure to the orbital composition of the wave function expressed by the coefficients C. In the case of more than one atom in the unit cell, we have to sum up the spin components on each atom. For the considered case of the Si-terminated $GdIr_2Si_2$ surface, the dominating contribution to the spin structure of the surface states comes from the Ir $5d$ orbitals of the two Ir sites in the second atomic layer and Si $3p$ orbitals from the surface layer. The results for the spin structure obtained by the formalism described above are shown in Fig. 5.7. In (a) and (c) the spin components S_x and S_y obtained from Eqns. 5.8 and 5.9, respectively, are shown for the two Ir sites. Note, that the prefactor $\pm\zeta/|\boldsymbol{B}|$ has been neglected and only the imaginary part is shown. One can see that the spin structure of the α and γ surface states expected from their orbital composition corresponds to the cubic and classical Rashba models with their characteristic triple and single winding of the spin, respectively. The band β shows intermediate properties, described by comparable contributions of linear and cubic Rashba effects. Corresponding results for $3p$ states of the surface Si according to Eqns. 5.5 and 5.6 are given in (d). Apparently, the contribution of the Si $3p$ orbitals of the topmost Si layer to the wave functions of surface states favours a triple and single winding of the spin vector for the α and γ bands, too.

5.2.2. Magnetically ordered phase

In the following, we are going to discuss the modifications of the electronic structure of the Si-terminated surface in the AFM phase, i.e. below the ordering temperature $T_\mathrm{N} = 87\,\mathrm{K}$. Fig. 5.8 provides a comparison of the ARPES-derived band structure along the high-symmetry direction $\overline{\mathrm{X}}$–$\overline{\mathrm{M}}$–$\overline{\mathrm{X}}$ and Fermi maps around the $\overline{\mathrm{M}}$ point of the SBZ in the PM and AFM phases. The ARPES spectra were acquired at 120 K (a, b) and 23 K (c, d) using a photon energy of $h\nu = 55\,\mathrm{eV}$. For the cuts along $\overline{\mathrm{X}}$–$\overline{\mathrm{M}}$–$\overline{\mathrm{X}}$ raw and normalised data are shown, as well as a 1D curvature plot [122]. As we already discussed above, the dispersion in the PM phase is symmetric with respect to the $\overline{\mathrm{M}}$ point and shaped by a strong Rashba effect, which causes a large splitting of the surface

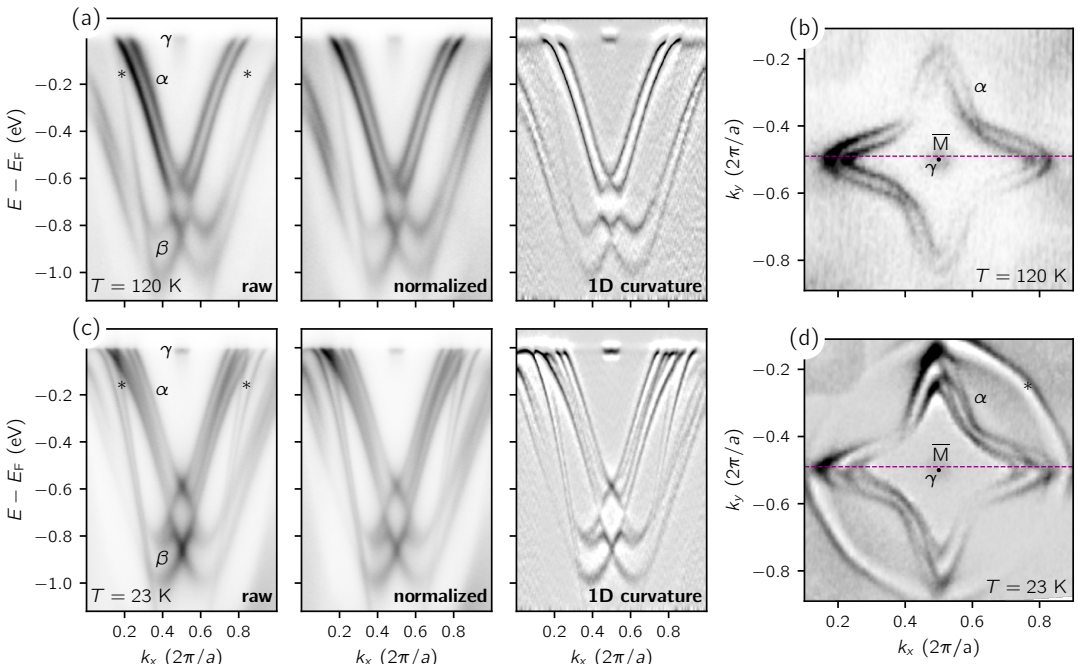

Fig. 5.8.: Band structure of the Si-terminated surface of $GdIr_2Si_2$ measured with ARPES in the PM ($T = 120\,\mathrm{K}$) and AFM ($T = 23\,\mathrm{K}$) phases. The photon energy is $h\nu = 55\,\mathrm{eV}$. The band maps along $\overline{\mathrm{X}}$–$\overline{\mathrm{M}}$–$\overline{\mathrm{X}}$ are shown as measured, after normalisation and after curvature treatment [122] for (a) the PM and (c) the AFM phases. In (b) and (d) the corresponding Fermi surfaces are shown around the $\overline{\mathrm{M}}$ point of the SBZ. The bands of the surface states are labelled α, β and γ, the surface resonant state is marked by an asterisk (*). The purple dotted lines in the Fermi maps show the direction in the SBZ along which the cuts in (a, c) were taken.

state bands. Comparison between the high-symmetry cuts in (a) and (c), and between the Fermi maps in (b) and (d), reveals that the bands undergo strong modifications in the magnetic phase. Let us consider the bands formed by the α state first. In the PM phase, Fig. 5.8(a), α forms one pair of Rashba spin-split bands, whereas in the AFM phase, Fig. 5.8(c), four bands can be distinguished along $\overline{\mathrm{X}}$–$\overline{\mathrm{M}}$–$\overline{\mathrm{X}}$, i.e. the number of bands has doubled. The doubling is well visible in the Fermi surface of the α state, too. In particular, at the corners of the star-shaped contours, additional contour lines are clearly visible in Fig. 5.8(d). Similarly, the β state shows an additional band in the AFM phase which appears in the energy range between $-0.8\,\mathrm{eV}$ and $-0.7\,\mathrm{eV}$ and is best seen in the curvature plot. Since the degeneracy of the bands is already lifted in the PM phase due to the Rashba effect the observed band doubling cannot be attributed to an additional Zeeman-like splitting of the surface state bands but points to the formation of magnetic domains. If different magnetic domains are probed simultaneously the spectrum is a superposition of the spectral patterns associated with each domain. A multi-domain scenario can be easily simulated with DFT comparing the band structure of calculations for different orientations of the Gd $4f$ moments but this requires knowledge of the magnetisation direction. It is known that the Gd $4f$ moments order ferromagnetically in the ab plane, perpendicular to the c axis but the

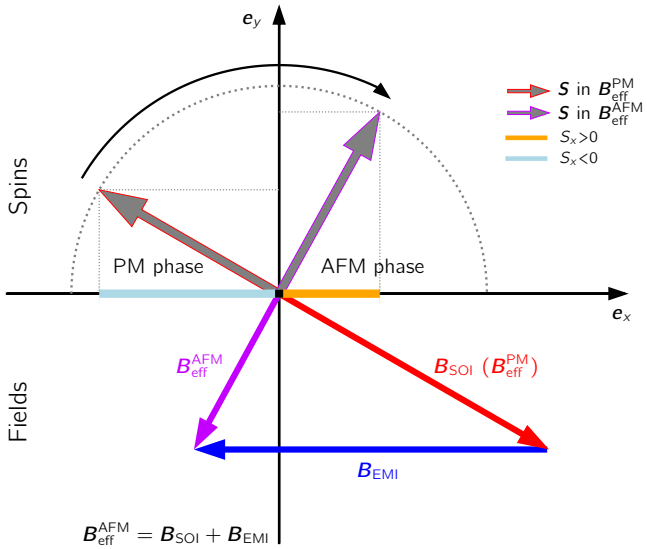

Fig. 5.9.: Schematic illustration of the vector sum of the effective fields and the resulting orientation of the spin for the exchange field pointing along $[\bar{1}00]$.

precise orientation of the magnetisation within the ab plane is unknown. Therefore, we will start with a DFT study, where we consider two different magnetisation directions, [100] and [110]. Those are not only the two simplest cases but correspond to the easy axes observed in closely related compounds of the 122 family. Moreover, for $GdRh_2Si_2$ it was reported, that the magnetisation direction is tunable with short laser pulses, which allow for a rotation from the easy [100] axis to [110] in a controllable fashion [40].

In the previous section, we introduced the Rashba field $\boldsymbol{B}_{\text{R}}$ as the effective magnetic field $\boldsymbol{B}_{\text{eff}}^{\text{PM}}$ of the PM phase to explain the spin structure and splitting of the surface state bands. With the same intention we are now going to introduce for the AFM phase the effective magnetic field $\boldsymbol{B}_{\text{eff}}^{\text{AFM}}$ as the vector sum

$$\boldsymbol{B}_{\text{eff}}^{\text{AFM}} = \boldsymbol{B}_{\text{eff}}^{\text{PM}} + \boldsymbol{B}_{\text{xc}} = \boldsymbol{B}_{\text{R}} + \boldsymbol{B}_{\text{xc}} \tag{5.10}$$

of the spin-orbit and the exchange field $\boldsymbol{B}_{\text{xc}}$ with

$$\boldsymbol{B}_{\text{xc}} = -J\boldsymbol{e}_{\boldsymbol{M}}, \tag{5.11}$$

where $\boldsymbol{e}_{\boldsymbol{M}}$ is a unit vector along the magnetisation direction of the ferromagnetically ordered Gd moments in the first Gd layer below the Si-terminated surface, and J is the strength of the exchange coupling and in general $k_{\parallel}$-dependent. Fig. 5.9 illustrates schematically, how the adding-up of the two fields changes the spin of an electron for the case that $\boldsymbol{B}_{\text{xc}} = -J\boldsymbol{e}_x$. The spin-orbit and the exchange fields are represented in the lower half plane as red and blue arrows, respectively. The purple-coloured arrow is the sum of the latter, representing the effective magnetic field of the AFM phase. In the upper half plane, the orientation of a majority spin (antiparallel in the field) in the effective magnetic fields of the PM and AFM phases is shown. In the first case, the

majority spin is antiparallel to the spin-orbit field as represented by the red-rimmed grey arrow. In the second case, it is antiparallel to the effective magnetic field of the AFM phase, as indicated by the purple-rimmed grey arrow. This simple scheme can be used to predict qualitatively, how the spin structure of a system described by $\boldsymbol{B}_{\mathrm{R}}$ in the PM phase may change under the action of an exchange interaction described by $\boldsymbol{B}_{\mathrm{xc}}$. The amount by which the spin gets rotated by the exchange field depends on the angle and the absolute value of the latter with respect to the spin-orbit field. For the given case in which the exchange field is $-J\boldsymbol{e}_x$, we see, that only the x component of the effective magnetic field can change, while the y component remains unaltered. For the spin, in general both, S_x and S_y will change, however, the sign of S_y will be conserved, whereas the sign of S_x may change for particular configurations of the spin-orbit and exchange fields.

Firstly, we want to collect some information about the exchange field. Since the Gd moments that form the source of the exchange interaction order ferromagnetically, we assume that the orientation of the exchange field coincides with the magnetisation axis in the subsurface Gd layer. This contrasts with the effective spin-orbit field, which has a different orientation at each $\boldsymbol{k}_{\parallel}$. The absolute value of the exchange field varies with $\boldsymbol{k}_{\parallel}$ and is given by the exchange-induced band splitting. Fig. 5.10 shows the band structure of the surface state bands along the vertical $\overline{\mathrm{X}}$–$\overline{\mathrm{M}}$–$\overline{\mathrm{X}}$ path $\parallel k_y$ for different computational setups assuming (a) neither SOI nor exchange interaction, (b) exchange interaction only, (c) SOI only, and (d) both SOI and exchange interaction with the Gd moments pointing along the $[\bar{1}00]$ direction. First, we consider the bare exchange coupling without SOI, Fig. 5.10(b). In this case, spin is a good quantum number and each band state has either $m_s = \uparrow$ or $m_s = \downarrow$ with m_s being the z component of the spin. Note, that in a scalar-relativistic calculation without SOI the exchange interaction is isotropic, i.e. the total energy is independent of the choice of the magnetisation axis and m_s could equally be the x or y component of the spin. Comparison of (a) and (b) shows *how* the exchange interaction lifts the degeneracy of the bands. A general trend for all three surface states is the lowering of the "$\uparrow$" bands in energy, while the "$\downarrow$" bands are raised by the exchange interaction, indicating a predominantly parallel coupling between the spins of the itinerant surface state electrons and the spin of the Gd $4f$ shell. Only at the $\overline{\mathrm{M}}$ point a two-fold degeneracy remains between each of the $\uparrow$ and $\downarrow$ states of α and β, which are equally lowered or raised in energy, respectively. The k_y dependence of the exchange field correlates with the k_y dependence of the splitting $\Delta E = E_{\downarrow} - E_{\uparrow}$ between the $\uparrow$ and $\downarrow$ bands. We identify ΔE with the exchange coupling strength J_i for $i \in \{\alpha, \beta, \gamma\}$ introduced in Eqn. 5.11. In the case of a parallel coupling, $J > 0$, whereas $J < 0$ if the surface-state spins couple antiparallelly to the $4f$ spins. In Fig. 5.10(f) the splitting $\Delta E_i = J_i$ is shown in orange, blue and green for α, β and γ, respectively. The largest (smallest) values of the splitting reached by α, β and γ are 176 meV (144 meV), 149 meV (−14 meV) and 62 meV (−32 meV), respectively. The maximum value reached by α is thus about three times larger than for γ and about 1.2 times larger than for β. Moreover, for α the minimum and maximum values of the splitting differ by 32 meV, while the difference amounts to 153 meV and 94 meV for β and γ, respectively, emphasizing the strong $k_{\parallel}$ dependence of the exchange field experienced by the latter two states. In that regard J_α can be considered constant and

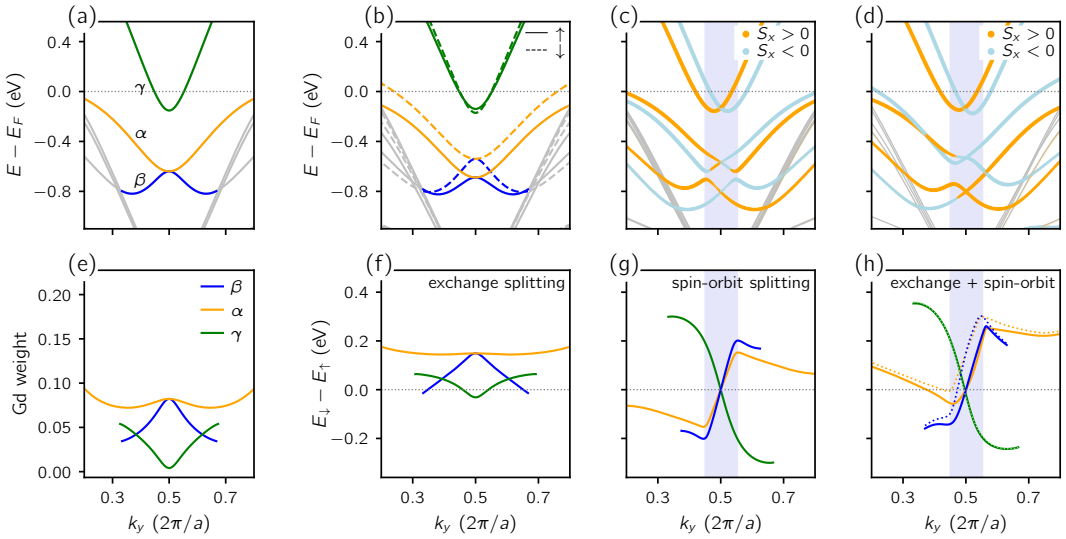

Fig. 5.10.: Dispersion and spin structure of the surface states along $\overline{\mathrm{X}}$–$\overline{\mathrm{M}}$–$\overline{\mathrm{X}}$ for (a) neither SOI nor exchange interaction, (b) exchange interaction, (c) SOI and (d) both SOI and exchange interaction with magnetisation along $[\bar{1}00]$. In (b) spin-up and spin-down polarised bands are shown as solid and dashed lines, whereas orange and light blue markers indicate $S_x > 0$ and $S_x < 0$, respectively, for the expectation value S_x in (c) and (d). The marker size corresponds to the absolute value of S_x multiplied by the surface weight. The second row shows (e) the band weights of the Gd subsurface layer, and (f)-(h) the splitting $\Delta E = E_\downarrow - E_\uparrow$ between states with (predominantly) minority ($\downarrow$) and majority ($\uparrow$) spins. In (a) and (b) the bands formed by α, β and γ are coloured in orange, blue and green, respectively. The same colour scheme is used for the corresponding band weights and splittings. The dotted lines in (h) are the sums of the curves in (f) and (g).

because $J_\alpha > 0$ for all k_y, the coupling to the Gd spins is always parallel. In contrast J_β shows a pronounced maximum at the $\overline{\mathrm{M}}$ point from which it falls off to zero at about $k_y = (0.5 \pm 0.15)\,\frac{2\pi}{a}$ up to which the coupling is parallel, too. Upon further approaching the bulk bands, $J_\beta < 0$, i.e. the exchange coupling becomes antiparallel at the edges of the band gap. For γ the exchange splitting, and hence J_γ, changes sign from positive for $k_y \gtrless (0.5 \pm 0.04)\,\frac{2\pi}{a}$ to negative in the vicinity of the $\overline{\mathrm{M}}$ point, i.e. the coupling to the Gd moments is mostly parallel, except for a small region of antiparallel coupling around the $\overline{\mathrm{M}}$ point. Finally, take note of the strong similarity in the $k_\parallel$-dependent curve shape of the exchange-splitting and the Gd weight function, Fig. 5.10(e), for each surface state α, β and γ. It can be seen that the splitting scales with the Gd weight or in other words, the strength of the exchange interaction and the nature of the coupling seem to depend on the overlap between the surface state wave function with the Gd layer. α for example, which has the largest and comparatively most constant Gd contribution, shows the greatest splitting with only small variations in k_y.

Let us now consider the splitting calculated for pure SOC, Fig. 5.10(c) and (g). Since here spin is not a good quantum number, the expectation value S_x is plotted and the splitting is given by the energy difference $\Delta E = E_\downarrow - E_\uparrow$ between states with $S_x < 0$ (light blue) and $S_x > 0$ (orange) in analogy to $m_S = \downarrow$ and $m_S = \uparrow$ in (b)

Tab. 5.1.: Values ΔE of the minimal and maximal band splitting in units of meV which are reached at $k_{\min}$ and $k_{\max}$, respectively.

State	$\Delta E^{\mathrm{xc}}_{\min}$	$\Delta E^{\mathrm{xc}}_{\max}$	$\Delta E^{\mathrm{SOI}}_{\min}$	$\Delta E^{\mathrm{SOI}}_{\max}$	$\Delta E^{\mathrm{SOI+xc}}_{\min}$	$\Delta E^{\mathrm{SOI}}_{\mathrm{max+xc}}$	$k_{\min}, k_{\max}$
α	144	176	-153	153	-58	252	$0.2\frac{2\pi}{a}, 0.8\frac{2\pi}{a}$
β	-14	149	-300	300	-155	260	$0.33\frac{2\pi}{a}, 0.67\frac{2\pi}{a}$
γ	-32	62	-202	202	-243	354	$0.37\frac{2\pi}{a}, 0.63\frac{2\pi}{a}$

and (f), respectively. Note, that for α and β this definition cannot be applied to the exotic region in the vicinity of the $\overline{\mathrm{M}}$ point, where spin has the same sign on the split branches of each band. Therefore, the sign of the splitting is chosen such, that the splitting function is steady in k_y. In analogy to the exchange field and in accordance with our findings for the spin-orbit field in the previous section, we express the latter as

$$\boldsymbol{B}^{(i)}_{\mathrm{R}} = -\Delta E^{(i)}(k_y)\boldsymbol{e}_x \tag{5.12}$$

with $i \in \{\alpha, \beta, \gamma\}$. Apparently, $\boldsymbol{B}^{(i)}_{\mathrm{R}}(\overline{\mathrm{M}}) \equiv 0$, while with increasing distance from $\overline{\mathrm{M}}$ the absolute value of $\boldsymbol{B}^{(i)}_{\mathrm{R}}$ first increases linearly in k_y for all three surface states. For α and β the linear behaviour is restricted to the exotic region of the intrinsic SOI. At $k_y = (0.5 \pm 0.05)\frac{2\pi}{a}$ which lies at the boundary of the latter, the splitting reaches its maximal absolute value with 153 meV for α and 202 meV for β. Further, the slope of the splitting function changes sign and becomes increasingly smaller with increasing distance from $\overline{\mathrm{M}}$. In accordance with our extensive discussion of the Rashba field, the splitting has opposite sign to the right and left of the $\overline{\mathrm{M}}$ point, i.e. $\boldsymbol{B}^{(i)}_{\mathrm{R}}(0.5-\Delta k) = -\boldsymbol{B}^{(i)}_{\mathrm{R}}(-(0.5+\Delta k))$, where Δk describes the distance from $\overline{\mathrm{M}}$. As we will see in the following, it is important to notice, that the spin-orbit and the exchange interactions are of similar strengths. Comparing (f) and (g) we immediately see, that the exchange splitting J is an even function in $k_\parallel$, i.e. $J(0.5-\Delta k) = J(-(0.5+\Delta k))$, whereas the spin-orbit splitting $\boldsymbol{B}^{(i)}_{\mathrm{R}}(k_\parallel)$ is odd, $\boldsymbol{B}^{(i)}_{\mathrm{R}}(0.5-\Delta k) = -\boldsymbol{B}^{(i)}_{\mathrm{R}}(-(0.5+\Delta k))$. This implies that on one side of $\overline{\mathrm{M}}$ the two fields point in the same direction, while on the other side they are antiparallel. For $k_y < 0.5$ the effective exchange and spin-orbit fields of α and β are antiparallel, while for $k_y > 0.5$ both $B^{(\alpha,\beta)}_{\mathrm{R}}$ and $J_{\alpha,\beta}$ are positive, the fields must thus be parallel. In the case of γ exchange and spin-orbit fields are parallel for $k_y < 0.5-0.04$ and $0.5 < k_y < 0.5+0.04$, whereas for $0.5-0.04 < k_y < 0.5$ and $k_y > 0.5 + 0.04$ they are antiparallel.

Fig. 5.10(d) shows the band and spin structure when both the spin-orbit and exchange interactions are taken into account. According to Fig. 5.9 and our assumption that $\boldsymbol{B}^{\mathrm{AFM}}_{\mathrm{eff}}$ is the vector sum of the spin-orbit and exchange fields, the mutual orientation and the respective strength of the latter two determines how the spin-structure and dispersion change in the AFM phase. In Fig. 5.10 we consider the high-symmetry direction for which spin-orbit and exchange fields are collinear. In the case of a parallel alignment of the latter, they augment each other and consequently the splitting of the bands increases, whereas in the case of an antiparallel alignment they weaken

each other and consequently the splitting of the bands becomes smaller. If in the antiparallel scenario $B_{\mathrm{R}}^{(i)} = J_i$ the splitting may even vanish and for $B < J$, spin may even change sign. Looking at Fig. 5.10(d), we find indeed that each of the considered cases is realised. The corresponding band splitting is given in (h) and defined in the same way as for the case, where only SOI is considered. Comparing (h) to (g) we find that the splitting functions are shifted upward. This implies for α and β that for $k < 0.5$ the splitting is mostly reduced in the AFM phase, while for $k > 0.5$ the splitting becomes larger, which is in accordance with our discussion of the weakening or augmentation of the effective magnetic field due to the mutually antiparallel and parallel alignment of the spin-orbit and exchange fields to the left and right of $\overline{\mathrm{M}}$, respectively. For α we even meet the cases in which (1) the two fields cancel each other and the splitting vanishes, and (2) the effective magnetic field changes sign in the AFM phase, which is seen in a change of sign of the splitting function from negative in the PM to positive in the AFM phase. In the dispersion, this appears in form of the crossing of the α bands with opposite spin characters. In the $\overline{\mathrm{M}}$ point itself, the splitting remains zero but the energy separation between α and β increases by 31 meV from 238 meV to 269 meV proving that the exchange field does not vanish. For γ the spin-orbit field has the opposite sign than for α and β, thus the splitting increases for $k_y < 0.5$ and decreases for $k_y > 0.5$. Moreover, the crossing point of the γ bands at which the splitting vanishes is shifted slightly away from $\overline{\mathrm{M}}$.

To check if $\boldsymbol{B}_{\mathrm{eff}}^{\mathrm{AFM}}$ is indeed the sum of the bare exchange field in (b, f) and the spin-orbit field in (c, g), the sums of the respective splitting functions are shown as dotted lines in (h). We find, that outside of the exotic region around the $\overline{\mathrm{M}}$ point the splitting of α is well approximated by the sum $J_\alpha + B_\alpha$, whereas in the vicinity of $\overline{\mathrm{M}}$ the offset between the solid and dotted orange lines is very large. For β, whose bands are mostly confined to the exotic $k_\parallel$ region, we get a very similar result. On the other hand, the summation works well for γ, for which, however, the exchange interaction around the $\overline{\mathrm{M}}$ point is much weaker than the SOI. Thus we may conclude, that outside of the exotic region around the $\overline{\mathrm{M}}$ point $\boldsymbol{B}_{\mathrm{eff}}^{\mathrm{AFM}}$ can be indeed described as the sum of the bare exchange and the spin-orbit field, whereas close to $\overline{\mathrm{M}}$ the exchange field strongly deviates. Finally, Table 5.1 summarises the minimum and maximum values of the splittings.

Spin structure In the following, we are going to analyse the band and spin structure of α and γ for the other high-symmetry directions and the CECs, too. In our discussion, we will omit the exotic region around the $\overline{\mathrm{M}}$ point as well as the β state, whose bands range mostly within the latter. Instead, we will focus on the combination of the linear and cubic Rashba-like SOI with the exchange interaction. Fig. 5.11 shows the DFT-derived dispersion and the spin structure of α and γ in terms of isoenergy contours and high-symmetry cuts for the PM (a, d) and AFM phases (b, e, c, f). For the magnetisation direction we consider $[\bar{1}00]$ and $[\bar{1}\bar{1}0]$. The calculated band structure for either case is given in (b, e) and (c, f), respectively. Note, that a given magnetisation direction refers to the first Gd layer below the Si-terminated surface, while the global magnetic order in the slab is of course antiferromagnetic. In Fig. 5.11 each row presents one spin component: red and blue colours encode $S_y > 0$ and $S_y < 0$, orange and light

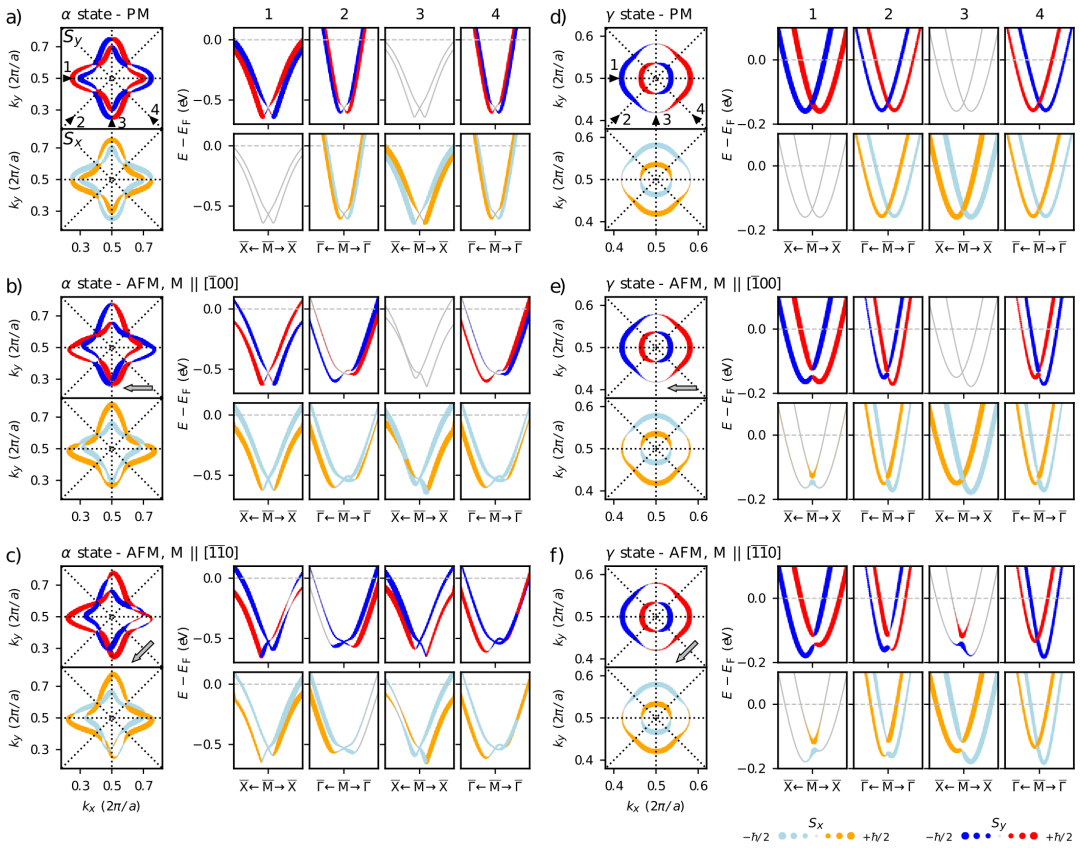

Fig. 5.11.: Dispersion and spin structure of the surface states α and γ in (a, d) the PM and (b, e, c, f) the AFM phases. The expectation values of the spin components S_x and S_y are shown in orange ($S_x > 0$) or light blue ($S_x < 0$) and red ($S_y > 0$) or blue ($S_y < 0$), $S_z = 0$. The line width reflects the absolute value of the single spin components. In the left column, isoenergy cuts are drawn. The black dotted lines indicate the high-symmetry directions $\overline{\text{X}}$–$\overline{\text{M}}$–$\overline{\text{X}}$ or $\overline{\Gamma}$–$\overline{\text{M}}$–$\overline{\Gamma}$. In (a) and (d) they are numbered consecutively from 1 to 4. Small black arrows mark the direction in which we move along a particular k path in the four accordingly numbered panels on the right. Gray arrows drawn with the isoenergy cuts indicate the direction of the exchange field, which is $[\bar{1}00]$ in (b, e), and $[\bar{1}\bar{1}0]$ in (c, f).

blue $S_x > 0$ and $S_x < 0$, respectively. The columns containing the $E(k_\parallel)$ plots are numbered from ① to ④. Each number corresponds to a particular $\overline{\text{X}}$–$\overline{\text{M}}$–$\overline{\text{X}}$ or $\overline{\Gamma}$–$\overline{\text{M}}$–$\overline{\Gamma}$ high-symmetry path, specified by the dotted lines drawn in the upper CECs plot in Fig. 5.11(a). There, small black arrows additionally indicate the direction along which the bands are plotted.

Obviously, there are pronounced differences in the dispersion and the spin structure between the PM and the two considered AFM phases. We can make several general statements that are valid for both magnetisation directions. A comparison of the CECs reveals that the fourfold rotational symmetry of the PM phase reduces to mirror symmetry in the magnetic phases. The mirror line is the axis that is perpendicular to the magnetisation axis. The reduced symmetry is reflected in the high-symmetry $E(k_\parallel)$ cuts, too. While in the PM phase the bands disperse symmetrically with respect

to the $\overline{\mathrm{M}}$ point for all high-symmetry directions, in the magnetic phases the dispersion is only symmetric for the high-symmetry direction that is parallel to the magnetisation axis. Those are the $\overline{\mathrm{X}}$–$\overline{\mathrm{M}}$–$\overline{\mathrm{X}}$ path ① for $[\bar{1}00]$ and the $\overline{\Gamma}$–$\overline{\mathrm{M}}$–$\overline{\Gamma}$ path ② for $[\bar{1}\bar{1}0]$. As we will discuss in detail below, a symmetric dispersion is found when exchange and spin-orbit fields are perpendicular to each other. The dispersion of the bands along the remaining high-symmetry directions shows strong asymmetries, which are most pronounced for those who are perpendicular to the magnetisation axis. The changes in the dispersion are closely related to changes in the spin structure. For example, along the horizontal $\overline{\mathrm{X}}$–$\overline{\mathrm{M}}$–$\overline{\mathrm{X}}$ path ① in the PM phase the spin structure is S_y-only, i.e. the expectation value S_x vanishes for all k_x, whereas in the magnetic phases $S_x \neq 0$. Another interesting observation is the change of the spin expectation value along a particular band as seen, for example, in Fig. 5.11(c) in the left branch along the vertical $\overline{\mathrm{X}}$–$\overline{\mathrm{M}}$–$\overline{\mathrm{X}}$ path ③.

Let us now consider the surface states in detail, starting with α for the $[\bar{1}00]$ magnetisation direction. According to our previous discussion the changes in spin and dispersion are related to the mutual alignment and relative strength of spin-orbit and exchange fields, which add up to the total effective field of the AFM phase, as was schematically shown in Fig. 5.9. For α we found a negligible $k_\parallel$ dependence of the exchange field having an absolute value of about 180 meV, and a slightly varying absolute value of the spin-orbit field, which decreases with increasing distance from $\overline{\mathrm{M}}$, cf. Fig. 5.10(f, g). Moreover, the orientation of the exchange field is fixed along $[\bar{1}00]$, while the Rashba field possesses the triple-winding symmetry, continuously changing direction with the polar angle $\varphi_{\boldsymbol{k}}$. Here, we consider three limiting cases for the mutual alignment between the Rashba and exchange fields:

1. $\boldsymbol{B}_\mathrm{R} \perp \boldsymbol{B}_\mathrm{xc}$ The first case is realised along the horizontal $\overline{\mathrm{X}}$–$\overline{\mathrm{M}}$–$\overline{\mathrm{X}}$ path ①. Here, the spin structure is S_y-only in the PM phase, i.e. $S_x = 0$ for all k_x and the Rashba field points into negative ($k_x < 0.5$, left branch) or positive ($k_x > 0.5$, right branch) y direction. The addition of the exchange field to the Rashba field implies that the effective magnetic field acquires an x component in the AFM phase, which is the same for all k_x (assuming that $J = \text{const.}$) on the given path and leads to $S_x > 0$ (orange) on the outer and $S_x < 0$ (light blue) on the inner band of the α state. Moreover, the absolute value of the effective magnetic field increases in the AFM phase which results in a larger energy splitting of the surface state bands.

2. $\boldsymbol{B}_\mathrm{R} \uparrow\uparrow \boldsymbol{B}_\mathrm{xc}$ In the second case, the Rashba and exchange fields point in the same direction ($-\boldsymbol{e}_x$). In this scenario, which is realised along the $\overline{\mathrm{X}}$–$\overline{\mathrm{M}}$–$\overline{\mathrm{X}}$ path ③ for $k_y > 0.55$, each field considered separately would induce an S_x–only spin structure with $S_y = 0$ for all k_y. Hence, the spin structure does not change in the AFM phase but the parallel alignment increases the effective magnetic field and hence, the energy splitting of the bands.

3. $\boldsymbol{B}_\mathrm{R} \uparrow\downarrow \boldsymbol{B}_\mathrm{xc}$ The third case with an antiparallel configuration of the Rashba and exchange fields is realised along the $\overline{\mathrm{X}}$–$\overline{\mathrm{M}}$–$\overline{\mathrm{X}}$ path ③, too, for $k_y < 0.45$. Looking at Fig. 5.11 we find, that at $k_y \approx 0.38$ the two bands of the left branch are degenerate

implying that the exchange field compensates the Rashba field and $\boldsymbol{B}_{\text{eff}}^{\text{AFM}} = 0$. For larger k_y (closer to $\overline{\text{M}}$) the Rashba field is larger than the exchange field, and thus the spin structure is the same as in the PM phase, while the splitting is reduced since the exchange field partly compensates the Rashba field. For $k_y < 0.38$ (further away from $\overline{\text{M}}$) the exchange field is stronger than the Rashba field and thus, spin changes sign. A similar argumentation can be applied to the $\overline{\Gamma}$–$\overline{\text{M}}$–$\overline{\Gamma}$ directions, which are intermediate cases.

For magnetisation along $[\overline{1}\overline{1}0]$ the exchange field is given by $\boldsymbol{B}_{\text{xc}} = -J/\sqrt{2}(\boldsymbol{e}_x + \boldsymbol{e}_y)$. For this arrangement, the limiting cases in which the exchange and Rashba fields are mutually collinear or perpendicular emerge along the $\overline{\Gamma}$–$\overline{\text{M}}$–$\overline{\Gamma}$ paths ④ and ②, respectively. Since the modification of the spin structure in the AFM phase follows the same principles as in the $[\overline{1}00]$ case, we will refrain from a detailed discussion of the band and spin structure in Fig. 5.11(c). The only thing to be pointed out is the spin structure for the $\overline{\text{X}}$–$\overline{\text{M}}$–$\overline{\text{X}}$ high-symmetry path ③. Moving from $\overline{\text{M}}$ leftwards along one of the α bands towards smaller k_y, we find that the sign of S_x changes on the band without passing of a degeneracy as we observed it for $[\overline{1}00]$. In difference to $[\overline{1}00]$, here the Rashba and exchange fields are not antiparallel and thus, the sign of one spin component may change without band crossing. A crossing as for $\overline{\text{X}}$–$\overline{\text{M}}$–$\overline{\text{X}}$ in the $[\overline{1}00]$ case, we find for $[\overline{1}\overline{1}0]$ along the $\overline{\Gamma}$–$\overline{\text{M}}$–$\overline{\Gamma}$ path ④.

For the γ state the Rashba field is characterised by a single winding with opposite winding sense in comparison to α. In difference to α, here we can expand our discussion to the $\overline{\text{M}}$ point and its immediate vicinity since γ is not subject to the intrinsic SOI. The principles apply to the description of the changes in spin and dispersion in terms of two effective magnetic fields due to the Rashba effect and exchange interaction. For γ the exchange field lifts the degeneracy of the bands at the $\overline{\text{M}}$ point, shifting the crossing point into the close vicinity of $\overline{\text{M}}$. For magnetisation along $[\overline{1}00]$ the crossing point is shifted along $\overline{\text{X}}$–$\overline{\text{M}}$–$\overline{\text{X}}$ path ③ toward smaller k_y, i.e. leftward. For $[\overline{1}\overline{1}0]$, it is shifted leftward, too, but along the $\overline{\Gamma}$–$\overline{\text{M}}$–$\overline{\Gamma}$ path ④. As we may expect from our previous discussion, in both cases the crossing point is shifted along the high-symmetry directions for which the Rashba and exchange fields are collinear to each other.

To conclude the discussion of the spin structure in the AFM phase Fig. 5.12 gives a compact, energy-projected view of the spin structure of the surface state bands. In the left and right columns, the results for the energetically lower and higher bands are shown, while the rows represent the PM, the $[\overline{1}00]$-AFM and the $[\overline{1}\overline{1}0]$-AFM phases. The colour map ranges from orange for $\boldsymbol{S} = \boldsymbol{e}_x$ over red for $\boldsymbol{S} = \boldsymbol{e}_y$ and light blue for $\boldsymbol{S} = -\boldsymbol{e}_x$ to dark blue for $\boldsymbol{S} = -\boldsymbol{e}_y$, or equally, the polar angles $\varphi_{\boldsymbol{S}}$ of $0, \frac{\pi}{2}, \pi, \frac{3\pi}{2}$, respectively. Note, that the absolute value of the spin is neglected and set to $S = \frac{\hbar}{2}$ for all $k_\parallel$. Moreover, on the right-hand side, the S_x and S_y spin components are shown separately in the previously used orange-light blue and red-dark blue colour schemes, respectively.

Comparing the results for the AFM phase with $[\overline{1}00]$ to those of the PM phase, we still recognise a triple winding of the spin along the CECs up to an energy of about $E \approx -0.36\,\text{eV}$, at which we observed the crossing point in the $E(k_y)$ plot along $\overline{\text{X}}$–$\overline{\text{M}}$–$\overline{\text{X}}$ path ③ in Fig. 5.11(b). For higher energies the triple winding collapses in the lower corner of the star-shaped plot where the exchange field is (almost) antiparallel to the Rashba field and becomes stronger than the latter, flipping the spins close to

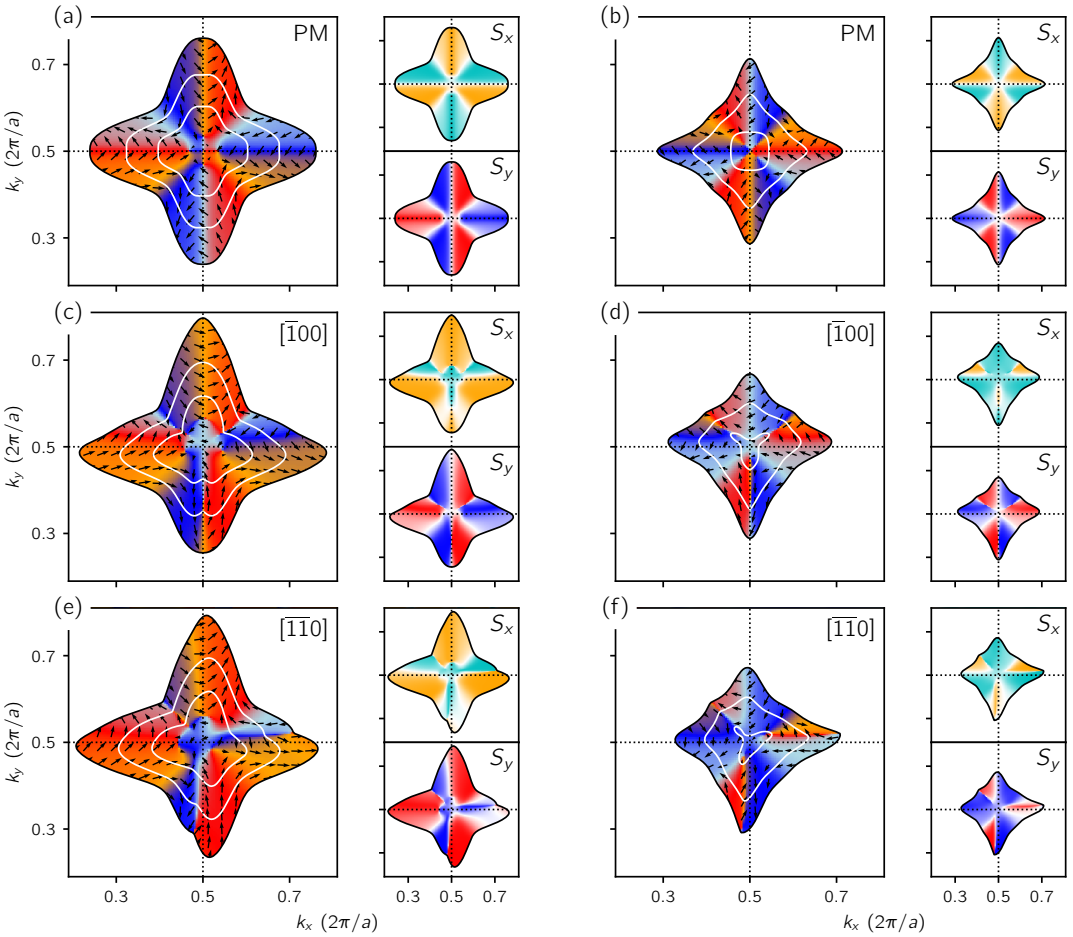

Fig. 5.12.: Calculated spin structure of α in (a, b) the PM phase, (b, c) the AFM [$\bar{1}$00] phase and (e, f) the AFM [$\bar{1}\bar{1}$0] phase for the lower and upper band, respectively. The colour scheme used to visualise the orientation of the spin is the same as before, see Fig. 5.6.

the vertical $\overline{\mathrm{X}}$–$\overline{\mathrm{M}}$–$\overline{\mathrm{X}}$ path and $k_y \approx 0.375$, $k_y > 0.565$. Note, that the spin-flip is nicely seen in the S_x map, too. S_y in turn widely preserves the symmetry of the PM phase. For AFM with magnetisation along [$\bar{1}\bar{1}$0], we can find CECs on which the triple winding is preserved, too. Equally, we find CECs where the triple winding collapses.

Magnetic domains

In Fig. 5.13 the ARPES-derived Fermi map taken at 23 K is compared with the results of DFT calculations simulating two magnetic domains with opposite magnetisation. Like before, we consider the two cases in which the moments are oriented collinear with the [110] or [100] directions. The results are plotted in Fig. 5.13(b) and (c), respectively, where states that belong to the positive sign of the magnetisation are plotted in green, and those reflecting the opposite magnetisation in purple. Accordingly coloured arrows drawn in the lower right corner point into the corresponding magnetisation direction. Apparently, the shape of the Fermi contours of the α state differs notably not only

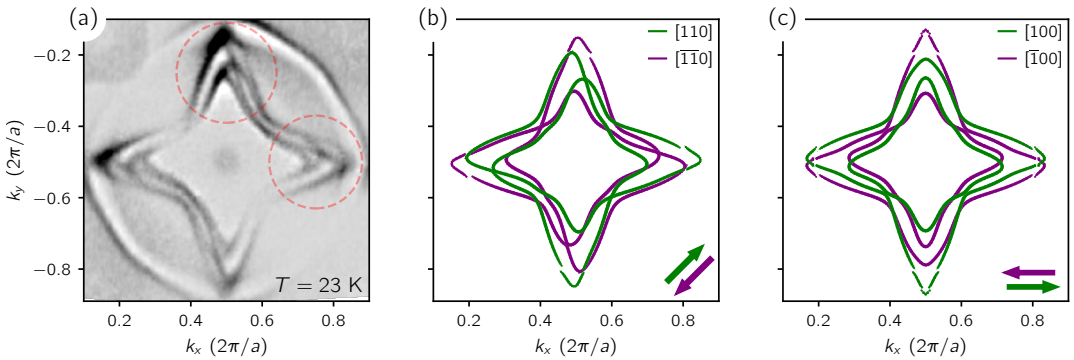

Fig. 5.13.: Fermi surface of $GdIr_2Si_2$ in presence of magnetic domains. (a) ARPES data taken at 23 K from the Si-terminated surface of $GdIr_2Si_2$. DFT simulations in the case of two domains associated with an antiparallel magnetisation for (b) the [110] and (c) the [100] direction. Purple and green correspond to the sign of magnetisation.

between (b) and (c) but also for opposite magnetisation directions with respect to the same axis. A closer look at the green and purple CECs reveals that they are mirror images of each other with the mirror line being perpendicular to the magnetisation axis. Comparison of the calculated data with the measured Fermi map thus supports the interpretation that the band doubling is due to domain formation. Moreover, the very good agreement of the measured CECs with those shown in Fig. 5.13(b) gives strong evidence that the magnetisation axis is [110], at least for the measurement temperature of 23 K. However, we cannot exclude that the easy axis changes with temperature.

The domain formation that leads to the doubling of the surface state bands can be of different origins. If we assume an ideal, atomically flat and uniform surface a band doubling can be observed only if magnetic domains form in the crystal and are probed simultaneously, which is inevitable if the size of the domains is smaller than the probed area, i.e. smaller than the spot size of the photon beam. Another possibility is the probing of different surface domains due to an imperfect, stepped surface. In the cleaving procedure that is applied to prepare the atomically clean surface indispensable for UV-ARPES experiments, a manifold of atomically flat regions of uniform termination is produced. Assuming exclusively Si termination those uniform "crystallites" are separated from each other by multiple steps of three atomic layers (Gd-Si-Ir). If the number of steps between neighbouring, uniform areas is uneven, the adjacent crystallites will have opposite magnetisation, for an even number of steps, they will have the same magnetisation. This is a consequence of the AFM order of $GdIr_2Si_2$ in the bulk and holds only if the considered crystallites belong to the same magnetic domain. The two scenarios are schematically sketched in Fig. 5.14.

Note, that we observe additional bands for β, too. Moreover, we find that the surface resonant band (*) splits in the magnetic phase into two bands. This state is rather located at the Gd-terminated surface, indicating an admixture of the latter in our spectra. Nonetheless, in the PM phase, this band is not split or the splitting is too small to be resolved experimentally, which implies that the surface resonant state is not subject to the Rashba effect since, as surface resonance, it underlies the

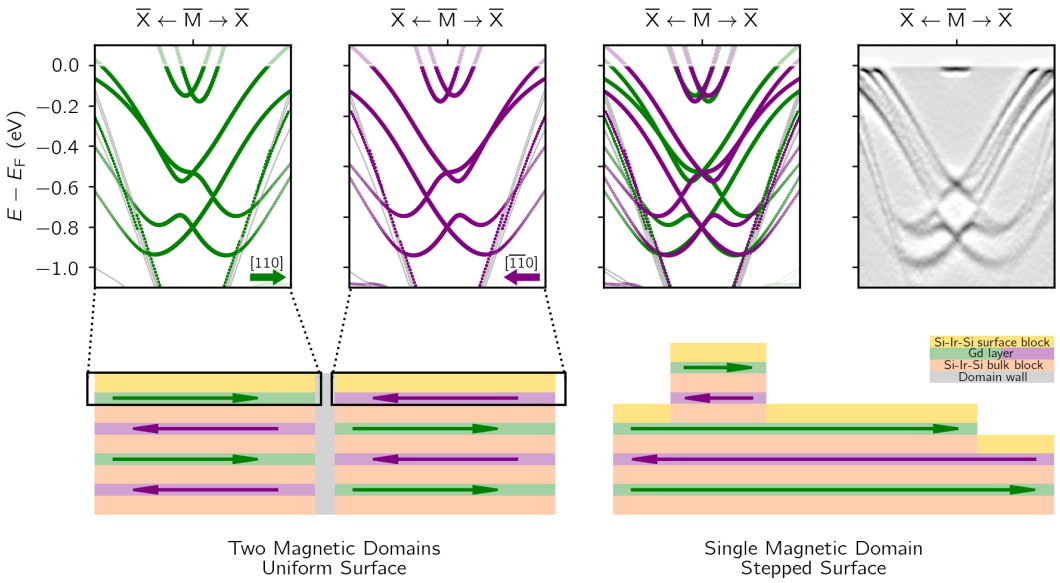

Fig. 5.14.: Domain formation. Schematic view on the origin of the doubling of the surface-state bands due to magnetic domains or a stepped surface.

symmetry restrictions of the bulk, and hence, it must be degenerate. Therefore the splitting must be pure magnetic splitting, i.e. the spin degenerate bands split under the influence of some exchange interaction due to the ordering of the Gd moments.

5.3. Summary

Extensive and long-term studies of LnT_2Si_2, compounds showed, that the surface Si–T–Si–Ln block forms a promising system for studying the Rashba-like SOI and its joint action with exchange magnetism on 2D charge carriers. Particularly, the surface states located in a large projected band gap around the $\overline{\mathrm{M}}$ point attracted great interest. To combine a strong SOC with exchange magnetic interaction it seems logical to bring together heavy Ir with magnetically active Gd within the respective Si–T-Si–Ln block. Due to its half-filled $4f$ shell, implying $L = 0$, and therefore pure spin moment $J = S = 7/2$, Gd is the simplest magnetically active rare-earth element which is rather insensitive to the CEF environment. Following this chain of thought, we arrived at the system $GdIr_2Si_2$, which is a layered AFM material. We thus performed a study of the surface electronic structure of $GdIr_2Si_2$, in the PM and AFM phases, thereby focusing on the surface states α and γ located in the large band gap around the $\overline{\mathrm{M}}$ point of the SBZ. In accordance with our expectations and with former studies, we find the surface state electrons to be subject to a strong Rashba effect, which leads to highly spin-polarized and strongly spin-split bands. Here, only the γ state shows the spin structure of a classical, linear Rashba effect. In turn, the α band shows a so-called cubic Rashba effect, which is characterised by a triple winding of the spin around the CECs. The origin of the different spin characters lies in the orbital composition of the surface states. Further, we found that with the magnetic ordering

of the $4f$ moments the spin structure gets strongly modified and asymmetries occur in the band dispersion and thus, also in the CECs. Both the Rashba-like SOC and the exchange interaction can be described by effective magnetic fields, a k dependent Rashba field and the exchange field. Considering the resulting total field allows us to understand the complex spin structures of the aforementioned surface states in the PM and AFM phases. The wave function of the α state extends over the whole Si–Ir–Si–Gd surface block. The overlap with the Gd layer results in a direct exchange coupling of the itinerant spins to the localized $4f$ moments. Since the wave function of the γ state concentrates within the topmost Si-Ir double layer it has a negligible overlap with Gd, suggesting an indirect coupling to the ordered $4f$ moments, which is strongly energy-dependent.

We have also shown and discussed that the formation of a mosaic of magnetic domains essentially complicates the analysis of ARPES patterns in comparison to a single-domain case but as we show here it is still possible to derive the orientation of the easy magnetisation axis even for the multi-domain case. It is assumed that further insight into the properties of a single domain can be obtained using an alternative experimental technique, namely with nano-ARPES. The formation of magnetic domains and domain walls might also be of interest for further investigations, e.g. within the framework of spin-resolved photoemission electron microscopy (PEEM) experiments. Another point is that similar to the $GdRh_2Si_2$ system, for $GdIr_2Si_2$ may also exist the temperature window where the surface and bulk magnetic systems experience only weak coupling to each other [35]. If this was the case, the application of a relatively small external magnetic field could help to re-orient the magnetic domains within the surface, which would simplify spectroscopic measurements aiming at the investigation of the magnetic properties of the surface and bulk system of this compound.

6. $EuIr_2Si_2$

In this chapter, our results for $EuIr_2Si_2$ are presented. Despite the non-magnetic ground state of the bulk, we discovered 2D ferromagnetism at both the Si- and Eu-terminated surfaces of this mixed-valent Eu compound. Conclusions on the presence of (nearly) divalent Eu in the surface region, and on the ordering of the respective magnetic moments at low temperatures were drawn from ARPES measurements. More precisely, we utilized well-known properties of the surface states and the Eu $4f$ final-state multiplets as they appear in PE spectra. From DFT modelling and by employing complementary experimental techniques, we were able to confirm our findings. Simultaneously, we show that the temperature dependence of the mean Eu valence is reflected in the electronic structure of the bulk. Please note, that parts of the presentation given below are taken from Ref. [123] and the corresponding supplementary information.

6.1. Introduction

Mixed valency and structural properties Among the $Ln Ir_2Si_2$ compounds which are known for their polymorphism $EuIr_2Si_2$ forms an exception because it crystallises solely in the $ThCr_2Si_2$ structure, while for the other lanthanides also the $CaBe_2Ge_2$-type exists [59, 124]. Moreover, Eu is in a valence fluctuating state and the mean valency in the bulk changes continuously over a wide temperature range. In Fig. 6.1(a) the value of the mean Eu valency is shown for different temperatures ranging from 7 K to room temperature; the dashed line connecting the data points is drawn to guide the eye. The data, which have been obtained from XAS measurements, show a strong decrease of the mean valency with increasing temperature from a value of about 2.8 at 10 K to a value of 2.35 at 300 K [125]. Thus, at low temperatures the trivalent state dominates, while at room temperature and above, $EuIr_2Si_2$ is closer to a divalent configuration. This trend is typical of valence-fluctuating Eu compounds [58] and will be further elucidated below. The change of the mean valence with temperature is reflected in an anomalously large thermal expansion of the lattice parameters a and c, which are plotted in Fig. 6.1(b) in light blue and black colours, respectively. The dashed line refers to c and is a guide to the eye. It can be seen that both lattice parameters follow the same trend and resemble the T curve of the mean valence,

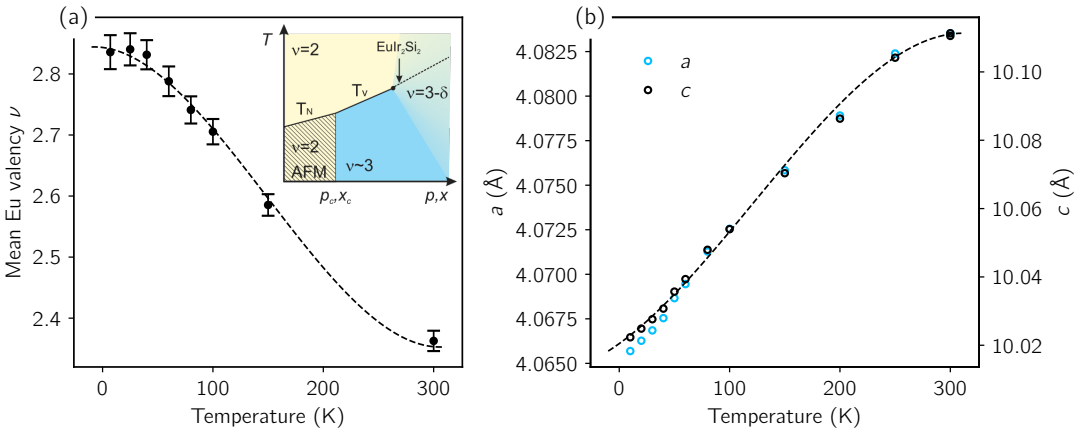

Fig. 6.1.: In (a) the temperature dependence of the mean Eu valency ν of $EuIr_2Si_2$ derived from XAS in partial fluorescence yield is shown. The phase diagram in the upper right shows which Eu valency is stabilised for different combinations of temperature T and pressure p, or concentration x of the transition metal in alloy series of the type $Eu(Rh_{1-x}Ir_x)_2Si_2$. In (b) the temperature dependence of the lattice parameters a and c is given. Dashed lines for ν and c serve as guides for the eye. The data are reproduced from Ref. [125], and the phase diagram is taken from Ref. [58].

Tab. 6.1.: Lattice parameters a and c and cell volume V for stable trivalent $EuCo_2Si_2$, stable divalent $EuRh_2Si_2$ and valence-fluctuating $EuIr_2Si_2$ at low and room temperatures from Ref. [125]. The values of a and c are rounded to the third digit.

Compound	$EuCo_2Si_2$ (Eu^{3+})		$EuRh_2Si_2$ (Eu^{2+})		$EuIr_2Si_2$ ($Eu^{(3-\delta)+}$)	
T	300 K	30 K	300 K	10 K	300 K	10 K
a (Å)	3.922	3.913	4.091	4.083	4.084	4.066
c (Å)	9.836	9.825	10.225	10.192	10.111	10.022
V (Å^3)	151.305	150.410	171.111	169.951	168.596	165.668

too. The increase of the lattice parameters a and c with increasing temperature is in accordance with the smaller and larger ionic radii of the trivalent and divalent Eu ions, respectively. In Ref. [125] the T dependence of the structural properties of $EuIr_2Si_2$ has been investigated and compared to that of the isostructural, isoelectronic and integer-valent sister compounds $EuCo_2Si_2$ and $EuRh_2Si_2$ that serve as trivalent and divalent reference systems for valence-fluctuating $EuIr_2Si_2$, respectively. In accordance with the larger and smaller ionic radii of Eu^{2+} and Eu^{3+}, respectively, the lattice constants a and c are largest in $EuRh_2Si_2$ and smallest in $EuCo_2Si_2$, while for $EuIr_2Si_2$ they take intermediate values that approach those of $EuRh_2Si_2$ with increasing and those of $EuCo_2Si_2$ with decreasing temperatures, see Tab. 6.1. That the thermal expansion of the lattice parameters in $EuIr_2Si_2$ with increasing temperature is anomalous, i.e. related to the decreasing mean valence, can be seen in Fig. 6.2(a), where the relative change of the lattice parameters of $EuIr_2Si_2$ is compared to that of the integral-valent reference compounds. While the relative change of $\Delta a/a$ and $\Delta c/c$ is similarly small

for the integer-valent materials, it is much larger in $EuIr_2Si_2$. Further, it can be seen that the thermal expansion of $EuIr_2Si_2$ is larger along c than in the basal plane. Together with the findings for other structural parameters in Ref. [125] that are not discussed here, it was concluded that the extra conduction electron for Eu^{3+} makes $EuIr_2Si_2$ a more three-dimensional material than $EuRh_2Si_2$, leading to a worse cleaving behaviour of the former. Note, that the results in Ref. [125] are consistent with earlier studies performed on polycrystalline samples of $EuIr_2Si_2$ in which the T dependence of the mean valence has been determined from the isomer shift and susceptibility using Mössbauer spectroscopy and magnetisation measurements, respectively [59, 124].

Magnetic, thermal and transport properties [125] $EuIr_2Si_2$ has a non-magnetic ground state. In a magnetic field, however, it exhibits a finite magnetic susceptibility which is in particular at low temperatures larger than expected for a metallic system. The temperature dependence of the susceptibility χ of $EuIr_2Si_2$ has been determined for a magnetic field H applied parallel and perpendicular to the tetragonal c axis. The results published in Ref. [125] are reproduced in Fig. 6.2(d), where open (closed) purple markers correspond to $H \perp c$ ($H \parallel c$). In both cases a broad maximum centred around 75 K is observed and a small anisotropy with $\chi_{H\perp c} > \chi_{H\parallel c}$ that decreases with increasing temperature, which has been related to the CEF splitting of excited J states of the Eu^{3+} multiplet. Moreover, the susceptibility χ_{poly} that corresponds to a polycrystalline sample is plotted in green. To obtain a good fit of the latter, both a trivalent Van-Vleck and a divalent Curie-Weiss contribution to the susceptibility had to be considered in terms of their valency-weighted average. The fit is shown as a black line.

The valence fluctuations are reflected consistently with the susceptibility data in the thermal and transport properties of $EuIr_2Si_2$, Fig. 6.2(c) and (e), respectively. While the specific heat is almost the same for $EuRh_2Si_2$ (green triangles) and $EuCo_2Si_2$ (grey squares), it is notably larger for $EuIr_2Si_2$ (open circles) in the temperature range where the mean valence changes continuously. As for the susceptibility, the excess heat (filled circles) with respect to the reference compounds has a broad maximum at a temperature of about 75 K, too. The resistivity of $EuIr_2Si_2$, shown by purple circles in Fig. 6.2(e), increases by two orders of magnitude over a wide temperature range reaching a maximum for $T \approx 160$ K, from which it slowly falls off to a constant value that is still quite high. The first derivative of the resistivity is plotted as a purple line and shows a pronounced maximum at about 75 K, which coincides with that of excess specific heat and susceptibility. In $EuRh_2Si_2$ and $EuCo_2Si_2$, in contrast, the resistivity is comparably small and increases only slightly with T. Note, that the low-temperature data ($T < 20$ K) of $EuIr_2Si_2$ for specific heat, resistivity and susceptibility show a Fermi-liquid behaviour with a moderate renormalisation of the electron mass.

Phase diagram A typical experiment to study the evolution of mixed valency in EuT_2Si_2 and similar compounds, is to consider an isoelectronic sister compound with integer valency and to successively replace the transition metal element. For valence-fluctuating $EuIr_2Si_2$ isoelectronic and isostructural $EuRh_2Si_2$ and $EuCo_2Si_2$ serve as di-

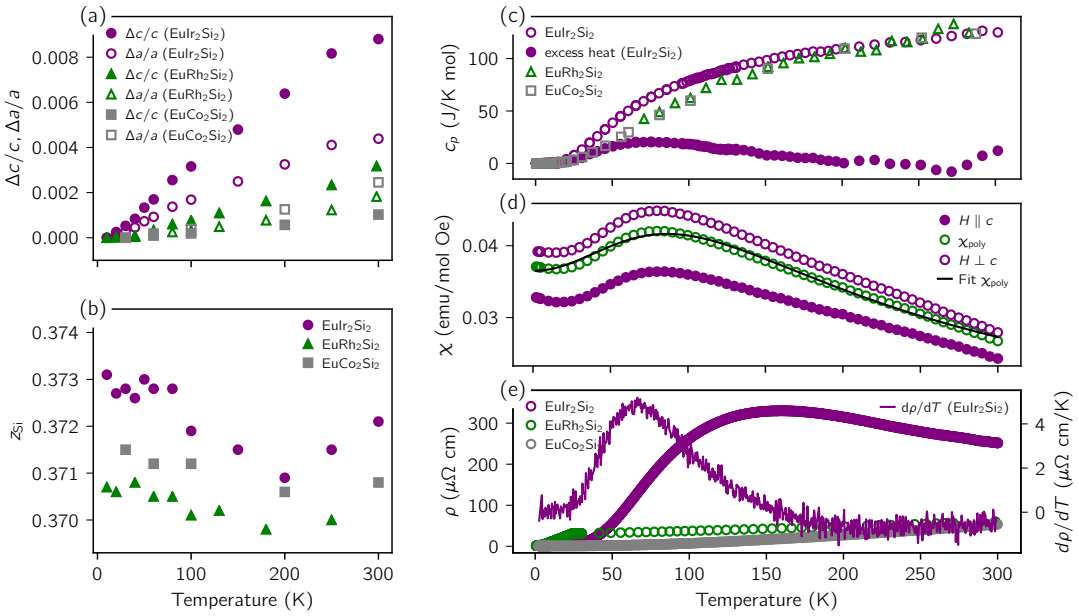

Fig. 6.2.: Structural, thermal, magnetic and electric properties of $EuIr_2Si_2$ and the di- and trivalent reference compounds $EuRh_2Si_2$ and $EuCo_2Si_2$ plotted in purple, green and grey, respectively. (a) Relative change $\Delta a/a$, $\Delta c/c$ of lattice parameters a and c with temperature; (b) z value of the Si atom in the I4/mmm unit cell; (c) Specific heat c_p and excess specific heat for $EuIr_2Si_2$; (d) Magnetic susceptibility χ in a field of 5 T applied parallel and perpendicular to the tetragonal c axis together with the polycrystalline susceptibility and the fit result for the latter; (e) Resistivity (left y axis). For $EuIr_2Si_2$ the first derivative of the resistivity is shown, too (right y axis). The symbols are explained in the legend. Data from Ref. [125] provided by S. Seiro.

valent and trivalent reference compounds. In Ref. [67] the alloy series $Eu(Rh_{1-x}Ir_x)Si_2$ has been investigated with resistivity, susceptibility and specific heat measurements from which the phase diagram has been constructed for the relation between temperature T and Ir content x, see Fig. 6.3, which shows the same qualitative behaviour as the generic phase diagram of Eu compounds that is shown as inset in Fig. 6.1. For $x \leq 0.25$ Eu is stable divalent and orders antiferromagnetically below 25 K. For $x \geq 0.3$ Eu has a mean valence of 2.8 close to a trivalent state, that can be tuned through a first-order phase transition into the divalent configuration by increasing the temperature above the critical value T_v of 30 K for $x = 0.3$ and 80 K for $x = 0.5$. The valence transition temperature T_v thus increases steeply with increasing Ir content. The crossover behaviour that is characterised by the continuous decrease of the mean valence with increasing temperature as it is observed in $EuIr_2Si_2$, is established for Ir concentrations greater than 0.75. Apparently, successive replacement of Rh by Ir enhances the hybridisation between $4f$ and conduction electrons characteristic of the trivalent valence state. Because of the similar metallic radii of Rh and Ir which differ by only 1 %, chemical pressure has been ruled out to cause the increase in hybridisation. Instead, a change in chemical bonding because of the different binding energies of the Rh $4d$ and Ir $5d$ states seems to be the reason for the different behaviour of europium

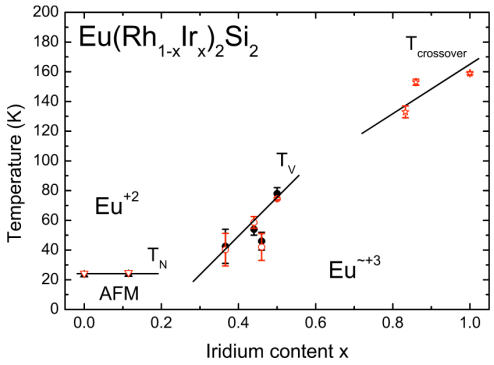

Fig. 6.3.: Phase diagram of $Eu(Rh_{1-x}Ir_x)Si_2$. Red and black data points were obtained from resistivity and susceptibility, respectively. For $0.3 \leq x \leq 0.6$ the average for heating and cooling is taken. Figure from Ref. [67].

in $EuRh_2Si_2$ and $EuIr_2Si_2$. In $EuIr_2Si_2$ the Eu $5d$ and the Ir valence states have higher binding energies than the corresponding Rh $4d$ states and hence, promotion of an electron from the $4f$ shell into an Eu $5d$ valence state becomes energetically favourable.

Comparison to isostructural Ce and Yb compounds Mixed-valent properties are also known for the isostructural Rh and Ir disilicides with Ce and Yb. In these compounds, the mean valency is in general close to a trivalent configuration and decreases in comparison to $EuIr_2Si_2$ only weakly with increasing temperature. In the mostly trivalent Ce compounds the $4f^0$ and $4f^2$ states are located 1.7 eV and more than 3 eV above the trivalent $4f^1$ state [126], respectively, and hence, the deviation from unity in the occupancy of the $4f$ shell in the ground state is apparently the result of strong hybridisation. In this case, the influence of thermal fluctuations which are in the order of several tenths of meV can be neglected. In PE on $YbRh_2Si_2$ and $YbIr_2Si_2$ the excited $4f^{13}$ final-state multiplet lies slightly below the Fermi energy [127]. In this case, thermal excitations should be considered. Similar to $EuIr_2Si_2$ the mean Yb valency takes a value of 2.9 at low temperatures but with increasing temperature it decreases only slightly, whereas in $EuIr_2Si_2$ the mean Eu valency reaches a value of 2.3 at room temperature. The strong change of the mean valency in $EuIr_2Si_2$ from 2.8 at low temperatures to 2.3 at room temperature cannot be explained within a rigorous two-level picture in which the trivalent $4f^6(5d6s)^3$ and the divalent $4f^7(5d6s)^2$ states are separated by a fixed energy with the former state having slightly lower energy. In such a model the $4f$ occupancy would be close to 6 at low temperatures, at high temperatures, however, the two levels would be equally populated giving a valency of 2.5. The atomic volume of Eu is notably larger for the divalent configuration of the $4f$ shell than for a trivalent state. With increasing internal pressure due to thermal contraction when the temperature is lowered, the trivalent configuration becomes thus energetically more favourable. Indeed it was shown for divalent $EuRh_2Si_2$ that application of an external static pressure of 0.96 GPa leads to a transition from a purely divalent Eu to a mixed-valent state, while for a pressure larger than 2 GPa Eu becomes trivalent [128]. If we now consider the effect of increasing temperature to be equivalent

to a lowering of pressure, then for a system that is trivalent at $T = 0\,\mathrm{K}$ the divalent state should become more favourable with increasing temperature, i.e. it should be increasingly lowered in energy with respect to the trivalent state. Then, at a certain temperature, the di- and trivalent levels should be crossing and for further increasing temperature the divalent configuration should stay somewhere below the trivalent, which would correspond to an abrupt change of the ground state from trivalent to divalent. Since the two states are nearly degenerate in energy a configurational mixing is to be expected and level crossing will be replaced by the formation of mixed states, thus preventing an abrupt valence transition. Such a configurational mixing can be described within the framework of a Landau-Zener model by the mixing matrix

$$\begin{pmatrix} 0 & \Delta \\ \Delta & \varepsilon(T) \end{pmatrix} \tag{6.1}$$

where the unhybridised $4f^6$ and $4f^7$ states are expressed as unit vectors along the x and y directions, respectively. 0 and $\varepsilon(T)$, where T is the temperature, correspond to their energy positions and Δ is the hybridisation parameter describing possible hopping processes between the two states. Such an ansatz is indeed used in the simplest form of the Anderson model for the modelling of PE spectra, where, however, the $4f^5$ state must be considered, too [127, 129]. After diagonalisation of the matrix in Eqn. 6.1, the calculated eigenvectors can be used to model a continuous transition from the trivalent to the divalent configuration, where the mean $4f$ occupancy can be additionally modified by thermal excitation of the hybrid states. In principle, the function $\varepsilon(T)$ could be estimated from compression data considering the work function, which results from the multiplication of the volume change ΔV with the applied pressure, as the upper boundary for ε. Unfortunately, corresponding data are not available. From the pressure difference of 1 GPa in the valence transition in $EuRh_2Si_2$ from 2+ to 3+, however, the total variation of ε can be estimated to be 96 meV, if ΔV is interpolated from the lattice parameters of divalent $EuRh_2Si_2$ and trivalent $GdRh_2Si_2$. Using the lattice parameters of Eu and Gd metal instead of those of the ternary compounds, the resulting value for ε is 57 meV, which is in the order of magnitude of the thermal energy scale with $k_\mathrm{B}T = 26\,\mathrm{meV}$. The latter might be the more realistic estimation since the compressibilities of Rh and Si do not have to be considered. The same scenario can, in principle, also be applied to the Yb compounds. However, here it must be taken into account that the volume difference between di- and trivalent Yb is due to the lanthanide contraction with 9.5 Å much smaller than in Eu (11.8 Å). At the same time, $\varepsilon(0)$ must be assumed to be higher than in Eu, which immediately follows from the larger measured mean valence of 2.9 compared to 2.8 at low temperatures. As a consequence, the formal level crossing is either not reached at all, or just at higher temperatures, which would give at least a qualitative explanation of the smaller temperature dependence of the mean valency observed experimentally.

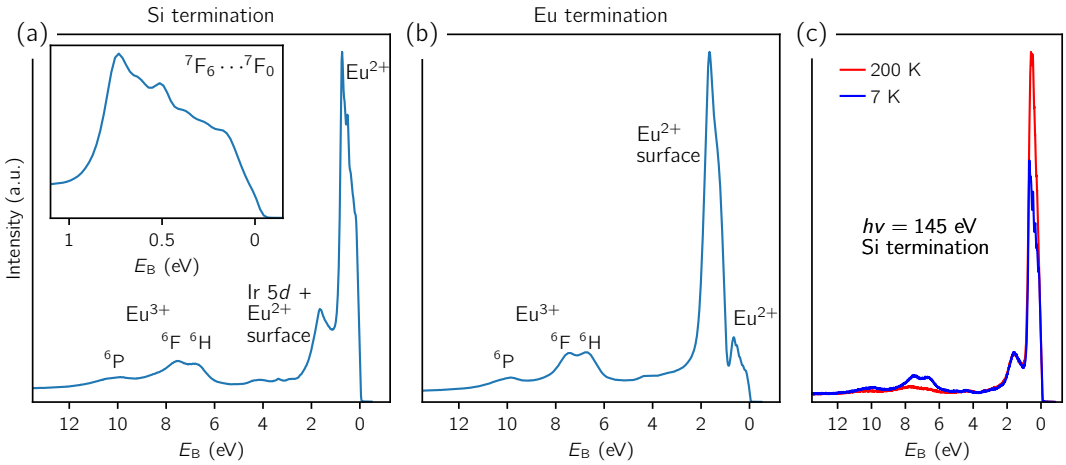

Fig. 6.4.: Angle-integrated ARPES spectra showing the Eu $4f$ emission for $EuIr_2Si_2$ in the case of (a) Si termination ($T \approx 7\,K$) and (b) Eu termination ($T \approx 5\,K$) for $h\nu = 146\,eV$. In the inset in (a) the Eu^{2+} multiplet is shown. In (c) spectra acquired from a Si-terminated surface with $h\nu = 145\,eV$ at 200 K and 7 K are shown in red and blue, respectively. Note that the spectra in (a, b) and (c) were taken from different samples at different facilities.

6.2. Results and discussion

6.2.1. Photoemission from the Eu 4*f* shell

Fig. 6.4 shows angle-integrated RPES spectra that were acquired from (a) the Si-terminated and (b) the Eu-terminated surfaces of $EuIr_2Si_2$ at low temperatures below 8 K. The photon energy $h\nu = 146\,eV$ is close to the maximum of the $4d \rightarrow 4f$ Beutler-Fano resonance of Eu^{3+} that is reached at 145 eV. The Eu^{2+} emission reaches its resonance maximum at the slightly lower excitation energy of 141 eV, however, since the Eu^{2+} resonance is quite broad the divalent emission is still resonantly enhanced for 146-eV photons. The spectra reveal the multiplet structure associated with both the $4f^5$ and $4f^6$ final states of europium, which are seen respectively at binding energies between 6 eV and 11 eV, and in the vicinity of the Fermi level. They are separated by the Coulomb repulsion energy U of approximately 6 eV. In the inset, a magnification of the much narrower Eu^{2+} multiplet is given. The ^6P, ^6F, ^6H final-states of Eu^{3+} as well as the seven $^7F_{J'}$ lines forming the Eu^{2+} multiplet with $J' = \{0, ..., 6\}$ are well resolved in the experiment. The presence of both the Eu^{2+} and Eu^{3+} multiplets in the same PE spectrum and the localisation of the Eu^{2+} multiplet close to E_F reflect the valence fluctuating properties of $EuIr_2Si_2$. Note, that the $4f^6$ final state of Eu^{2+} coincides with the initial state of Eu^{3+}. That it lies close to the Fermi level ($E_B = 0$) shows that the Eu^{2+} and Eu^{3+} initial states are nearly degenerate, which is a prerequisite for valence fluctuations. The spectrum of the Eu-terminated surface, Fig. 6.4(b), is dominated by the intense surface-core-level shifted multiplet of the Eu surface layer that is seen at a binding energy of approximately 1 eV and gives clear evidence of the purely divalent configuration of Eu in the surface layer. While in the bulk the gain in cohesive energy and the $4f \rightarrow 5d$ excitation energy are approximately

of the same size, which leads to the valence instability, the lack of binding partners at the surface stabilises the divalent configuration, which is manifested in the shift of the Eu^{2+} surface multiplet toward higher binding energy. The extremely high intensity of the surface multiplet in comparison to its bulk counterpart reflects the surface sensitivity of PE. For the given photon energy of 146 eV the inelastic mean free path λ can be estimated from the universal curve to be in the order of 6 to 10 Å, i.e up to one unit cell in c direction. Since the PE intensity can be assumed to decrease exponentially with $e^{-x/\lambda}$, where x is the distance from the surface, the bulk-like $4f$ signal is dominated by emissions from the first subsurface Eu layer. Comparison of the bulk-like $4f$ signals in (a) and (b) reveals a large difference in the intensity ratio of the Eu^{2+} and Eu^{3+} contributions. While for Si termination the Eu^{2+} multiplet strongly exceeds the trivalent signal, in the spectrum acquired from the Eu-terminated surface the Eu^{3+} multiplet is more intense than the Eu^{2+} signal from bulk-like layers. Since the $4f$ PE intensity can be assumed to be proportional to the concentration of divalent and trivalent ions on the one hand, and considering the strong surface sensitivity, on the other hand, the differences in the spectra of the two surface terminations suggest a deviation from the mean valency in the subsurface Eu layers from the literature value for the bulk, which is 2.8 at the given temperature. In particular, the huge Eu^{2+} signal for Si termination could hint at a divalent Eu state in the corresponding first subsurface layer. To get a feeling for the behaviour of the valency in the subsurface, we assume for simplicity that the bulk-like PE signal originates solely from the subsurface layer. To obtain the corresponding Eu valence, we determine the intensities I^{2+} and I^{3+} which are given by integration of the Eu^{2+} and Eu^{3+} multiplets after subtraction of a linear background, using the same energy intervals for the Si- and Eu-terminated surfaces. Using the expression

$$\nu_{\mathrm{Eu}} = 3 - \frac{I^{2+}}{I^{2+} + I^{3+}}, \tag{6.2}$$

gives the values 2.34 and 2.76 for the mean valency in the case of Si and Eu termination, respectively. Apparently, for Si termination the value is much smaller, while for the Eu-terminated surface it is close to the literature value of 2.8. Of course, this is an extremely crude approximation for several reasons. First of all, despite the small mean free path, the contribution of the deeper-lying Eu layers should be taken into account, too. Secondly, the actual value of the inelastic mean free path is not known. Thirdly, we do not have any knowledge of the PE cross sections in the resonant regime. A better estimation could be gained, if at least the second subsurface layer would be taken into account, too, and if the spectra are fitted using for example the model of Gerken [68]. However, since we are going to determine the valency in the first and second subsurface layers by combining PED with photon-energy-dependent PES, we refrain from a more elaborate analysis at this point.

Now let us have a look at how the $4f$ emission from the Si-terminated surface changes with temperature. In Fig. 6.4(c) respective spectra are shown in blue and red colours that were taken at 7 K and 200 K, respectively, with $h\nu = 145$ eV. Between 7 K and 200 K, the mean valency of the bulk decreases from 2.8 to 2.5, i.e. the system becomes more divalent, which is reflected in an increase of the anyway large Eu^{2+} signal between 7 K and 200 K, and a simultaneous decrease in the PE intensity of

Eu^{3+}. Although the data have been acquired in the maximum of the Eu^{3+} Beutler-Fano resonance, the trivalent contribution is almost completely outshone by the Eu^{2+} emission, particularly at higher temperatures. Similar observations of an unexpectedly large Eu^{2+} emission in mixed-valent Eu systems have been reported in the literature for $EuPd_2Si_2$ [130, 57] and $EuNi_2(Si_{0.25}Ge_{0.75})_2$ [131], where the existence of a divalent subsurface layer has been considered possible, too. Note, that a divalent character of the subsurface layer bares the possibility of magnetic properties because the Eu^{2+} state is associated with a large, spin-only magnetic moment. Moreover, we observed a qualitative change in the shape of the Eu^{2+} multiplet between high and low T. This, in combination with the huge divalent signal, gives strong evidence for a magnetically active subsurface layer. In our previous works on magnetic LnT_2Si_2 compounds like $EuRh_2Si_2$, $GdRh_2Si_2$ and $HoRh_2Si_2$ we showed that the magnetic properties of the subsurface Ln layer can be tested straightforwardly by exploiting the exchange coupling of surface state electrons to ordered lanthanide moments in the subsurface layer, see section 2.2. In that sense, magnetic ordering of the $4f$ moments in the subsurface Eu layer in $EuIr_2Si_2$, should be reflected in a large exchange splitting of the surface-state bands at low temperatures. A respective study is presented in the next section.

6.2.2. ARPES on the Si-terminated surface

In Fig. 6.5(a) ARPES-derived Fermi maps taken from the Si-terminated surface of $EuIr_2Si_2$ at $T = 7\,\mathrm{K}$ (upper right) and $T = 200\,\mathrm{K}$ (lower right) are shown with the four-cornered Fermi contour formed by the surface state α dispersing around the $\overline{\mathrm{M}}$ point of the SBZ. α's Fermi contours look very differently in the low- and high-temperature Fermi maps. The star-shaped CECs which show a fourfold rotational symmetry at 200 K, are strongly distorted at 7 K. In (b) corresponding $E(k_{\|})$ cuts along $\overline{\mathrm{X}}$–$\overline{\mathrm{M}}$–$\overline{\mathrm{X}}$ are shown. With the emerging asymmetry, the mutually perpendicular $\overline{\mathrm{X}}$–$\overline{\mathrm{M}}$–$\overline{\mathrm{X}}$ paths must be considered separately in the low-temperature phase. The inset in the lower right relates the given cut to the Fermi contours. In the upper map acquired at 200 K, both directions are equivalent, the dispersion is symmetric. At 7 K the horizontal cut through the Fermi contour is symmetric and the band splitting is notably enhanced in comparison to the previous cut. Along the vertical path shown in the lower panel, the band dispersion is strongly asymmetric. According to our preceding discussion, this modification is likely due to an exchange coupling of the itinerant electrons to magnetically ordered $4f$ moments in the subsurface. To test this, we modelled the ARPES data within a DFT slab calculation using the open core approximation which allows us to fix the occupancy of the Eu shell to the desired value. For Eu in the subsurface, we assumed a divalent configuration with a half-filled $4f$ shell, once unpolarised to describe the spectrum measured at 200 K, and with a ferromagnetic alignment of the $4f$s along the $[\bar{1}00]$ direction to account for the low-temperature data. For the other, bulk-like Eu layers of the slab as well as in our modelling of the bulk bands in separate calculations, the occupancy was chosen by the literature values for the mean valency given in Fig. 6.1(a). The computed Fermi contours of α are plotted in correspondence to the ARPES data on the left in Fig. 6.5(a). Note, that for the slab-derived band structure only the Fermi contours of the surface state α are shown,

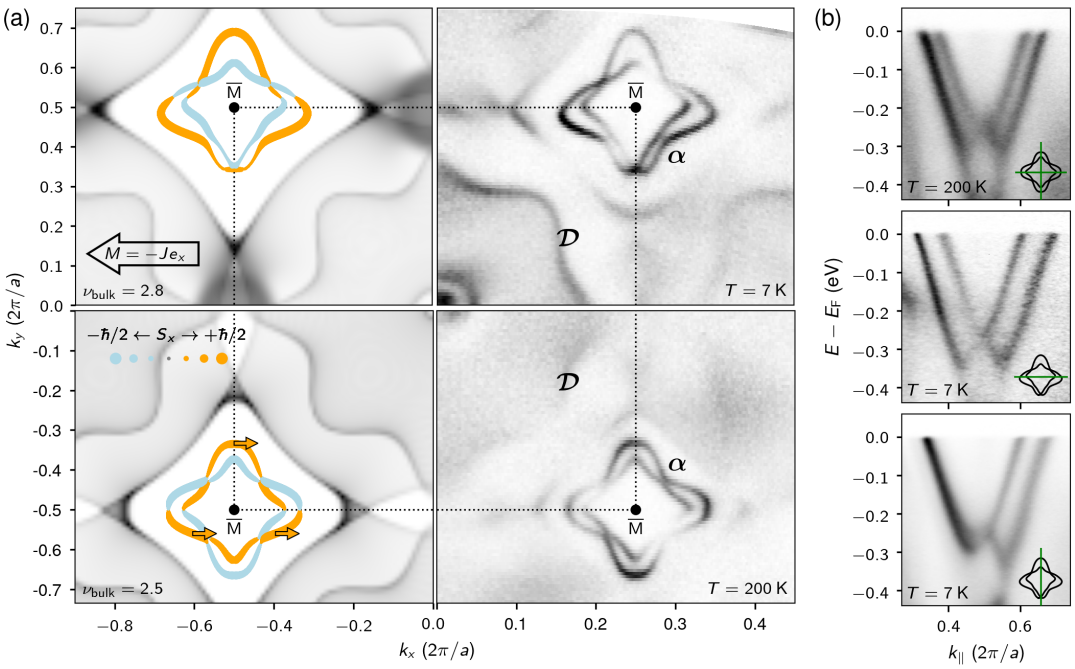

Fig. 6.5.: Surface electronic structure of the Si-terminated $EuIr_2Si_2$ surface for 7 K ($\nu_{\mathrm{bulk}} = 2.8$) and 200 K ($\nu_{\mathrm{bulk}} = 2.5$). (a) DFT- and ARPES-derived Fermi maps. In the calculated spectra, surface-projected bulk bands are shown as grey shading. From the slab band structure accounting for the surface, only the Fermi contours of the surface state α are shown for which the expectation value of the spin x component is plotted in orange and light blue for $S_x > 0$ and $S_x < 0$, respectively. The line width is proportional to the absolute value of S_x. Orange arrows mark the three points on the outer Fermi contour where the $S_x = \hbar/2$. (b) $E(k_{\|})$ cuts measured with ARPES along $\overline{\mathrm{X}}$–$\overline{\mathrm{M}}$–$\overline{\mathrm{X}}$. The green line in the inset shows the relation of a given $\overline{\mathrm{X}}$–$\overline{\mathrm{M}}$–$\overline{\mathrm{X}}$ path to the Fermi contours. All ARPES data have been acquired with $h\nu = 55$ eV.

while all other slab bands have been dropped. Orange and light blue colours represent the expectation value for the x component of the spin with $S_x > 0$ and $S_x < 0$, respectively, while the line width corresponds to the absolute value. The projection of calculated bulk bands along k_z is plotted in grey. Comparison of the DFT results for α with the measured bands reveals a stunning agreement. The high-temperature Fermi contours are perfectly reproduced by the DFT calculation for an unpolarised $4f$ shell, while the assumption of ferromagnetically ordered $4f$ moments in the subsurface layer ideally reproduces the asymmetric dispersion seen in the ARPES spectrum. We thus conclude that the subsurface Eu layer of mixed-valent Eu behaves indeed divalently with the associated moments ordering at low temperatures ferromagnetically along the $[\bar{1}00]$ direction.

In the non-magnetic calculation, S_x shows a smooth change between orange and blue segments on the CECs that is characteristic of the triple-winding spin structure, where due to the smooth rotation of the spin in the surface plane the sign of S_x changes six times on a closed loop along the CEC, resulting in three orange- and three blue-coloured segments on the CECs. In the magnetic phase the calculated

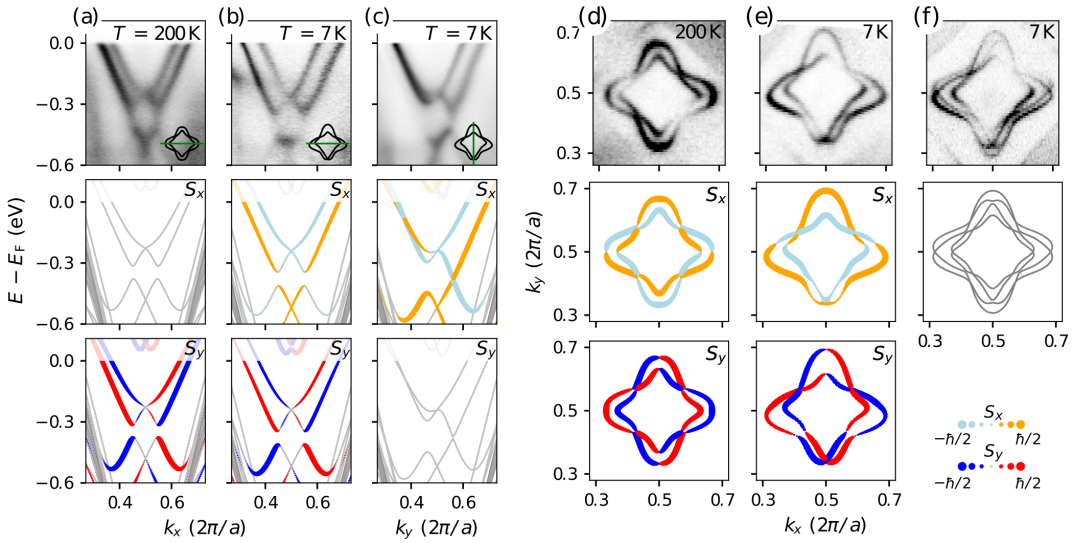

Fig. 6.6.: Electronic and spin structure of the Si-terminated surface of $EuIr_2Si_2$ measured with ARPES ($h\nu = 55\,\mathrm{eV}$) and modelled using DFT. (a) - (c) Band maps along $\overline{\mathrm{X}}$–$\overline{\mathrm{M}}$–$\overline{\mathrm{X}}$ taken for (a) $T = 200\,\mathrm{K}$ and (b+c) $T = 7\,\mathrm{K}$. In the ARPES data the given $\overline{\mathrm{X}}$–$\overline{\mathrm{M}}$–$\overline{\mathrm{X}}$ paths are indicated by a green bar in the calculated Fermi contours of the α state. (d) - (f) Fermi maps showing the surface state α for (d) $T = 200\,\mathrm{K}$ and (e+f) $T = 7\,\mathrm{K}$. The computational setup comprises an asymmetric slab of 32 atomic layers. Surface relaxation is taken into account for the topmost four layers of each side of the slab. In the first layer of the Eu-terminated and the fourth layer below the Si-terminated side of the slab, the configuration of the Eu $4f$ shell is chosen $4f^7$ (divalent). In the low T phase these $4f$ shells are spin polarised, and the resulting magnetisation is along the $[\bar{1}00]$ direction. All other Eu layers are treated as bulk, i.e. the occupancy of the $4f$ shell is fixed to 6.5 and 6.2 to account for the bulk valency in the high and low T phase, respectively. The expectation values of the spin components S_x and S_y are plotted in light blue/orange or blue/red, respectively. Slab bands are shown in grey, and projected bulk bands as a grey shading.

spin structure changes notably with the outer Fermi contour becoming orange almost everywhere, and only two small, blue segments are retained, i.e. on a closed loop, S_x changes sign only four times indicating a breakdown of the triple winding in the magnetic phase. For completeness, the entire spin structure for both $\overline{\mathrm{X}}$–$\overline{\mathrm{M}}$–$\overline{\mathrm{X}}$ cuts and along the CECs is given in Fig. 6.6.

The surface-projected bulk bands are well reproduced by DFT, too. To model the bulk, the Eu valency has been fixed within the open-core approach to the literature values published in Ref. [125] in accordance with the measurement temperatures. Both in the ARPES and the DFT data the Doughnut Fermi surface sheet labelled $\mathcal{D}$ can be clearly distinguished and shows a different size at 7 K and 200 K. At 200 K the Doughnut is notably larger than at 7 K. At the same time, the band gap to which the α state is confined is large at 200 K and small at 7 K. In the calculation this behaviour is reproduced, only the size of the gap is overestimated in our DFT modelling. For a detailed discussion of the Doughnut, see the last section of this chapter.

According to our previous discussion, the enhanced band splitting and the evolving asymmetry in the dispersion of the bands formed by the surface state α are clear

proof of the existence of magnetically ordered $4f$ moments in the subsurface Eu layer. While the large splitting at 200 K is due to the cubic Rashba effect, an anisotropic exchange interaction of the 2D surface states with the ordered $4f$ moments leads to the strongly $\boldsymbol{k}_{\parallel}$ dependent changes in the dispersion of the surface state bands. DFT band structure calculations in which we assume that the $4f$ moments are ferromagnetically ordered along the $[\bar{1}00]$ direction almost perfectly reproduce the spectral patterns that we observed in ARPES. The experimental and computational results show the generic properties of the surface state α in LnT_2Si_2 compounds with $T = \{\mathrm{Co}, \mathrm{Rh}, \mathrm{Ir}\}$. Since the spin structure and its modifications in the magnetic phase have been discussed in great detail in the previous chapter on $GdIr_2Si_2$ we will not repeat it here and leave it at showing the computational results for $EuIr_2Si_2$ for completeness in Fig. 6.6. Instead, we restrict the discussion to pointing out the main differences between the Gd and the Eu systems.

Comparison to $GdIr_2Si_2$ Our results for the surface state α located in the surface four-layer block of the Si-terminated surface of $EuIr_2Si_2$ are consistent with our findings for the corresponding state in $GdIr_2Si_2$. In the comparison of the bands formed by the α state in $GdIr_2Si_2$ and $EuIr_2Si_2$, we find that the Fermi level experiences a downward shift in $EuIr_2Si_2$ in comparison to the Gd compound. This is a band-filling effect: trivalent Gd with its $[\mathrm{Xe}]4f^7(5d6s)^3$ configuration has one more valence electron than the almost divalent Eu in the subsurface. For $GdIr_2Si_2$ we established [110] as the magnetisation axis, whereas our DFT calculations prove that in $EuIr_2Si_2$ the Eu moments are oriented along [100] and therefore the spin structure and dispersion are slightly different in the magnetically ordered phases. Despite our similar findings for the electronic and magnetic structure of the Si-terminated surface of $GdIr_2Si_2$ and $EuIr_2Si_2$, we must keep in mind that we are dealing with two compounds of fundamentally different bulk properties. $GdIr_2Si_2$ is a bulk antiferromagnet, whereas the fluctuating Eu valence leads to a non-magnetic ground state in the bulk of $EuIr_2Si_2$. With the divalent and magnetically active behaviour of Eu in the subsurface layer and the simultaneously non-magnetic bulk, we discovered quasi-2D magnetism in the Si-Ir-Si-Eu surface block, which is, in difference to $GdIr_2Si_2$, completely decoupled from the bulk. This could also explain, why we can observe single magnetic domains in ARPES in the low-temperature phase for α in $EuIr_2Si_2$ but not in $GdIr_2Si_2$, where steps *and* magnetic domains essentially enhance the probability for the observation of multiple domains, see the discussion in on page 91. Note, that we probed multiple magnetic domains for $EuIr_2Si_2$, too, see Fig. 6.6(f). Interestingly, for both $GdIr_2Si_2$ and $EuIr_2Si_2$ we observed only domains with antiparallel magnetisation. Since the [100] and [010] crystallographic directions are equivalent in the basal plane of the tetragonal lattice, one could expect to see signatures of domains with mutually perpendicular magnetisation, which, however, has not been the case. In $EuIr_2Si_2$ the magnetisation in the subsurface Eu layer, being magnetically decoupled from the bulk, can be easily controlled with an external magnetic field, whereas in $GdIr_2Si_2$ the strong and three-dimensional AFM coupling of the Gd moments in the subsurface to those in the bulk, will require extremely large fields to break up or change the magnetisation. Moreover, as it is demonstrated in Ref. [132], for a single magnetic domain the spin structure of

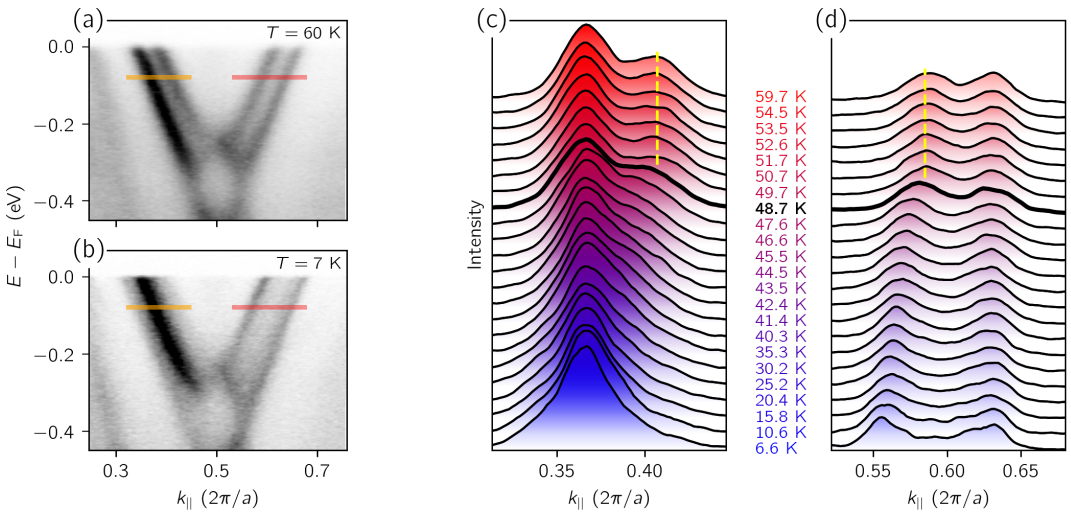

Fig. 6.7.: T dependence of the surface state α and estimation of the surface Curie temperature. Band maps along $\overline{\text{X}}$–$\overline{\text{M}}$–$\overline{\text{X}}$ taken (a) above and (b) below T_C. The yellow and orange bars indicate the region for which the T dependence is shown in (c) and (d), separately for the left and right branches of the band, respectively. For better comparability, the MDCs are shifted in $k_{||}$ such, that the left peak in (c) and the right peak in (d) align for all T with the one measured at 59.7 K. The yellow dashed lines serve as guides to the eye marking the spectra with identical peak separation.

the surface state can be derived from the dispersion of the surface state bands in the PM and magnetic phases measured with ARPES.

Surface Curie temperature To determine the ferromagnetic ordering temperature T_C of the Eu $4f$ moments in the subsurface of Si-terminated $EuIr_2Si_2$ we traced the evolution of the surface state dispersion along the high-symmetry direction $\overline{\text{X}}$–$\overline{\text{M}}$–$\overline{\text{X}}$ with temperature. For our experiment, we chose the $\overline{\text{X}}$–$\overline{\text{M}}$–$\overline{\text{X}}$ path along which the pronounced asymmetry is observed in the band dispersion, starting at the lowest available temperature $T = 7\,\text{K}$ and then slowly heating the sample. The results are shown in Fig. 6.6, where (a) and (b) show band maps measured above (60 K) and below (7 K) the magnetic transition, respectively, while in (c) and (d) the MDCs (MDCs) for the measured temperature series are shown for the left and right branches, respectively. Note, that each MDC has been integrated over a small energy window between $-0.085\,\text{eV}$ and $-0.075\,\text{eV}$ as it is indicated by yellow and red bars in the band maps in (a) and (b). To optimally visualize the onset of the splitting, the MDCs were slightly shifted in $k_{||}$, such that in (c) the left peak always aligns with the one measured at the highest temperature $T = 59.7\,\text{K}$, while in (d) the spectra were aligned in the same way but referenced to the right peak. In (c) the MDC measured at the lowest T and plotted in blue forms a single peak. With the increasing temperature, a shoulder starts to evolve on its right side which moves rightwards until a double peak structure establishes around 50 K. For the MDCs representing the right branch shown in (d), we see two peaks for all T, which are strongly separated at 7 K and approach each other with increasing temperature. In accordance with our findings

in (c), the distance between the two peaks takes a constant value close to $T = 50\,\mathrm{K}$. From our analysis, we estimate the surface Curie temperature T_C to be about 49 K, the spectrum for which we see the onset of the transition is highlighted.

6.2.3. X-ray magnetic linear and circular dichroism

To settle any doubts about the divalent and magnetically active properties of Eu in the near-surface region, we employed complementary experimental techniques, namely magnetic linear and circular dichroism in XAS and PE, which exploit the dependence of the photoexcitation cross sections on the polarisation of the incident light. The magnetic dichroism experiments based on XAS have been performed and evaluated by Kurt Kummer at the ESRF, while Dmitry Usachov evaluated and modelled the data presented below for magnetic dichroism in PE.

Magnetic dichroism in XAS To prove experimentally that Eu $4f$ moments in the first subsurface layer order ferromagnetically at low temperatures, and to verify that this leads to the asymmetric dispersion of the surface state bands and the increased splitting due to exchange coupling of the surface state electrons to the magnetically ordered Eu $4f$ moments, we performed soft XAS measurements. In particular, we measured the magnetic circular and linear dichroism at the Eu $M_{4,5}$ edges using total electron yield detection which contains a sizeable contribution of the first Eu layer [133, 127, 134]. The x-ray absorption measurements were done at the ESRF beamline ID32 using the high-field magnet end station [135, 107]. The samples were cleaved inside the high-field magnet at low temperature and a base pressure better than $1x10^{-10}$ mbar. Measurements were done in normal incidence with the c axis parallel to the incoming beam and at gracing incidence with an angle of 70° between the c axis and the incoming beam. The a axis was oriented to be in the horizontal plane, i.e. parallel to the $\boldsymbol{E}$ vector of the x-rays for linear horizontally polarised light and normal incidence geometry. The light polarisation is always close to 100 % for both linear and circular polarisation. Bulk magnetisation measurements were performed at $T = 5\,\mathrm{K}$ in fields up to 7 T using a SQUID-VSM (MPMS3, Quantum Design).

For the XMCD measurements a magnetic field was applied along the beam direction $\hat{\boldsymbol{u}}_{\boldsymbol{k}}$, i.e. out of the surface plane. The XMCD signal, i.e. the difference in absorption for circular left and right polarisation, is proportional to the aligned moment along $\hat{\boldsymbol{u}}_{\boldsymbol{k}}$. The integrated XMCD signal of $EuIr_2Si_2$ as a function of applied magnetic field and temperature is shown in Fig. 6.8 (right panel). For reference the magnetisation curve obtained from bulk measurements at $T = 5\,\mathrm{K}$ is given, too. Another useful reference is the XMCD signal obtained from trivalent $EuCo_2Si_2$ which at low temperatures contains only a small contribution from van-Vleck-type bulk paramagnetism [136] and is dominated by the paramagnetic response of the Eu^{2+} terminated surface. The field-induced magnetic polarisation in $EuIr_2Si_2$ found from XMCD is larger than what is seen in bulk magnetisation measurements. Evidently, it has a second contribution which can be easily polarised and for which saturation is reached at a few Tesla already. The comparison with the $EuCo_2Si_2$ XMCD shows that this contribution is not due to the Eu^{2+} terminated surface. Hence, it is logical to assume that the additional magnetic contribution in $EuIr_2Si_2$ that saturates at a few Tesla already is coming from

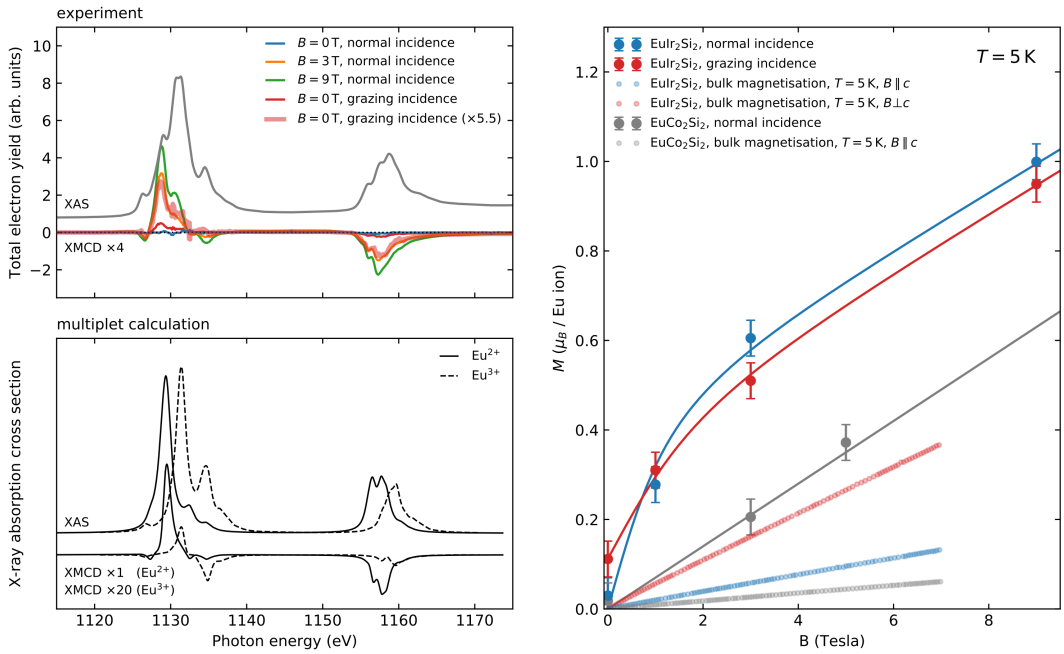

Fig. 6.8.: **Left top:** Experimentally observed XMCD in $EuIr_2Si_2$ as a function of applied magnetic in normal and grazing incidence at $T = 5\,\mathrm{K}$. The observation of a finite zero field XMCD signal at grazing incidence requires a net magnetic moment in the ab plane which is not observed in the bulk. It thus confirms ferromagnetic in-plane order at the surface of this material. **Left bottom:** Full multiplet calculations of the XMCD of free Eu^{2+} and Eu^{3+} ions at $B = 9\,\mathrm{T}$ at $T = 5\,\mathrm{K}$. **Right:** Integrals over the absolute value of the XMCD signals of $EuIr_2Si_2$ at normal and grazing incidence. For reference, we also show the XMCD data for trivalent $EuCo_2Si_2$ during the same experiment and the previously reported low-temperature bulk magnetisation of the two compounds for $B \parallel c$ [125, 136].

an easily polarised Si-terminated Eu layer, i.e. the same surface that we studied with ARPES.

We get direct evidence of ferromagnetic order in the Si–Ir–Si–Eu surface block by looking at the zero field XMCD in grazing incidence geometry where it is sensitive to the in-plane net magnetic moment. The data are shown in Fig. 6.8, too, and have been obtained from a freshly cleaved sample before applying a magnetic field. Already at zero field, there is a sizeable XMCD signal in grazing incidence geometry which has the same shape as the high field XMCD obtained at normal incidence. This spectral shape is also well reproduced in full multiplet calculations [137] for an Eu^{2+} ion at $T = 5\,\mathrm{K}$ and $B = 9\,\mathrm{T}$ applied along c (Fig. 6.8, lower panel). The observation of a zero field XMCD signal in grazing incidence but not in normal incidence geometry shows that there must be an in-plane net magnetic moment with no or only a very small component along c. It therefore confirms the in-plane ferromagnetic order concluded from our ARPES results.

In addition to the XMCD measurements, we also performed XLD measurements at normal incidence using the same experimental end-station. The alignment of the samples was the same as for the XMCD measurements, i.e. the a axis was in the

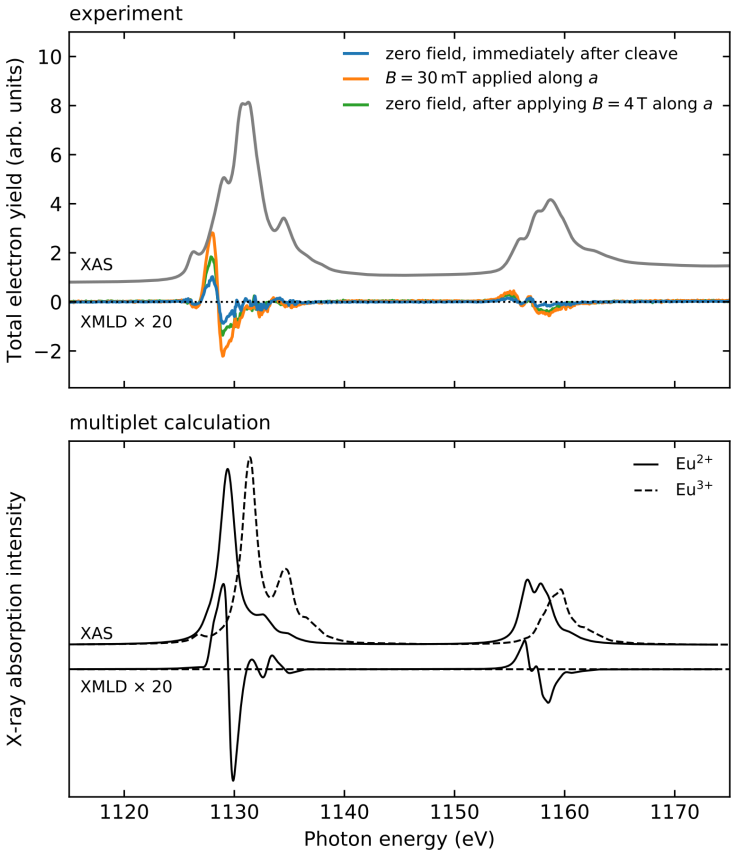

Fig. 6.9.: **Top:** Experimentally observed XMLD signal in $EuIr_2Si_2$ at $T = 5\,\mathrm{K}$ and normal incidence. The finite XMLD signal in zero applied field requires the presence of in-plane magnetic order with moments along or close to the [100] direction. **Bottom:** Full multiplet calculations of the XMLD of Eu^{2+} and Eu^{3+} ions at $T = 5\,\mathrm{K}$ with an exchange field of $\mu_B H_{ex} = 0.2\,\mathrm{meV}$ applied along a.

horizontal plane and the b axis in the vertical plane. At normal incidence, the $\boldsymbol{k}$ vector of the incident light is parallel to the c axis and a field of up to 4 T can be applied along a. The XLD is the difference in the absorption of x-rays with linear horizontal or vertical polarisation, i.e. for the $\boldsymbol{E}$ vector parallel to a or b. In the tetragonal I4/mmm structure of $EuIr_2Si_2$ the local point symmetry of the Eu ions is D_{4h} and the a and b directions are exactly equivalent. Therefore, in the chosen experimental geometry a CEF cannot lead to an XLD signal. However, as we show in Fig. 6.9 a small but clear XLD signal is observed for $EuIr_2Si_2$ already in zero magnetic field. We can exclude that this signal is due to sample misalignment, because the Eu^{2+} ($L = 0$, $J = S = 7/2$) and the low-temperature Eu^{3+} ($J = 0$) electronic configurations with $2J + 1$ degeneracy are both not split by a CEF and therefore can also not produce an XLD even between the non-equivalent a and the c axes. By contrast, in the presence of magnetic order, the $J = 7/2$ ground state of Eu^{2+} will Zeeman-split due to the presence of the exchange field and give rise to XMLD which is what we see in the experiment. The shape of the experimental XMLD spectrum can be compared again

with the results of full atomic multiplet calculations which we show in the bottom panel of Fig. 6.9. The calculations have been performed for $T = 5\,\mathrm{K}$ and assuming an exchange field $\mu_B H_{ex} = 0.2\,\mathrm{meV}$ along the a direction. As for the XMCD, we obtain a very good agreement between the calculated and experimentally observed dichroism. The experimental data also show that the application of a very small magnetic field along the a direction, $B = 30\,\mathrm{mT}$, strongly enhances the XMLD which one would expect as a consequence of the alignment of magnetic domains in the external field. We additionally observe a complete suppression of the XMLD signal when we apply $B = 5\,\mathrm{T}$ along the c direction (not shown here) which again is in line with expectations. We have seen that at $B = 5\,\mathrm{T}$ along c the subsurface XMCD signal has reached saturation and the ferromagnetically ordered moments will be fully aligned along c. As a consequence, in-plane XMLD should not be observed anymore.

In summary, both the observation of the XMCD as well as the XMLD in zero magnetic field prove the presence of in-plane magnetic order in the subsurface region. In addition to that, we obtained complementary information from both techniques. The XMCD is proportional to $\boldsymbol{M} \cdot \hat{\boldsymbol{u}}_{\boldsymbol{k}}$ averaged over all probed Eu sites. The zero field signal at grazing incidence but not at normal incidence therefore requires the presence of ferromagnetism perpendicular to the c axis, i.e. in the plane. But it cannot tell, whether the moments are aligned along the [100] or the [110] direction because in both cases one obtains a finite projection of $\boldsymbol{M}$ on $\hat{\boldsymbol{u}}_{\boldsymbol{k}}$. The XMLD in our geometry, on the other hand, is proportional to $(\boldsymbol{M} \cdot \hat{\boldsymbol{u}}_{\boldsymbol{a}} - \boldsymbol{M} \cdot \hat{\boldsymbol{u}}_{\boldsymbol{b}})^2$ averaged over all sites. A zero-field signal therefore does show the presence of in-plane order but cannot tell whether it is ferro- or antiferromagnetic. By contrast, it does contain more information about the orientation of the ordered moments in the plane, because moments along [110] would give the same projection of $\boldsymbol{M}$ on the a and b axes and produce no XMLD, while moments along [100] give a finite XMLD. In combination, both techniques confirm the presence of in-plane ferromagnetic order in the subsurface Eu layer with moments aligned along the [100] direction, which is in line with the presented ARPES results.

Magnetic dichroism in photoemission In the investigation of the magnetic properties of $4f$ materials, magnetic dichroism can be exploited in PE studies, too. While in XAS the photon energy is varied and all electrons are counted independently on their kinetic energy, in PE the photon energy is fixed and the intensity is measured in dependence on the kinetic energy of the photoelectrons for different polarisations of the incident radiation. Fig. 6.10 shows the results of a light-polarisation dependent PE study of the Eu^{2+} multiplet performed on the Si-terminated surface of $EuIr_2Si_2$ using elliptical light polarisation. The measured spectra shown in (a) and (c) have been acquired at a temperature of 30 K, i.e. below the ordering temperature of the subsurface layer, with positive and negative elliptical polarisations plotted in black and grey, respectively. In (a) the magnetisation axis, the incident beam, the analyser axis and the surface normal lie in one plane. For negative elliptical polarisation the Eu^{2+} multiplet exhibits a peaked structure at its high binding energy side, while for positive elliptical polarisation, the multiplet has a rather flat, plateau-like shape. Repeating the measurements after rotating the sample by an angle of 90° about the surface normal, the pronounced differences in the shape of the spectra acquired with

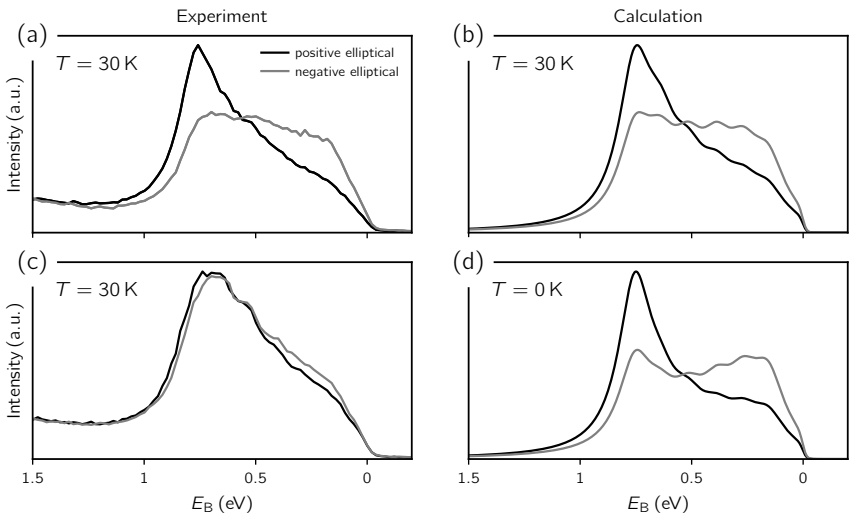

Fig. 6.10.: Magnetic circular dichroism in the Eu $4f$ PE spectra of the Si-terminated surface of $EuIr_2Si_2$ measured (a) before and (c) after rotation of the sample by 90° at 30 K with the resonance photon energy 141 eV. Spectra acquired with elliptical positive and negative light polarisations are plotted in black and grey colours, respectively. The result of computational modelling of (a) is given in (b), while (d) shows the computational results for the ground state ($T = 0\,\mathrm{K}$).

elliptical positive and negative polarisations vanish almost completely, Fig. 6.10(c). The observation of strong magnetic dichroism in (a) and its absence in (c), is consistent with our previous findings, i.e. the in-plane magnetisation due to ferromagnetically ordered Eu $4f$ in the subsurface along the tetragonal a axis and a single magnetic domain. Due to different matrix elements for the excitation of one of the ^{7}F final states of the Eu^{2+} multiplet for a parallel and antiparallel alignment of photon spin and magnetisation, different spectral shapes emerge for positive and negative elliptical polarisation. With the rotation of the sample, the magnetisation axis becomes perpendicular to the reference plane and thus, there is no difference in the excitation probability for positive and negative elliptical polarisation.

In Fig. 6.10(b) and (d) simulated PE spectra for the two polarisations and magnetisation collinear to the photon spin are shown for the temperatures 30 K and zero, respectively. Comparison of the simulated spectra for $T = 30\,\mathrm{K}$ and the ground state shows a temperature dependence of the spectral shape, which is related to the temperature-dependent occupancy of the M_J states, and a little more pronounced for the red curves. Comparison to experimental data shows a very good agreement of the spectrum measured at 30 K and the corresponding simulation given in (c), whereas the agreement with the simulated spectrum for the ground state is notably worse, emphasizing that temperature effects should be considered in theoretical models. Details of the computational model in which PED is considered, too, can be found in Ref. [138].

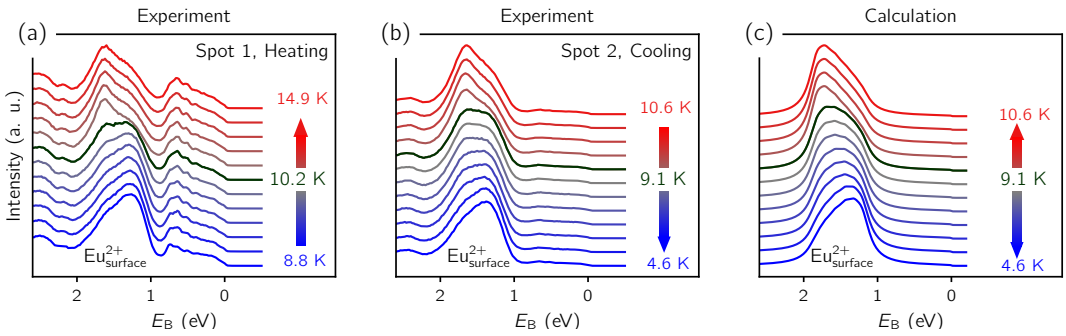

Fig. 6.11.: Temperature evolution of the Eu^{2+} surface multiplet measured with $h\nu = 110\,\mathrm{eV}$ and circular light polarisation (C^+) (a) at spot 1 upon heating the sample from 8.8 K to 14.9 K, and (b) at spot 2 upon cooling the sample down from 10.6 K to 4.6 K. The results of the corresponding modelling of the temperature-dependent change of the multiplet are shown in (c). The single angle-resolved spectra were integrated over a small angular range of 2°.

6.2.4. Eu termination

While for Si termination the surface states could be efficiently utilised to disclose the magnetic properties in the subsurface of a material that is non-magnetic in the bulk, in the case of Eu termination there are no surface states that could be used to gain respective information about a possible magnetic ordering of the moments carried by the purely divalent Eu atoms at the surface. However, the previous section showed us that the $4f$ multiplet can provide valuable insight into the magnetic properties of $4f$ materials investigating magnetic dichroism or temperature-dependent changes in the shape of the multiplet, too. Photoemission measurements conducted at 1 K (not shown here), revealed a significant change in the shape of the Eu^{2+} surface multiplet in comparison to spectra acquired at $T \geq 30\,\mathrm{K}$, which we ascribed to the magnetic ordering of the Eu $4f$ moments in the surface layer. Respective model calculations suggest a ferromagnetic alignment of the $4f$ moments along the crystallographic [100] axis, see Ref. [138]. To determine the ferromagnetic Curie temperature of the surface Eu layer, we measured the temperature dependence of the corresponding Eu^{2+} surface multiplet at two different spots on the sample with dominating Eu termination using $h\nu = 110\,\mathrm{eV}$ and circular light polarisation. In Fig. 6.11(a), we present the data for the first spot where we started at low temperature and traced the multiplet upon heating the sample from 8.8 K to 14.9 K. At 8.87 K the surface multiplet is peaked at its high-binding-energy side. Upon heating we observe a change in the multiplet shape that consists in a flattening of the multiplet at around 10.2 K. Upon further heating, a new maximum evolves on the high-binding-energy side. In Fig. 6.11(b) respective results of a temperature series for another spot and cooling of the sample in small steps from 10.6 K to 4.6 K are given. The temperature-dependent changes in the spectra are qualitatively the same like in (a). However, the temperature at which we observe the flattening of the multiplet is now 9.1 K, i.e. about 1 K lower than the transition temperature that we observed for spot 1 upon heating. This discrepancy is most likely related to sample ageing due to contaminations. Note, that in (a) the divalent bulk multiplet near E_F is more intense than in (b), indicating a larger admixture of Si

termination in the spectra acquired from the first spot. It can be seen that the shape of the bulk multiplet does not change with temperature, indicating that the subsurface Eu layer is not magnetically active. In (c) we present the corresponding modelling of the experimental data. For details of the modelling, see Ref. [138].

6.2.5. Determination of the mean Eu valency in the subsurface layers

Our results from PE and magnetic-dichroism studies prove the magnetic behaviour of Eu in the subsurface layer for the Si-terminated surface and the magnetic ordering of the $4f$ moments in the topmost Eu layer of the Eu-terminated surface. However, open questions remain that concern the values of the mean valency in the near-surface Eu layers, not only in the case of Si termination but for the Eu-terminated surface, too. While the surface-core-level shifted peak in the $4f$ spectra leaves no doubt about the purely divalent state of Eu at the surface, it remains unclear which values the valency takes in the subsurface Eu layers for both the Si- and Eu-terminated surfaces. Moreover, structural information in particular on the interlayer spacings is desirable for comparison to the results of our DFT calculations which predict strong relaxation of the near-surface layers. To address these questions we investigated the angular and photon energy dependence of the Eu^{2+} and Eu^{3+} multiplets with special focus paid to photoelectron diffraction (PED), i.e. intensity variations in the angular distribution in the $4f$ PE due to the scattering of the photoelectron wave function at neighbouring atoms.

Taking PED in PE from the $4f$ shell into consideration, allows us to address the Eu valency in the surface region layer-wise and to gain deeper insight into structural and magnetic properties of the Si- and Eu-terminated surfaces of $EuIr_2Si_2$. The PED measurements were conducted at the PEARL beamline of the Swiss Light Source with linearly polarised light and the photon energies $h\nu = 141\,\mathrm{eV}$ and $h\nu = 145\,\mathrm{eV}$ corresponding to the $4d \rightarrow 4f$ Beutler-Fano resonances of Eu^{2+} and Eu^{3+}, respectively, to achieve a significant increase of the $4f$ PE signal over valence band emissions from overlapping Ir $5d$ valence band states. To study PED a large set of ARPES spectra has been acquired for different polar and azimuthal angles with a step size of 1° and 15°, respectively, while the acceptance angle of the analyser was about ±25°. Fig. 6.12 shows the resulting PED patterns in orthographic projection for the Si- and Eu-terminated surfaces obtained at a temperature of 30 K along with the results of corresponding simulations. To construct the PED patterns from the experimental data for each spectrum the multiplet has been fitted after subtraction of a smooth background, where for Eu^{3+} only the ^{6}F peak has been taken into account because of its smaller overlap with the valence band states in comparison to the other multiplet lines. In the case of the Eu^{2+} multiplet, the integral over the seven J' has been taken.[1] Since the resulting PED patterns expose a fourfold rotational symmetry, symmetrisation procedures have been applied additionally to reduce noise and to minimise possible influence of deviations of the emission direction from the horizontal plane. To draw conclusions from the experimentally obtained PED patterns they are compared to simulations, whereby the agreement between theory and experiment is

[1] For the labelling of the single multiplet components see Fig. 2.2.

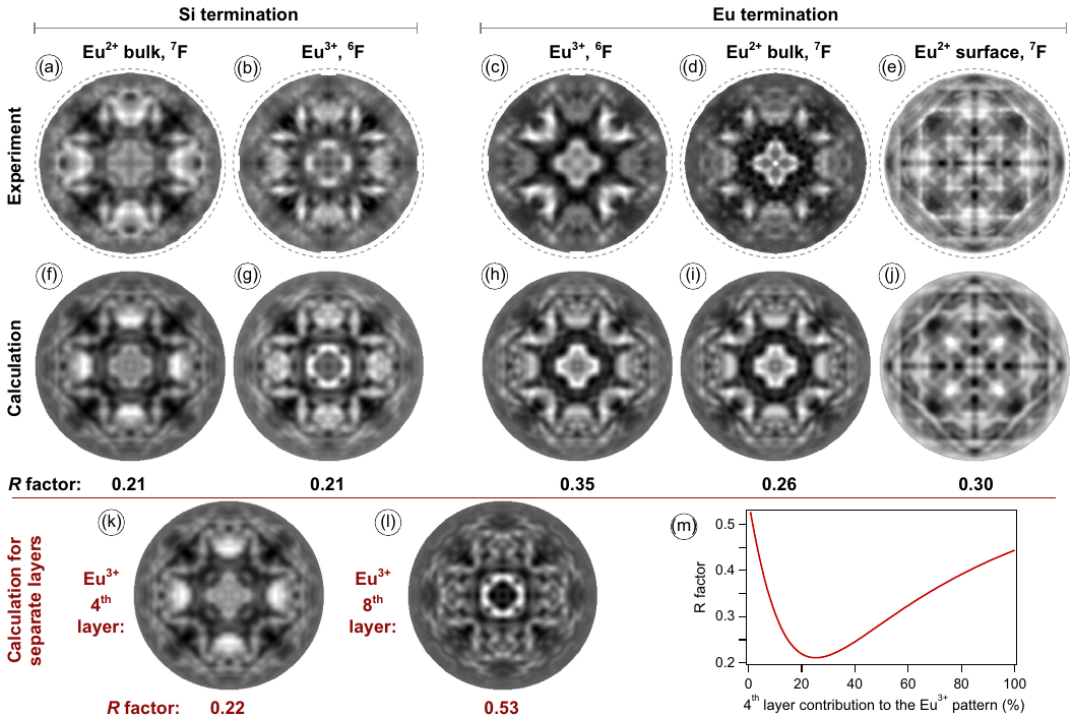

Fig. 6.12.: PED results for the Si- and Eu-terminated surfaces of $EuIr_2Si_2$. (a)-(e) Experimental and (f)-(g) theoretical PED patterns constructed from the Eu^{2+} and Eu^{3+} multiplets using the method of orthographic projection [139]. Dashed circles indicate a polar emission angle of 90°. The employed photon energies 141 eV and 145 eV correspond to the $4d \rightarrow 4f$ Beutler-Fano resonances of Eu^{2+} and Eu^{3+}, respectively. (k, l) Individual Eu^{3+} PED patterns calculated for the fourth and eighth layers. (m) Dependence of the R factor on the contribution of the fourth layer to the Eu^{3+} pattern given in (g).

quantified by the so-called reliability or R factor. The smaller the R factor, the better the agreement. To minimise the R factor the model is fitted to the experimental data.

Modelling of the spectra requires first of all an expression for the PE matrix elements. Note, that traditionally, PED studies are performed on *closed* atomic shells for which standard methods are available to calculate PE spectra. To perform a respective analysis for PE from the *open* $4f$ shell of $EuIr_2Si_2$, a new methodology has been developed by D. Usachov, see Ref. [138]. With the resulting expression for the many-electron PE matrix elements, the angular dependence of the PE spectra has been simulated for a given cluster[2] using the EDAC code [106]. The model parameters comprise the interlayer distances, the mean Eu valency in the first (surface) and fifth (first subsurface) layers for Eu termination, and in the fourth (first subsurface) and eighth (second subsurface) layers for the Si-terminated surface in terms of the concentration of Eu atoms in Eu^{2+} and Eu^{3+} states. Further fitting parameters are

[2]Here, a cylindrical cluster with 24 atomic layers and the radius $r = 30$ Å has been used. Scattering, however, has only been considered in the part of the cluster that can be reached by photoelectrons travelling from the emitter to the surface, with a maximal path length of $r_{max} = 20$ Å giving a parabolic embedded cluster.

the inner potential V_0 and the inelastic mean free path λ which are introduced on pages 44ff. Note, that the valency of deeper lying Eu layers is due to the small escape depth of the photoelectrons fixed to the bulk value 2.8 [125].

The diffraction patterns obtained for the **Si-terminated surface** from the integrated Eu^{2+} and Eu^{3+} multiplets are shown in Fig. 6.12(a) and (b), respectively, while the corresponding results of the modelling are given in (f) and (g). Comparing the calculated patterns with the experimental ones we find a good agreement, which is quantified by a reasonably small R factor of 0.21 in both cases. For the valency of Eu in the fourth and eighth layers below the Si-terminated surface, the PED analysis gives the values $\nu = 2.15 \pm 0.15$ and 2.55 ± 0.4, respectively. Despite the large uncertainty, the result shows that the valency in the first subsurface Eu layers deviates notably from the bulk value of 2.8. In Fig. 6.12(m) the dependency of the R factor on the contribution of that layer to the Eu^{3+} diffraction pattern is given. The pronounced minimum shows that there is a finite admixture of trivalent Eu in the subsurface layer and hence, despite its magnetic properties that have been proven by employing different and complementary experimental techniques, Eu is not in an exactly divalent state. To reduce the extremely large uncertainty of the determined valencies, we combined the on-resonance PED analysis with the evaluation of individual off-resonance PE spectra acquired with photon energies of 110 eV, 160 eV and 200 eV. The respective PE intensities have been calculated taking PED into account. To determine the concentrations of Eu^{2+} and Eu^{3+} in the single Eu layers, and thus the mean per-layer valency, the individual concentrations served as fitting parameters that were tuned until the best agreement between measured and calculated spectra has been achieved for all photon energies simultaneously. This approach allowed us to dramatically reduce the uncertainty giving the results $\nu = 2.1 \pm 0.05$ and $\nu = 2.4 \pm 0.2$ for the Eu valency in the fourth and eighth layers, respectively. Thus, for the Si-terminated surface, we find that the valency in the near-surface Eu layers increases stepwise from almost divalent with a small admixture of trivalent Eu in the fourth, subsurface layer to 2.4 in the eighth layer, where it still deviates strongly from the bulk value.

For the **Eu-terminated surface** the experimentally obtained diffraction patterns are given in Fig. 6.12(c) and (d) for Eu^{3+} and Eu^{2+} bulk-like signals in terms of the ^6F and the J'-integrated ^7F lines, respectively, with the corresponding simulated patterns shown below in (h) and (i). The diffraction pattern constructed from the highly intense surface-core-level-shifted Eu surface peak, that appears in the PE spectrum at about 1 eV binding energy, is shown in (e), the respective modelling in (j). The comparison of the experimental and calculated PED patterns reveals a good agreement. The strong similarity of the patterns in (c) and (d) indicates that they originate from the same Eu layer, which, due to the limited escape depth of the photoelectrons, must be mainly layer number five. There is thus strong evidence for a non-integer Eu valence in the latter. As in the case of the Si-terminated surface, we combined the PED analysis for the Eu termination with off-resonance spectra to determine the Eu valency with great precision. In the modelling, the ratio between the Eu^{2+} emission from the fourth layer and the surface has been used to determine the valency in the fifth layer, while the ninth layer was treated as bulk. The final result is $\nu = 2.77 \pm 0.07$ showing that the valency takes almost the bulk value in layer number five.

In comparison to the PED results for the Si-terminated surface, the agreement

between experiment and theory is a little worse for the Eu termination, which is also reflected in larger R factors reaching values up to 0.35 in the case of the trivalent PED pattern. The larger R factor may be attributed to the weaker PE signal in comparison to the Si-terminated surface. In the case of Eu termination the bulk-like Eu signal originates from the fifth and ninth atomic layers, whereas for the Si-terminated surface it comes from layers number four and eight and the deeper the layer, the larger the probability for scattering events reducing the intensity of the corresponding PE signal and increasing the overall noise. Moreover, the PE signal of Eu^{3+} is generally weak in comparison to its divalent counterpart and at certain emission angles, it becomes vanishingly small which makes the peak fitting for the construction of the diffraction pattern difficult. In difference, the divalent bulk signal is of good intensity for all emission angles and the R factor is only a little worse than for the Si-terminated surface.

Moreover, the PED analysis confirms the strong inward relaxation of the surface Eu layer predicted by our DFT calculations. The Eu-Si interlayer distance along the c axis reduces from 1.27 Å in the bulk to 1.22 Å at the surface, showing that DFT in the open-core approximation is indeed capable of describing our system properly.

J'-resolved PED analysis In the resonance spectra acquired from the Si-terminated surface the single J' lines of the Eu^{2+} final-state bulk multiplet are well resolved which calls for their separate analysis in terms of PED. In the upper row of Fig. 6.13 the

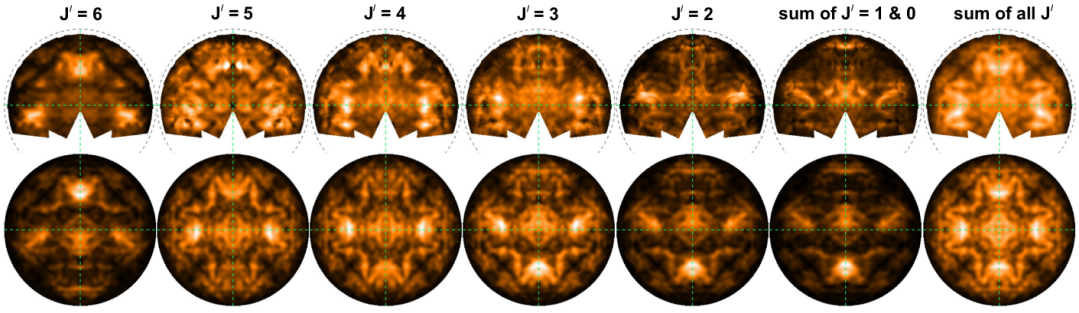

Fig. 6.13.: J'-resolved PED patterns derived from the Eu^{2+} multiplet for Si termination at 30 K and a photon energy of 141 eV. Experimental and computational results are shown in the upper and lower row, respectively. In the calculations, the magnetisation was assumed to point leftwards, which corresponds to the crystallographic $[\bar{1}00]$ direction.

experimental J'-resolved PED patterns are shown starting with $J' = 6$ and decreasing by one when moving from the left to the right. Since the lines for $J' = 0, 1$ cannot be separated their sum is considered. On the right-hand side, the sum over the single J' plots is shown. The PED patterns of the single J' components have a different symmetry than the integrated one, independent of whether the latter was constructed after the summation over the single J' components (Fig. 6.12(a)), or by summing up of the single J' PED patterns (Fig. 6.13). We find that the J'-resolved PED patterns expose the same mirror symmetry that we already observed for the ARPES-derived CECs of the surface state α when the subsurface Eu layer is magnetically ordered. In the lower row, the corresponding results of the modelling are shown. Note, that

here only the first subsurface Eu has been considered in the modelling. Magnetic ordering of the Eu $4f$s has been taken into account, too, and a good fitting of the experimental data is achieved if the magnetisation vector is assumed to point along the $[\bar{1}00]$ direction. The asymmetry in the PED patterns indicates that the data have been collected predominantly from a single magnetic domain. Note, that an equivalent analysis performed for the fifth layer in the case of Eu termination did not reveal any changes in symmetry and hence no magnetic order is expected in the latter.

6.2.6. Bulk properties

In the remainder of this chapter about $EuIr_2Si_2$, a short overview of our ARPES and DFT results for the bulk electronic structure shall be given. Fig. 6.14(a) compares Fermi maps that show the projection of the Doughnut $\mathcal{D}$ in the SBZ at 200 K (left) and 7 K (right). At 200 K the Doughnut is large with its necks extending far towards the $\overline{\mathrm{X}}$ points, while at 7 K it is notably smaller and the necks at a fair distance from $\overline{\mathrm{X}}$. The Doughnut is built from bands with a hole-like dispersion. Therefore, its shrinking between 200 K and 7 K is likely due to a band-filling effect. In this case, the re-scaling of the Doughnut would happen smoothly throughout the T dependent valence crossover. In Fig. 6.14(b) we consider the T dependence of the Doughnut and show the results of DFT calculations modelling the experimental data. In doing so, we fix the occupancy of the Eu $4f$ shell such that it corresponds to the literature value for the mean valency at the respective reference temperature. We find that the size of the Doughnut changes indeed smoothly with temperature and correlates with the mean Eu valency assumed in the DFT calculations, Fig. 6.14(c). With increasing T the average occupancy of the $4f$ core-shell increases at the cost of the valence band. With a smaller number of valence electrons, the filling of the valence band reduces. This, as it is schematically drawn in Fig. 6.14(d), implies an expansion of the Fermi surface for hole-like states like the Doughnut. Correspondingly, we find that the band gap around the $\overline{\mathrm{M}}$ point shrinks when the temperature increases, as it is formed by bands with an electron-like dispersion.

Note on the projected bulk band structure Bulk states are described by itinerant wave functions that expand over the entire crystal. Being reflected at the surface they form standing waves that can be detected with ARPES in the region near the surface. For $h\nu = 55$ eV the inelastic mean free path of the photoelectrons is about 6 Å and thus only of about half a lattice constant c along the direction that is perpendicular to the surface. Due to the uncertainty relation the spatial restriction of the probed region results in the smearing-out of the $\boldsymbol{k}_\perp$ component of the wave vector over a $\boldsymbol{k}_\perp$ interval that is in the order of the corresponding reciprocal lattice vector. Respective bulk bands are therefore usually seen in ARPES not as discrete curves but as broad areas of increased intensity. This corresponds to an integration of the band structure over $\boldsymbol{k}_\perp$ and hence, the projection of the bulk band structure onto the surface. In Fermi-surface mapping, the distribution of the states at the Fermi level is measured in k_x, k_y direction and hence, the corresponding projection of the Fermi surface onto the surface. In the previous sections we were dealing with surface-specific deviations from the electronic bulk structure, in the form of localised $4f$ states or surface states

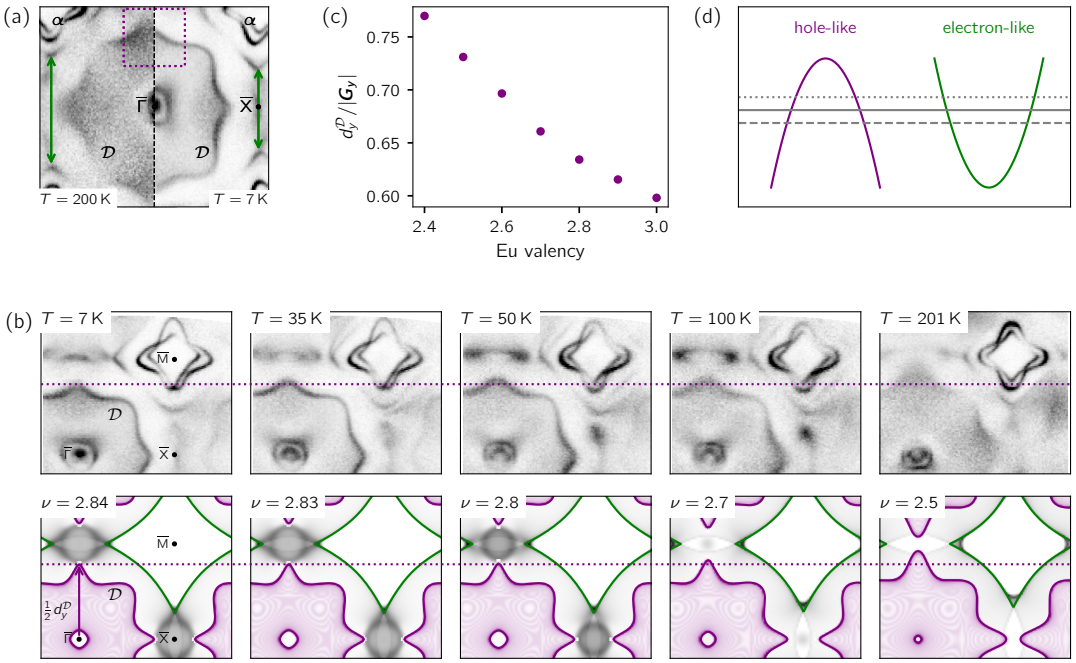

Fig. 6.14.: T dependence of Doughnut $\mathcal{D}$ and $\overline{\mathrm{M}}$ gap in $EuIr_2Si_2$. **(a)** Fermi maps comparing the projected Doughnut at 200 K (left) and 7 K (right). The purple rectangle marks the necks. There, the re-scaling of $\mathcal{D}$ between 200 K and 7 K is maximal visible. The green arrows indicate the distance between the edges of neighbouring $\overline{\mathrm{M}}$ gaps. **(b)** Upper row: experimental Fermi surfaces measured at 7 K, 35 K, 50 K, 100 K and 200 K with $h\nu = 55$ eV. Below, the computed Fermi surfaces are plotted with $\mathcal{D}$ highlighted in purple. The occupancy of the Eu $4f$ shell chosen for the DFT modelling of a particular T corresponds to the respective literature value for the mean valence. The purple-coloured dotted line marks the maximal extent of the Doughnut along $\overline{\Gamma} - \overline{\mathrm{X}}$ at 7 K or for $n_{4f} = 6.16$. **(c)** DFT derived extent of $\mathcal{D}$ along $\overline{\mathrm{X}} - \overline{\Gamma} - \overline{\mathrm{X}}$ divided by the absolute value of the reciprocal lattice vector in y direction for Eu valencies between 2.4 and 3.0. **(d)** Schematic illustration of the band-filling effect for the hole- and electron-like bands. A higher band filling (dotted grey line) in comparison to a lower band filling (dashed line) implies a smaller or larger cross-section area in case of a hole- or electron-like band, respectively.

and surface resonances, i.e. itinerant states that are restricted to the near-surface region thus having a mostly 2D character. Therefore, those states do not have a $\boldsymbol{k}_\perp$ dependence and appear in the ARPES spectra as well-defined curves.

6.3. Summary

In summary, we discovered strong 2D ferromagnetism at the surface of $EuIr_2Si_2$, a metallic compound that is non-magnetic in the bulk due to a mixed-valent Eu state. The surface magnetism is found below 49 K in the first Eu layer below the Si-terminated surface, buried by a Si–Ir–Si trilayer block. It is enabled via a strong divalent deviation of the Eu valency from its value in the bulk with only small admixtures of the trivalent Eu state and probably due to structural relaxation near the surface. The divalent and

magnetically active properties of this Eu layer might be further related to the existence of surface states in the Si–Ir–Si–Eu surface block and their exchange interaction with the Eu moments in the subsurface. A similar scenario has been suggested to explain the different ordering temperatures in the bulk and at the surface of $EuRh_2Si_2$ where the surface Curie temperature is about 40 % higher than the Néel temperature of the bulk [35]. The role played by surface states for the evolution of magnetic properties in non-magnetic Eu compounds could be a subject of further studies. A disclosure would allow for specifically designing Eu- or Sm-based $4f$ systems with a non-magnetic bulk and a magnetically active surface which could be of interest for spintronics applications.

In the PM phase of $EuIr_2Si_2$, the surface state electrons at the Si-terminated surface experience a strong cubic Rashba effect which induces a huge splitting of the respective bands and a triple-winding spin structure. When their spins start to couple to the ordered $4f$ moments, the triple-winding spin structure is destroyed and the surface state bands experience a pronounced asymmetric distortion. This has its origin in the joint action of the strongly $\boldsymbol{k}_{\parallel}$-dependent Rashba-like SOC and the unidirectional exchange interaction that are of similar strength in the given system.

At the Eu-terminated surface, we discovered 2D ferromagnetism, too. Due to the changed coordination and missing binding partners, at the surface Eu is in a purely divalent state. The respective moments order ferromagnetically within the surface plane along the [100] crystallographic axis below 10 K. Note, that T_C is about five times lower than for the Si-terminated surface which might be due to the reduced coordination at the surface.

For the bulk we observe a smooth shrinking of the projected Doughnut Fermi surface with decreasing temperature reflecting the change of the mean valence within the valence-crossover regime. At the same time the large band gap centred at the $\overline{\mathrm{M}}$ point becomes larger. Both effects can be understood as band-filling effect when Eu becomes more trivalent at low temperatures.

The ferromagnetic order of Eu as well as the spin structure of the 2D electrons can be controlled by temperature, manipulated by an external magnetic field or by tuning the valence of Eu in the bulk, e.g. using chemical substitution. Our results call for the reconsideration of a large class of materials containing heavy $5d$ elements together with lanthanide or transition metal elements, which show mixed-valent or PM bulk properties. Just like $EuIr_2Si_2$, many of them may exhibit unique magnetic properties at the surface which have been overlooked so far.

7. Conclusion

This work is the continuation of a systematic study of the surface electronic and magnetic properties of LnT_2Si_2 compounds, where T = transition metal and Ln = lanthanide, that crystallise in the $ThCr_2Si_2$ structure. Common to all LnT_2Si_2 compounds with T = Co, Rh, Ir the Si–T–Si–Ln surface block bears quasi-2D electron states which are subject to the Rashba effect. In particular, both the classical and an exotic cubic Rashba effect are represented in the aforementioned model system. The strength of the Rashba-like spin-orbit interaction scales with the atomic number Z of the transition metal element and is tuned by the choice T = Ir to be comparable in magnitude with the exchange interaction between the two-dimensional electrons and the $4f$ moments, provided they order magnetically at low temperatures. Here, we consider two compounds with fundamentally different bulk properties: the robust bulk antiferromagnet $GdIr_2Si_2$ and mixed-valent $EuIr_2Si_2$, which is non-magnetic in the bulk. In addition to the surface-state properties, for the rather exotic $EuIr_2Si_2$ it is of particular interest whether and how the mixed-valent properties change in the near-surface region. For our study, we used different experimental methods based on synchrotron radiation, in particular, angle-resolved photoelectron spectroscopy which we combined with density functional theory calculations.

In accordance with our expectations, we find that in the considered LnT_2Si_2 compounds the replacement of rhodium by iridium enhances the strength of the Rashba-like spin-orbit interaction significantly, while the spin structure remains unchanged. This emphasizes the surface states' generic character and intimate relation to the crystal structure. The joint action of the Rashba-like spin-orbit and the exchange interactions evokes pronounced asymmetries in the surface states' band dispersion at low temperatures. Similar asymmetries have been shown to create spin-polarised currents which are relevant for spintronics applications [33]. In our study, they allowed us to determine the magnetisation axis along which the $4f$ moments in the first lanthanide layer below the surface align in the magnetically ordered regime. We demonstrate that the asymmetries can be explained in terms of two effective magnetic fields – the strongly $\boldsymbol{k}_\parallel$ dependent Rashba field and the exchange field which is unidirectional in momentum space – adding up to a total effective field. The strength and orientation of the latter at a given point in momentum space depend on the mutual alignment and strength of Rashba and exchange fields for the considered $\boldsymbol{k}_\parallel$ according to the rules of

vector addition. The dependence of the surface states' properties on the orientation of the exchange field opens a further avenue for the tuning of their spin structure and band dispersion. This can be realised by optical excitation as it was shown for $GdRh_2Si_2$, where the magnetisation axis can be rotated deterministically with short laser pulses [40]. Another possibility is to take advantage of the crystal electric field, which, in systems with Ln = Tb, Dy, Ho where $L \neq 0$, rotates the $4f$ moments out of the tetragonal ab plane and aligns them parallel to the c axis. For $DyRh_2Si_2$, moreover, a temperature-dependent canting away from the c axis was reported [140]. In the paramagnetic phase, an external magnetic field can be applied to align the $4f$ moments, thus inducing the asymmetry of the surface state bands. The control of the surface state properties in an external magnetic field in terms of the orientation and strength of the latter would be of interest for future studies. This, however, requires another experimental technique since ARPES experiments cannot be conducted if an external magnetic field is applied.

Interestingly, we observed respective asymmetries not only for antiferromagnetic $GdIr_2Si_2$ but for mixed-valent and hence non-magnetic $EuIr_2Si_2$, too, revealing magnetically ordered Eu $4f$ moments in the Si–Ir–Si–Eu surface block at low temperatures. Extending our photoemission study taking also photoelectron diffraction into account, we could prove that the valency in the respective Eu layer is almost divalent. Thus, it deviates strongly from its bulk value, where Eu is close to a trivalent configuration. This deviation is likely due to surface relaxation which may create more space for the larger divalent Eu ions. Also exchange coupling of the surface states and Eu $4f$ states may play a role in the stabilisation of the magnetically active, divalent Eu state. For $EuIr_2Si_2$ we found the moments to order along the [100] direction below 49 K, while for $GdIr_2Si_2$ the magnetisation axis is [110]. At the same time, the strong temperature dependence of the mean Eu valency in the bulk is explicitly reflected in a continuous size change of the projected bulk Fermi surface. In particular, the hole-like Doughnut Fermi surface sheet, which has been subject to intense studies in Yb and Eu compounds, shrinks gradually when the system approaches the trivalent state. At the same time, the band gap to which the surface states are confined grows larger. This is in contrast to mixed-valent Yb compounds. For example in $YbRh_2Si_2$, the volume of the Fermi surface changes abruptly with the Kondo breakdown [77], which emphasizes the different nature of mixed-valent Eu and Yb or Ce compounds which is also reflected in different phase diagrams. Thus, our findings for mixed-valent $EuIr_2Si_2$ show that surface and bulk have fundamentally different properties being widely decoupled from each other. This calls for the consideration of an entire class of materials with mixed-valent properties, especially Eu and Sm compounds, where similar surface phenomena may be expected.

Another interesting finding is the observation of magnetic domains at the surface of both $GdIr_2Si_2$ and $EuIr_2Si_2$. Formation and manipulation of magnetic domains and domain walls are of interest for fundamental studies and discussed for the use in spintronics applications [141]. Domain walls are also discussed to take the role of neurons in artificial neural networks used in neuromorphic computing [142]. The nature of the domains and domain walls in the studied materials is still completely unknown. Here, nano spot techniques could help to disentangle their size and formation. Moreover, the study of LnT_2Si_2 thin films might gain attention in the future with the recent success

in growing thin films of $YbRh_2Si_2$ using molecular beam epitaxy [143, 144]. Extension of this technique to other members of the LnT_2Si_2 family may become a source of new fascinating physics in the close future and possibly qualify these compounds, which currently serve rather as a model system or are mainly of interest for fundamental research, for applications.

In the future, the systematic study of $4f$-based tetragonal 122 compounds will be continued for systems in which the transition metal sublattice is magnetically active, too, with the focus on a possible magnetic coupling between the lanthanide and transition metal sublattices. Respective candidates are LnT_2P_2 compounds where phosphorus replaces silicon and T is a magnetic $3d$ transition metal like Co or Mn. First results on $CeCo_2P_2$ show that non-compensated Co moments induce a magnetic moment on Ce in the first subsurface layer, while Ce behaves tetravalently and thus non-magnetic in the bulk [145].

In summary, our results show once more the versatile physics realised in $4f$ based materials. In particular, the surface region where the electronic and magnetic properties may differ significantly from the bulk, offers a rich playground for the investigation of fundamental interactions. At the same time, with the ongoing miniaturisation of devices understanding of surfaces and discovery of surface-specific effects become more important for the development of novel electronics and spintronics devices.

Bibliography

[1] M. Hilbert and P. López, "The World's Technological Capacity to Store, Communicate, and Compute Information," *Science*, vol. 332, no. 6025, pp. 60–65, 2011.

[2] C. A. Mack, "Fifty Years of Moore's Law," *IEEE Transactions on Semiconductor Manufacturing*, vol. 24, no. 2, pp. 202–207, 2011.

[3] M. Lundstrom, "Moore's law forever?," *Science*, vol. 299, no. 5604, pp. 210–211, 2003.

[4] T. N. Theis and H.-S. P. Wong, "The end of Moore's law: A new beginning for information technology," *Computing in Science and Engineering*, vol. 19, no. 2, pp. 41–50, 2017.

[5] A. Hirohata, K. Yamada, Y. Nakatani, I.-L. Prejbeanu, B. Diény, P. Pirro, and B. Hillebrands, "Review on spintronics: Principles and device applications," *Journal of Magnetism and Magnetic Materials*, vol. 509, p. 166711, 2020.

[6] S. Datta and B. Das, "Electronic analog of the electro-optic modulator," *Applied Physics Letters*, vol. 56, no. 7, pp. 665–667, 1990.

[7] S. Datta, "How we proposed the spin transistor," *Nature Electronics*, vol. 1, no. 11, p. 604, 2018.

[8] R. Jansen, S. P. Dash, S. Sharma, and B. C. Min, "Silicon spintronics with ferromagnetic tunnel devices," *Semiconductor Science and Technology*, vol. 27, no. 8, p. 083001, 2012.

[9] M. D. Stiles and J. Miltat, *Spin-Transfer Torque and Dynamics*, pp. 225–308. Berlin, Heidelberg: Springer Berlin Heidelberg, 2006.

[10] G. Hu and B. Xiang, "Recent advances in two-dimensional spintronics," *Nanoscale Research Letters*, vol. 15, no. 1, pp. 1–17, 2020.

[11] R. E. I and S. V. I, "Symmetry of energy bands in crystals of wurtzite type: II. Symmetry of bands including spin-orbit interaction," *Fiz. Tverd. Tela: Collected Papers 2*, pp. 162–76, 1959.

[12] Y. A. Bychkov and E. I. Rashba, "Properties of a 2D electron gas with lifted spectral degeneracy," *JETP Lett*, vol. 39, no. 2, p. 78, 1984.

[13] A. Manchon, H. C. Koo, J. Nitta, S. Frolov, and R. Duine, "New perspectives for Rashba spin–orbit coupling," *Nature materials*, vol. 14, no. 9, pp. 871–882, 2015.

[14] H. C. Koo, S. B. Kim, H. Kim, T.-E. Park, J. W. Choi, K.-W. Kim, G. Go, J. H. Oh, D.-K. Lee, E.-S. Park, I.-S. Hong, and K.-J. Lee, "Rashba effect in functional spintronic devices," *Advanced Materials*, vol. 32, no. 51, p. 2002117, 2020.

[15] I. Mihai Miron, G. Gaudin, S. Auffret, B. Rodmacq, A. Schuhl, S. Pizzini, J. Vogel, and P. Gambardella, "Current-driven spin torque induced by the Rashba effect in a ferromagnetic metal layer," *Nature Materials*, vol. 9, no. 3, pp. 230–234, 2010.

[16] I. M. Miron, K. Garello, G. Gaudin, P.-J. Zermatten, M. V. Costache, S. Auffret, S. Bandiera, B. Rodmacq, A. Schuhl, and P. Gambardella, "Perpendicular switching of a single ferromagnetic layer induced by in-plane current injection," *Nature*, vol. 476, no. 7359, pp. 189–193, 2011.

[17] D. A. Allwood, G. Xiong, C. C. Faulkner, D. Atkinson, D. Petit, and R. P. Cowburn, "Magnetic domain-wall logic," *Science*, vol. 309, no. 5741, pp. 1688–1692, 2005.

[18] S. S. P. Parkin, M. Hayashi, and L. Thomas, "Magnetic domain-wall racetrack memory," *Science*, vol. 320, no. 5873, pp. 190–194, 2008.

[19] G. Bihlmayer, O. Rader, and R. Winkler, "Focus on the Rashba effect," *New Journal of Physics*, vol. 17, no. 5, p. 050202, 2015.

[20] Y. A. Bychkov and E. I. Rashba, "Oscillatory effects and the magnetic susceptibility of carriers in inversion layers," *J. Phys. C*, vol. 17, no. 33, p. 6039, 1984.

[21] J. Nitta, T. Akazaki, H. Takayanagi, and T. Enoki, "Gate control of spin-orbit interaction in an inverted $In_{0.53}Ga_{0.47}As/In_{0.52}Al_{0.48}As$ heterostructure," *Phys. Rev. Lett.*, vol. 78, pp. 1335–1338, 1997.

[22] S. LaShell, B. A. McDougall, and E. Jensen, "Spin splitting of an Au(111) surface state band observed with angle resolved photoelectron spectroscopy," *Phys. Rev. Lett.*, vol. 77, pp. 3419–3422, 1996.

[23] M. Hoesch, M. Muntwiler, V. N. Petrov, M. Hengsberger, L. Patthey, M. Shi, M. Falub, T. Greber, and J. Osterwalder, "Spin structure of the Shockley surface state on Au(111)," *Phys. Rev. B*, vol. 69, p. 241401, 2004.

[24] G. Nicolay, F. Reinert, S. Hüfner, and P. Blaha, "Spin-orbit splitting of the L-gap surface state onAu(111) and Ag(111)," *Phys. Rev. B*, vol. 65, p. 033407, 2001.

[25] Y. M. Koroteev, G. Bihlmayer, J. E. Gayone, E. V. Chulkov, S. Blügel, P. M. Echenique, and P. Hofmann, "Strong spin-orbit splitting on Bi surfaces," *Phys. Rev. Lett.*, vol. 93, p. 046403, 2004.

[26] A. Kimura, E. E. Krasovskii, R. Nishimura, K. Miyamoto, T. Kadono, K. Kanomaru, E. V. Chulkov, G. Bihlmayer, K. Shimada, H. Namatame, and M. Taniguchi, "Strong Rashba-type spin polarization of the photocurrent from bulk continuum states: Experiment and theory for Bi(111)," *Phys. Rev. Lett.*, vol. 105, p. 076804, 2010.

[27] A. Varykhalov, D. Marchenko, M. R. Scholz, E. D. L. Rienks, T. K. Kim, G. Bihlmayer, J. Sánchez-Barriga, and O. Rader, "Ir(111) surface state with giant Rashba splitting persists under graphene in air," *Phys. Rev. Lett.*, vol. 108, p. 066804, 2012.

[28] C. R. Ast, J. , A. Ernst, L. Moreschini, M. C. Falub, D. Pacilé, P. Bruno, K. Kern, and M. Grioni, "Giant spin splitting through surface alloying," *Phys. Rev. Lett.*, vol. 98, p. 186807, 2007.

[29] H. Nakamura, T. Koga, and T. Kimura, "Experimental evidence of cubic Rashba effect in an inversion-symmetric oxide," *Phys. Rev. Lett.*, vol. 108, p. 206601, 2012.

[30] R. Moriya, K. Sawano, Y. Hoshi, S. Masubuchi, Y. Shiraki, A. Wild, C. Neumann, G. Abstreiter, D. Bougeard, T. Koga, and T. Machida, "Cubic Rashba spin-orbit interaction of a two-dimensional hole gas in a strained-Ge/SiGe quantum well," *Phys. Rev. Lett.*, vol. 113, p. 086601, 2014.

[31] O. Krupin, G. Bihlmayer, K. Starke, S. Gorovikov, J. E. Prieto, K. Döbrich, S. Blügel, and G. Kaindl, "Rashba effect at magnetic metal surfaces," *Phys. Rev. B*, vol. 71, no. 20, p. 201403, 2005.

[32] O. Krupin, G. Bihlmayer, K. Döbrich, J. Prieto, K. Starke, S. Gorovikov, S. Blügel, S. Kevan, and G. Kaindl, "Rashba effect at the surfaces of rare-earth metals and their monoxides," *New J. Phys.*, vol. 11, no. 1, p. 013035, 2009.

[33] C. Carbone, P. Moras, P. M. Sheverdyaeva, D. Pacilé, M. Papagno, L. Ferrari, D. Topwal, E. Vescovo, G. Bihlmayer, F. Freimuth, Y. Mokrousov, and S. Blügel, "Asymmetric band gaps in a Rashba film system," *Phys. Rev. B*, vol. 93, p. 125409, 2016.

[34] A. Chikina, M. Höppner, S. Seiro, K. Kummer, S. Danzenbächer, S. Patil, A. Generalov, M. Güttler, Y. Kucherenko, E. V. Chulkov, Y. M. Koroteev, K. Koepernik, C. Geibel, M. Shi, M. Radovic, L. C., and D. V. Vyalikh, "Strong

ferromagnetism at the surface of an antiferromagnet caused by buried magnetic moments," *Nat. Commun.*, vol. 5, no. 1, pp. 1–7, 2014.

[35] M. Güttler, A. Generalov, M. M. Otrokov, K. Kummer, K. Kliemt, A. Fedorov, A. Chikina, S. Danzenbächer, S. Schulz, E. V. Chulkov, Y. M. Koroteev, N. Caroca-Canales, M. Shi, M. Radovic, C. Geibel, C. Laubschat, P. Dudin, T. K. Kim, M. Hoesch, C. Krellner, and D. V. Vyalikh, "Robust and tunable itinerant ferromagnetism at the silicon surface of the antiferromagnet $GdRh_2Si_2$," *Sci. Rep.*, vol. 6, p. 24254, 2016.

[36] A. Y. Vyazovskaya, M. M. Otrokov, Y. M. Koroteev, K. Kummer, M. Güttler, D. V. Vyalikh, and E. V. Chulkov, "Origin of two-dimensional electronic states at Si-and Gd-terminated surfaces of $GdRh_2Si_2(001)$," *Phys. Rev. B*, vol. 100, no. 7, p. 075140, 2019.

[37] D. Yu. Usachov, I. A. Nechaev, G. Poelchen, M. Güttler, E. E. Krasovskii, S. Schulz, A. Generalov, K. Kliemt, A. Kraiker, C. Krellner, K. Kummer, S. Danzenbächer, C. Laubschat, A. P. Weber, J. Sánchez-Barriga, E. V. Chulkov, A. F. Santander-Syro, T. Imai, K. Miyamoto, T. Okuda, and D. V. Vyalikh, "Cubic Rashba effect in the surface spin structure of rare-earth ternary materials," *Phys. Rev. Lett.*, vol. 124, no. 23, p. 237202, 2020.

[38] A. Generalov, J. Falke, I. A. Nechaev, M. M. Otrokov, M. Güttler, A. Chikina, K. Kliemt, S. Seiro, K. Kummer, S. Danzenbächer, D. Usachov, T. K. Kim, P. Dudin, E. V. Chulkov, C. Laubschat, C. Geibel, C. Krellner, and D. V. Vyalikh, "Strong spin-orbit coupling in the noncentrosymmetric Kondo lattice," *Phys. Rev. B*, vol. 98, p. 115157, 2018.

[39] I. A. Nechaev and E. E. Krasovskii, "Relativistic splitting of surface states at Si-terminated surfaces of the layered intermetallic compounds RT_2Si_2 (R=rare earth; T=Ir, Rh)," *Phys. Rev. B*, vol. 98, no. 24, p. 245415, 2018.

[40] Y. W. Windsor, A. Ernst, K. Kummer, K. Kliemt, C. Schüßler-Langeheine, U. Pontius, U. Staub, E. V. Chulkov, C. Krellner, D. V. Vyalikh, and L. Rettig, "Deterministic control of an antiferromagnetic spin arrangement using ultrafast optical excitation," *Comm. Physics*, vol. 3, p. 139, 2020.

[41] T. T. Jungwirth, J. Sinova, A. Manchon, X. Marti, J. Wunderlich, and C. Felser, "The multiple directions of antiferromagnetic spintronics," *Nat. Phys.*, vol. 14, p. 200, 2018.

[42] V. Baltz, A. Manchon, M. Tsoi, T. Moriyama, T. Ono, and Y. Tserkovnyak, "Antiferromagnetic spintronics," *Reviews of Modern Physics*, vol. 90, no. 1, p. 015005, 2018.

[43] O. Gomonay, V. Baltz, A. Brataas, and Y. Tserkovnyak, "Antiferromagnetic spin textures and dynamics," *Nature Physics*, vol. 14, no. 3, pp. 213–216, 2018.

[44] S. Schlauderer, C. Lange, S. Baierl, T. Ebnet, C. P. Schmid, D. Valovcin, A. Zvezdin, A. Kimel, R. Mikhaylovskiy, and R. Huber, "Temporal and spectral fingerprints of ultrafast all-coherent spin switching," *Nature*, vol. 569, no. 7756, pp. 383–387, 2019.

[45] M. Shatruk, "$ThCr_2Si_2$ structure type: The "perovskite" of intermetallics," *Journal of Solid State Chemistry*, vol. 272, pp. 198–209, 2019.

[46] Q. Si and F. Steglich, "Heavy fermions and quantum phase transitions," *Science*, vol. 329, no. 5996, pp. 1161–1166, 2010.

[47] J. Custers, P. Gegenwart, H. Wilhelm, K. Neumaier, Y. Tokiwa, O. Trovarelli, C. Geibel, F. Steglich, C. Pépin, and P. Coleman, "The break-up of heavy electrons at a quantum critical point," *Nature*, vol. 424, no. 6948, pp. 524–527, 2003.

[48] F. Steglich, J. Aarts, C. D. Bredl, W. Lieke, D. Meschede, W. Franz, and H. Schäfer, "Superconductivity in the presence of strong Pauli paramagnetism: $CeCu_2Si_2$," *Phys. Rev. Lett.*, vol. 43, pp. 1892–1896, 1979.

[49] I. Felner and I. Nowik, "Itinerant and local magnetism, superconductivity and mixed valency phenomena in RM_2Si_2, (R = rare earth, M = Rh, Ru)," *Journal of Physics and Chemistry of Solids*, vol. 45, no. 4, pp. 419–426, 1984.

[50] Y. Lai, J. Y. Chan, and R. E. Baumbach, "Electronic landscape of the f-electron intermetallics with the $ThCr_2Si_2$ structure," *Science Advances*, vol. 8, no. 32, p. eabp8264, 2022.

[51] J. M. Lawrence, P. S. Riseborough, and R. D. Parks, "Valence fluctuation phenomena," *Reports on Progress in Physics*, vol. 44, no. 1, pp. 1–84, 1981.

[52] W. Iha, T. Yara, Y. Ashitomi, M. Kakihana, T. Takeuchi, F. Honda, A. Nakamura, D. Aoki, J. Gouchi, Y. Uwatoko, T. Kida, T. Tahara, M. Hagiwara, Y. Haga, M. Hedo, T. Nakama, and Y. Ōnuki, "Electronic states in $EuCu_2(Ge_{1-x}Si_x)_2$ based on the Doniach phase diagram," *Journal of the Physical Society of Japan*, vol. 87, no. 6, p. 064706, 2018.

[53] S. Kuniyoshi and R. Shiina, "Valence Fluctuation, Spin–Orbit Coupling, and Magnetic–Nonmagnetic Crossover in Eu Compounds," *Journal of the Physical Society of Japan*, vol. 89, no. 12, p. 124711, 2020.

[54] A. Mitsuda, S. Hamano, N. Araoka, H. Yayama, and H. Wada, "Pressure-induced valence transition in antiferromagnet $EuRh_2Si_2$," *Journal of the Physical Society of Japan*, vol. 81, no. 2, p. 023709, 2012.

[55] A. Mitsuda, S. Hamano, and H. Wada, "Valence transition induced by pressure and magnetic field in antiferromagnet $EuRh_2Si_2$," *Journal of Korean Physical Society*, vol. 62, no. 12, pp. 1787–1791, 2013.

[56] E. V. Sampathkumaran, L. C. Gupta, R. Vijayaraghavan, K. V. Gopalakrishnan, R. G. Pillay, and H. G. Devare, "A new and unique Eu-based mixed valence system: $EuPd_2Si_2$," *J. Phys. C: Solid State Phys.*, vol. 14, no. 9, pp. L237–L241, 1981.

[57] K. Mimura, Y. Taguchi, S. Fukuda, A. Mitsuda, J. Sakurai, K. Ichikawa, and O. Aita, "Bulk-sensitive high-resolution photoemission study of a temperature-induced valence transition system $EuPd_2Si_2$," *Journal of Electron Spectroscopy and Related Phenomena*, vol. 137-140, pp. 529–533, 2004. ICESS-9 Proceedings of the 9th International Conference on Electronic Spectroscopy and Structure.

[58] V. Guritanu, S. Seiro, J. Sichelschmidt, N. Caroca-Canales, T. Iizuka, S. Kimura, C. Geibel, and F. Steglich, "Optical study of archetypical valence-fluctuating Eu systems," *Phys. Rev. Lett.*, vol. 109, p. 247207, 2012.

[59] B. Chevalier, J. M. D. Coey, B. Lloret, and J. Etourneau, "$EuIr_2Si_2$: a new intermediate valence compound," *J. Phys. C*, vol. 19, no. 23, pp. 4521–4528, 1986.

[60] H. Sepehri-Amin, T. Ohkubo, T. Shima, and K. Hono, "Grain boundary and interface chemistry of an Nd-Fe-B-based sintered magnet," *Acta Materialia*, vol. 60, no. 3, pp. 819–830, 2012.

[61] O. Gutfleisch, K.-H. Müller, K. Khlopkov, M. Wolf, A. Yan, R. Schäfer, T. Gemming, and L. Schultz, "Evolution of magnetic domain structures and coercivity in high-performance SmCo 2:17-type permanent magnets," *Acta Materialia*, vol. 54, no. 4, pp. 997–1008, 2006.

[62] J. Coey, "Perspectives in permanent magnetism," *Journal of Magnetism and Magnetic Materials*, vol. 140-144, pp. 1041–1044, 1995. International Conference on Magnetism.

[63] L. Tung, J. Franse, K. Buschow, P. Brommer, and N. Thuy, "A study of magnetic coupling in GdT_2Si_2 compounds (T=transition metal)," *Journal of Alloys and Compounds*, vol. 260, no. 1, pp. 35–43, 1997.

[64] G. Kaindl, A. Höhr, E. Weschke, S. Vandré, C. Schüβler-Langeheine, and C. Laubschat, "Surface core-level shifts and surface states for the heavy lanthanide metals," *Phys. Rev. B*, vol. 51, pp. 7920–7923, 1995.

[65] C. U. Segre, M. Croft, J. A. Hodges, V. Murgai, L. C. Gupta, and R. D. Parks, "Valence instability in $Eu(Pd_{1-x}Au_x)_2Si_2$: The global phase diagram," *Phys. Rev. Lett.*, vol. 49, pp. 1947–1950, 1982.

[66] A. Mitsuda, Y. Ikeda, N. Ietaka, S. Fukuda, and Y. Isikawa, "Collapse of antiferromagnetism induced by Ni-substitution in $Eu(Pt_{1-x}Ni_x)_2Si_2$," *Journal of Magnetism and Magnetic Materials*, vol. 310, no. 2, Part 1, pp. 319–321, 2007. Proceedings of the 17th International Conference on Magnetism.

[67] S. Seiro and C. Geibel, "From stable divalent to valence-fluctuating behaviour in $Eu(Rh_{1-x}Ir_x)_2Si_2$ single crystals," *Journal of Physics: Condensed Matter*, vol. 23, no. 37, p. 375601, 2011.

[68] F. Gerken, "Calculated photoemission spectra of the 4f states in the rare-earth metals," *Journal of Physics F: Metal Physics*, vol. 13, no. 3, pp. 703–713, 1983.

[69] N. Mårtensson, B. Reihl, W. D. Schneider, V. Murgai, L. C. Gupta, and R. D. Parks, "Highly resolved surface shifts in a mixed-valent system: $EuPd_2Si_2$," *Phys. Rev. B*, vol. 25, pp. 1446–1448, 1982.

[70] C. Laubschat, B. Perscheid, and W. D. Schneider, "Final-state effects and surface valence in Eu—transition-metal compounds," *Phys. Rev. B*, vol. 28, pp. 4342–4348, 1983.

[71] W. D. Schneider, C. Laubschat, G. Kalkowski, J. Haase, and A. Puschmann, "Surface effects in Eu intermetallics: A resonant photoemission study," *Phys. Rev. B*, vol. 28, pp. 2017–2022, 1983.

[72] Y. Ohno and T. Urata, "Photoelectron spectra and surface valence fluctuation of Eu in the misfit-layer compound $(EuS_{1.15})_{1.5}NbS_2$," *Journal of Electron Spectroscopy and Related Phenomena*, vol. 125, no. 3, pp. 171–180, 2002.

[73] P. Maslankiewicz and J. Szade, "Valence instability of europium in $EuCo_2Si_2$," *Journal of Alloys and Compounds*, vol. 423, no. 1-2, pp. 69–73, 2006. Fall Symposium on Multicomponent Alloys and Intermetallic Compounds for Magnetic Applications and Nanotechnology, Warsaw Polytech Univ, Warsaw, Poland, Sep 05-09, 2005.

[74] Z. Hu, K. Starke, G. van der Laan, E. Navas, A. Bauer, E. Weschke, C. Schüßler-Langeheine, E. Arenholz, A. Mühlig, G. Kaindl, J. B. Goodkoep, and N. B. Brookes, "Spin flip in resonant photoemission from Gd," *Phys. Rev. B*, vol. 59, pp. 9737–9740, 1999.

[75] M. Güttler, K. Kummer, S. Patil, M. Höppner, A. Hannaske, S. Danzenbächer, M. Shi, M. Radovic, E. Rienks, C. Laubschat, C. Geibel, and D. V. Vyalikh, "Tracing the localization of $4f$ electrons: Angle-resolved photoemission on $YbCo_2Si_2$, the stable trivalent counterpart of the heavy-fermion $YbRh_2Si_2$," *Phys. Rev. B*, vol. 90, no. 19, p. 195138, 2014.

[76] K. Kummer, S. Patil, A. Chikina, M. Güttler, M. Höppner, A. Generalov, S. Danzenbächer, S. Seiro, A. Hannaske, C. Krellner, Y. Kucherenko, M. Shi, M. Radovic, E. Rienks, G. Zwicknagl, K. Matho, J. W. Allen, C. Laubschat, C. Geibel, and D. V. Vyalikh, "Temperature-independent Fermi surface in the Kondo lattice $YbRh_2Si_2$," *Phys. Rev. X*, vol. 5, p. 011028, 2015.

[77] M. Güttler, K. Kummer, K. Kliemt, C. Krellner, S. Seiro, C. Geibel, C. Laubschat, Y. Kubo, Y. Sakurai, D. V. Vyalikh, and A. Koizumi, "Visualizing the Kondo lattice crossover in $YbRh_2Si_2$ with Compton scattering," *Phys. Rev. B*, vol. 103, p. 115126, 2021.

[78] J. H. Dil, "Spin and angle resolved photoemission on non-magnetic low-dimensional systems," *Journal of Physics: Condensed Matter*, vol. 21, no. 40, p. 403001, 2009.

[79] A. Generalov, M. M. Otrokov, A. Chikina, K. Kliemt, K. Kummer, M. Höppner, M. Güttler, S. Seiro, A. Fedorov, S. Schulz, S. Danzenbächer, E. V. Chulkov, C. Geibel, C. Laubschat, P. Dudin, M. Hoesch, T. Kim, M. Radovic, M. Shi, N. C. Plumb, C. Krellner, and D. V. Vyalikh, "Spin orientation of two-dimensional electrons driven by temperature-tunable competition of spin–orbit and exchange–magnetic interactions," *Nano Lett.*, vol. 17, no. 2, pp. 811–820, 2017.

[80] A. Generalov, M. M. Otrokov, A. Chikina, K. Kliemt, K. Kummer, M. Höppner, M. Güttler, S. Seiro, A. Fedorov, S. Schulz, S. Danzenbächer, E. V. Chulkov, C. Geibel, C. Laubschat, P. Dudin, M. Hoesch, T. Kim, M. Radovic, M. Shi, N. C. Plumb, C. Krellner, and D. V. Vyalikh, "Supporting information for *Spin orientation of two-dimensional electrons driven by temperature-tunable competition of spin–orbit and exchange–magnetic interactions*," *Nano Lett.*, vol. 17, no. 2, pp. 811–820, 2017.

[81] X. Zhang, Q. Liu, and J. e. a. Luo, "Hidden spin polarization in inversion-symmetric bulk crystals.," *Nat. Phys.*, vol. 10, p. 387–393, 2014.

[82] A. Y. Vyazovskaya, M. M. Otrokov, Y. M. Koroteev, K. Kummer, M. Güttler, D. V. Vyalikh, and E. V. Chulkov, "Origin of two-dimensional electronic states at Si- and Gd-terminated surfaces of $GdRh_2Si_2(001)$," *Phys. Rev. B*, vol. 100, p. 075140, 2019.

[83] A. Damascelli, "Probing the electronic structure of complex systems by ARPES," *Physica Scripta*, vol. T109, p. 61, 2004.

[84] B. Lv, T. Qian, and H. Ding, "Angle-resolved photoemission spectroscopy and its application to topological materials," *Nature Reviews Physics*, vol. 1, no. 10, pp. 609–626, 2019.

[85] H. Iwasawa, H. Takita, K. Goto, W. Mansuer, T. Miyashita, E. F. Schwier, A. Ino, K. Shimada, and Y. Aiura, "Accurate and efficient data acquisition methods for high-resolution angle-resolved photoemission microscopy," *Scientific Reports*, vol. 8, no. 1, 2018.

[86] Scienta Omicron, "DA30-L deflection analyser." `https://scientaomicron.com/en/Instruments/Electron-Analysers/DA30-L`, accessed: 20.06.2022.

[87] H. Beutler, "Über Absorptionsserien von Argon, Krypton und Xenon zu Termen zwischen den beiden Ionisierungsgrenzen $^2P_3^{2/0}$ und $^2P_1^{2/0}$," *Zeitschrift für Physik*, vol. 93, no. 3-4, pp. 177–196, 1935.

[88] U. Fano, "Sullo spettro di assorbimento dei gas nobili presso il limite dello spettro d'arco," *Il Nuovo Cimento (1924-1942)*, vol. 12, pp. 154–161, 1935.

[89] S. Blundell, *Magnetism in Condensed Matter*. Oxford Master Series in Condensed Matter Physics, OUP Oxford, 2001.

[90] G. Schütz, W. Wagner, W. Wilhelm, P. Kienle, R. Zeller, R. Frahm, and G. Materlik, "Absorption of circularly polarized x rays in iron," *Phys. Rev. Lett.*, vol. 58, pp. 737–740, 1987.

[91] B. T. Thole, G. van der Laan, and G. A. Sawatzky, "Strong magnetic dichroism predicted in the $M_{4,5}$ x-ray absorption spectra of magnetic rare-earth materials," *Phys. Rev. Lett.*, vol. 55, pp. 2086–2088, 1985.

[92] C. S. Fadley, *The Study of Surface Structures by Photoelectron Diffraction and Auger Electron Diffraction*, pp. 421–518. Boston, MA: Springer US, 1992.

[93] F. J. García de Abajo, M. A. Van Hove, and C. S. Fadley, "Multiple scattering of electrons in solids and molecules: A cluster-model approach," *Phys. Rev. B*, vol. 63, p. 075404, 2001.

[94] M. Greif, L. Castiglioni, D. Becker-Koch, J. Osterwalder, and M. Hengsberger, "Acquisition of photoelectron diffraction patterns with a two-dimensional wide-angle electron analyzer," *Journal of Electron Spectroscopy and Related Phenomena*, vol. 197, pp. 30–36, 2014.

[95] "Synchrotron layout (Paris SOLEIL)." `https://commons.wikimedia.org/wiki/File:Schéma_de_principe_du_synchrotron.jpg`, accessed: 14.07.2022.

[96] P. Hohenberg and W. Kohn, "Inhomogeneous electron gas," *Phys. Rev.*, vol. 136, pp. B864–B871, 1964.

[97] W. Kohn and L. J. Sham, "Self-consistent equations including exchange and correlation effects," *Phys. Rev.*, vol. 140, pp. A1133–A1138, 1965.

[98] V. I. Anisimov, J. Zaanen, and O. K. Andersen, "Band theory and Mott insulators: Hubbard U instead of Stoner I," *Phys. Rev. B*, vol. 44, pp. 943–954, 1991.

[99] B. Himmetoglu, A. Floris, S. de Gironcoli, and M. Cococcioni, "Hubbard-corrected DFT energy functionals: The LDA+U description of correlated systems," *International Journal of Quantum Chemistry*, vol. 114, no. 1, pp. 14–49, 2014.

[100] K. Koepernik and H. Eschrig, "Full-potential nonorthogonal local-orbital minimum-basis band-structure scheme," *Phys. Rev. B*, vol. 59, no. 3, p. 1743, 1999.

[101] K. Kliemt, M. Peters, F. Feldmann, A. Kraiker, D.-M. Tran, S. Rongstock, J. Hellwig, S. Witt, M. Bolte, and C. Krellner, "Crystal growth of materials with the $ThCr_2Si_2$ structure type," *Cryst. Res. Technol*, vol. 55, no. 2, p. 1900116, 2020.

[102] Bloch beamline, MAX IV laboratory. `https://www.maxiv.lu.se/accelerators-beamlines/beamlines/bloch/`.

[103] M. Hoesch, T. K. Kim, P. Dudin, H. Wang, S. Scott, P. Harris, S. Patel, M. Matthews, D. Hawkins, S. G. Alcock, T. Richter, J. J. Mudd, M. Basham, L. Pratt, P. Leicester, E. C. Longhi, A. Tamai, and F. Baumberger, "A facility for the analysis of the electronic structures of solids and their surfaces by synchrotron radiation photoelectron spectroscopy," *Review of Scientific Instruments*, vol. 88, no. 1, p. 013106, 2017.

[104] SIS beamline, SLS, PSI. `https://www.psi.ch/en/sls/sis`.

[105] M. Muntwiler, J. Zhang, R. Stania, F. Matsui, P. Oberta, U. Flechsig, L. Patthey, C. Quitmann, T. Glatzel, R. Widmer, E. Meyer, T. A. Jung, P. Aebi, R. Fasel, and T. Greber, "Surface science at the PEARL beamline of the Swiss Light Source," *Journal of Synchrotron Radiation*, vol. 24, no. 1, pp. 354–366, 2017.

[106] "Electron diffraction in atomic clusters (EDAC) for the simulation of photoelectron diffraction (PD)." `http://garciadeabajos-group.icfo.es/widgets/edac/manual/edac.html`, Accessed: 2022-03-22.

[107] K. Kummer, A. Fondacaro, E. Jimenez, E. Velez-Fort, A. Amorese, M. Aspbury, F. Yakhou-Harris, P. van der Linden, and N. B. Brookes, "The high-field magnet endstation for X-ray magnetic dichroism experiments at ESRF soft X-ray ID32," *Journal of Synchrotron Radiation*, vol. 23, no. 2, pp. 464–473, 2016.

[108] J. P. Perdew, K. Burke, and M. Ernzerhof, "Generalized gradient approximation made simple," *Phys. Rev. Lett.*, vol. 77, pp. 3865–3868, 1996.

[109] V. I. Anisimov, F. Aryasetiawan, and A. I. Lichtenstein, "First-principles calculations of the electronic structure and spectra of strongly correlated systems: the LDA+U method," *Journal of Physics: Condensed Matter*, vol. 9, no. 4, pp. 767–808, 1997.

[110] "Vienna Ab initio Simulation Package." `https://www.vasp.at/`.

[111] J. P. Perdew and Y. Wang, "Accurate and simple analytic representation of the electron-gas correlation energy," *Phys. Rev. B*, vol. 45, pp. 13244–13249, 1992.

[112] S. Schulz, A. Y. Vyazovskaya, G. Poelchen, A. Generalov, M. Güttler, M. Mende, S. Danzenbächer, M. M. Otrokov, T. Balasubramanian, C. Polley, E. V. Chulkov, C. Laubschat, M. Peters, K. Kliemt, C. Krellner, D. Y. Usachov, and D. V. Vyalikh, "Classical and cubic Rashba effect in the presence of in-plane $4f$ magnetism at the iridium silicide surface of the antiferromagnet $GdIr_2Si_2$," *Phys. Rev. B*, vol. 103, p. 035123, 2021.

[113] R. Coehoorn, K. Buschow, M. Dirken, and R. Thiel, "Valence-electron contributions to the electric-field gradient in hcp metals and at Gd nuclei in intermetallic compounds with the $ThCr_2Si_2$ structure," *Physical Review. B, Condensed matter*, vol. 42, pp. 4645–4655, 1990.

[114] D. Rossi, R. Marazza, and R. Ferro, "Ternary RMe_2X_2 alloys of the rare earths with the precious metals and silicon (or germanium)," *Journal of the Less Common Metals*, vol. 66, no. 2, pp. P17–P25, 1979.

[115] Ślaski M. and Szytuła A., "Crystal structure and magnetic properties of $REMe_2Si_2$ compounds (RE≡Gd, Dy, Ho, Er; Me≡ Ru, Rh, Pd, Ir)," *Journal of The Less-Common Metals*, vol. 87, no. 2, p. L1–L3, 1982.

[116] M. Dirken, R. Thiel, and K. Buschow, "Crystal-field effects in rare earth compounds with the $ThCr_2Si_2$ structure," *Journal of the Less Common Metals*, vol. 147, no. 1, pp. 97–104, 1989.

[117] G. Czjzek, V. Oestreich, H. Schmidt, K. Łąka, and K. Tomala, "A study of compounds GdT_2Si_2 by Mössbauer spectroscopy and by bulk magnetization measurements," *Journal of Magnetism and Magnetic Materials*, vol. 79, no. 1, pp. 42–56, 1989.

[118] K. Łątka, "^{155}Gd isomer shifts. The case study: GdT_2Si_2," *Nukleonika*, vol. 58, pp. 23–26, 2013.

[119] K. Kliemt, J. Reusch, M. Bolte, and C. Krellner, "Effect of symmetry reduction on the magnetic properties of $LnIr_2Si_2$ polymorphs," *Journal of Magnetism and Magnetic Materials*, vol. 552, p. 169199, 2022.

[120] J. Henk, M. Hoesch, J. Osterwalder, A. Ernst, and P. Bruno, "Spin–orbit coupling in the L-gap surface states of Au(111): spin-resolved photoemission experiments and first-principles calculations," *Journal of Physics: Condensed Matter*, vol. 16, no. 43, pp. 7581–7597, 2004.

[121] I. A. Nechaev and E. E. Krasovskii, "*Ab initio* $\boldsymbol{k}\cdot\boldsymbol{p}$ theory of spin-momentum locking: Application to topological surface states," *Phys. Rev. B*, vol. 102, p. 115437, 2020.

[122] P. Zhang, P. Richard, T. Qian, Y.-M. Xu, X. Dai, and H. Ding, "A precise method for visualizing dispersive features in image plots," *Review of Scientific Instruments*, vol. 82, no. 4, p. 043712, 2011.

[123] S. Schulz, I. A. Nechaev, M. Güttler, G. Poelchen, A. Generalov, S. Danzenbächer, A. Chikina, S. Seiro, K. Kliemt, A. Y. Vyazovskaya, T. K. Kim, P. Dudin, E. V. Chulkov, C. Laubschat, E. E. Krasovskii, C. Geibel, C. Krellner, K. Kummer, and D. V. Vyalikh, "Emerging 2D-ferromagnetism and strong spin-orbit coupling at the surface of valence-fluctuating $EuIr_2Si_2$," *npj Quantum Mater.*, vol. 4, no. 1, pp. 1–8, 2019.

[124] S. Patil, R. Nagarajan, L. Gupta, R. Vijayaraghavan, and B. Padalia, "^{151}eu-mössbauer investigations in a new Eu-based mixed valent material $EuIr_2Si_2$," *Solid State Communications*, vol. 63, no. 11, pp. 955–958, 1987.

[125] S. Seiro, Y. Prots, K. Kummer, H. Rosner, R. C. Gil, and C. Geibel, "Charge, lattice and magnetism across the valence crossover in $EuIr_2Si_2$ single crystals," *Journal of Physics: Condensed Matter*, vol. 31, no. 30, p. 305602, 2019.

[126] S. Patil, A. Generalov, M. Güttler, P. Kushwaha, A. Chikina, K. Kummer, T. C. Rödel, A. F. Santander-Syro, N. Caroca-Canales, C. Geibel, S. Danzenbächer, Y. Kucherenko, C. Laubschat, J. W. Allen, and D. V. Vyalikh, "ARPES view on surface and bulk hybridization phenomena in the antiferromagnetic Kondo lattice $CeRh_2Si_2$," *Nature Comm.*, vol. 7, p. 11029, 2016.

[127] K. Kummer, Y. Kucherenko, S. Danzenbächer, C. Krellner, C. Geibel, M. G. Holder, L. V. Bekenov, T. Muro, Y. Kato, T. Kinoshita, S. Huotari, L. Simonelli, S. L. Molodtsov, C. Laubschat, and D. V. Vyalikh, "Intermediate valence in Yb compounds probed by $4f$ photoemission and resonant inelastic x-ray scattering," *Phys. Rev. B*, vol. 84, p. 245114, 2011.

[128] F. Honda, K. Okauchi, Y. Sato, A. Nakamura, H. Akamine, Y. Ashitomi, M. Hedo, T. Nakama, T. Takeuchi, J. Valenta, J. Prchal, V. Sechovský, D. Aoki, and Y. Ōnuki, "Pressure-induced valence change and moderate heavy fermion state in Eu-compounds," *Physica B: Condensed Matter*, vol. 536, pp. 182–191, 2018.

[129] J. M. Imer and E. Wuilloud, "A simple model calculation for XPS, BIS and EELS 4f-excitations in Ce and La compounds," *Zeitschrift für Physik B Condensed Matter*, vol. 66, no. 2, pp. 153–160, 1987.

[130] N. Mårtensson, B. Reihl, W. D. Schneider, V. Murgai, L. C. Gupta, and R. D. Parks, "Highly resolved surface shifts in a mixed-valent system: $EuPd_2Si_2$," *Phys. Rev. B*, vol. 25, pp. 1446–1448, 1982.

[131] S.-i. Kimura, M. Okuno, H. Iwata, T. Saitoh, T. Okuda, A. Harasawa, T. Kinoshita, A. Mitsuda, H. Wada, and M. Shiga, "Temperature-induced valence transition of $EuNi_2(Si_{0.25}Ge_{0.75})_2$ studied by Eu $4d-4f$ resonant photoemission and optical conductivity," *Journal of the Physical Society of Japan*, vol. 71, no. Suppl, pp. 255–257, 2002.

[132] D. Yu. Usachov, M. Güttler, S. Schulz, G. Poelchen, S. Seiro, K. Kliemt, K. Kummer, C. Krellner, C. Laubschat, E. V. Chulkov, and D. V. Vyalikh, "Spin structure of spin-orbit split surface states in a magnetic material revealed by spin-integrated photoemission," *Phys. Rev. B*, vol. 101, no. 24, p. 245140, 2020.

[133] M. Abbate, J. B. Goedkoop, F. M. F. de Groot, M. Grioni, J. C. Fuggle, S. Hofmann, H. Petersen, and M. Sacchi, "Probing depth of soft x-ray absorption spectroscopy measured in total-electron-yield mode," *Surface and Interface Analysis*, vol. 18, no. 1, pp. 65–69, 1992.

[134] B. H. Frazer, B. Gilbert, B. R. Sonderegger, and G. De Stasio, "The probing depth of total electron yield in the sub-keV range: TEY-XAS and X-PEEM," *Surface Science*, vol. 537, no. 1, pp. 161–167, 2003.

[135] N. Brookes, F. Yakhou-Harris, K. Kummer, A. Fondacaro, J. Cezar, D. Betto, E. Velez-Fort, A. Amorese, G. Ghiringhelli, L. Braicovich, R. Barrett, G. Berruyer, F. Cianciosi, L. Eybert, P. Marion, P. van der Linden, and L. Zhang,

"The beamline ID32 at the ESRF for soft X-ray high energy resolution resonant inelastic X-ray scattering and polarisation dependent X-ray absorption spectroscopy," *Nuclear Instruments and Methods in Physics Research Section A: Accelerators, Spectrometers, Detectors and Associated Equipment*, vol. 903, pp. 175–192, 2018.

[136] S. Seiro, K. Kummer, D. Vyalikh, N. Caroca-Canales, and C. Geibel, "Anomalous susceptibility in single crystals of $EuCo_2Si_2$ with trivalent Eu: Influence of excited J multiplets," *physica status solidi (b)*, vol. 250, no. 3, pp. 621–625, 2013.

[137] M. W. Haverkort, "*Quanty* for core level spectroscopy - excitons, resonances and band excitations in time and frequency domain," *Journal of Physics: Conference Series*, vol. 712, p. 012001, 2016.

[138] D. Yu. Usachov, A. V. Tarasov, S. Schulz, K. A. Bokai, I. I. Tupitsyn, G. Poelchen, S. Seiro, N. Caroca-Canales, K. Kliemt, M. Mende, K. Kummer, C. Krellner, M. Muntwiler, H. Li, C. Laubschat, C. Geibel, E. V. Chulkov, S. I. Fujimori, and D. V. Vyalikh, "Photoelectron diffraction for probing valency and magnetism of $4f$-based materials: A view on valence-fluctuating $EuIr_2Si_2$," *Phys. Rev. B*, vol. 102, p. 205102, 2020.

[139] Wikipedia, the free encyclopedia, "Orthographic projection." `https://en.wikipedia.org/wiki/Orthographic_projection`, accessed: 10.08.2022.

[140] M. Melamud, H. Pinto, I. Felner, and H. Shaked, "Neutron diffraction study of the magnetic structure of the intermetallic compound $DyRh_2Si_2$," *Journal of Applied Physics*, vol. 55, no. 6, pp. 2034–2035, 1984.

[141] E. Raymenants, M. Heyns, and V. D. Nguyen, "Spintronic logic based on magnetic domain walls," 2022.

[142] J. Grollier, D. Querlioz, K. Camsari, K. Everschor-Sitte, S. Fukami, and M. D. Stiles, "Neuromorphic spintronics," *Nature electronics*, vol. 3, no. 7, pp. 360–370, 2020.

[143] L. Prochaska, X. Li, D. C. MacFarland, A. M. Andrews, M. Bonta, E. F. Bianco, S. Yazdi, W. Schrenk, H. Detz, A. Limbeck, Q. Si, E. Ringe, G. Strasser, J. Kono, and S. Paschen, "Singular charge fluctuations at a magnetic quantum critical point," *Science*, vol. 367, no. 6475, pp. 285–288, 2020.

[144] E. Bakali, W. Artner, M. Beiser, J. Bernardi, H. Detz, G. Eguchi, A. Foelske, M. Giparakis, C. Herzig, A. Limbeck, H. Nguyen, L. Prochaska, A. Prokofiev, M. Sauer, S. Schwarz, W. Schrenk, G. Strasser, R. Svagera, M. Taupin, A. Thirsfeld, M. Waas, X. Yan, D. Zocco, A. Andrews, and S. Paschen, "A Knudsen cell approach for the molecular beam epitaxy of the heavy fermion compound $YbRh_2Si_2$," *Journal of Crystal Growth*, vol. 595, p. 126804, 2022.

[145] G. Poelchen, I. P. Rusinov, S. Schulz, M. Güttler, M. Mende, A. Generalov, D. Y. Usachov, S. Danzenbächer, J. Hellwig, M. Peters, K. Kliemt, Y. Kucherenko,

V. N. Antonov, C. Laubschat, E. V. Chulkov, A. Ernst, K. Kummer, C. Krellner, and D. V. Vyalikh, "Interlayer coupling of a two-dimensional Kondo lattice with a ferromagnetic surface in the antiferromagnet $CeCo_2P_2$," *ACS Nano*, vol. 16, no. 3, pp. 3573–3581, 2022. PMID: 35156797.

A. Surface relaxation effects

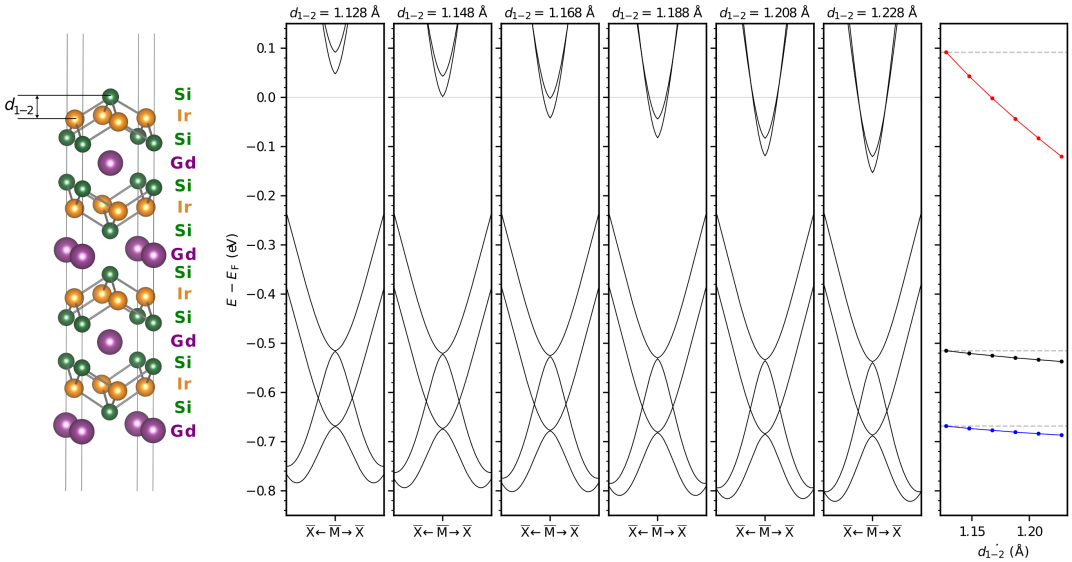

Fig. A.1.: Interlayer distance d_{1-2} between the Si-surface and the adjacent Ir layer and the dependence of the energy position of surface state bands on the former. Left: 16-layer slab with Si- and Gd-terminated surfaces. Middle: Band dispersions for the surface states α, β and γ for d_{1-2} increasing from 1.128 Å (left) to 1.228 Å (right). Right: Energy of the α, β and γ bands in the $\overline{\mathrm{M}}$ point in black, blue and red, respectively, in dependence on the interlayer spacing.

Throughout this work, the calculated band structure of $GdIr_2Si_2$ is given for a fully relaxed slab. This implies that at first the total energy has been minimised with respect to the lattice parameters a and c of the tetragonal bulk unit cell, as well as to the z position of Si. Then these parameters have been used to build a slab of 16 atomic layers for which the total energy has been minimised, too, by variation of the z positions of all atomic layers. For the Si-terminated surface, the relaxation procedure results in a strongly reduced interlayer spacing between the topmost Si and the adjacent Ir layer. While in the bulk the computed Si–Ir interlayer distance is about 1.295 Å, at the surface, it reduces by about 4.4 % to 1.238 Å. Since the surface state

γ is strongly localised in the two topmost layers it is highly sensitive to the distance between the latter. To demonstrate the dependence of the energy position of the γ bands on the interlayer spacing d_{1-2}, we performed band structure calculations for different values of d_{1-2} in a scalar-relativistic setting neglecting the spin-orbit coupling. The resulting band structures are shown in Fig. A.1 along $\overline{\mathrm{X}}$–$\overline{\mathrm{M}}$–$\overline{\mathrm{X}}$ with increasing interlayer spacing from left to right and d_{1-2} ranging between 1.128 Å and 1.228 Å. On the right-hand side of Fig. A.1 the energy of the bands belonging to α, β and γ in the $\overline{\mathrm{M}}$ point is plotted in dependence on the interlayer spacing in black, blue and red, respectively. It is obvious, that the stepwise increase of the interlayer spacing results in a rather strong downward shift of the γ bands toward higher binding energies. At the same time, the bands formed by the surface states α and β show the same trend but shift much less than for γ. We may thus conclude, that the FPLO relaxation routine correctly describes the general trend of approaching Si and Ir layers at the surface. However, correctly reproducing the ARPES data for the γ bands, which hardly cross the Fermi level, would require a further reduction of the interlayer spacing d_{1-2}.

Although manually changing d_{1-2} can improve the agreement of the calculated surface electronic structure with the experimental data around the $\overline{\mathrm{M}}$ point, note, that this is not the case for other features in other regions of the SBZ that were not discussed in this thesis. This is particularly true for the Dirac cone located around the $\overline{\Gamma}$ point of the SBZ. Trying to fit all prominent features of the surface electronic structure to the experimental data it turned out, that a fair agreement of the calculated bands with the ARPES data is achieved if the z positions of at least eight atomic layers on top of the slab are close to the ones obtained from the relaxation procedure. Further improvement could be achieved considering larger slabs with more than 16 atomic layers.

List of Publications

Peer reviewed

1. Tarasov, A. V., Glazkova, D., Schulz, S., Poelchen, G., Kliemt, K., Kraiker, A., Muntwiler, M., Laubschat, C., Generalov, A., Polley, C., Krellner, C., Vyalikh, D. V. & Usachov, D. Yu. Crystal electric field and properties of $4f$ magnetic moments at the surface of the rare-earth compound $TbRh_2Si_2$. *Phys. Rev. B* **106**, 15, 155136 (2022)

   https://doi.org/10.1103/PhysRevB.106.155136

2. Usachov, D. Yu., Glazkova, D., Tarasov, A., Schulz, S., Poelchen, G., Bokai, K., Vilkov, O., Dudin, P., Kummer, K., Kliemt, K., Krellner, C. & Vyalikh, D. V. "Estimating the Orientation of 4f Magnetic Moments by Classical Photoemission" *The Journal of Physical Chemistry Letters* **13** (33), 7861-7869 (2022)

   https://doi.org/10.1021/acs.jpclett.2c02203

3. Tarasov, A. V., Mende, M., Ali, K., Poelchen, G., Schulz, S., Vilkov, O. Yu., Bokai, K. A., Muntwiler, M., Mandic, V., Laubschat, C., Kliemt, K., Krellner, C., Vyalikh, D. V. & Usachov, D. Yu. Structural instability at the In-terminated surface of the heavy-fermion superconductor $CeIrIn_5$. *Surfaces and Interfaces* **32**, 102126 (2022).

   https://doi.org/10.1016/j.surfin.2022.102126.

4. Poelchen, G., Rusinov, I. P., Schulz, S., Güttler, M., Mende, M., Generalov, A., Usachov, D. Yu., Danzenbächer, S., Hellwig, J., Peters, M., Kliemt,K., Kucherenko, Yu., Antonov, V. N., Laubschat, C., Chulkov, E. V., Ernst, A., Kummer, K., Krellner, C. & Vyalikh, D. V. Interlayer Coupling of a Two-Dimensional Kondo Lattice with a Ferromagnetic Surface in the Antiferromagnet $CeCo_2P_2$. *ACS Nano* **16**, 3573-3581 (2022).

   https://doi.org/10.1021/acsnano.1c10705

5. Mende, M., Ali, K., Poelchen, G., Schulz, S., Mandic, V., Tarasov, A. V., Polley, C., Generalov, A., Fedorov, A. V., Güttler, M., Laubschat, C., Kliemt, K.,

Koroteev, Y. M., Chulkov, E. V., Kummer, K., Krellner, C., Usachov, D. Yu. & Vyalikh, D. V., Strong Rashba Effect and Different *f*-*d* Hybridization Phenomena at the Surface of the Heavy-Fermion Superconductor $CeIrIn_5$. *Adv. Electron. Mater.* **8**, 2100768 (2022).

https://doi.org/10.1002/aelm.202100768

6. Fedorov, A. V., Poelchen, G., Eremeev, S. V., Schulz, S., Generalov, A., Polley, C., Laubschat, C., Kliemt, K., Kaya, N., Krellner, C., Chulkov, E. V., Kummer, K., Usachov, D. Yu., Ernst, A. & Vyalikh, D. V. Insight into the Temperature Evolution of Electronic Structure and Mechanism of Exchange Interaction in EuS. *The Journal of Physical Chemistry Letters* **12**, 8328-8334 (2021).

   https://doi.org/10.1021/acs.jpclett.1c02274

7. Schulz, S., Vyazovskaya, A. Yu., Poelchen, G., Generalov, A., Güttler, M., Mende, M., Danzenbächer, S., Otrokov, M. M., Balasubramanian, T., Polley, C., Chulkov, E. V., Laubschat, C., Peters, M., Kliemt, K., Krellner, C., Usachov, D. Yu. & Vyalikh, D. V. Classical and cubic Rashba effect in the presence of in-plane $4f$ magnetism at the iridium silicide surface of the antiferromagnet $GdIr_2Si_2$. *Phys. Rev. B* **103**, 035123 (2021).

   https://doi.org/10.1103/PhysRevB.103.035123

8. Usachov, D. Yu., Tarasov, A. V., Schulz, S., Bokai, K. A., Tupitsyn, I. I., Poelchen, G., Seiro, S., Caroca-Canales, N., Kliemt, K., Mende, M., Kummer, K., Krellner, C., Muntwiler, M., Hang Li, Laubschat, C., Geibel, C., Chulkov, E. V., Fujimori, S. I. & Vyalikh, D. V. Photoelectron diffraction for probing valency and magnetism of $4f$-based materials: A view on valence-fluctuating $EuIr_2Si_2$. *Phys. Rev. B* **102**, 205102 (2020).

   https://doi.org/10.1103/PhysRevB.102.205102

9. Poelchen, G., Schulz, S., Mende, M., Güttler, M., Generalov, A., Fedorov, A. V., Caroca-Canales, N., Geibel, C., Kliemt, K., Krellner, C., Danzenbächer, S., Dudin, P., Antonov, V. N., Allen, J. W., Laubschat, C., Kummer, K., Kucherenko, Y. & Vyalikh, D. V. Unexpected differences between surface and bulk spectroscopic and implied Kondo properties of heavy fermion $CeRh_2Si_2$ *npj Quantum Mater.* **5**, 70 (2020).

   https://doi.org/10.1038/s41535-020-00273-7

10. Usachov, D. Y., Nechaev, I. A., Poelchen, G., Güttler, M., Krasovskii, E. E., Schulz, S., Generalov, A., Kliemt, K., Kraiker, A., Krellner, C., Kummer, K., Danzenbächer, S., Laubschat, C., Weber, A. P., Sánchez-Barriga, J., Chulkov, E. V., Santander-Syro, A. F., Imai, T., Miyamoto, K., Okuda, T. & Vyalikh, D. V. Cubic Rashba Effect in the Surface Spin Structure of Rare-Earth Ternary Materials. *Phys. Rev. Lett.* **124**, 237202 (2020).

    https://doi.org/10.1103/PhysRevLett.124.237202

11. Usachov, D. Y., Güttler, M., Schulz, S., Poelchen, G., Seiro, S., Kliemt, K., Kummer, K., Krellner, C., Laubschat, C., Chulkov, E. V. & Vyalikh, D. V. Spin Structure of Spin-Orbit Split Surface States in a Magnetic Material Revealed by Spin-Integrated Photoemission. *Phys. Rev. B* **101**, 245140 (2020).

https://doi.org/10.1103/PhysRevB.101.245140

12. Schulz, S., Nechaev, I. A., Güttler, M., Poelchen, G., Generalov, A., Danzenbächer, S., Chikina, A., Seiro, S., Kliemt, K., Vyazovskaya, A. Y., Kim, T. K., Dudin, P., Chulkov, E. V., Laubschat, C., Krasovskii, E. E., Geibel, C., Krellner, C., Kummer, K. & Vyalikh, D. V. Emerging 2D-Ferromagnetism and Strong Spin-Orbit Coupling at the Surface of Valence-Fluctuating $EuIr_2Si_2$. *npj Quantum Mater.* **4**, 26 (2019).

https://doi.org/10.1038/s41535-019-0166-z

13. Generalov, A., Otrokov, M. M., Chikina, A., Kliemt, K., Kummer, K., Höppner, M., Güttler, M., Seiro, S., Fedorov, A., Schulz, S., Danzenbächer, S., Chulkov, E. V., Geibel, C., Laubschat, C., Dudin, P., Hoesch, M., Kim, T., Radovic, M., Shi, M., Plumb, N. C., Krellner, C. & Vyalikh. Spin Orientation of Two-Dimensional Electrons Driven by Temperature-Tunable Competition of Spin–Orbit and Exchange–Magnetic Interactions. *Nano Lett.* **17**, 811–820 (2017).

https://doi.org/10.1021/acs.nanolett.6b04036

14. Güttler, M., Generalov, A., Otrokov, M. M., Kummer, K., Kliemt, K., Fedorov, A., Chikina, A., Danzenbächer, Schulz, S., S., Chulkov, E. V., Koroteev, Y. M., Caroca-Canales, N., Shi, M., Radovic, M., Geibel, C., Laubschat, C., Dudin, P., Kim, T. K., Hoesch, M., Krellner, C. & Vyalikh, D. V. Robust and Tunable Itinerant Ferromagnetism at the Silicon Surface of the Antiferromagnet $GdRh_2Si_2$. *Sci. Rep.* **6**, 24254 (2016).

https://doi.org/10.1038/srep24254

Acknowledgements

A comprehensive work like this thesis is the result of an extensive teamwork. Once a research question has been formulated, funding needs to be organised and beamtime proposals need to be written. For measurements, samples are required and a large amount of data has to be measured, analysed, modelled and discussed before a new puzzle piece is ready to be shared with the community, hopefully contributing to a better understanding of the field. Therefore, I wish to express my sincere gratitude to all the people, who have been directly or indirectly involved in this work.

First of all, I wish to acknowledge my supervisor Denis Vyalikh, who is the driving force behind our team taking care of simply everything, from the design of the research to successful application for and realisation of beamtimes to publication, and in this, always striving to combine the useful with the pleasant. Thanks a lot to our team from Dresden with whom the ARPES measurements presented here were performed, discussed and analysed. In this regard, I thank Steffen Danzenbächer, Monika Güttler and Max Mende. Special thanks to Georg Poelchen for being the best buddy ever, for your immense support throughout the years, for your almost infinite patience and for making sure it never gets boring. I also want to thank Alexander Generalov from MAX IV who supported many ARPES beamtimes and was especially involved in measuring $GdIr_2Si_2$. Also, I am grateful to Kurt Kummer from the ESRF for performing and evaluating complementary XMCD and XMLD measurements on $EuIr_2Si_2$ and giving me the opportunity to participate in similar measurements. Beautiful data have been obtained from high-quality single crystals. In this sense, many thanks to Cornelius Krellner and Kristin Kliemt from the Goethe Universität Frankfurt am Main, who provide us not only with high-quality crystals but also ideas and advice. Accordingly, I want to thank Christoph Geibel, Silvia Seiro and Nubia Caroca-Canales from the Max-Planck Institute in Dresden, especially for the amazing $EuIr_2Si_2$ crystals. For his great efforts concerning measurements and modelling I acknowledge Dmitry Usachov from the Saint Petersburg State University. For support in theoretical modelling and fruitful discussions, I wish to acknowledge our collaborators Evgueni Chulkov from the Donostia International Physics Centre (DIPC) as well as Mikhail Otrokov and Ilya Nechaev from the Centro de Física de Materiales (CFM) in Donostia. Special thanks to Alexandra Vyazovskaya from the Tomsk State University for productive cooperation in studying $GdIr_2Si_2$. Many thanks to the beamline staff at DLS, SLS, BESSY II,

MAX IV for their support during many hours of beamtime. I am deeply grateful to my family, especially my parents, and my friends for accompanying me on this journey and being patient, understanding and supportive. Finally, I wish to express my sincere gratitude to my doctorate supervisor professor Clemens Laubschat who gave me the chance to complete my PhD in his group, for all-encompassing support and the liberty in learning and developing freely.

Statement of authorship

I hereby certify that I have authored this Dissertation entitled *Two-dimensional ferromagnetism, strong Rashba effect and valence changes in lanthanide intermetallics* independently and without undue assistance from third parties. No other than the resources and references indicated in this thesis have been used. I have marked both literal and accordingly adopted quotations as such. There were no additional persons involved in the intellectual preparation of the present thesis. I am aware that violations of this declaration may lead to subsequent withdrawal of the degree.

Dresden, 24 October 2022

Susanne Schulz